Ultra narrow band based IoT networks

Yuqi Mo

N°d'ordre NNT : 2018LYSEI069

THESE de DOCTORAT DE L'UNIVERSITE DE LYON
opérée au sein de
l'Institut National des Sciences Appliquées de Lyon

Ecole Doctorale 160
Electronique, Electrotechnique et Automatique

Spécialité/ discipline de doctorat :

Traitement du Signal et de l'Image

Soutenue publiquement le 26/09/2018, par:
Yuqi MO

Ultra Narrow Band based IoT networks

Devant le jury composé de :

ANTON-HARO Carles	Directeur de recherche	Centre technology de Télécommunications de Catalunya, Catalunya	Rapporteur
DI RENZO Marco	HDR	Université Paris-Saclay, France	Rapporteur
HELARD Maryline	Professeur	INSA-Rennes, France	Examinatrice
VERDONE Roberto	Professeur	University of Bologna, Italie	Examinateur
GORCE Jean-Marie	Professeur	INSA-Lyon, France	Directeur de thèse
GOURSAUD Claire	HDR	INSA-Lyon, France	Co-directrice de thèse
PONSARD Benoît	Ingénieur	Sigfox, France	Invité

Département FEDORA – INSA Lyon - Ecoles Doctorales – Quinquennal 2016-2020

SIGLE	ECOLE DOCTORALE	NOM ET COORDONNEES DU RESPONSABLE
CHIMIE	**CHIMIE DE LYON** **http://www.edchimie-lyon.fr** Sec. : Renée EL MELHEM Bât. Blaise PASCAL, 3e étage **secretariat@edchimie-lyon.fr** INSA : R. GOURDON	M. Stéphane DANIELE Institut de recherches sur la catalyse et l'environnement de Lyon IRCELYON-UMR 5256 Équipe CDFA 2 Avenue Albert EINSTEIN 69 626 Villeurbanne CEDEX **directeur@edchimie-lyon.fr**
E.E.A.	**ÉLECTRONIQUE, ÉLECTROTECHNIQUE, AUTOMATIQUE** **http://edeea.ec-lyon.fr** Sec. : M.C. HAVGOUDOUKIAN **ecole-doctorale.eea@ec-lyon.fr**	M. Gérard SCORLETTI École Centrale de Lyon 36 Avenue Guy DE COLLONGUE 69 134 Écully Tél : 04.72.18.60.97 Fax 04.78.43.37.17 **gerard.scorletti@ec-lyon.fr**
E2M2	**ÉVOLUTION, ÉCOSYSTÈME, MICROBIOLOGIE, MODÉLISATION** **http://e2m2.universite-lyon.fr** Sec. : Sylvie ROBERJOT Bât. Atrium, UCB Lyon 1 Tél : 04.72.44.83.62 INSA : H. CHARLES **secretariat.e2m2@univ-lyon1.fr**	M. Philippe NORMAND UMR 5557 Lab. d'Ecologie Microbienne Université Claude Bernard Lyon 1 Bâtiment Mendel 43, boulevard du 11 Novembre 1918 69 622 Villeurbanne CEDEX **philippe.normand@univ-lyon1.fr**
EDISS	**INTERDISCIPLINAIRE SCIENCES-SANTÉ** **http://www.ediss-lyon.fr** Sec. : Sylvie ROBERJOT Bât. Atrium, UCB Lyon 1 Tél : 04.72.44.83.62 INSA : M. LAGARDE **secretariat.ediss@univ-lyon1.fr**	Mme Emmanuelle CANET-SOULAS INSERM U1060, CarMeN lab, Univ. Lyon 1 Bâtiment IMBL 11 Avenue Jean CAPELLE INSA de Lyon 69 621 Villeurbanne Tél : 04.72.68.49.09 Fax : 04.72.68.49.16 **emmanuelle.canet@univ-lyon1.fr**
INFOMATHS	**INFORMATIQUE ET MATHÉMATIQUES** **http://edinfomaths.universite-lyon.fr** Sec. : Renée EL MELHEM Bât. Blaise PASCAL, 3e étage Tél : 04.72.43.80.46 Fax : 04.72.43.16.87 **infomaths@univ-lyon1.fr**	M. Luca ZAMBONI Bât. Braconnier 43 Boulevard du 11 novembre 1918 69 622 Villeurbanne CEDEX Tél : 04.26.23.45.52 **zamboni@maths.univ-lyon1.fr**
Matériaux	**MATÉRIAUX DE LYON** **http://ed34.universite-lyon.fr** Sec. : Marion COMBE Tél : 04.72.43.71.70 Fax : 04.72.43.87.12 Bât. Direction **ed.materiaux@insa-lyon.fr**	M. Jean-Yves BUFFIÈRE INSA de Lyon MATEIS - Bât. Saint-Exupéry 7 Avenue Jean CAPELLE 69 621 Villeurbanne CEDEX Tél : 04.72.43.71.70 Fax : 04.72.43.85.28 **jean-yves.buffiere@insa-lyon.fr**
MEGA	**MÉCANIQUE, ÉNERGÉTIQUE, GÉNIE CIVIL, ACOUSTIQUE** **http://edmega.universite-lyon.fr** Sec. : Marion COMBE Tél : 04.72.43.71.70 Fax : 04.72.43.87.12 Bât. Direction **mega@insa-lyon.fr**	M. Jocelyn BONJOUR INSA de Lyon Laboratoire CETHIL Bâtiment Sadi-Carnot 9, rue de la Physique 69 621 Villeurbanne CEDEX **jocelyn.bonjour@insa-lyon.fr**
ScSo	**ScSo*** **http://ed483.univ-lyon2.fr** Sec. : Viviane POLSINELLI Brigitte DUBOIS INSA : J.Y. TOUSSAINT Tél : 04.78.69.72.76 **viviane.polsinelli@univ-lyon2.fr**	M. Christian MONTES Université Lyon 2 86 Rue Pasteur 69 365 Lyon CEDEX 07 **christian.montes@univ-lyon2.fr**

ScSo : Histoire, Géographie, Aménagement, Urbanisme, Archéologie, Science politique, Sociologie,

三年如一梦。
愿这个梦可以伴我走过以后的万水千山。
致爱我和我爱的人。

Abstract

Sigfox rises as a promising candidate dedicated for long-distance and low-power transmissions in the IoT backgrounds. Ultra Narrow Band (UNB), being the communication technology chosen by Sigfox, allows to transmit information through signals whose bandwidth is very limited, typically 100 Hz. Due to the imprecision restraint on electronic devices, it is impossible to transmit UNB signals in orthogonal channels. The natural radio access for this kind of system is thus random ALOHA, in both time and frequency domain. This random access can induce collisions which degrades the networks performance.

The aim of this thesis is to characterize the capacity of UNB based networks, as well as to enhance its performance, by considering the randomness in time and frequency.

The first contribution of the thesis, is the theoretical and numerical capacity evaluation under idealized and realistic channel conditions, for mono base station (BS) case. Under idealized conditions, we have quantified this capacity for generalized ALOHA case and extended for replications. We highlight the time-frequency duality in UNB systems, and that there exists an optimum replication number for a given network parameter set.

Under realistic conditions, we have taken into account the specific spectral interference of UNB systems and propagation path loss (without and with Rayleigh fading) to characterize the performance, with the aid of stochastic geometry.

The second contribution is the enhancement of UNB network performance in single BS case. We propose to use successive interference cancellation (SIC) in UNB networks, which allows to mitigate the interference. We have provided a theoretical analysis by considering both SIC and the spectral interference, for mono-BS case. We bring to light the efficiency of SIC in enhancing UNB system performance.

The third contribution is the improvement of UNB systems, by exploiting the multiple BS diversity. An analytical performance evaluation considering the simplest selection combining is conducted. In particular, we consider the interference viewed by all the BSs are correlated. Then we apply more complex signal combining technologies such as MRC (max ratio combining) and EGC (equal gain combining), and even interference cancellation across multi-BS in UNB networks. We evaluate the performance improvement that each technology can bring, and compare them with each other. We highlight the efficiency of these multi-BS technologies which allow us to achieve significant performance enhancement compared to mono-BS (e.x. 125 times better performance with global SIC).

Last but not least, we experimentally verify the the spectral interference model and network capacity on a cognitive radio testbed.

Résumé

La compagnie Sigfox est reconnue comme un acteur prometteur pour des transmissions de longue-distance et faible consommation, dans le contexte de l'IoT. La modulation à bande ultra étroite (Ultra Narrow Band (UNB)), la technologie de communication choisie par Sigfox, permet de transmettre des informations dans des bandes de signal très étroites (typiquement 100 Hz). A cause de l'imprécision fréquentielle causée par les oscillateurs générateurs de fréquence, il n'est pas réaliste de transmettre des signaux UNB dans des canaux parfaitement orthogonaux. L'accès naturel au canal radio pour le système de UNB est de type ALOHA, avec un aspect aléatoire à la fois en en temps et en fréquence. Cet accès aléatoire peut introduire des collisions qui dégradent la performance du réseau.

Le but de cette thèse est de caractériser la capacité des réseaux basés sur UNB, ainsi que d'améliorer la performance en considérant l'aspect aléatoire en temps et en fréquence.

La première contribution de cette thèse, est une évaluation de la capacité en théorie et en simulation pour une seule station de base (BS), sous des conditions de canal idéaliste ou réaliste. En conditions idéalistes, nous avons exprimé la capacité pour le cas de l'ALOHA généralisé, et l'avons étendu aux cas de réplications. Pour les conditions réalistes, nous avons pris en compte l'interférence spectrale d'UNB et le path loss (sans et avec Rayleigh fading) afin de caractériser la performance des réseaux UNB, avec l'outil géométrie stochastique.

La deuxième contribution est d'appliquer l'annulation successive d'interférence (SIC), qui nous permet d'atténuer les interférences, dans des réseaux de UNB. Nous avons fourni une analyse théorique de la performance des réseaux en considérant le SIC et l'interférence spectrale de UNB, pour le cas de mono-BS. Nous avons démontré que le SIC permet d'améliorer efficacement les performances des systèmes UNB.

La troisième contribution est l'amélioration de la performance des réseaux UNB, en exploitant la diversité de multi-BS. Nous avons fait une analyse théorique de performance en considérant multi-BS et selection combining (SC). En particulier, nous avons considéré que l'interférence vue par chaque BS est corrélée. Nous avons ainsi démontré mathématiquement que cette corrélation ne peut pas être supprimée dans des systèmes UNB. Ensuite, nous avons appliqué les technologies de la combinaison des signaux plus complexes comme MRC (max ratio combining) et EGC (equal gain combining), ainsi que le SIC à travers multi-BS. Nous avons évalué l'amélioration de performance que chaque technologie apporte, et les avons comparées. Nous avons souligné l'efficacité de ces technologies qui nous permettent d'obtenir des gains importants comparés au cas mono-BS (e.x. 125 fois plus de réduction d'erreur avec SIC globale).

La dernière contribution est une validation expérimentale du modèle d'interférence spectrale de UNB, ainsi que la capacité des réseaux UNB, sur un testbed de radio FIT/Cortexlab.

Acknowledgements

First and foremost, I would like to express my sincere gratitudes to my advisors: Claire GOURSAUD and Prof. Jean-Marie GORCE, and my responsible in Sigfox: Christophe FOURTET. I want to thank them for the trust they brought to me, the time they spent to help me, the energy and patience they consumed to support me, and the wide knowledge and expertise they brought to facilitate me. Especially Claire, a very professional and attentive person. She had spent so much time to facilitate me, to give feedbacks and correct my papers and thesis. She always managed to be there whenever I needed her help or advices, and to talk to me whenever something went wrong. She is one of the best advisors I have had in academies.

I want to take this opportunity to thank the jury members for spending the time to read my thesis, giving comments and feedbacks, and traveling to attend my defense. I am also very grateful for the financial support that Sigfox has given me, and for the persons in Sigfox that have worked with me: Guillaume, Laurence and Benoit.

Next, I would like to thank my colleagues at CITI lab as well, for the funny or weird discussions at the coin-café, for the pots every Friday, for their laughter which makes the everyday routine more interesting. Especially, I want to thank my dear office-mate Diane, who is such a caring and lovely person, who has shared a lot with me, and helped me with all the defense logistics. I want to thank those who have helped me with the experiments: Othmane, Cyrille, Léo, Olivier. N, Pascal, Régis. I want to thank all the administration staffs who have helped me with all the "emergencies": Gaelle, Aude, Sophie and Sandrine. I also want to thank Ayse and Selma for the lovely tea-time every day, and for their support that helped me a lot through though times. Then I want to thank all the PhDs and post-docs that I have met at CITI, for their sharing and encouragement which made me feel that I was not alone.

Finally, I want to thank my family for their unconditional love and support from the other side of the world, even though none of them would really understand what I did during this thesis. I want to thank Clément's family, for treating me like a family, making me feel cared and loved in this foreign country. And of course, I wan to thank my dear boyfriend Clément, who has always been there for me, who has always supported me, for all the good and bad things.

Contents

List of Figures

List of Tables

List of Abbreviations

AIP	Aggregated Interference Power
BER	Bit Error Rate
BLE	Bluetooth Low Energy
BPSK	Binary Phase-Shift Keying
BS	Base Station
CDMA	Code Division Multiple Access
CDF	Cumulative Distribution Function
CSMA/CA	Carrier-Sense Multiple Access with Collision Avoidance
CSS	Chirp Spread Spectrum
DBPSK	Differential Binary Phase-Shift Keying
DSSS	Direct-Sequence Spread Spectrum
EGC	Equal Gain Combining
FDMA	Frequency Division Multiple Access
FFT	Fast Fourier Transform
GPS	Global Positioning System
GSM	Global System for Mobile Communications
IoT	Internet of Things
ISM	Industrial Scientific and Medical
LEO	Low Earth Orbit
LPWAN	Low Power Wide Area Network

LTE	Long Term Evolution
MAC	Medium Access Control
MGL	Moment Generating Function
MRC	Maxi ratio Combining
M2M	Machine to Machine
NB-IoT	Narrow Band Internet of Things
NFC	Near Field Communication
OFDMA	Orthogonal Frequency Division Multiple Access
OP	Outage Probability
PDF	Probability Density Function
PHY	Physical
PPP	Poisson Point Process
QPSK	Offset Quadrature Phase Shift Keying
RAN	Radio Access Network
RFID	Radio-Frequency Identification
RFTMA	Random Frequency-Time Multiple Access
RPMA	Random Phase Multiple Access
RSSI	Received Signal Strength Indicator
RTS/CTS	Request to Send/ Clear to Send
SC	Selection Combining
SDR	Software Design Radio
SHF	Super High Frequency
SIC	Successive Interference Cancellation
SINR	Signal to Interference and Noise Ratio

SIR	Signal to Interference Ratio
TDMA	Time Division Multiple Access
UHF	Ultra High Frequency
UNB	Ultra Narrow Band
USRP	Universal Software Radio Peripheral
UWB	Ultra Wide Band
WPAN	Wireless Personal Area Network
3GPP	3rd Generation Partnership Project
5G	5th Generation

Notations

Throughout this thesis, the probability is represented by $\mathbb{P}$, while the power is represented by P. The probability of event A on the condition of variable a is denoted by $\mathbb{P}(A|a)$. And the joint probability of event A and event B is denoted by $\mathbb{P}(A \cap B)$.

For a random continuous variable X, its CDF (cumulative distribution function) is defined by $F_X(x) = \mathbb{P}(X < x) = \mathbb{P}\left(\int_{-\infty}^{x} f_X(t)\mathrm{d}t\right)$, with f_X as its probability density function. Its expectation is denoted and defined by $\mathbb{E}[X] = \int_{-\infty}^{\infty} xf(x)\mathrm{d}x$.

Synthèse de contributions

Cette thèse est pour buts de fournir une vision scientifique à la première technologie (i.e. Ultra Narrow Band) dédiée commercialement à l'IoT, de donner une évaluation de la capacité des réseaux basés sur UNB, et d'en plus proposer des solutions pour améliorer sa performance.

Les contributions principales de cette thèse, qui répondent aux objectives mentionnés d'avant, sont:

1. Une caractérisation de capacité fondamentale des réseaux UNB, sous les conditions de canal idéalistes pour une seul stations de base (BS). Cette contribution quantifie théoriquement la capacité des réseaux pour l'accès multiple spécifique de UNB (i.e. le Random-FTMA) qui est unslotté en temps et en fréquence [1]. Puis elle a été étendue en cas de ALOHA généralisé qui inclue quatre cas: slotté/unslotté en temps/fréquence ALOHA. Cette analyse de ALOHA généralisé est ensuite poursuivie par le cas avec des réplications [2]. Je souligne la dualité de temp-fréquence dans le systèmes de UNB, ainsi que l'obtention d'un nombre optimal de réplications pour une configuration de paramètres. Les résultats principaux de cette contribution vont être détaillés en Section 0.2.

2. Une évaluation de performance des réseaux UNB sous les conditions de canal réalistes, toujours pour mono-BS. Cette contribution fournit des expressions théoriques de la probabilité de coupure (OP) : la première considère le path-loss due à la propagation, l'interférence spectrale causée par l'accès au canal aléatoire de UNB, ainsi que l'hypothèse d'un seul interférent à chaque collision [3]; la deuxième prend en compte le fading de Rayleigh et l'interférence agrégée (où la perte d'un paquet peut venir de la collision de plusieurs interférents) conjointement [4]. Ces analyses sont faites avec l'aide de l'outil géométrie stochastique. Les résultats principaux de cette contribution vont être détaillés en Section 0.3.

3. L'optimisation de performance des réseaux UNB en appliquant la technologie SIC (annulation successive d'interférence) qui permet d'atténuer les interférences d'une manière récursive, dans le cas de mono-BS [5]. Cette contribution analyse l'OP en prenant en compte le SIC et l'aspect aléatoire de UNB conjointement, sous les conditions réalistes. Cette contribution a démontré que le SIC est pertinent à améliorer la performance de UNB, et que le fading favorise l'efficacité de SIC. Ces résultats vont être détaillés en Section 0.4.

4. L'amélioration de performance des systèmes UNB, en exploitant la diversité spatiale de multi-BS. Cette contribution applique les technologies de la combinaison des signaux et SIC à travers de multiples BSs. Le plus simple slection combining (SC) a été d'abord considéré dans l'analyse théorique, en

supposant que les interférences perçus par toutes les BS sont corrélées [6]. Puis MRC (max ratio combining) et EGC (equal gain combining) sont appliqués, dans le but de combiner les signaux non-décodés pour obtenir un output de meilleure qualité. Deux façons d'appliquer SIC (localement et globalement) ont été réalisées. Enfin, cette contribution évalue et compare l'amélioration apportée par chaque technologie mentionnée [7]. Les résultats principaux de cette contribution vont être détaillés en Section 0.7.

5. Une validation expérimentale du modèle d'interférence spectrale de UNB, ainsi que la capacité des réseaux UNB, sur un testbed de radio FIT/Cortexlab. Les résultats principaux de cette contribution vont être détaillés en Section 0.8.

0.1 Modélisation de UNB

La technologie UNB vise à réaliser des transmissions à longue distance et basse consommation, de même que, CSS (LoRa) et RPMA (Ingenu) [8]. La spécificité d'un système UNB, est que l'occupation spectrale du signal est très petite (typiquement 100 Hz), comparée aux systèmes classiques. Cela permet d'avoir une portée de transmission très large (jusqu'à 50km), et une consommation d'énergie ultra basse (l'autonomie de batterie d'un device peut aller jusqu'à 20 ans). UNB est donc adapté pour des objets qui envoient des messages de petite taille (typiquement 100 à 200 bits), et qui ont besoin d'une autonomie de 10 à 20 ans.

0.1.1 Accès multiple

La principale caractéristique de UNB est liée à un phénomène typique dans des objets électroniques : l'imprécision des oscillateurs lors de la génération de la fréquence porteuse. Actuellement, les oscillateurs ordinaires (0.25 ppm) ont une incertitude de 217Hz à la fréquence de 868MHz, ce qui est plus large que la bande individuelle de UNB [9]. De ce fait, la séparation du spectre en canaux n'est plus pertinente. Par conséquent, l'accès au canal est RFTMA (Random Frequency and Time Multiple Access), où les objets choisissent leur moment d'émission et leur fréquence porteuse d'une manière aléatoire et continue, comme illustrée dans la Fig. 1. D'un côté, cela permet de s'affranchir des échanges nécessaires à l'allocation de ressources, et d'utiliser des oscillateurs de low-cost. Mais d'un autre côté, cela ne protège pas des interférences et collisions.

Les transmissions des nœuds ne sont pas slottées en temps, puisque chaque nœud peut commencer ou terminer une émission à un moment aléatoire. Par conséquent, le niveau d'interférence peut varier lors d'une transmission. Cela corresponde à ALOHA classique qui a déjà été étudié dans beaucoup de littérature [10, 11]. Dans cette thèse, nous ne considérons pas cet aspect-là. Nous nous intéressons plus à l'aspect aléatoire et continue en fréquence, ce qui n'a jamais été étudié dans dans des réseaux cellulaires.

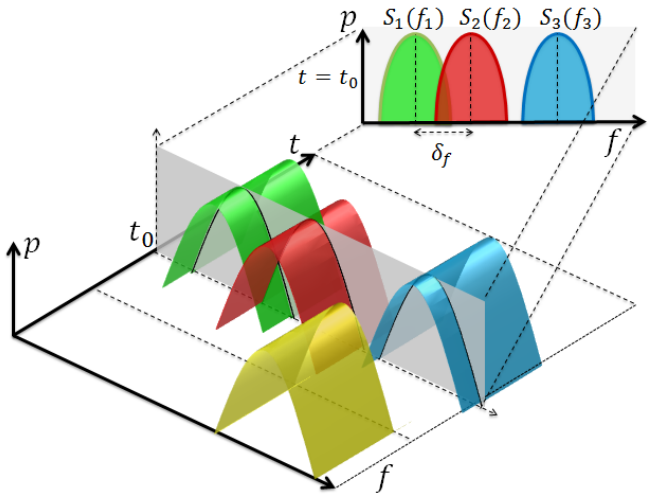

FIGURE 1: Exemple de répartition des nœuds en temps et en fréquence

0.1.2 Topologie et hypothèses

Dans cette thèse, nous nous concentrons sur un moment observé. Nous supposons que la densité spatiale de nœuds soit λ_0. Les localisations de nœuds suit une distribution HPPP (Poisson point process homogène). A chaque moment, les nœuds décident indépendamment de transmettre un paquet, avec la probabilité p. Donc sur le moment observé, la densité de nœuds actifs vaut $\lambda_n = p\lambda_0$. UNB est dédié à des devices qui transmettent sporadiquement, cette probabilité p est donc très basse, ce qui conduit à $\lambda << \lambda_0$. Nous utilisons dans cette thèse λ_n au lieu de λ_0 pour indiquer que la densité actifs de nœuds (ou N le nombre actifs de nœuds).

Les nœuds sont supposés d'avoir le même comportement: les transmissions se dont avec la même puissance d'émission et gain d'antenne. L'évaluation de performance est donc basée sur la distribution de SINR (signal to interference and noise ratio) instantanée, afin d'assurer que le niveau de SINR soit stable au moment observé.

Mono-BS

Pour le cas de mono-BS, nous considérons une cellule avec une seule BS en son centre, comme montrée dans la fig. 2. La BS est constamment en mode réception, et scanne toute la ressource fréquentielle B pour détecter toute transmission. Les nœuds sont distribués aléatoirement et uniformément dans le disque, de rayon $[r_m, r_M]$, avec r_m définissant une zone d'exclusion où aucun nœud est déployé.

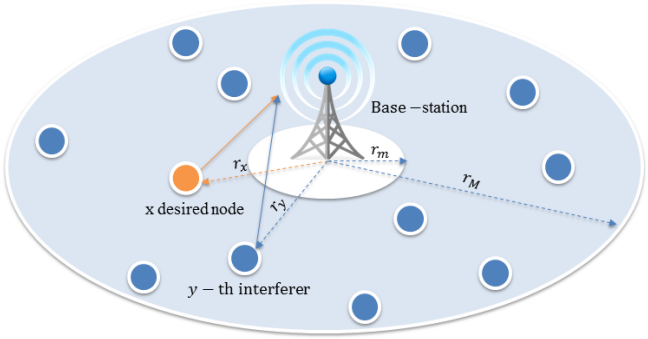

FIGURE 2: Exemple de topologie mono-BS: la zone couverte est $[r_m, r_M]$, en orange le nœud désiré situé à la distance r_x; en bleu les interférents à une distance r_y

Multi-BS

Pour le cas de multi-BS, nous avons considéré deux scénarios: le premier est la topologie tradition ale, où les localisations des BSs se forment en treillis carré et la distance entre chaque BS est identique, comme montré dans la Fig. 3(a); l'autre est la topologie souvent utilsée dans des analyses théoriqurs, où la distribution des BSs suit une loi HPPP (ce qui est indépendante de celle de nœuds), avec la densité λ_b, , comme montré dans la Fig. 3(b).

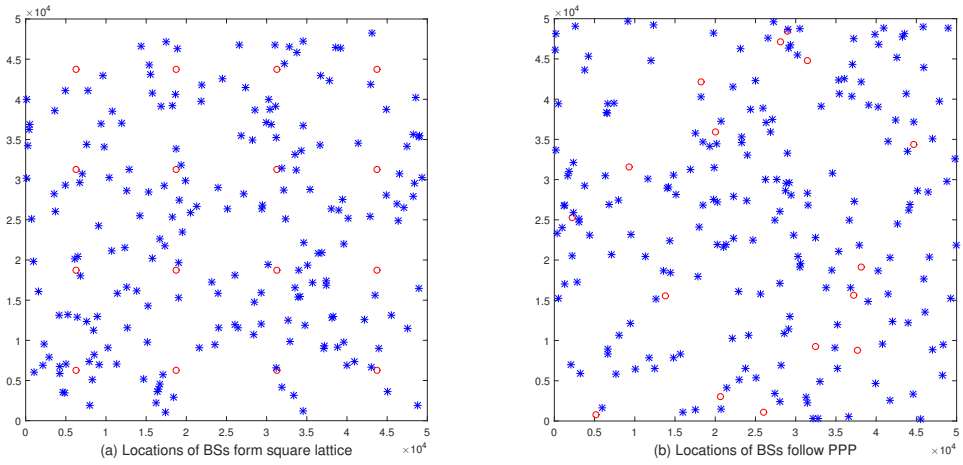

FIGURE 3: Topologie de multi-BS. Les points blues sont des nœuds distribués, les points rouges sont des BSs. (a) les localisations des BS sont quadrillées où la distance entre chacune des BSs est identique; (b) la localisations des BS suit une loi HPPP avec la densité λ_b.

0.1.3 Modèle d'interférence spectrale

Les nœuds sélectionnent leur fréquence porteuse aléatoirement et indépendamment. Pour 2 nœuds transmettant simultanément, le niveau d'interférence perçu dépend de l'écart fréquentiel entre le paquet désiré (à la fréquence f_x) et le paquet interférent (à f_y) : $\delta f = \mid f_x - f_y \mid$. Nous avons estimé le facteur d'interférence à

partir du filtre réaliste de Sigfox, avec deux modèles: une fonction rectangulaire et une fonction Gaussienne.

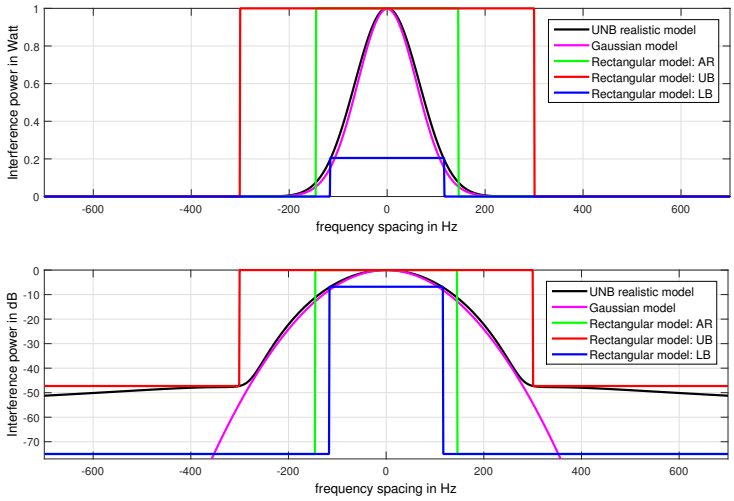

FIGURE 4: Le coefficient d'interférence vs la différence en fréquence δ_f entre le paquet désiré et le paquet interférant

Modèle rectangulaire

D'abord, nous notons que l'interférence peut être divisés en deux parties. Dans la première partie, le niveau d'interférence est au alentour de -50 dB. Un seul interférent dans cette partie n'a pas d'impact au packet désiré puisque son niveau est très bas. Dans la deuxième partie, le niveau d'interférence augmente très rapidement quand δf se réduit, ce qui peut aller jusqu'à 0 dB. Un paquet qui apporte une contribution d'interférence comme celle-ci a beaucoup plus de chance à perturber le paquet désiré. La transition se fait dans la zone de $100 - 400$Hz, qui dépend de la critère imposée par le système.

Par conséquent, nous considérons que le niveau d'interférence soit constant dans la zone fréquentielle superposée de deux signaux. La contribution d'un interférent peut alors être modélisée comme une fonction rectangulaire:

$$\beta(\delta f) = \begin{cases} I_{max} & for \quad \delta f \leq \triangle/2, \\ I_{min} & for \quad \delta f > \triangle/2. \end{cases} \tag{1}$$

où $\triangle$ correspond au largeur de bande qui transite le niveau d'interférence.

Modèle Gaussienne

Le modèle rectangulaire peut faciliter les calculs comme il est très simple, cependant il perd des détails de l'évolution d'interférence en fonction de δf. Nous avons donc l'approximé avec une fonction Gaussienne :

$$\beta\left(\delta f\right) = \frac{150}{\sigma\sqrt{2\pi}} \exp^{\frac{-\Delta f^2}{2\sigma^2}} \tag{2}$$

avec $\sigma = 60$ pour une transmission de 100 bit/s [12].

Nous pouvons voir dans la Fig. 4 que le modèle Gaussienne (en rose) reflète presque tous les détails du filtre réaliste de Sigfox (en noir). Il va être utilisé dans toutes les analyses où nous considérons l'interférence spectrale spécifique de UNB. Alors que le modèle rectangulaire inclue la borne supérieure UB (en rouge), la borne intérieure LB (en bleu), et l'optimal AR (en vert). Ces trois bornes vont être utilisées en Section 0.3.

0.2 La 1ère contribution

Cette section présente les résultats principaux de la première contribution: l'analyse de la performance des réseaux UNB sous les conditions de canal idéaliste, pour le cas de mono-BS.

Les études existantes basées sur ALOHA considèrent souvent FH (frequency hopping) où la ressource fréquentielle est découpé parfaitement en canaux orthogonaux [13]. L'aspect aléatoire et continue dans le domaine de fréquence comme celui de UNB n'a jamais été considéré. Nous complétons donc ces études de ALOHA en prenant en compte l'aspect totalement aléatoire de fréquences centrales dans cette contribution, afin de caractériser la voie montant d'ALOHA basé sur UNB.

0.2.1 Hypothèses

Dans cette étude, le réseau est limité à une BS qui collecte les données des nœuds qui sont à portée. Nous considérons que tous les nœuds sont perçus avec la même puissance. A chaque instant, seulement un sous-ensemble de ces nœuds N transmet. Nous supposons que tous les nœuds ont le même comportement: Un nœud se réveille toutes les T_p secondes pour envoyer un message qui dure τ secondes. La condition de canal est idéaliste, donc la puissance reçue de chaque paquet est identique peu importe où se situe des nœuds. Avec cette hypothèse-là, quand deux paquets sont en collisions, nous perdons les deux. Cela représente le pire cas.

Pour le cas TS (slotté en temps), comme la ressource en temps est découpé en slots, chaque nœud actif choisit un time-slot aléatoirement pour transmettre. Donc la probabilité qu'un interférant transmette pendant le même slot que l'utilisateur désiré est : $P_t = \tau / T_p$. Alors que pour le cas TU (non-slotté en temps, ce qui correspond au cas réaliste de UNB Sigfox), le recouvrement partiale peut aussi introduire des collisions. Nous supposons qu'une fois qu'il y a un recouvrement temporale entre deux paquets (peu importe que c'est 1% ou 99%), nous perdons les deux. C'est-à-dire que quand un interférent sélectionne son moment d'émission au tour de $[-\tau, \tau]$ comparé à celui du nœud désiré, nous perdons le paquet désiré. Par conséquent, la probabilité d'être en collision en temps devient $2\tau / T_p$ en TU.

Le même principe s'applique dans le domaine des fréquences. La ressource fréquentielle totale est B Hz. Nous utilisons le modèle rectangulaire présent en Section 0.1.3 pour définir la bande fréquentielle de sensibilité aux interférences b. Nous définissons $b = 116$Hz. Pour le cas FS (slotté en fréquence), la probabilité d'être en collision est $p_f = b/B$. Alors que pour le cas FU, cette probabilité devient $p_f = 2b/B$ puisque le découvrement partiale en fréquence peut aussi introduire des collisions.

0.2.2 ALOHA généralisé

Nous considérons un utilisateur désiré qui est choisi aléatoirement. Nous évaluons la probabilité que cet utilisateur désiré perd ses messages, avec la présence de N autres utilisateurs.

Analyse théorique

Dans le protocole de ALOHA classique, tous les paquets sont transmis dans le même canal. Donc il est aléatoire seulement en domaine temporal. Si le nombre totale de paquets générés suit une distribution de Poisson, la probabilité de succès d'un paquet donné est [10]:

$$\mathbb{P}_{\mathrm{1D}} = e^{-\alpha_t G_t} \tag{3}$$

avec $\alpha_t = 1$ pour le cas TS, $\alpha_t = 2$ pour TU, et $G_t = Np_t$ comme le nombre moyen de paquet générés par tous les autres utilisateurs durant la transmissions du paquet désiré.

Pour des systèmes de frequency hopping qui possèdent $\frac{1}{p_f} = B/b$ canaux orthogonaux [11], eq.(3) devient :

$$\mathbb{P}_{\mathrm{FH}} = e^{-\alpha_t p_f G_t} \tag{4}$$

Nous étendons ces deux équations au cas ALOHA généralisé, qui décrit tous les cas. La probabilité de coupure (OP) pour ALOHA généralisé est alors :

$$\mathrm{OP} = 1 - e^{-\alpha_t \alpha_f G_{tf}} \tag{5}$$

avec $G_{tf} = Np_t p_f = \dfrac{N\ \tau\ b}{T_p\ B}$ comme le trafic moyen durant la transmission du paquet désiré, $\alpha_t = 2$ (resp.1) pour time-unslotted (TU) (resp. time-slotted (TS)), $\alpha_f = 2$ (resp.1) pour frequency-unslotted (FU) (resp. frequency slotted (FS)). Le cas FUTU correspond au scénario réaliste de Sigfox.

Cette expression OP eq.(5) nous montre la dualité temporale et fréquentielle dans le protocole de ALOHA, où nous pouvons inter-échanger les paramètres en temps (α_t et p_t) et ceux en fréquence (α_f et p_f) pour obtenir la même OP. Cette découverte apporte une flexibilité à la configuration du réseau. Si c'est difficile de réaliser TS et FS conjointement, cette dualité nous permet de choisir lequel relaxer selon les critères imposées, par exemple le coût de déploiement des nœuds.

Résultats numériques et comparaison

Nous avons lancé des simulations de Monte-Carlo sur Matlab, en prenant la même hypothèses que l'analyse théorique, dans le but de valider l'expression de OP eq.(5). Nous présentons les résultats pour le cas de FUTS ($\alpha_f = 2$, $\alpha_t = 1$) et FUTU ($\alpha_f = 2$, $\alpha_t = 2$) dans cette section. Pour être plus réaliste, les transmissions sont faites sur la bande ISM 868 MHz.

Nous présentons en Fig. 5 la comparaison de OP en théorie et en simulations, en variant deux paramètres : le nombre total d'utilisateurs $N + 1$ et la ressource spectrale totale B.

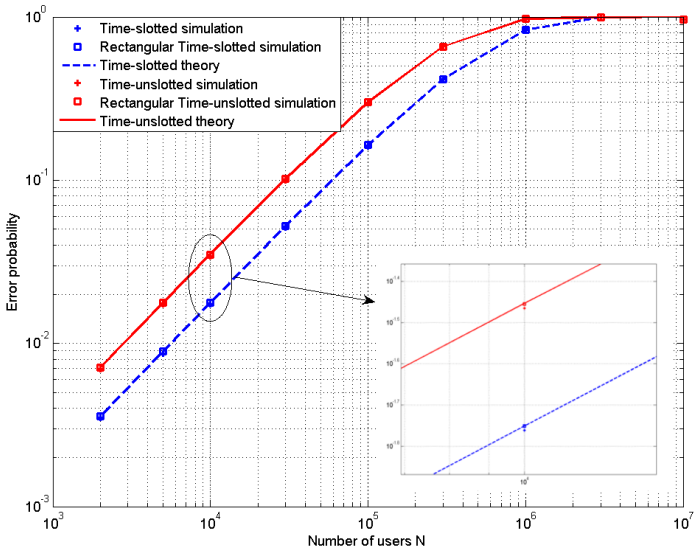

FIGURE 5: OP en théorie et en simulations, en variant le nombre d'utilisateurs non-désirés N, pour les cas de FUTS et FUTU, $b = 116$Hz, $B = 12000$Hz, $\tau = 2$s, et $T_p = 12$ heures.

Nous avons aussi tracé le throughput en Fig. 6, en variant la charge de réseaux G_{tf}. Cette fois-ci nous considérons tous les 4 cas. Nous pouvons remarquer que le FSTS apporte la meilleure performance, puisque l'espace temporale et spectrale est toute divisée en canaux orthogonaux, la probabilité de collision est donc minimisée. Au contraire, FUTU a la pire performance à cause de recouvrement temporel et fréquentiel. Finalement, FSTU et FUTS se superposent grâce à la dualité en temps-fréquence.

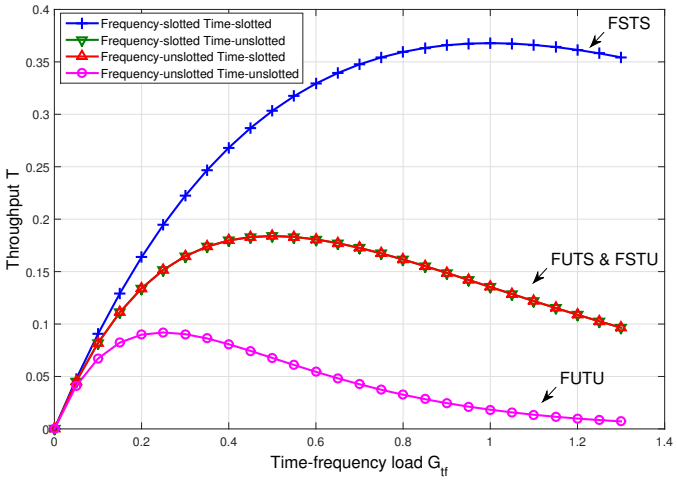

FIGURE 6: Network throughput as a function of the load for all $\left(\alpha_t, \alpha_f\right)$.

0.2.3 ALOHA généralisé avec répliques

Pour améliorer le taux de succès des transmissions, le mécanisme (nous montrons ici que pour le cas FUTS) de réplication illustré dans la Fig. 7 est appliqué. Nous supposons que chaque message est transmis exactement n_r fois durant le T_b, indépendamment du succès ou non de la transmission précédente. n_r est donc prédéfini et identique pour tous les nœuds. Chaque nœud actif $i \in [1, \cdots, N+1]$ choisit au hasard une fréquence porteuse f_i et un time-slot t_i pour chaque réplique. La fenêtre temporale allouée pour une réplique est $\frac{T_p}{n_r \cdot \tau}$. De même, la largeur en fréquence alloué pour chaque réplique est ainsi $\frac{B}{n_r \cdot b}$. Un message est considéré succès en transmission si au moins une de ses n_r répliques réussit.

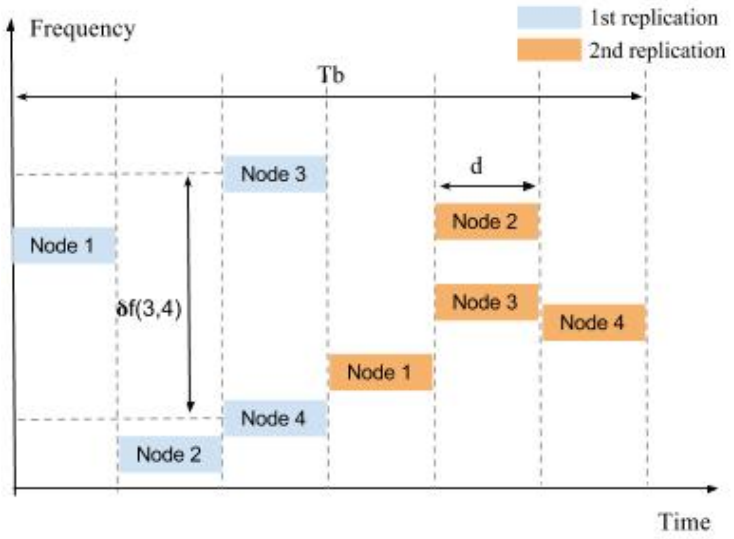

FIGURE 7: Illustration de réplique $n_r = 2$ pour la durée de message d et la période de message T_p

Analyse théorique

Dans le cas avec des répliques n_r, le nombre de paquets générés durant l'intervalle temporal et fréquentiel augmente. Donc la charge de réseau devient $n_r \cdot G_{tf} = \frac{n_r\ N\ \tau\ b}{T_p\ B}$. Ainsi, la probabilité qu'une réplique donnée soit correctement reçue devient:

$$\mathbb{P}_s(n_r) = e^{-\alpha_t \alpha_f G_{tf} n_r} \tag{6}$$

Nous supposons que la probabilité de succès d'une réplique est indépendent de celles d'avant. En conséquent, l'OP d'un messsage est la probalité que toutes ses n_r répliques soient perdues :

$$\mathrm{OP}(n_r) = \left(1 - e^{-\alpha_t \alpha_f G_{tf} n_r}\right)^{n_r} \tag{7}$$

les notations sont identiques que celles dans eq.(5).

Résultats numériques et comparaison

Nous avons choisi le cas FUTS à appliquer dans des simulations pour valider l'expression de l'OP avec des répliques eq.(7).

Sur la Fig. 8, on peut vérifier que la théorie décrit correctement l'évolution de l'OP en fonction de n_r et de N. En conséquence, le paramètre G_{tf} est un paramètre unifié qui modélise correctement la charge du réseau. Ainsi, dans la suite du papier, nous utiliserons eq.(7) pour l'évaluation des performances.

D'autre part, la Fig. 8 confirme que le mécanisme de réplication est capable d'améliorer la probabilité de succès d'un message transmis. En effet, la croissance de n_r permet d'augmenter la chance qu'au moins un paquet soit bien reçu, donc de réduire l'OP. En revanche, la réplication multiplie aussi le nombre de messages envoyés dans l'intervalle temporel fixé. Cela accroît l'utilisation du canal et la probabilité de collision.

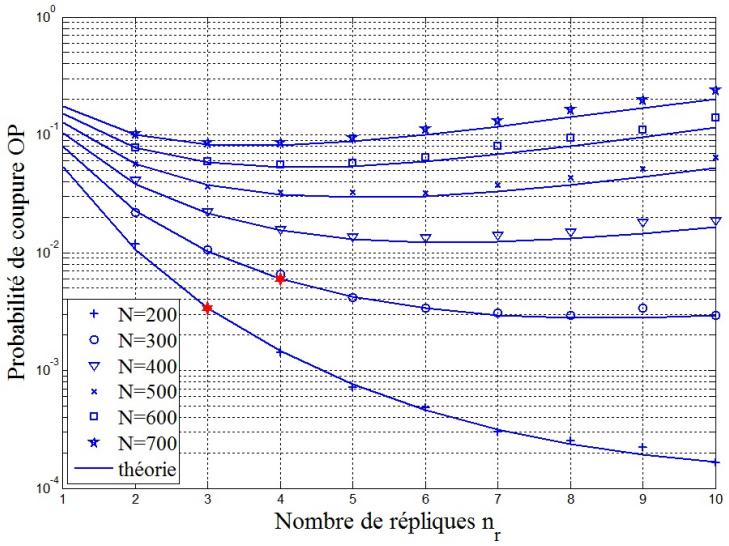

FIGURE 8: OP vs nombre de répliques n_r avec différents nombres de nœuds actives N, $b = 116$ Hz, $B = 12$ kHz, $\tau = 2$s, $T_p = 75$s.

0.3 La 2ème contribution

Cette section présente les résultats principaux de la deuxième contribution: l'analyse de la performance des réseaux UNB sous les conditions de canal réalistes, pour le cas de mono-BS. Nous avons dérivé deux expressions théorique de l'OP: (1) nous considérons que le path-loss due à la propagation en espace libre et l'interférence spectrale spécifique de UNB qui vient d'un interférant; (2) nous considérons le Rayleigh fading et la contribution agrégée de plusieurs interférants, et le path-loss pour toutes les propagations. La géométrie stochastique est utilisé dans le deuxième cas.

0.3.1 Hypothèses

Dans cette étude, le réseau est toujours limité à une unique BS (Base Station) qui collecte les données des nœuds à sa portée. Comme illustré dans la Fig. 2, les nœuds sont distribués uniformément dans un disque, dont la portée est $[r_m, r_M]$.

La positionnement des nœuds peut être modélisé par un HPPP (Poisson point processus homogène) spatiale [14], avec la densité λ_t sue l'espace Euclidien $\mathbb{R}^2$. Dans cette contribution, nous nous focalisons sur un moment échantillonné pour observer les transmissions simultanées. Comme les nœuds n'envoient pas très souvent, nous utilisons la *densité active de nœuds* λ (qui est très petite par rapport à λ_t) pour observer le réseau.

Nous nous concentrons sur un nœud désiré donnée x à la distance r_x. Et tous les autres nœuds actifs sont des interférents potentiels y à la distance r_y. La BS est supposée être constamment en mode réception, et capable de scanner toute la bande B pour des transmissions potentielles. Nous considérons que tous les nœuds transmettent avec la même puissance d'émission et gain d'antenne.

0.3.2 Analyse théorique

L'OP sous les conditions réalistes est définie comme la probabilité que le paquet donnée soit perdu, donc son SINR (rapport de Signa-Interference-bruit) est en-dessous d'un seuil prédéfini γ^*. L'OP est basé sur le SINR instatanée qui est assumé être stable durant le moment observé. Donc l'OP pour un nœud désiré x qui se situe à distance r_x par rapport à la BS est:

$$\mathrm{OP} = \mathbb{P}(\mathrm{SINR}_x \leq \gamma^*) = \mathbb{P}\left(\frac{P_s}{P_I + W} \leq \gamma^*\right) \tag{8}$$

avec la puissance reçu du nœud désiré, P_I le coefficient d'interférence, W le bruit et γ^* le seuil de SINR prédéfini.

La puissance reçue peut être écrire comme :

$$P_s = g_x \cdot r_x^{-\alpha} \cdot P_0' \tag{9}$$

avec $\alpha \geq 2$ le path-loss; g le coefficient de Rayleigh fading qui est une variable aléatoire suivant une lois exponentielle $g \sim exp\,(1)$; et h_0 le gain de canal de référence à la distance r_0.

P_I peut être obtenue par la somme des contributions de tous les interférents :

$$P_I = \sum_{y \in \{\mathcal{A} - x\}} g_y \cdot r_y^{-\alpha} \cdot \beta(\delta f) \cdot P_0' \tag{10}$$

Impact de path-loss et modèle d'interférence en Gaussien

Pour avoir une première intuition de l'accès aléatoire spectrale de UNB, nous avons d'abord négligé le fading et le bruit. Nous considérons que l'atténuation en espace libre ($\alpha = 2$). Ainsi, nous utilisons le SIR (rapport signal-interférence) comme une version simplifiée de SINR. Nous considérons que l'interférence nécessaire à la perte d'un paquet provient d'un seul interférent, car c'est le cas le plus fréquent dans un système de UNB [12]. Avec ces hypothèses, l'OP s'écrit:

$$\mathrm{OP} = \mathbb{P}(\mathrm{SIR} \leq \gamma^*) = \mathbb{P}\left(\frac{P_s}{P_I} \leq \gamma^*\right) \tag{11}$$

Nous considérons tout d'abord le cas où seuls deux nœuds sont actifs (un nœud désiré x, et un interférent y). À partir de eq.(9) et eq.(10), nous pouvons exprimer le SIR du nœud désiré :

$$SIR = \frac{P_s}{P_I} = \frac{r_x^{-2} \cdot P_0}{r_y^{-2} \cdot \beta(\delta f) \cdot P_0} = \left(\frac{r_y}{r_x}\right)^2 \frac{1}{\beta(\delta f)} \tag{12}$$

avec $\beta(\delta f)$ le coefficient d'interférence en Gaussien illustrée en eq.(2).

Un paquet est considéré perdu si son $SIR \leq \gamma^*$, i.e. quand :

$$r_y \leq r_x \sqrt{\gamma^* \beta(\delta f)} \tag{13}$$

Nous décomposons (13) en appliquant la formule des probabilités totales en fonction de δf. L'OP devient :

$$\mathrm{OP} = \int_0^B \mathbb{P}\left(r_y \leq r_x \sqrt{\gamma^* \beta(\delta f)} | \delta f\right) \mathbb{P}(\delta f)\ \mathrm{d}\delta f \tag{14}$$

Nous exprimons tout d'abord $\mathbb{P}(\delta f)$. Le nœud désiré et l'interférent choisissent leur fréquence f_x et f_y aléatoirement, indépendamment et uniformément dans $[0, B]$. Donc, l'écart fréquentiel δf suit la distribution suivante :

$$\mathbb{P}(\delta f) = \begin{cases} \frac{2}{B}\left(1 - \frac{\delta f}{B}\right) & \text{for } \delta f \in [0, B] \\ 0 & \text{elsewhere} \end{cases} \tag{15}$$

Nous calculons ensuite $\mathbb{P}\left(r_y \leq r_x \sqrt{\gamma^* \beta(\delta f)} | \delta f\right)$, en intégrant sur le variable aléatoire r_y. Les nœuds sont supposés être distribués selon un processus ponctuel de Poisson. Leur distance respective à la BS suit donc une distribution linéaire. $\mathbb{P}(r)$ représente la probabilité qu'un nœud soit à la distance (rayon) r dans une surface discoïde $[r_m, r_M]$:

$$\mathbb{P}(r) = \begin{cases} \frac{2r}{r_M^2 - r_m^2} = \frac{2r}{k^2} & \text{for } r \in [r_m, r_M] \\ 0 & \text{elsewhere} \end{cases} \tag{16}$$

avec $k^2 = r_M^2 - r_m^2$.

Puis les calcules sont faites en fonction de la valeur de $r_x \sqrt{\gamma^* \beta(\delta f)}$. Nous le présentons pas tous les détails dans cette section, mais nous référons les intéressés à lire le chapter 4. Nous présentons l'OP finale avec une r_x donnée :

$$\begin{aligned} \mathrm{OP} &= \int_{b_1}^{b_2} \left(\frac{{r_x}^2 \gamma^* \beta(\delta f) - {r_m}^2}{k^2}\right) \mathbb{P}(\delta f)\ \mathrm{d}\delta f + \int_{b_0}^{b_1} 1 \cdot \mathbb{P}(\delta f)\ \mathrm{d}\delta f \qquad (17) \\ &= \left[75 a \gamma^* \operatorname{erf}\left(\frac{\delta f}{\sqrt{2\sigma^2}}\right) + \frac{150 a \gamma^* \sigma}{B\sqrt{2\pi}} \exp\left(\frac{-\delta f^2}{2\sigma^2}\right) + e\frac{\delta f^2}{2} - eB\delta f\right]_{b_1}^{b_2} + \frac{B}{2}\left[\delta f - \frac{\delta f^2}{2B}\right]_{b_0}^{b_1} \end{aligned}$$

avec les constantes suivantes :

$$d = \frac{2{r_x}^2}{Bk^2}, \qquad e = \frac{2{r_m}^2}{B^2k^2}, \qquad b_0 = 0$$
$$b_1 = min\left(\beta^{-1}\left(\left(\frac{r_M}{r_x}\right)^2 \frac{1}{\gamma^*}\right), B\right), \; b_2 = min\left(\beta^{-1}\left(\left(\frac{r_m}{r_x}\right)^2 \frac{1}{\gamma^*}\right), B\right)$$

Nous étendons (17) au cas où $N > 2$ nœuds sont actifs. Cependant, nous considérons que l'interférence nécessaire à la perte d'un paquet provient d'un seul interférent, car c'est le cas le plus fréquent dans un système de UNB. Dans ce cas, n'importe lequel de ces $N-1$ (tous les nœuds sauf celui désiré) peut être l'interférent. En conséquence, la probabilité de succès est la probabilité qu'aucun de ces $N-1$ n'interrompe le nœud désiré. Donc la probabilité de coupure devient :

$$\mathrm{OP}_{(N)} = 1 - (1 - \mathrm{OP})^{N-1} \tag{18}$$

Impact conjoint de Rayleigh fading, path-loss et modèle d'interférence rectangulaire

Dans cette partie, nous considérons un canal plus complexe: avec path-loss, Rayleigh fading, le bruit et l'interférence agrégée (AIP). Cependant, pour obtenir une expression tractable, nous utilisons le coefficient d'interférence $\beta(\delta f)$ rectangulaire (i.e. les courbes en verte, rouge et bleu en Fig. 4) comme présenté en eq.(1).

L'expression de SINR avec ces hypothèses devient :

$$\mathrm{SINR} = \frac{g_x \cdot r_x^{-\alpha} \cdot P_0'}{P_I + W} \tag{19}$$

avec P_I l'interférence aggrégée comme montrée en eq.(10), et W le bruit Gaussien filtré.

Ainsi, pour un nœud donné x à la distance r_x, son OP s'écrit :

$$\mathrm{OP} = \mathbb{P}\left(g_x \leq \frac{\gamma^*(W + P_I)}{r_x^{-\alpha} \cdot P_0'}\right) \tag{20}$$

Comme l'AIP est une variable aléatoire, cette probabilité peut s'écrire comme la suivante :

$$\mathrm{OP} = \mathbb{E}_{P_I}\left[\mathbb{P}\left(g_x \leq \frac{\gamma^*(W + P_I)}{r_x^{-\alpha} \cdot P_0'}\middle| P_I\right)\right] \tag{21}$$
$$\overset{(a)}{=} 1 - \mathbb{E}_{P_I}\left[\exp\left(-\frac{\gamma^*(W + P_I)}{r_x^{-\alpha} \cdot P_0'}\right)\right] \tag{22}$$
$$= 1 - \exp\left(\frac{-\gamma^* W}{r_x^{-\alpha} \cdot P_0'}\right) \cdot \mathbb{E}_{P_I}\left[\exp\left(-\frac{\gamma^* P_I}{r_x^{-\alpha} \cdot P_0'}\right)\right]$$
$$\overset{(b)}{=} 1 - \exp(-W \cdot s) \cdot \mathbb{E}_{P_I}[\exp(-P_I \cdot s)]$$
$$\overset{(c)}{=} 1 - \exp(-W \cdot s) \cdot \mathcal{L}_{P_I}(s)$$

où $\mathbb{E}_{P_I}$ représente l'espérance de P_I, selon la théorie de probabilité.; (a) vient de CDF (cumulative density function) de la variable exponentiel g_x; (b) nous replaçons $s = \frac{\gamma^*}{r_x^{-\alpha} \cdot P_0'}$; (c) nous replaçons le second terme par la Laplace de Laplace de l'AIP [14].

Les calcules se poursuivent par la dérivation de la transformée de Laplace $\mathcal{L}_{P_I}(s)$. Nous référons les intéressés à lire la Section 4.3.2 pour des détails. Nous donnons l'expression finale de cette transformée de Laplace :

$$\mathcal{L}_{P_I}(s) = \exp\left(-2\pi\lambda \int_{r_m}^{r_M} \left(1 - \frac{p}{1 + s \cdot b \cdot r_y^{-\alpha}} - \frac{1-p}{1 + s \cdot c \cdot r_y^{-\alpha}}\right) r_y dr_y \right) \tag{23}$$

où b et c sont définis par les paramètres de modèle rectangulaire $b = I_{max} \cdot P_0'$ et $c = I_{min} \cdot P_0'$, $s = \frac{\gamma^*}{r_x^{-\alpha} \cdot P_0'}$.

0.3.3 Résultats numérique et validation

Nous présentons les résultats de simulations avec différents coefficients d'interférence. Pour le modèle rectangulaire, nous considérons trois groupes de paramètres: le modèle approximé (AR, la courbe verte en Fig. 4), la borne supérieure (UB, la courbe rouge), et la borne inférieure (LB, la courbe bleu). Leurs valeurs sont :

$$\begin{aligned} AR: \triangle &= 145Hz, \quad I_{max} = 0dB, \quad I_{min} = -75dB \\ UB: \triangle &= 300Hz, \quad I_{max} = 0dB, \quad I_{min} = -47.28dB \\ LB: \triangle &= 116Hz, \quad I_{max} = -6.8dB, \quad I_{min} = -75dB \end{aligned} \tag{24}$$

Nous montrons en Fig. 9-10 la comparaison des résultats en simulations et en théorie. Nous avons tracé l'OP en fonction de la distance du nœud désiré r_x et la densité de nœuds actifs λ. Sur ces deux figures, nous pouvons valider la théorie pour la cas sans-fading eq.(18). Pour le cas avec fading, l'OP obtenue par la théorie eq.(21) corresponde bien à celle obtenue par les modèles rectangulaires. Donc nous pouvons en déduire que les deux expressions de l'OP sont validées.

De plus, l'évolution de l'OP avec le modèle réaliste de Sigfox (la courbe noire en trait) est entre la UB et la LB, ce qui est cohérent. Le modèle AR surestime légèrement quand r_x est petit, puis il devient plus précis quand r_x grandit. Ces résultats confirment le choix de paramètres pour les modèle AR, UB at LB, ainsi que la scalabilité des modèles rectangulaires.

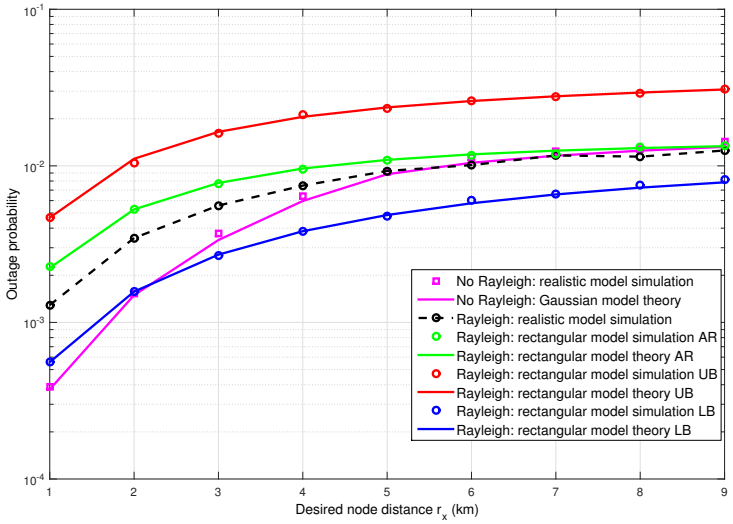

FIGURE 9: OP as a function of the desired node's distance r_x, for $B = 96$ kHz, $N = 6$, $r_M = 10$ km, $r_m = 1$ m, $\gamma^* = 6.8$ dB and path loss $\alpha = 2$.

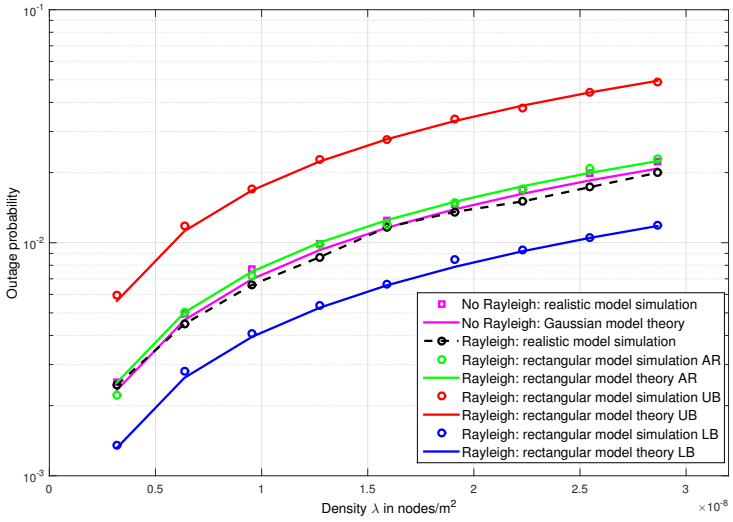

FIGURE 10: OP as a function of active nodes number N, for $B = 96$ kHz, $r_x = 7$ km, $r_M = 10$ km, $r_m = 1$ m, $\gamma^* = 6.8$ dB and path loss $\alpha = 2$.

Les phénomènes classiques sont aussi vérifiés dans : la croissance de l'OP est induite par la croissance de r_x et N. En effet, quand les transmissions simultanées sont nombreuses, les nœuds ont plus de chance d'être en collision. De même, quand le nœud désiré est trop loin de la BS, l'interférent potentiel a plus de chance d'avoir une puissance plus élevée. L'OP du nœud désiré est donc plus élevée.

0.4 La 3ème contribution

Cette section présente les résultats principaux de la troisième contribution: l'application de annulation d'interférence successive (SIC) dans les réseaux de UNB, ainsi que

l'analyse de performance en considérant conjointement le SIC et l'interférence spectrale de UNB, pour le cas de mono-BS.

Depuis les deux conributions précédentes, nous avone bien réalisé que la limitation de performance des réseaux UNB est son accès aléatoire en fréquence. Afin de mutualiser les ressources nécessaires, nous nous concentrons sur la réduction des interférences du côté BS. Nous considérons le SIC, une technologie qui permet d'enlever les interférences d'une manière récursive, en exploitant la dynamique des puissances reçues. Le SIC a été démontré comme très avantageux pour des transmissions à bas débit [15], et les réseaux l'IoT en particulier [16]. Néanmoins, ces études ne peuvent pas être directement appliquées aux transmissions UNB. En effet, le modèle spécifique d'interférence doit être pris en compte.

Dans cette contribution, nous proposons d'analyser le bénéfice du SIC dans des réseaux UNB. Nous exploitons les résultats dans la première partie de la Section 0.3.2, qui caractérise la performance de UNB sans SIC en prenant en compte que le path-loss.

0.5 Modélisation et Hypothèse

Les hypothèses sont identique que la première partie de la Section 0.3.2. Nous considérons une cellule avec une seule BS en son centre. La BS est constamment en mode réception, et scanne toute la bande B pour détecter toute transmission. Les nœuds sont distribués aléatoirement et uniformément dans le disque, de rayon $[r_m, r_M]$, avec r_m définissant une zone d'exclusion où aucun nœud est déployé. Nous supposons que N nœuds sont actifs (chacun envoie un paquet) au moment observé, et que leur paquets sont émis avec les même puissance et gain d'antenne. La propagation étant supposée se faire en espace libre, la puissance perçue à la BS dépend uniquement de la distance parcourue.

Les nœuds sélectionnent leur fréquence porteuse aléatoirement et indépendamment. Il a été montré que l'interférence nécessaire pour perdre un paquet était généralement imputable à un seul interférent [12]. Pour 2 nœuds transmettant simultanément, le niveau d'interférence perçu dépend de l'écart fréquentiel entre le paquet désiré (à la fréquence f_x) et le paquet interférent (à f_y) : $\delta f = \mid f_x - f_y \mid$. Dans cette contribution, nous utilisons le facteur d'interférence Gaussien $\beta(\delta f)$ en eq.(2).

0.5.1 Principale du SIC

Le principe du SIC est de décoder les paquets supplémentaires après le processus d'un récepteur simple. Supposons que la BS reçoit l paquets en même temps, qui sont tous en collision. Avec un récepteur simple, seulement le paquet le plus fort (en terme de SINR ou la puissance reçue) peut être correctement décodé, tant que son SINR est au dessus du seuil prédéfini. Mais avec un récepteur SIC, ce paquet premièrement décodé va être reconstruit puis soustrait de la somme de signaux en collision. La contribution du premier paquet étant retirée, de paquets supplémentaires deviennent décodables. Ainsi, le récepteur SIC arrive à décoder plus de paquets qu'un récepteur simple. Le processus de reconstruire, soustraire et décoder est une itération du SIC. SIC continue en itération jusqu'à ce que le plus haut SIR ne dépasse plus le seuil prédéfini.

Comme illustrée en Fig. 11, la *itération 0* représente le processus d'un récepteur simple, et SIC commence par la *itération 1*. Le récepteur simple arrive à décoder de signaux singleton (i.e. paquets 4, 7 sur le schéma), ou le signal le plus fort en collisions (i.e. paquet 1, 9). Basé sur les signaux décodés par le récepteur simple, SIC va les reconstruire et retirer leur contribution, ainsi le paquet 2 et 8 deviennent décodables. Après une SIC itération, nous avons déjà décodé deux paquets supplémentaires. Le paquet 5 et 6 ne sont décodable ni par le récepteur simple, ni par le récepteur SIC. Cela vient du fait que leur puissances reçues sont déjà très bas, ainsi leur interférence mutule rend leur SIR encore plus bas. Par conséquent, leur SIR ne dépasse jamais le seuil, ils restent alors undécodés.

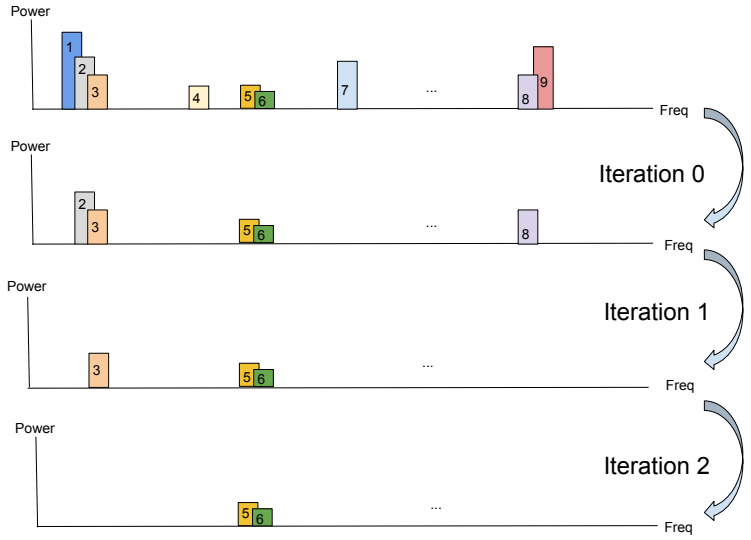

FIGURE 11: Schéma du SIC. Le paquets sont positionnés à différentes fréquences centrales, avec différents niveau de puissance reçue.

0.6 Analyse théorique

Pour mesurer la performance du réseau, nous utilisons toujours la métrique OP (Outage Probability).

Nous considérons deux nœuds actifs au moment d'observation : un nœud désiré x (resp. interférent y) à la distance r_x (resp r_y). En espace libre, le SIR (Signal to Interference Ratio) du paquet désiré (celui envoyé par le nœud désiré) s'écrit :

$$SIR_x = \frac{P_0 \left(\frac{r_0}{r_x}\right)^2}{P_0 \left(\frac{r_0}{r_y}\right)^2 \beta(\delta f)} = \left(\frac{r_y}{r_x}\right)^2 \frac{1}{\beta(\delta f)} \tag{25}$$

avec P_0 la puissance à la distance de référence r_0.

L'expression de l'OP dans le cas d'un récepteur simple a été dérivée dans la première partie de la Section 0.3.2. Dans ce cas, seulement le paquet le plus fort pouvait être décodé (si son SIR était supérieur à γ^*). Avec un récepteur SIC, ce

paquet va être reconstruit et sa contribution retirée du signal reçu. Ce processus continue tant qu'un nouveau paquet peut être décodé. Cependant, dans cette analyse théorique, nous nous concentrons sur une seule itération du SIC, puisque que nous avons fait l'hypothèse qu'il y a un seul interférent. Nous supposons que le récepteur SIC retire parfaitement les paquets décodés. Ainsi, quand deux paquets interfèrent mutuellement, une fois que l'un est correctement décodé, l'autre va aussi être décodé grâce au SIC.

Pour que le paquet du nœud désiré x soit perdu malgré la présence du SIC, il faut que les SIR de x et de y soient tous les 2 inférieurs à γ^*. L'OP du paquet d'intérêt avec SIC donc s'écrit:

$$\begin{aligned} \mathrm{OP}_{SIC} &= \mathbb{P}\left(SIR_x < \gamma^* \cap SIR_y < \gamma^*\right) \\ &= \mathbb{P}\left(r_y < r_x\sqrt{\gamma^*\beta\left(\delta f\right)} \cap r_y > \frac{r_x}{\sqrt{\gamma^*\beta\left(\delta f\right)}}\right) \end{aligned} \tag{26}$$

Puisque le SIR du x et y dépendent d'un même δf, ces probabilités sont corrélées. Nous ne pouvons donc pas les traiter indépendamment. Nous calculons l'OP avec SIC en utilisant la loi de la probabilité totale: avec comme variables d'intégration r_y, r_x et δf. L'intégration a été faite en décomposant le calcul sur plusieurs supports d'intégration selon la valeur de$\sqrt{\gamma^*\beta\left(\delta f\right)}$ (plus de détails peuvent être trouvés dans le chapter 5). Enfin, nous étendons eq.(26) au cas de N utilisateurs (dont un nœud désiré, et $N-1$ interférents potentiels). Dans ce cas-là, le paquet du nœud désiré est correctement reçu si aucun de ces $N-1$ l'interrompe. L'expression finale de l'OP avec du SIC devient:

$$\mathrm{OP}_{SIC(N)} = 1 - \left(1 - \mathrm{OP}_{SIC}\right)^{N-1} \tag{27}$$

L'obtention de cette expression est montrée dans le **??**. Elle dépend de plusieurs paramètres: la taille du cellule $[r_m, r_M]$, la bande totale B, le nombre de nœuds actifs N, et le seuil du SIR γ^*.

0.6.1 Résultats numérique et validation

Nous avons lancé des simulations de Monte Carlo pour valider eq.(27). La topologie du réseau et les hypothèse restent identiques à celles de la théorie. Dans un premier temps, nous n'imposons pas de limitation sur les itérations du SIC. Nous avons évalué le pourcentage des paquets décodés par rapport à différentes itérations du SIC sur Fig. 12. L'itération 0 correspond au décodage d'un récepteur simple, et les itérations supérieures au SIC. Nous observons que les itérations nécessaires augmentent lors que le nombre de nœuds accroît. Néanmoins, c'est toujours la 1ère itération qui apporte l'amélioration la plus importante. Cela confirme la pertinence de l'hypothèse d'une seule itération.

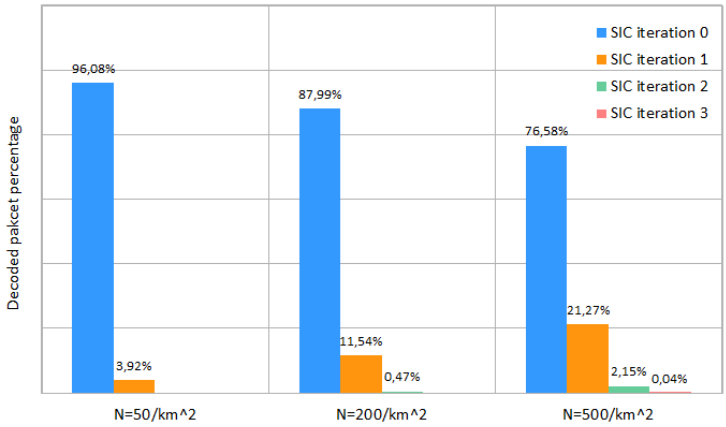

FIGURE 12: Pourcentage de paquets décodés vs itération du SIC, pour différentes nombres de nœuds, $B = 96$ kHz, $r_m = 30$ m, $r_M = 1000$ m, $\gamma^* = 6.8$ dB.

La Fig. 13 présente la performance du récepteur simple et celle du SIC, théoriquement et par simulation. Nous pouvons voir que les simulations du SIC (points) coïncident parfaitement avec la théorie (ligne). Nous avons obtenus les même comportements en variant B et γ^* (à voir dans le chapter 5). Par conséquent, l'expression théorique eq.(27) est validée. En plus, nous vérifions les comportements classiques, par exemple l'OP augmente quand le nombre de nœuds augmente. En effet, quand le trafic est plus dense, la performance du réseau se dégrade.

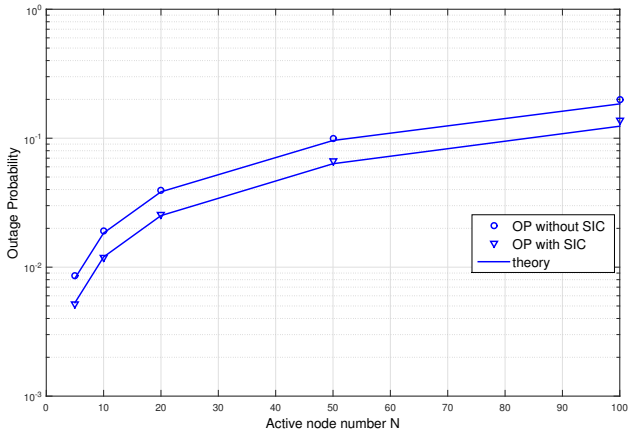

FIGURE 13: OP sans SIC vs avec SIC, pour différents nombres de nœuds N, $B = 96$ kHz, $r_m = 30$ m, $r_M = 1000$ m, $\gamma^* = 6.8$ dB.

0.6.2 Analyse de la performance du SIC

Nous analysons l'efficacité du SIC dans cette partie. Nous définissons $\frac{OP_{noSIC} - OP_{SIC}}{OP_{noSIC}}$ comme le *gain* du SIC, pour caractériser l'amélioration relative du SIC sur le récepteur simple. Pour généraliser l'étude, nous caractérisons l'activité du réseau par la densité normalisée de nœuds, i.e. l'occupation spectrale moyenne. Cela est défini par l'occupation spectrale de tous les nœuds actifs sur la bande totale $\frac{100N}{B}$ (un signal de UNB occupe 100 Hz typiquement).

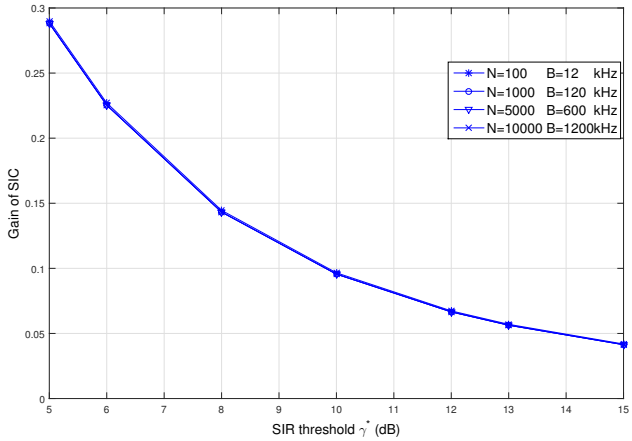

FIGURE 14: Gain de SIC, pour différents seuils de SIR γ^* (dB), et la densité de nœuds $\frac{100N}{B}$ constante, $r_m = 30$ m, $r_M = 1000$ m.

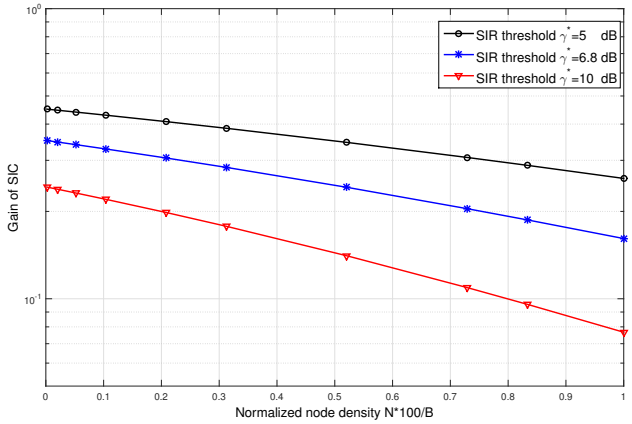

FIGURE 15: Gain de SIC, pour différentes densités de nœuds $\frac{100N}{B}$, et différents seuils du SIR γ^* (dB), $r_m = 30$ m, $r_M = 1000$ m.

Nous avons évalué ce gain en maintenant la densité normalisée constante. Comme montré dans la Fig. 14, peu importe à quel ordre de grandeur est le nombre de nœuds, l'amélioration apportée par le SIC est identique une fois que la densité normalisée reste constante. De plus, nous avons vérifié l'évolution du gain quand la densité de nœuds n'est plus constante. Comme nous pouvons voir dans Fig. 15, la performance du SIC dégrade lors que la densité normalisée ou le seuil du SIR augmente.

Ces résultats peuvent être directement exploités pour ajuster les paramètres du système en fonction du trafic visé. Par exemple, pour un nombre de nœuds donné, nous pourrons adapter la bande passante totale pour atteindre les performances attendues.

0.7 La 4ème contribution

Cette section présente la quatrième contribution de la thèse : l'exploitation de la diversité spatiale de multiple BS dans le but d'améliorer la performance des systèmes UNB. Nous appliquons différents technologies de combinaison de signaux, puis l'annulation d'interférence à travers des multi-BS. Nous analysons en théorie pour le cas slection combining, puis nous évaluons numériquement l'amélioration de performance par rapport à mono-BS pour toutes les technologies.

Dans la plus part de réseaux cellulaires, une BS serve les utilisateurs (i.e. les nœuds) dans sa cellule. Les nœuds sont alors attachés à cette spécifique BS, les échanges sont faites qu'avec la BS concernée. Mais dans le réseau de Sigfox, les nœuds ne sont attachés à aucune BS. Cela introduit la conséquence où un signal peut être aperçu par plusieurs BS. De plus, chaque BS a un point de vu différente pour des signaux transmis. Parce que les BSs ne sont pas toutes à la même distance pour un nœud donné (donc l'atténuation n'est pas la même), ainsi que le signal passe de conditions de canal diverses pour arriver à chaque BS. De même, le signal en question n'a pas vécu la même scénarios d'interférence. Donc c'est possible que le signal soit perdu à une BS, et qu'il soit décodé proprement à une autre BS. Cette diversité spatiale (en temps, en fréquence et en espace) peut être très pertinente à exploiter pour améliorer la performance du réseau.

Les technologies de combinaison de signaux est le plus commun pour exploiter a diversité spatiale de multi-récepteurs. Elles visent à combiner les signaux reçus par chaque BS, même si aucun entre eux est décodé. Avec la combinaison, la contribution du signal désiré est ajoutée de façon constructive, cependant l'interférence et le bruit sont moyennés. Cela conduit à une augmentation significative en SINR. Ainsi, le signal désiré a plus de chance d'être décodé.

Dans cette contribution, nous évaluons la SC (slection combining), la EGC (equal gain combining) et la MRC (max ratio combining). Puis nous appliquons le SIC (déjà introduit dans la 3ème contribution) à travers des multiple BS.

0.7.1 Principe de SC/EGC/MRC

Un signal donné est aperçu par chaque BS avec de différents niveaux de SIR. Nous considérons le canal de ce signal à chaque BS comme une branche de combinateur de signaux. Nous supposons que les signaux de toutes les branches ont la même phase, donc c'est juste le niveau de puissance qui joue.

Nous avons présenté en Fig. 16 le schéma de SC/EGC/MRC. Un symbole x (dont l'amplitude est ± 1) est transmit et perçu par les BSs (i.e. les branches). Sur la $i$ème branche, son amplitude est impactée par h_i qui représente la condition de canal (donc le gain de canal) de la BS_i. Durant la transmission, le bruit et l'interférence est ajouté. Cela changera l'amplitude du symbole.

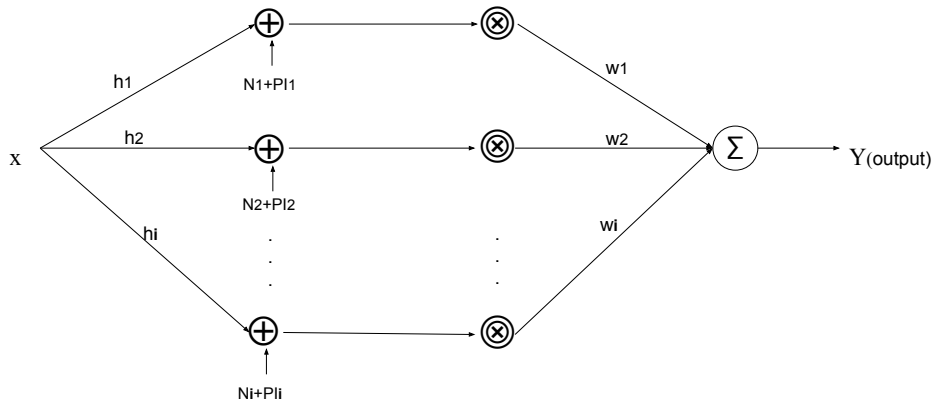

FIGURE 16: Schéma de SC/EGC/MRC. x représente le symbole transmit, h_i le gain de canal de BS_i, N_i et PI_i sont le bruit et l'interférence vecu par le signal sur la branche BS_i, et w_i le poids sur la $i$ème branche.

SC sélectionne le signal de la meilleur qualité (en terme de SIR) parmi toutes les branches, pour décider si le message contenu dans le signal peut être décodé ou pas (i.e. si son SIR dépasse ou pas le seuil). Si SC échoue, le paquet sera envoyé dans le combinateur EGC ou MRC.

Dans le cas de EGC et MRC, la sortie du combinateur est l'enveloppe de la somme des signaux pondérées sur toutes les branches. L'objectif est de maximiser le SINR de la sortie en choisissant les poids. En EGC, les poids sont identiques pour chaque branche. Alors qu'en MRC, dans la plus part de littérature où l'interférence n'est pas considérée, le poids est proportionnel au gain de canal de la branche. Mais dans les réseaux de UNB où l'accès à radio est aléatoire, l'interférence ne peut pas être ignorée. Par conséquent, quand le gain du canal h_i est élevé sur une branche, le SINR_i n'est pas nécessairement élevé (quand le signal est gravement affecté par l'interférence).

Donc dans cette contribution, nous considérons que le poids pertinent w_i est proportionnel au SINR de la branche, qui reflètent la condition de canal et le niveau d'interférence. Nous pouvons alors exprier le SINR du combinateur EGC et MRC comme la suivante :

$$SINR_y = \sum_{i=1}^{K} w_i \cdot SINR_i \tag{28}$$

avec K branches, et les poids comme :

$$w_i(MRC) = \frac{SINR_i}{\sum_{i=1}^{K} SINR_i} \cdot K;$$
$$w_i(EGC) = 1$$

0.7.2 Principe de SIC locale

Pour mieux exploiter la diversité de multi-BS, nous appliquons le SIC à travers plusieurs BSs. Cela nous permet de bénéficier conjointement la diversité spatiales et la diversité en puissance reçue. Nous proposons de le faire en deux façons : la

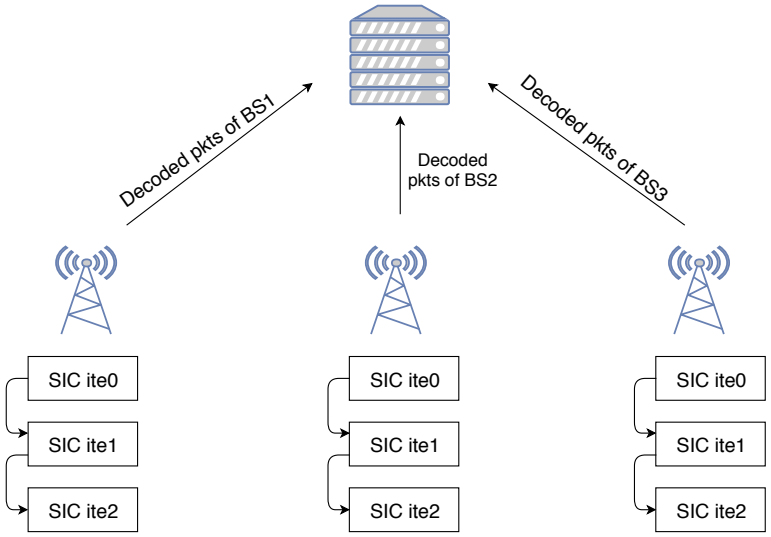

FIGURE 17: Schéma de SIC locale chez chaque BS. Les BSs procèdent SIC localement, puis transmettent leur paquets décodés au back-haul. *Ite*0 représente le procésus d'un récepteur simple; L'itération maximum du SIC est défini à 2.

manière local et la minière globale. Nous supposons que toutes les BS arrivent à reconstruire et soustraire les signaux parfaitement.

Pour le SIC locale à chaque BS, les BSs ne communique pas directement entre elles. Elles procèdent SIC localement jusqu'à la dernière itération, puis elles envoient leur paquets décodés au back-haul, comme montré en Fig. 17. Avec la présence de diversité spatiale, les paquets non-décodés chez une BS peut être décodés chez une autre. Puisque le back-haul collecte tous les paquets décodés depuis toutes les BSs, la performance est meilleure que mono-BS qui procède SIC. L'itération maximum est prédéfinie.

0.7.3 Principe de SIC globale

Dans le cas globale, les BSs coopèrent pour effectuer le SIC. Toutes les BSs fait le SIC localement, puis envoyer leur paquets décodés à leur voisines par des liens directs, après chaque itération de SIC. Comme illustrée en Fig. 18, le terme $\mathbb{P}(i,j)$ contient les paquet décodés par BS_i, après la $j$ème SIC itération. Nous supposons que $\mathbb{P}(i,j)$ contient tous les détails de signaux nécessaire pour qu'ils puissent être reconstruites par les BSs voisines.

Après chaque SIC itération, $\mathbb{P}(i,j)$ va être broadcast à toutes les BSs voisines. Puis, les BSs peuvent exploiter les $\mathbb{P}(i,j)$ envoyés par leur voisines, reconstruire les paquets qu'elles ont besoin, et éliminer la contribution des paquets indésirables. En conséquence, le paquets qui étaient interféré deviennent décodable chez des BSs grâce à $\mathbb{P}(i,j)$. Ce processus est effectué par toutes les BSs après chaque itération. A la fin, toutes les BSs groupent leur paquets décodés de toutes les itération sum($\mathbb{P}(i,j)$), et les transfèrent au back-haul.

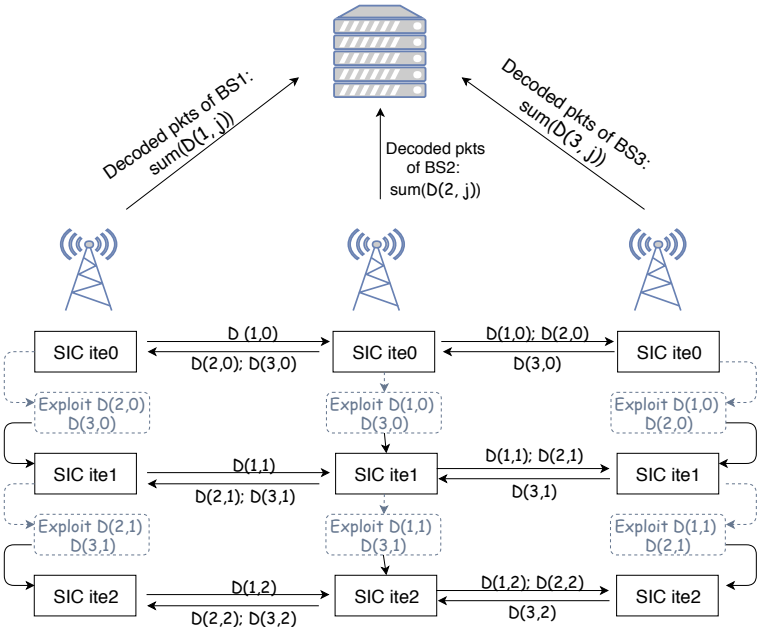

FIGURE 18: Schéma du SIC globale à travers multi-BS. $\mathbb{P}(i,j)$ contient les paquets décodés par la $i$ème BS, après la $j$ème SIC itération.

0.7.4 Résultats numériques

Dans cette section, nous évéaluons la performance de toutes technologies mentionnés avant : SC, MRC, EGC, local SIC chez chaque BS et SIC globale à travers multi-BS. Pour observer le gain apporté par les multi-BS, nous avons aussi tracé la performance de mono-BS et la BS la plsu proche (en terme de distance physique). C'est toujours le terme OP=$\mathbb{P}(SIR < \gamma^*)$ qui représente la performance du réseau. Nous avons négligé le bruit dans cette contribution parce que son niveau est beaucoup plus bas que l'interférence.

Nous avons fait les simulations de Monte-Carlo sur Matlab, avec ces paramètres prédéfinis : les nœuds et les BSs sont distribués aléatoirement en HPPP (comme montrée en Fig. 3 (b)) dans une carré de $200km \times 200km$; l'exposant de propagation $\alpha = 2$; le Rayleigh fading qui suit une lois exponentielle avec le moyenne égale à 1; et le seuil de SIR $\gamma^* = 7$dB. Nous avons présenté en Fig. 19-20 l'OP en fonction de la charge normalisée $\frac{\lambda_n}{\lambda_b}$ et la ressource fréquentielle totale B, pour toutes les technologies.

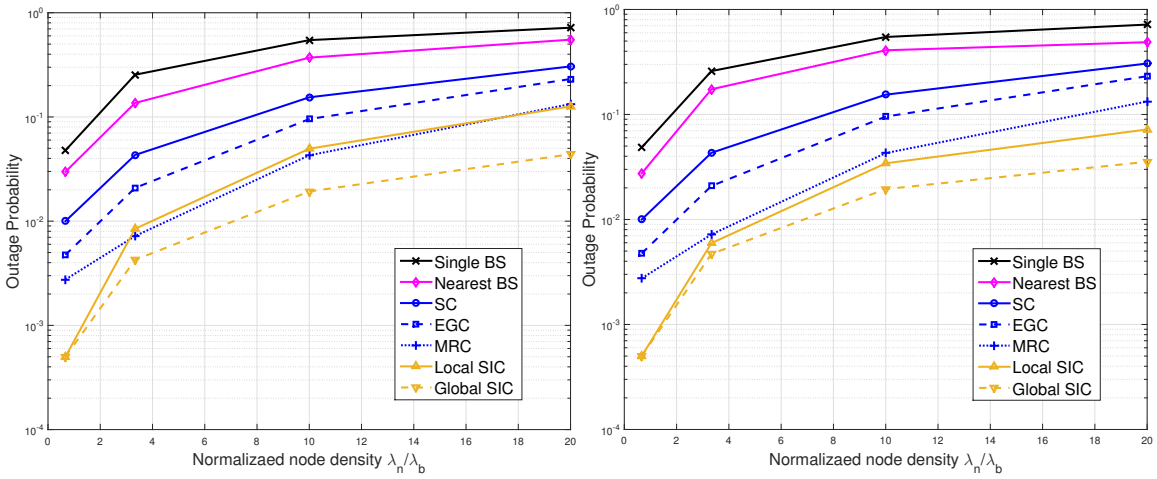

(A) OP vs $\frac{\lambda_n}{\lambda_b}$, maximum 1 SIC itération

(B) OP vs $\frac{\lambda_n}{\lambda_b}$, maximum 2 SIC itération

FIGURE 19: OP vs la charge normalisée $\frac{\lambda_n}{\lambda_b}$, avec $B = 12$kHz, $\gamma^* = 7$ dB.

D'abord, nous pouvons observer que les technologies de multi-BS ont toujours une meilleure performance que mono-BS. Puis nous remarquons que $OP_{(nearest\ BS)}$ est moins bon que le SC. C'est du fait d'avoir plusieurs variables aléatoires comme fading et l'interférence de UNB qui impactent le SIR. Ainsi, la plus courte distance (i.e la BS la plus proche) n'a pas nécessairement meilleur performance.

Ensuite, nous notons que EGC/MRC sont toujours plus performants que SC. C'est parce que le processus de EGC/MRC est basé sur les résultats de SC. Si un paquet réussit à être décodé par une des BS, il n'y a pas besoin de l'envoyer dans le EGC ou MRC combinateur. Nous combinons seulement les paquets qui sont de faible qualité (bas SIR_i) sur toutes les branches. Ainsi, c'est normal que EGC/MRC sont plus performant que SC.

En outre, nous remarquons que le MRC est plus performant que EGC. En effet, les poids de MRC prennent en compte la gain de canal et l'interférence, donc ils sont capable de maximiser le SIR de la sortie du combinateur MRC. Au contraire, les poids de EGC sont identiques sur toutes les branches, qui égalise les signaux de bonne ou de faible qualité. En conclusion, EGC est moins performant que MRC, même s'il est plus simple à implémenter.

Puis nous pouvons noter que le SIC globale à travers multi-BS est plus performant que le SIC locale chez chaque BS. Ce n'est pas surprenant parque le SIC globale permet de partager les informations parmi toutes les BSs. Ainsi, le SIC globale arrivent à reconstruire et soustraire les paquets décodés par les autres BSs. Cela lui permet de décoder plus de paquets que faire du SIC localement chez chaque BS. C'est aussi la raison que le SIC globale est plus performant que MRC. Puisque MRC additionne en même temps les signaux et les interférences, alors que le SIC globale arrivent à retirer les interférences.

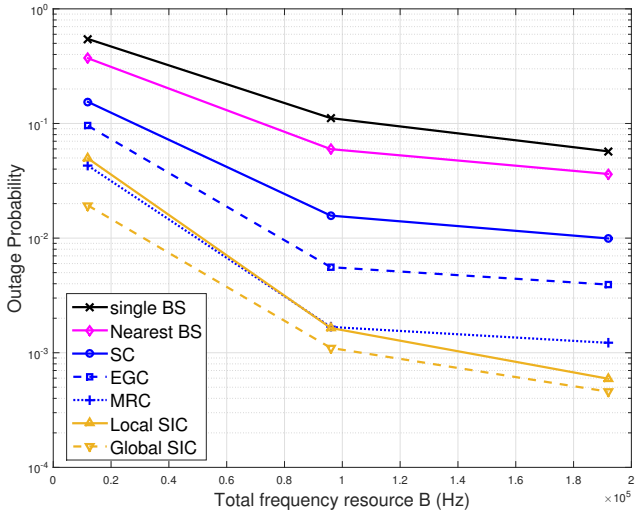

FIGURE 20: OP vs la bande totale B, maximum 1 SIC itération, avec $\frac{\lambda_n}{\lambda_b}$=10, $\gamma^* = 7$ dB.

Ce qui est intéressant c'est quand nous comparons Fig.19(A, B), nous remarquons que le SIC (locale ou globale) a seulement une amélioration légère de performance quand on augmente le nombre d'itération maximum. En outre, plus le nombre d'itération augment, plus la complexité de systèmes accroît, et plus nous avons besoin de ressources de calculs. Avec ces résultats, nous savons maintnant que nous pouvons avoir de performance similaire avec 1 ou plus de SIC itérations.

0.8 La 5ème contribution

Dans cette section, nous présentons les résultats principaux de la cinquième contribution : la validation expérimentale du modèle d'interférence, et de la capacité du réseau sous des conditions idéalistes.

0.8.1 Présentation des outils

FIT/CorteXlab

Nous utilisons la plate-forme radio FIT/Cortexlab (future internet of things cognitive radio testbed) pour faire des expérimentations. Cette plate-forme nous permet d'évaluer différent aspects de radio congnitivs dans des scénarios réalistes [17]. CorteXlab utilise architecture de réseau développé par IoT-lab, il intègre des nœuds SDR (software defined radio) et offre un accès et manipulation à distance.

Le testbed est installé dans une chambre isolée de toutes les ondes interférences externes, et est couverte de matériel qui absorbe des ondes électromagnétique. Donc la condition de canal (comme path-loss, fading, shadowing , etc.) est totalement sous contrôle des utilisateurs. En plus, cela nous permet de répéter des expérimentations avec le même scénario.

Les nœuds que nous utilisons pour faire de l'expérimentation, sont les nœuds SDR qui consistent à 22 cartes USRP (Universal Software Radio Peripheral). Ces

cartes peuvent être transmetteurs et récepteurs, dont la fréquence d'opération peut varier de 400 MHz à 4.4 GHz.

GNU Radio

Les cartes USRPs sont seulement programmable avec GNU Radio pour le moment. GNU Radio est un logiciel gratuit et open-source qui fournit des bloques de traitement de signal pour implémenter le software radio [18]. Le software radio est un système de radio qui faut le traitement de signal en logiciel à la place de circuit hardware intégré. Nous pouvons utiliser les bloques existants sur GNU Radio, ou créer nos bloques en programmant en Python ou C++. Nous utilisons le logiciel graphique GRC (GNU Radio companion) où nous pouvons mettre en place les bloques en flow-graph.

0.8.2 Planning de l'expérimentation

Comme montrée en Fig. 21, nous utilisons des cartes USRPs (les points en vert et bleu) pour émuler des signaux UNB et transmettre. La réception se fait par une station de base Sigfox qui est installée dans la salle de CorteXlab totalement isolée. Comme la chambre est couverte de matériels absorbant des ondes électromagnétiques, les murs et les sols n'engendrent pas de réflexion et obstacles indésirables. Ainsi, nous avons mis la puissance d'émission de chaque nœud au même niveau, leur puissance reçu est donc identique à celle d'émission peu importe où ils se situent. Une condition de canal idéaliste est donc émulée.

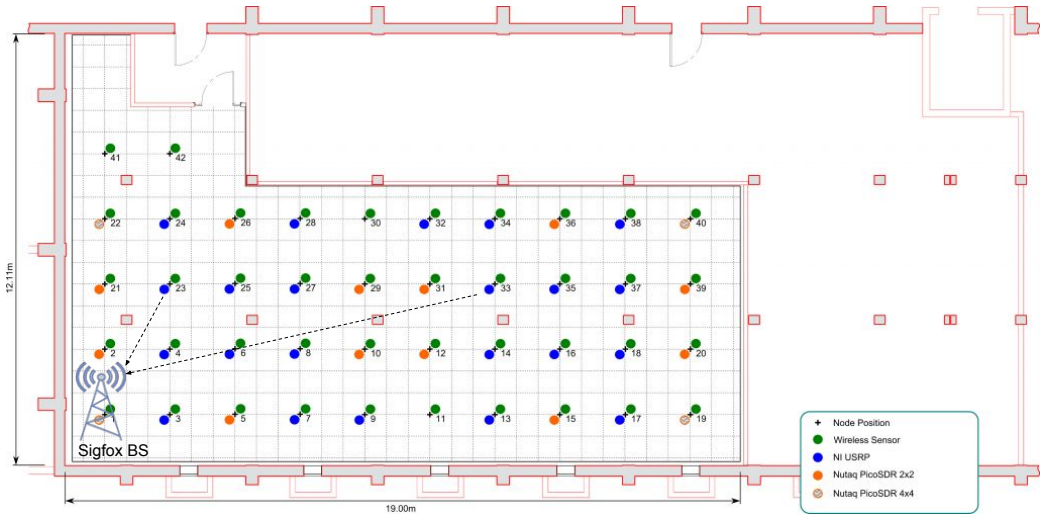

FIGURE 21: L'emplacement de la BS Sigfox et les cartes USRPs dans la chambre de Cortexlab.

0.8.3 Validation de coefficient d'interférence

Nous avons vérifié le coefficient d'interférence, comme il est le base de toutes les analyses théorique dans cette thèse.

Nous nous focalisons sur deux signaux, celui désiré x à la fréquence centrale f_x qui ne change pas, et celui d'interférent y à la fréquence f_y qui est d'abord

superposé avec f_x, puis décalé au fur et à mesures de f_x. Cette écarte génère $\delta f = |f_x - f_y|$ que nous avons mentionné dans toutes les autres contributions.

Nous avons tracé le coefficient expérimentale d'interférence en fonction de l'écarte fréquentielle δf, sur la Fig. 22. Nous remarquons les coefficients de Gaussien et de AR ont tous légèrement sur-estimé celui obtenu par des expérimentations. Globalement, le coefficient expérimental peut être mieux approximé par un modèle rectangulaire plus étroite.

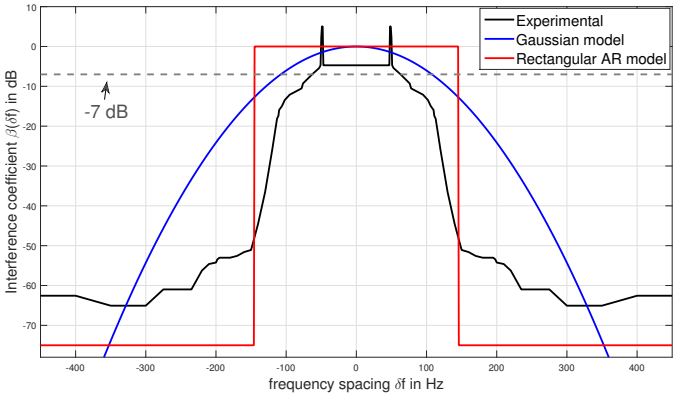

FIGURE 22: Le coefficient d'interférence expérimentale.

0.8.4 Validation de OP sous conditions de canal idéalistes

Puis nous avons vérifié la probabilité de coupure sous les conditions de canal idéalistes (où la puissance reçue de chaque paquet est identique) par les expérimentations. Nous nous concentrons sur l'interférence spectrale, donc les transmissions sont synchronisées pour négliger l'impact temporal. Le nombre de transmissions simultanées est N.

Nous avons dérivé les expression théorique de l'OP_{th}, en supposant qu'il y a un interférent à chaque collision et que le bruit est négligeable:

$$Exprimental : \mathrm{OP}_{th} = 1 - \left(1 - \frac{2 \cdot \Delta_{exprimental}}{B}\right)^{(N-1)} \tag{29}$$

$$Gaussien : \mathrm{OP}_{th} = 1 - \left(1 - \frac{2 \cdot \Delta_{Gaussien}}{B}\right)^{(N-1)} \tag{30}$$

$$RectangulaireAR : \mathrm{OP}_{th} = 1 - \left(1 - \frac{2 \cdot \Delta_{AR}}{B}\right)^{(N-1)} \tag{31}$$

avec $\Delta_{exprimental} = 63$ Hz, $\Delta_{Gaussien} = 116$ Hz, et $\Delta_{AR} = 145$ Hz. Ces valeurs de Δ viennent de la limite de δf quand le coefficient dépasse -7 dB, qui sont observables en Fig. 22.

Nous avons tracé en Fig. 23 une comparaison de l'OP obtenue par des expérimentations et par les théories. Nous pouvons observer que l'OP obtenue par des expérimentations (la ligne noire pointillée) est très proche de l'OP_{th} par le coefficient expérimentale (la ligne noire solide). La première est légèrement au-dessus de la seconde. Cette légère différence vient probablement de l'hypothèse en théorie où nous avons supposé un seul interférent (mais l'interférence agrégée

peut arriver en expérimentations), et la négligence de bruit en théorie. Mais globalement, le coefficient expérimental décrit bien l'évolution de l'OP réalistes. Cela montre la cohérence du coefficient expérimental.

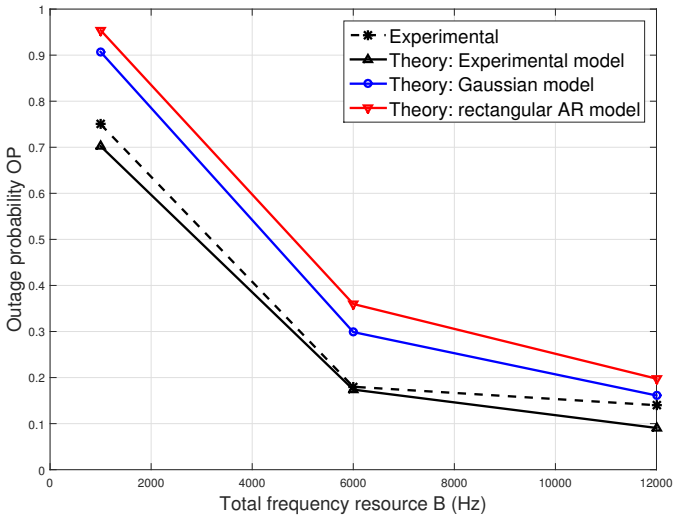

FIGURE 23: OP vs la ressource fréquentielle totale B en Hz. Le nombre de transmission simultanées $N = 10$, et la sensibilité de la Bs Sigfox $\gamma^* = 7$ dB.

Chapter 1

Introduction

Contents

1.1 Context of thesis

IoT (Internet of Things) has been a hot issue in recent years, both in the research fields, and on the market. It refers to networks of physical devices that have communications capabilities. The expectation that everything is going to be connected is leading the trend. It is foretold that, by 2020, there will be 20 billions of communicating objects in the world [19]. These objects collect and transfer information. They are also designed to support many sorts of applications: they can vary from indoor to outdoor, from smart meter's several bytes of data per day to vehicle monitor's huge amount of information per milliseconds, from bluetooth, WiFi to sub-GHz technologies, and from battery-based such as fire alarm to always charged such as video surveillance [20]. With different features, their particular requirements vary.

However, most of the devices do not have ultimate demands in terms of latency or data rate. They only have a small amount of data to transfer, and do not require a response within a milliseconds delay. Thus, a single collecting point can serve, from a capacity point of view, a high number of nodes. For low density deployments, this permits a coverage of tens of kilometers. Nonetheless, the majority of this kind of devices are battery-based. As the frequent battery maintenance is to be avoided due to the high number of nodes, a low energy consumption is also a strong requirement for IoT. Therefore, the challenges for IoT networks are to achieve high scalability to handle massive nodes, to be able to manage a bursty access to the medium, to have wide coverage, while keeping low energy consumption, and low node cost.

Devices which have these demands are difficult to be integrated into traditional cellular networks due to their sporadic activities. That's why recent technologies have come to the scene, dedicated to LPWAN (Low Power Wide Area Network) [8], such as NB-IoT, which has been included to the 3GPP standardization, and is the narrow band system based on LTE ; CSS, commercially known as LoRa, provides the possibility for people to build their own LoRaWAN; RPMA

which is developed by Ingenu; and UNB (Ultra Narrow Band), developed and patented by the French company Sigfox, was the first one to be commercially initiated for IoT purpose.

Interestingly, two opposite approaches have been exploited to perform the targeted long range transmission. Spreading spectrum is considered in LoRa and RPMA, while UNB permits to transmit messages by using extreme narrow-band signals (100-200 Hz, about one thousand times smaller than the whole channel bandwidth). Both approaches aim at realizing long-range transmissions, the former is achieved by by the spreading coding gain, whereas the latter is achieved by its very low noise level. The key advantages of UNB are its simplicity and its wider practical coverage than the others [8]. We focus on UNB in this thesis.

1.2 Motivations

In a UNB system, the signal used to transfer information occupies a very small band compared to classical systems, typically 100Hz. This is about one thousand times narrower than the whole frequency resources (typically 192kHz). UNB signal transmissions are performed on the 868 MHz (resp. 915 MHz) ISM band in Europe (resp. in the USA).

The main specificity of UNB is linked to the oscillator imprecision, which is a typical phenomenon in electronic devices. It characterizes the fact that there exists an offset between the targeted frequency and the actual generated one. This imprecision comes from oscillators factoring. To the best of our knowledge, regular low-cost oscillators (0.25ppm drift) can lead to an inaccuracy of 217Hz for a targeted frequency at 868MHz. This uncertainty is larger than the individual UNB signal bandwidth. Thus it is not realistic to obtain perfectly orthogonal channels in UNB systems, if we want to keep the low-cost attribute.

As a consequence, the natural and dedicated channel access scheme for UNB is RFTMA (Random Frequency and Time Multiple Access), which is an Aloha-type scheme. Different from traditional Aloha, RFTMA generates randomness in both time and frequency domains. Each node sends its messages at any moment and at a carrier frequency randomly chosen at its will, without preliminarily analyzing the channel state. The advantage of this approach, is that the classical overhead dedicated to the reservation of radio resources is saved, and that the use of low-cost oscillators is possible. Nonetheless, as there is no control, collisions may occur. This interference potentially generated by simultaneous transmissions needs to be alleviated.

Although Sigfox's network is deployed worldwide and renowned to be efficient for low data rate and long range transmissions, there are still many open questions such as: what's its scalability when numerous simultaneous transmissions happen? What is the network capacity in realistic conditions, when facing fading and internal/external interferences? How to deal with the collisions caused by non-synchronized unpredicted emissions? How to improve the network performance without changing its random radio access?

I have thus considered UNB during the three years of my thesis. The objectives are not only to provide a more scientific vision to this first technology commercially initiated for IoT purpose, but also to evaluate its network capacity, and to further propose solutions for enhancing the performance. I highlight that this thesis is based on the results of a previous PhD, and his two papers [9, 12].

1.3 Contributions and organization of thesis

The thesis starts firstly with the state of the art of IoT, the context of LPWAN and the problematics of the technology (i.e. UNB) that I study in this these, in chapter 2. Then I present my contributions from chapter 3 to chapter 7 which are stated in details in the following paragraph. Finally, I conclude the thesis and raise the perspectives in chapter 8.

My contributions which respond to the previously mentioned objectives are:

1. Fundamental capacity characterization of UNB networks, under idealistic channel conditions for single base station (BS) case. I theoretically quantify the capacity for the specific random-FTMA multiple access of UNB, then I extend it to generalized Aloha case (including slotted/unslotted time/frequency Aloha) and broadened it for replications. I highlight the time-frequency duality in UNB systems, and that there exists an optimum replication number for a given network parameter set. This contribution is reported in chapter 3.

2. Evaluation of the UNB system performance under realistic channel conditions, still for single BS case. I derive and exploit two theoretical expressions of the outage probability: the first one considers the path-loss due to the propagation, the spectral interference caused by the random radio access of UNB, and in the condition of only one interferer at each collision; the second one has included the joint impact of Rayleigh fading and the aggregated interference (where a failure can come from several collision packets) in addition. I highlight that these analysis are carried out by leveraging on the powerful mathematical tool stochastic geometry, and reported in chapter 4.

3. Enhancement of the UNB networks' performance from the single base station's side. I apply the well-known SIC (Successive Interference Cancellation) to mitigate the spectral interference of UNB systems in a recursive way. I provide a theoretical analysis of the outage probability, when considering jointly SIC and the specific spectral randomness of UNB. Realistic channel conditions with path-loss is considered. I note that SIC brings benefits in enhancing UNB system performance, and that fading delivers an additional degree of freedom which improves the performance of SIC. This contribution is reported in chapter 5.

4. Improvement the UNB systems performance, by exploiting the spatial diversity of multiple base stations. I propose to perform signal combining and interference cancellation technologies across multi-BS. Firstly, I demonstrate a theoretical performance analysis for the simplest Selection Combining (SC), when considering the correlation among the interferences viewed by all the BSs. Secondly, I attack more complex ones, such as Max Ratio Combining (MRC) and Equal Gain Combining (EGC), which combine undecoded signals of all the BSs in the purpose of obtaining a better-quality output. Then I propose to apply two methods: local SIC and global SIC across multi-BS. Finally, I evaluate the performance improvement of all the technologies (compared to single BS). These technologies exploiting multi-BS diversity are proved to be significantly beneficial in improving UNB networks' scalability. We can gain until 125 times better performance with global SIC. And

I highlight that these results provide a choice among the technologies according to the improvement needs and the implementation complexity. This contribution is reported in chapter 6.

5. Experimental verification of the the UNB spectral interference coefficient and the network capacity. I conduct the experiments on a cognitive radio testbed FIT/Cortexlab, where the transmissions are emulated by soft-ware defined radio equipments and the reception is performed by a Sigfox base station. I obtain the realistic interference coefficient from the experiments, and compare it with the Gaussian and rectangular models used in the theoretical analysis. The result shows that both Gaussian and rectangular models have over-estimated the realistic coefficient, but it also gives an insight of how to adapt it. Then I verify the experimental performance with the theoretical ones, under idealized channel conditions. This contribution is reported in chapter 7.

Chapter 2

State of the art

Contents

In this chapter, we present an overview of Internet of Things (IoT) concerning its evolution from wireless sensor networks, as well as its current needs and connectivity technologies. Among these enabling technologies, LPWAN (Low Power Wide Area Network) stands out as ideal candidate for the numerous power-critical, long-range and low-throughput IoT devices. The issued challenges and studies of LPWAN are presented, along with the introduction of several technologies existing on the market. Then, we focus on the Ultra-Narrow-Band (UNB) technique deployed by the company Sigfox, which is the main technology that I worked on during this thesis. Its definition, specificity and related scientific works are provided. Finally, we summarize and discuss some relevant and open issues in the research field.

2.1 IoT overview

2.1.1 Evolution and challenges of IoT

Internet of things (IoT), as a big part of evolution predicted in 5G (the fifth generation), has been gaining a lot of attention in recent years. IoT is the network which connects physical devices, vehicles, and even buildings without human involvement [21]. It extends the connectivity beyond computers and phones to virtually

any object that has a chip and a radio interface. It is expected to allow heterogeneous objects to communicate with each other, by bridging diverse technologies.

At the beginning, the services offered by IoT were focused on Smarthome that is realized by M2M (machine to machine) systems. They connect devices at home such as thermostats, energy meters, lighting control systems, music streaming and control systems, remote video streaming boxes, and pool systems, etc. Most of these systems have some connectivity through a Web site so that a user can manage them through a standard Web browser or a smartphone app. But the scale of devices was very limited. Gradually, the applications in M2M has been enlarged to all objects and even living things, such as health surveillance, smart grids and smart cities. Thus not only the number of people learning the advantages of IoT is growing, but also the number of objects to be connected is rising.

Over time, the needs towards IoT are also evolving. In terms of data rate need, it can vary from smart meter's several bytes of data per day to vehicle monitor's huge amount of information (some hundreds of megabytes) per milliseconds. In respect of latency criticality, it varies from several seconds such as animal tracking to less than one milliseconds such as real-time medical operations in distance. With regards to the connectivity, it varies from robot movements' several centimeters to outdoor tracking's some fifty kilometers. And in terms of scale of connected objects, it varies from several sensors at one's home to some thousands of sensors/actuators in a smart building.

To follow these growing needs, the challenges of IoT [22] [23] include :

- The scalability to manage bursty connection demands from massive objects
- Adapting the design of devices, in order to fit customers' requirements in respecting availability of anywhere and anytime
- Exploiting new enabling technologies, for the purpose of fulfilling the compatibility of heterogeneous things
- Upgrading the Internet architecture, in oder to fit the tremendous number of objects connecting to it
- Promoting the architecture standardization for IoT, in the favor of users' choices and the creating a competitive environments for companies
- Figuring out the solutions for numerous demands of low-power and event-driven communication
- Maintaining the security levels and respecting privacy issues
- Ensuring the quality of service to customers at an efficient cost

In this thesis, I focus on the connecting technologies, where lie my research interests in the PHY and MAC layers.

2.1.2 Enabling technologies in IoT

Enabling technologies, as a crucial element in IoT, allow heterogeneous objects to communicate with their gateways, with the base stations and with each other. As the technologies like 5G are coming, more and more applications requires high transmission speed and real-time monitoring. However, in the market of IoT,

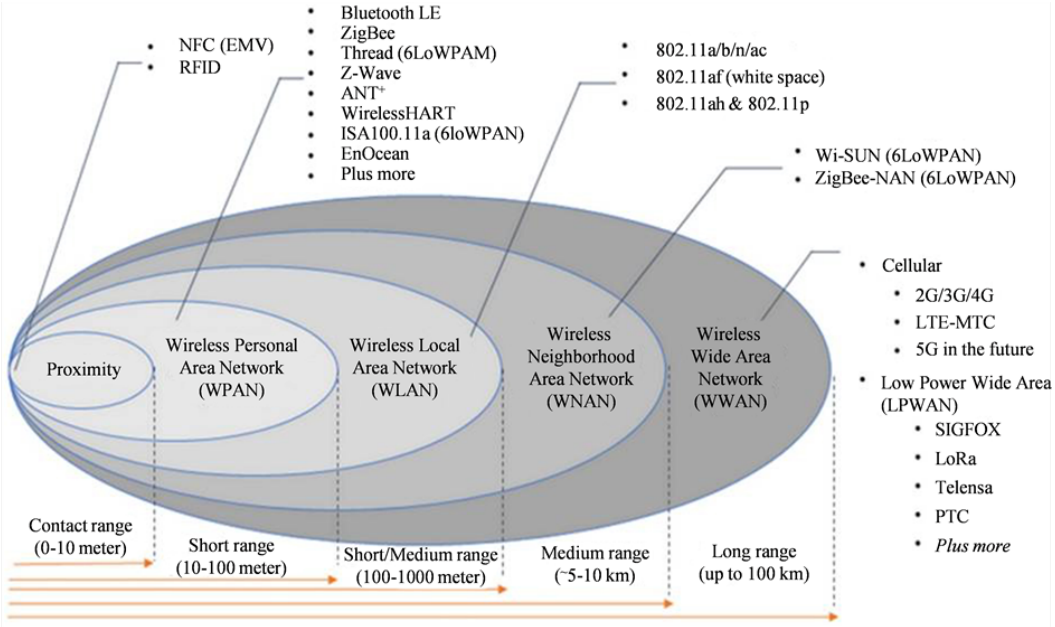

FIGURE 2.1: Wireless IoT connectivity technologies

there are still a lot of event-driven applications which demand the use of simple and power-critical devices. They request very low energy consumption and long battery life (which lasts several years) to avoid the cost of battery replacement.

There are many sorts of criteria to list these connectivity technologies into groups, for example the communication ranges, the topologies or the autonomies. From my point of view, they can be sorted into four main types depending on the power efficiency demand of the devices (high and low power), and the communication ranges (long and short range).

High power represents the connectivity technologies which consume much energy that their battery have to be always charged or often changed. Meanwhile, low power is dedicated to power-critical devices, whose battery has to last long time. Long and short ranges represent respectively the technologies that allow long and short communication distances, while ensuring the quality of service. As presented in Fig. 2.1, the wireless connectivity technologies for IoT are listed and sorted according to their communication range.

The part below will introduce the representative technologies of each type.

- High power & short range:

The two important representatives in this type are WiFi and Bluetooth [24]. WiFi allows devices to connect and exchange information within a distance of 100m, inside 2.4GHz UHF and 5GHz SHF ISM radio bands. It has the capability of video monitoring. Bluetooth represents the technology which allows data exchange within a short distance, by using the 2.4GHz ISM band.

The common features of this type are: high bandwidth, high data rate, low latency, and very short communication range. They are ideal candidates for IoT applications such as smart vehicles, smart grids and wearable devices, whose scale of data to deliver within a short time interval is very high. Meanwhile, their good features cause certainly high energy consumption, thus they do not fit applications that are power-critical.

- High power & long range:

Traditional cellular networks provide long range communication, typical ones are GSM and LTE. Thanks to their widely deployed base stations in the world, the large communication coverage can be ensured, and the additional deployment cost can be saved. However, LTE is neither originally designed to fit the link budget requirement of IoT devices, nor optimized for their traffic patterns [24]. To make LTE more suitable for IoT, some improvements targeting IoT devices have been taken into account in the 3GPP standardization [25].

Despite their advantages, the technologies of this type still consume high device energy because of the secure yet complex signaling mechanisms such as listen before talk and roaming, the high speed data service and high quality voice services. What's more, cellular networks connecting devices are mostly complex and at high cost (e.x. smart phones), thus it is difficult to deploy them at a large scale.

- Low power & short range:

Many technologies are conceived for this type of communication, there are Z-Wave, IEEE 802.15.4, Bluetooth Low Energy (BLE), and IEEE 802.11 PSM [26]. Some specific communication technologies are also in use like RFID, Near Field Communication (NFC) and ultra-wide bandwidth (UWB).

IEEE 802.15.4 standard is mainly refereed for ultra low power devices [27]. It intends to offer the fundamental lower network layers of a type of wireless personal area network (WPAN) which focuses on low-cost, low-speed ubiquitous communication between devices. It supports robust transmissions with DSSS (Direct-Sequence Spread Spectrum) and the O-QPSK (Offset Quadrature Phase Shift Keying) modulation scheme giving a bit rate of 250 kb/s. Multi-hop topologies can extend its relatively short ranges (at maximum 50m).

Bluetooth Low Energy (BLE) [28] can provide robust transmissions. It is mostly used for monitoring applications, such as heart rate monitors or temperature remote controllers. BLE is already popular in the majority of smart phones and largely used for mobile applications. It uses the GFSK (Gaussian Frequency-Shift Keying) modulation to obtain a maximal 2 Mb/s bit rate. And the maximal range announced is 10m.

IEEE 802.11 PSM (Power Saving Mode) [29] is an energy-optimized mode specified in the 802.11b version. With 22MHz of bandwidth, it can achieve until 11Mb/s within the range of 100m.

NFC [30] enables two electronic devices to communication within 10 cm. It works on the 13.56 MHz ISM band, and provides a data rate ranging from 106 to 424 kbs. It is mostly used in smart phone mobile payment, credit card contactless payment, and electronic tickets.

As for UWB [31], it can provide high data rate and robust communication, since it spreads the transmitting information over a very large bandwidth (>500 MHz). It can attain 1 Gbit/s, but the range is limited to less than 60 cm. Its recent applications include personal area network, indoor localization and precision tracking, etc.

On the whole, we can have a main idea of these technologies' common features: they are dedicated to ultra low power devices, but restraint to very short-range usage.

- Low power & long range:

The enabling technologies of this type are called LPWAN (Low Power Wide Area Networks) [32]. They have been emerging since recent years to fulfill the requirement of about 11% of IoT connections. The well-known technologies are: LoRa, Sigfox, Ingenu, Weightless and NB-IoT. LPWAN is a novel paradigm which treats the trade-off between communication range and energy efficiency. It is promising to achieve a few to tens of kiloliters of connectivity range, and a battery life of ten years or beyond jointly.

LPWAN is the main context of my thesis. In order to give an more global insight of LPWAN, each of the technologies will be introduced with more details and their issued studies in the section below.

2.2 The emergence of LPWAN

LPWAN (Low Power Wide Area Network) is a very recent term (appeared in 2013), referring to a very wide area network (covering up to several tens of kilometers range in rural areas with a single access point). The objective of such network is to provide a connectivity to the Internet for a huge number of nodes deployed anywhere, in the IoT context. LPWAN gateways are thus needed to settle communication with the devices in their vicinity. To limit the operational cost of the operators, a limited access infrastructure is expected. As a consequence, a collecting point should serve many nodes deployed in a very wide area. However, this can not be obtained by tuning up the emission power, because the low energy consumption is very essential for the IoT nodes.

In addition, the ISM license-free bands are usually used for LPWAN transmissions, which allows to further reduce the network cost (because the cost to use licensed bands can be very high). Furthermore, LPWAN is expected to handle sporadic small data packets, thus it targets new applications such as smart cities, smart metering, logistics, wildlife monitoring and tracking, home automation and safety, etc.

FIGURE 2.2: Examples of targeted applications for LPWAN

2.2.1 Objectives of LPWAN

As one of the fastest growing technologies in the emerging IoT environment, LPWAN is expected to provide ubiquitous connectivity for smart cities or rural areas. All these applications pave the way to new markets, and new business operators. Besides, as the infrastructure cost is low, newcomers have joined the historical telecoms operators by launching their proprietary transmission technology. Among them, we can cite SemTech along with LoRa Alliance with the LoRa technology, SigFox with UNB (Ultra Narrow Band) technology, and Ingenu with RPMA technology (Random Phase Multiple Access).

The LPWAN context reveals a new scientific challenge which is moving from the data rate expansion, to the forthcoming number of devices growth, and follow the path lead by dense WSN. To sum up, the objective is to define new techniques that verify:

- low energy consumption: data has to be sent with the least emission power, and with the smallest time duration;
- low device and infrastructure costs: BSs number should be the minimized, while the devices have to be simple, light and with low computation capabilities;
- capability of handling burst transmission of small size packets;
- scalability and capability to handle a very high number of nodes;
- extended coverage.

2.2.2 Existing technologies of LPWAN

The second requirement can be obtained, for the most shared vision, by a star topology with very long range (devices are directly communicating with the BS (Base Station)). To achieve such range, one can:

- Increase the transmission power (but this solution is not appropriate due to the increased power consumption)
- Design ultra sensitive and intelligent receivers (this can be expensive but feasible)
- Design new transmission technologies. This is the solution that has been adopted lately by operators and scientific community. In practice, two main directions have been taken:
  - spectrum spreading (LoRa with CSS, or Ingenu with RPMA): data is sent on a much larger band than their baseband occupation. This frequency diversity allows to recover a signal even if its PSD (Power Spectral Density) is lower than the noise floor, because specific coding patterns can provide attractive decoding gains. Besides, one transmission can choose among various spreading codes (which verify good correlation properties). Thus simultaneous transmissions are in control (when the number is not very high).

  - spectrum reducing (SigFox with UNB, and 3GPP NB-IoT): data is sent at a very low rate with a simple modulation scheme, so as to ensure a minimal spectrum occupation. The advantage of such technique is that the perceived noise (after signal filtering) is reduced as it linearly depends on the signal spectrum occupation.

  For both techniques, the long transmission range can be achieved, but by different methods: UNB achieves it thanks to the very narrow bandwidth which induces very low noise power; while LoRa achieves by its coding gain [8].

Currently, the available LPWA communication technologies include a large variety of alternatives such as 3GPP Narrow-Band IoT (NB-IoT), Long-Term Evolution for Machines (LTE-M), CSS (known as LoRa), UNB (known as Sigfox), and RPMA (used by Ingenu and Weightless).

- **LoRa:**

LoRa is a patented wireless communication technology developed by a French companyCycleo and then acquired by Semtech in 2012. It uses the ISM unlicensed bands 868 MHz (Europe) and 915 MHz (North America), and FSK (frequency-shift keying) modulation [33]. Its radio access scheme is CSS (Chirp Spread Spectrum), where the data is spread with a sequence obtained through a continuous varying carrier frequency. This spreading factor, varying from 2^7 to 2^{12}, affects the transmission bandwidth (from 500 Hz to 125 kHz), as well as the data rate (from 0.37 to 27 kbps) [34]. The communication range it can attain is announced to be 22 km.

- **RPMA:**

RPMA (Random Phase Multiple Access) is developed and used by an American company Ingenu in 2015. RPMA is based on DSSS (Direct-Sequence Spread Spectrum), where data is spread by a Gold Code after being DBPSK modulated. Its spreading factor varies from 2^4 to 2^{13} [35]. Transmissions are performed in the 2.4 GHz ISM band, with a typical bandwidth as 1 MHz, and with a random time delay. The data rate varied from 0.06 to 30 kbps, according to the used spreading factor. And the maximal communication distance it can achieve is 10 km [34].

- **NB-IoT:**

NB-IoT (Narrow band IoT) is made available as a part of Release-13 around mid 2016. It can be supported with only software upgrade on top of existing LTE infrastructure, and can co-exist with GSM, GPS and LTE. It can be deployed inside a single GSM carrier of 200 kHz, inside a single LTE physical resource block (PRB) of 180 kHz or inside an LTE guard band [36]. Thus its transmission bandwidth is relative narrow compared to GSM and LTE. NB-IoT uses single-carrier Frequency Division Multiple Access (FDMA) on the uplink and Orthogonal FDMA (OFDMA) on the downlink. The data rate is limited to 250 kbps for the multi-tone downlink communication and to 20 kbps for the single-tone uplink communication [32].

- **UNB:**

UNB (Ultra Narrow Band) is developed and patented by the French company Sigfox around 2011, which was the first one to be commercially initiated for IoT purpose. It is operated at the 868 MHz (resp 915 MHz) ISM band in Europe (resp in the USA). The specificity of UNB is that its transmitted signal occupies, typically 100 Hz (in Europe) and 600 Hz (in the USA) [37]. This occupied bandwidth is very narrow compared to its available total bandwidth, which is typically 192 kHz. The radio access is RFTMA (Random Frequency Time Multiple Access). By using simply the DBPSK modulation, UNB can achieve until 63 km as range, the data rate is yet constraint to 100 bit per second [34].

The Sigfox and LoRa ecosystems are mature and are now under commercialization in various countries and cities. While the NB-IoT specification was released in June 2016, thus it still needs time to be established. UNB and NB-IoT are both run by operators where the network is established by private companies. Unlike them, LoRa provides large flexibility, it offers local network deployment and its specification is open resource [38].

2.2.3 Studies of LPWAN

Aside from the market, LPWAN network has recently fostered many academic works. There exist enormous studies of LoRa, as it is frequently exposed as a promising technology and promoted by many companies (for example IBM, Orange, Bouygues, ZTE, etc.) which group the LoRa Alliance. The evaluation of its capacity and scalability [39–41] has been catching attention in the research filed. The performance enhanced by controlling the spreading factor and emission power [42] has been proposed as well.

Being the only standardized technology using cellular networks, NB-IoT has also been largely studied, such as the evaluation of its coverage [36, 43]. A work of its deployment when using the LTE infrastructure, shows that NB-IoT suffers from high path loss and high interference from non NB-IoT cells [44].

Apart from the individual work of each technology, UNB, NB-IoT, LoRa and RPMA are often compared technically, in terms of data rate, latency, communication range, and simultaneous active users [32, 45–47], etc.

Through the brief introduction of each technology, we can already have an insight about their data rate: NB-IoT has the highest data rate, at 250 kbps for the sake of using large bandwidth; LoRa and RPMA can achieve around 30 kbps thanks to the spread spectrum; while UNB is very limited in this aspect [34] due to its limited bandwidth.

However, the challenge of LAPWAN is not only about the expansion of data transmission speed, the coverage is a very important aspect as well. The coverage of LoRa and Sigfox are evaluated by real-world experimental tests [48]. As the UNB uses the spectrum efficiently, it experiences very low noise level which results in very high receiver sensibility and very wide coverage. LoRa achieves long range by its spread spectrum which is resistant to the noise and the coding gain [32]. With respect to the maximal number of users, while guaranteeing an acceptable quality of service, LoRa can simultaneously support 6 users, UNB 100 users, and RPMA is announced to be able to serve 1000 users [34].

Moreover, LoRa and Sigfox both operate in the 868 MHz ISM unlicensed band, their co-existence is thus also a hot research issue. Because they may cause conflicts to each other or to other existing systems in the same band [49]. As presented

in Fig. 2.3, the CSS spreads the signal over a wide bandwidth, which spreads also the signal power. The resulting signal amplitude is affected by the noise, which makes it hard to be detected or jammed. The processing gain enables the signal resilience to interference [50] and noise. Therefore, CSS signals is only affected by a very low proportion (in terms of frequency) when they are interfered by a UNB signal. On the contrary, UNB concentrates the signal power in a narrow band, which results in a rather good resistance when interfered by spreading signals like CSS.

Both CSS and UNB should be resistant when facing the interference with each pother. Nevertheless, the authors in [50] have proved that UNB performs better in long range communication when interfered with LoRa.

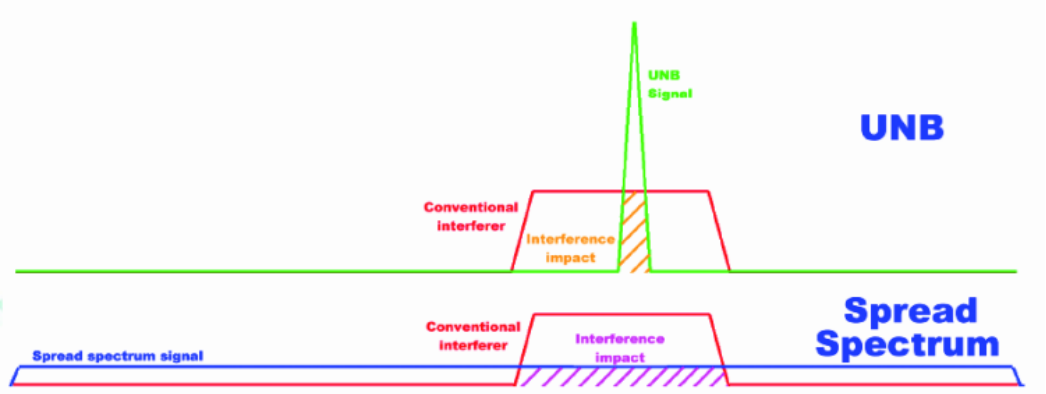

FIGURE 2.3: Illustration of Ultra-Narrow-Band and Spread Spectrum in the frequency domain (the figure source is from http://www.densenetworks.com)

For the aspect of energy efficiency, LoRa performs remarkably well, while UNB only achieves similar network lifetime to LoRa at extremely low data rate. Both of them consume much more energy when the payload size increases, compared to other technologies such as BLE [26]. The devices communicating on CSS or UNB thus have their lifetime dropping very quickly when the data packets have big size.

2.3 Ultra Narrow Band

Ultra-Narrow-Band systems are defined such that each individual node occupies an extremely narrow frequency band to transmit its signal. This band is significantly smaller than the total available frequency resource, and is usually around a few hundred Hz. In 2004, Walker [51, 52] was the first one to propose the use of VMSK (Very Minimum Shift Keying) to compress data transmission in the most possibly narrow band. However, in practice, this modulation technique did not reach the claimed ultra narrow frequency occupancy [53].

In 2011, networks based on Ultra-Narrow-Band are deployed by the company Sigfox for IoT purpose, dedicated to low-throughput, low-power, and long-range point-to-point transmissions. Since then, UNB has been catching attentions in both the IoT markets and the research fields.

2.3.1 Frequency Drift in UNB System

As presented in the previous section, the ultra narrow band occupancy is obtained by transmitting at a very low data rate (100bps) in SigFox's network. The transmitted signal of UNB thus occupies a band of 100 Hz (in Europe, and 600 Hz in USA), inside a typical possible band of 192kHz to 2MHz. The dedicated modulation technique is the DBPSK (Differential Binary Phase-Shift Keying) [54].

The specificity of such system is the "frequency drift" phenomenon: the oscillator's imprecision which induces an offset between the targeted frequency and the actual one. Regular low-cost oscillators have a deviation around 0.25-2 ppm (parts-per-million) [55]. For example, for an operating frequency band of $f = 800$ MHz and a typical oscillator jitter $d_f = 0.25 - 2$ ppm, the uncertainty of carrier frequency positioning would be around $D_f = 200 - 1600$ Hz. This imprecision is larger than the transmission band occupied by an individual UNB signal. In this case, i.e., when the frequency uncertainty is higher than the signal bandwidth, we refer the system as UNB. We note that precise oscillators exist, but they can be very expensive (up to several thousands of dollars each), thus it is not profitable to deploy them in large scales.

One may note that the carrier frequencies also suffer from an additional shift while the oscillators are heating during transmission, but this feature is well managed in SigFox's BS.

2.3.2 UNB Multiple Access

As the frequency drift is inevitable in UNB system, it is unrealistic to obtain non-overlapping frequency channels. Accordingly, the channelization is not pertinent, as it would just lead to the waste of frequency resources and high device cost. The transmissions of IoT devices are sporadic and unpredictable, it is thus hard to synchronize (in temporal domain) all the nodes since they don't have the same wake-up duty circle. As a consequence, a specific dedicated MAC (Multiple Access Control) is considered for UNB systems. This channel access scheme is named RFTMA (Random Frequency and Time Multiple Access) [12], which is ALOHA-based without preliminary channel sensing.

The traditional pure ALOHA [10] is a random scheme for the medium access, where there exists only one channel, and all devices transmit on the same channel at any moment they want. The only degree of freedom is the time, thus the transmitted data has a high probability to be lost and resent when it is in collisions. In the case of UNB, the medium access is both random in time and in frequency domain. The degrees of freedom is added to two, the collision probability is thus lower than pure ALOHA scheme.

With RFTMA, each device sends its messages at any moment and at a carrier frequency randomly chosen at its will, as illustrated in Fig. 2.4, without previously analyzing the channel state. The advantage of this approach is the reduce of nodes' energy consumption, complexity and cost. The classical overhead dedicated to the reservation of radio resources is saved, so is the energy consumed on exchanging data with the gateway. Moreover, this feature allows to use cheaper oscillators which are more suitable for massive deployment. Nonetheless, as there is no control, the network can suffer from high interference and collision probability [56]. Indeed, as nodes transmit randomly, partial overlap may occur in time and in frequency between two or several packets, as illustrated in Fig. 2.5. Thus

the interference may vary during the transmission of given packets. This interference generated by simultaneous transmissions can cause packet losses, thus needs to be avoided in UNB networks.

In the network of Sigfox, a mechanism of replications has been applied to ensure the reliability of the network, in spite of the potential interference caused by the random MAC protocol. The number of replications has been fixed at 3. Each of the replications is transmitted at a different frequency, within a random time interval despite the success state of the previous ones.

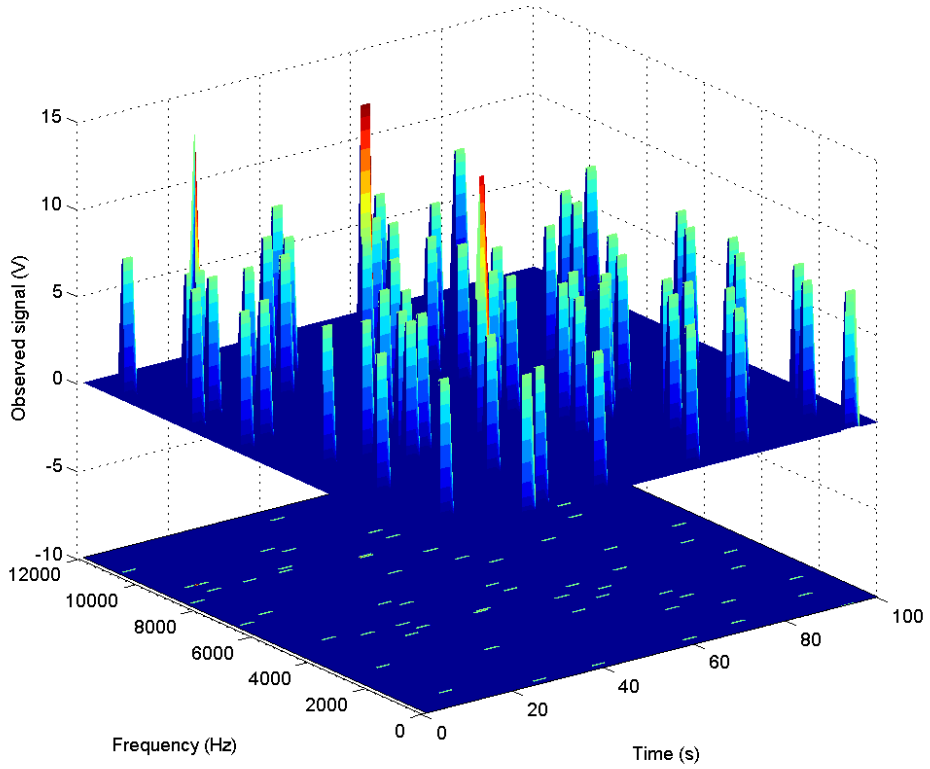

FIGURE 2.4: Global view of UNB signals' temporal & spectral repartitions

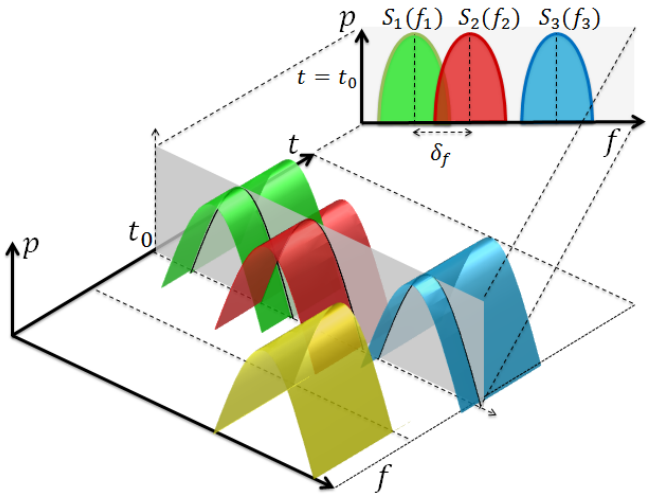

FIGURE 2.5: Precise example of nodes' temporal & spectral repartition

Indeed, there exist a lot of more complex and "optimized" medium access protocols for wireless sensor networks. The historical ones [57] [58] are : CSMA/CA (Carrier-Sense Multiple Access with Collision Avoidance), where a sensor node listens to the channel before transmitting, and it only emits when the channel is in the state "Idle" when no any nodes else are using it. CSMA/CA requires nodes to be able to sense the medium, and to sense it every time they have something to transmit. This demand consumes additional energy before transmitting; RTS/CTS (Request to Send/ Clear to Send) where nodes send a request to the destination in the first place. Then if the medium is free and the destination succeeds in receiving the request, it will send back a CTS to the source. After verifying the positive response of the destination, the source then transmits its data. RTS/CTS is inefficient because of its many exchanges with the destination which consume energy and cause intensify traffic loads. Besides, the packets of requirements and responses have almost the same size than a data packet in UNB (around 12 bytes). Thus sending a RTS packet has the same probability to be in collision than sending a UNB data packet. Therefore, RTS/CTS is less efficient than RFTMA in UNB systems; Slotted-ALOHA where the medium is organized by time-slot, so is the transmitting moment of nodes. The more recent ones are all based on scheduling, such as TDMA (Time Division Multiple Access) and FDMA (Frequency Division Multiple Access) and CDMA (Code Division MA). They require the knowledge of the network topology to divide the resources into time or frequency slots, and to establish a schedule to assign active nodes to different resources or codes. The collision probabilities are reduced because the transmissions are performed on assigned orthogonal channels.

Despite the various MAC protocols, there do not exist studies that propose to change the medium access scheme of Sigfox's network, to the best of our knowledge. The first reason is the inevitable frequency drift due to the oscillators, which makes the frequency scheduling-based schemes unrealistic. The second reason is that other MAC protocols can hardly reach such low energy consumption and low cost than RFTMA, since the listen-before-talk schemes oblige the nodes to wake up during longer time.

Therefore, in the purpose of maintaining the advantages of low cost and low power consumption, the Random-FTMA is currently the most pertinent multiple access for UNB systems.

2.3.3 Star topology

The atomic network element of SigFox's network is the star topology, where the one base station (BS) is centered in a large cell. The BS receives the data emitted by a huge amount of nodes (i.e. devices) spreading all over the cell. From a receiver's point of view, the monitored bandwidth B (which is also the total available frequency resource) is filled with a combination of narrow-banded signals randomly located in time and frequency, as shown in Fig.2.4. The demodulation of signals relies on efficient SDR (Software Design Radio) algorithms which are designed to analyze the total band, to detect transmitted signals and to retrieve the data. The process is accomplished by a FFT block applied to the received signal, which is followed by an adaptive detector. This detector aims at identifying the spectral signature of the transmitted UNB signals. Therefore, it is not problematic to detect UNB signals that are uncontrollably shifted in frequency. For each detected transmission, the appropriate frequency band is filtered and demodulated with a standard DBPSK demodulator.

2.3.4 Existing studies of UNB

Researches concerning UNB in the context of IoT started to show up after the launch of Sigfox company. Besides the studies of LPWAN where UNB is mentioned, the works which evaluate and optimize the UNB based IoT networks have emerged as well.

The authors in [12] have analyzed the Aloha-type multiple access scheme of UNB, and provided a modeling of the collisions between UNB packets. They have proved that in practice, when more than two simultaneous transmissions happen, the failure of the targeted message is generally due to a unique interferer. They have also evaluated UNB networks' capacity when comparing Discrete RFTMA (like frequency hopping) and Continuous RFTMA (this one correspond to the actual scheme of Sigfox). They have confirmed that Continuous RFTMA performs better with the presence of frequency drift [9], and that it was less expensive without an exigence of frequency precision.

Thanks to its long range and small RF power, UNB is also an attractive candidate for satellite communication. An analytical model to evaluate UNB networks' performance by considering the temporal and spectral randomness, in both terrestrial and satellite context, is provided in [59]. The authors went further to take into account the Doppler effect due to the LEO satellite. The resulting frequency drift causes interference, which has an significant impact of UNB performance [60].

An evaluation of Sigfox networks' performance for long-range localization is provided in [61], when using received signal strength indicator (RSSI) as criteria. Moreover, the authors in [62] proposed to use adjustable pulse UNB. And they demonstrated that its performance is better, in terms of coverage and the supported number of connections, than the 3GPP LTE repetition mechanism.

The authors in [63] have proposed an experimental architecture which enables to optimize Sigfox's UNB system, when considering the inter-cell and intra-cell

interference. Their preliminary results show the experimental architecture's feasibility of PHY and MAC context data collection, channel occupancy, link quality modeling and network optimization.

2.4 Summary and Discussion

In this chapter, we presented an overview of IoT and its current needs. From the base stations' side, it not only concerns the expansion of data rate, but also the scalability to connect a large scale of devices and the capacity to manage bursty transmissions. From the devices' side, the energy consumption and cost are big issues, as most of the devices are battery-based. We have sorted the enabling technologies into groups according to the power consumption and transmission range requirements. Among them, we cited LPWAN which has emerged recently to respond to the demands of low-power and long-range transmission applications. We provided an introduction and related scientific works of the main LPWAN technologies (i.e. LoRa, RPMA, NB-IoT and UNB).

From my point of view, these LPWAN technologies are complementary, e.x. Sigfox is dedicated to extremely low data rate and not latency-critical applications, whereas LoRa provides higher data rate and is able to deliver relatively low latency. From different aspects as energy consumption, communication range, maximal number of supported users, data rate and cost, etc., one can choose the technology that fits the best according to his/her needs. The choice among these technologies may be driven by the confidentiel consideration. For instance, if the user wants to be the owner of the data, the LoRa soluition (which gives the possibility to build local area networks) may be more suitable than Sigfox (which stores the clients' data).

Particularly, we introduced UNB with more details, as it builds the background of my thesis. We gave the definition of UNB. We presented the frequency drift phenomenon that exists in all the low-cost oscillators, which makes it unrealistic to obtain perfectly orthogonal channels in UNB systems. We thus presented the dedicated radio access for UNB: Random-FTMA which is random is time and in frequency domains, and which results in high collision probability. The reason why this access scheme has been chosen and why it is so far the most pertinent multiple access for UNB systems has been stated. The typical star network topology has also been mentioned. Finally, we presented the existing UNB-related research works in the context of IoT.

As we mentioned in Section 1.2, there are still many open questions in UNB networks. Some of them will be answered in the coming chapters.

Chapter 3

Performance of UNB networks with ideal channel

Contents

In this chapter, we characterize the UNB-based networks' performance with ideal channel conditions, where all transmissions are received with the same power level in a single cell. The first main contribution is the derivation of an expression of the outage probability, for the generalized ALOHA systems (which includes the frequency-unslotted systems such as UNB). This analysis brings to light the duality of ALOHA in time and frequency domain. The second contribution of this chapter is that we have extended the generalized ALOHA analysis to the case with replications. We show that the replications can bring significant improvement, and that there exists an optimal number of transmissions for the same message which allows to achieve the highest reliability.

3.1 Introduction

In this chapter, we take into account the carrier frequency uncertainty to evaluate the ALOHA protocol behavior. The Base Station (BS) collects signals that occur randomly, generated in an unslotted way both in the time and the frequency domains (RFTMA: Random Frequency and Time Multiple Access). This can be viewed as a more general case of the well-known ALOHA medium access [10]. The main difference is that, for UNB systems, interference occurs only *in a portion of the frequency band*. In this case, the interference cannot be easily processed, neither by transmitter cooperation or signal post-processing at the receiver as in literature [64]. One goal of this chapter is to introduce this new RFTMA scheme and provide its theoretical characterization. The other goal is to evaluate the UNB performance with replication mechanism, where we bring the diversity in transmissions.

3.1.1 Studies about ALOHA

Previous works on ALOHA-based schemes do not consider full and continuous randomness in frequency domain. Usually, the band is divided into several perfectly orthogonal channels, and frequency hopping (FH) is considered [13]. However, few works consider the frequency offset. In [65], its impact on the relative phase between considered symbols is taken into account. In [66], the authors consider that most of the frequency errors are within the signal bandwidth, thus they do not consider UNB. In [67], the authors consider K nodes with random frequency offsets relative to a common carrier frequency, and focus on the use of a wide-band receiver to take advantage of the jitters.

We thus complement these studies by considering a uniform and continuous randomness of the carrier frequencies to characterize an UNB-based ALOHA uplink in this chapter.

3.1.2 Studies about replication mechanism

In the literature [68], the reliability of data delivery can be achieved by two ways: *retransmission-based mechanism* and *redundancy-based mechanism*. The basic principle of the retransmission schemes is to repeatedly transmit the failed message which cannot be recovered at the receiver. The demand of replication happens until a correct message arrives. In order to know if the message is correctly received or not between the transmitter and receiver, an acknowledgment mechanism must be applied [69]. However, this kind of protocol requires a downlink transmission, in other words the reservation of transmission resources. This might further aggravate the inherent congestion of the medium.

Besides, in the *redundancy-based mechanism*, multiple copies of the same message are transmitted based on Erasures Coding [70], which allows a receiver to recover the information from independent message loss. The popular types of Erasure Coding are Reed-Solomon codes [71], low-density parity-check (LDPC) codes [72], Fountain Codes [73]. Among these coding schemes, the simplest one is the replication mechanism.

The performance of retransmission mechanism and redundancy-based mechanism are theoretically evaluated and compared in [74] in term of the energy efficiency. Indeed, both *retransmission-based mechanism* and *redundancy-based mechanism* are able to improve the data delivery reliability, but also consume a lot of battery-energy of a sensor node which is inherently limited. Besides, this theoretical analysis highlights that Erasure Coding mechanism is out-performing compared to the replication mechanism in term of reliability and energy efficiency, for the case of a low packet loss rate and low number of hops. In addition, a lot of studies have considered the compromise between the higher performance achieved by replications, and the higher energy consumption in classical transmission schemes [75–77].

In the UNB network using Random-FTMA scheme, the one-hop communication between active node and base-station is essential to reduce the energy consumption. We thus consider in this chapter the replication mechanism, which is *redundancy-based*.

The organization of the chapter is as follows. In Section 3.2 we define a general model of the network and give all the hypothesis. In Section 3.3-3.4, we develop a theoretical analysis of generalized ALOHA outage probability, and present the numerical validation and results. In Section 3.5-3.6 we extend the generalized ALOHA derivation along with replication mechanism, and present its numerical results and exploitation. Section 3.7 concludes the chapter.

3.2 Modeling and Hypothesis

In this chapter, we focus on a unique base-station (BS) covering a large number of nodes distributed in its coverage. We assume that there are $N + 1$ active nodes during the observed time interval, whose data is collected by the BS at the cell center. The nodes (IoT devices) are uniformly deployed in the cell, which can be modeled by a Poisson point process [78].

We consider that the messages of all nodes are received at the base station with the same power. This corresponds to the case with a perfect power control loop, thus idealized channel conditions. In idealized conditions, the distance between each node and the BS has no more impact on the performance (as there is no path loss). Accordingly, we can consider the topology as if the nodes are distributed at the same distance, as illustrated in Fig. 3.1.

Meanwhile, the performance under ideal channel conditions also correspond to the worst case. Indeed, when colliding packets are received at the same power level, both are lost. Whenever two packets are collided, we lose both of them. On the contrary, if the received powers are sufficiently unbalanced, the capture effect may allow to decode at least the strongest one [79]. This leads to better performance than the case of idealized conditions. We thus characterize in this chapter the lower bound of the network success probability.

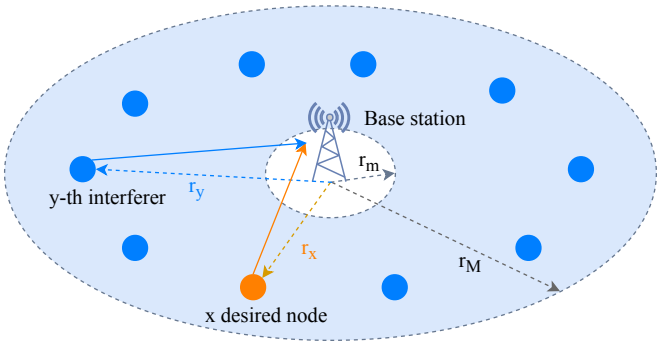

FIGURE 3.1: Illustration of network topology: area range is $[r_m, r_M]$, orange point is the desired node, at a distance of r_x; blue points are interfering nodes, at a distance of r_y.

3.2.1 Behaviors in the Time Domain

We assume that all nodes have the same behavior: each node transmits a message of duration τ seconds, every T_p seconds on average. For the time-slotted (TS) case, any active node randomly selects a time-slot, since the temporal resource is separated by slots. Thus in the time domain, the transmissions either do not collide at all (when they choose different time-slots), or collide for the whole duration (when they choose the same time-slot). Accordingly, when two packets select the same time-slot, they are in collision, and we lose both of them. Therefore, $p_t = \tau/T_p$ is the expected temporal generation rate for a single user, as well as the temporal collision probability, in time-slotted case.

As for the time-unslotted case (TU, which corresponds to the realistic case in Sigfox networks), partial overlap can also induce collisions. We assume that once there is an temporal overlap (no matter it covers 1% or 99% of the packet's duration) between two message packets, they are in collision. Thus both packets are lost because they have the same received power level. Consequently, when an interfering node selects its emission moment into $[-\tau, \tau]$ of the desired node, we lose the desired node's issued message. Accordingly, the temporal collision probability becomes $p_t = 2\tau/T_p$.

3.2.2 Behaviors in the Frequency Domain

Besides, transmissions are performed within a dedicated band, which has bandwidth B (Hz). Each transmission occupies a bandwidth b (Hz) which represents a very small fraction $p_f = b/B$ of the total channel bandwidth B. Thus, p_f is the spectral occupancy ratio for a single active user. Similarly, in frequency-slotted (FS) case, the signals are in collision of they choose the same frequency slot. Thus the frequency collision probability is b/B for FS case.

As for the frequency-unslotted (FU) system, the nodes chooses their carrier frequency randomly and continuously [9] on the total available band B. This choice is independent for each node without any prior knowledge on the occupation, exactly as performed in Sigfox network and in the previous chapters. There can be thus partial frequency overlapping among several signals. Since we consider ideal channel conditions where the received power of each packet is identical, the capture effect can not be applied in this chapter. When the frequency overlap is non null, the packets in collision will all be lost. Accordingly, when an interfering

packet selects its carrier frequency inside $[-b, b]$ to that of the desired packet, they run into collision which causes the loss of both packets. The frequency collision probability thus becomes $2b/B$ for the FU case. These notations are reported in Table 3.1.

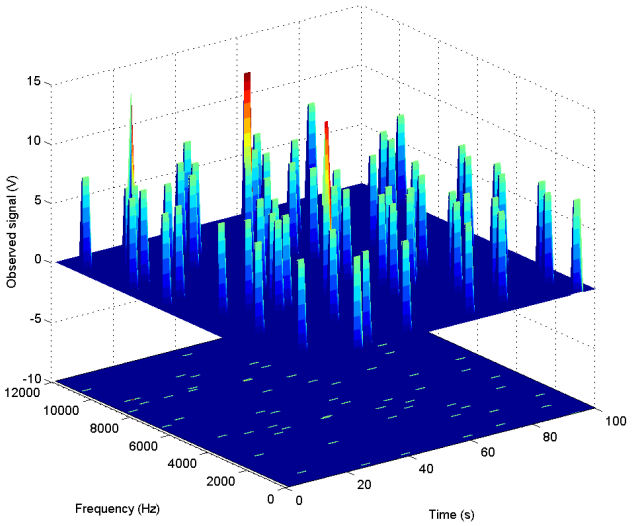

FIGURE 3.2: Example of a time-frequency UNB realization, for $b =$ 116Hz, $B =$ 12kHz, $\tau =$ 2s, during 100s.

From the base-station point of view, the total dedicated band contains, from time to time, transmitted ultra narrow signals at random carrier frequencies. For each detected transmission, the BS extracts the signal at the estimated frequency of interest, and decodes the packet. Such a detection and estimation can be done as described in a Sigfox patent [80].

An example of channel occupancy realization is presented on Fig. 3.2. We can observe the sparse time-frequency occupations of signals. The three highest peaks (in red) correspond to transmissions that experienced collisions, while the others are interference-free. One may note that the widths (both in time and frequency domain) differ among the collision peaks. This is due to the frequency-unslotted and time-unslotted selection, which induce partial collision in time and frequency domain.

Finally, one may note that a key advantage of UNB is that the noise floor $N_0 = k \cdot T \cdot b$ (with k Boltzmann constant, and T the temperature in Kelvin). The noise, which is proportional to the bandwidth, can highly reduced in UNB systems compared to classical systems. This allows to cover an exceptionally large area with each BS (up to 50km). The noise floor is very low compared to the interference which is the main limitation of the system performance. We thus neglect the noise in this chapter. This allows us to focus on the specific spectral interference due to the collisions issuing from uncontrolled random medium access, without the random impact of noise.

TABLE 3.1: Table of Notations

N	Number of potentially interfering nodes
τ	Packet duration
T_p	Average transmission period
b	Individual signal spectrum occupancy
B	Bandwidth of the available channel
p_t	Expected temporal generation rate $= \frac{\tau}{T_p}$
p_f	Frequential occupancy ratio $= \frac{b}{B}$
α_t	$= \begin{cases} 1, & \text{for time-slotted (TS) ALOHA} \\ 2, & \text{for time-unslotted (TU) ALOHA} \end{cases}$
α_f	$= \begin{cases} 1, & \text{for frequency-slotted (FS) ALOHA} \\ 2, & \text{for frequency-unslotted (FU) ALOHA} \end{cases}$
G_{tf}	Time-frequency load in the network $= N p_t p_f$
f_i	Carrier frequency of user $i \in \{1; N\}$
OP	Outage probability
n_r	Number of replications
$n_{r_{opt}}$	Optimum number of replications
$n_{r_{min}}$	Minimum number of replications

3.3 Generalized ALOHA: theoretical analysis

In this section, we theoretically analyze the outage probability of generalized ALOHA system, in particularly the FUTU (frequency-unslotted and time-unslotted) case which corresponds to the nodes' realistic behaviors in Sigfox networks.

The goal of the base station is to decode all transmitted messages, from all the users. However, without sake of generality, in this analysis, we consider the transmission status of a given user, called the *desired user*. We evaluate the probability to have its message lost, due to other N users called *interferers*.

We derive a theoretical expression for the OP (outage probability), as a function of the main system parameters : the whole transmission band B; each signal's frequency occupancy with respect to the carrier $[-b/2; b/2]$ Hz; the wake-up duty cycle of nodes T_p; the time duration of a message τ, the potential interfering nodes during the observed time interval N, and also the slotted/unslotted indicators α_t

and α_f in time and frequency. The first four factors influence the channel occupancy of each message in time and frequency domains.

3.3.1 Success Probability of Original ALOHA

In the original ALOHA protocol, all packets are sent on the same frequency channel. Thus, only the transmission time is random. As shown in [10], if the total number of generated packets in the network is Poisson distributed, and even if partial-time collision leads to the packet loss, the success probability of a given user denotes:

$$\mathbb{P}_{1D} = e^{-\alpha_t G_t} \tag{3.1}$$

with $\alpha_t = 1$ for time-slotted ALOHA (TS), $\alpha_t = 2$ for time-unslotted ALOHA (TU), and $G_t = Np_t$ the average number of packets generated by all the other users during the considered packet transmission.

3.3.2 Success Probability of Frequency Hopping System

In addition, it was shown in [11], that for frequency hopping systems with $\frac{1}{p_f} = B/b$ frequency channels having the same bandwidth, eq.(3.1) becomes

$$\mathbb{P}_{FH} = e^{-\alpha_t p_f G_t} \tag{3.2}$$

In the following, we extend these equations to the unslotted frequency selection, and provide a new expression that describes all cases.

3.3.3 Outage Probability of generalized ALOHA

Theorem 1. The ALOHA outage probability with slotted or unslotted time, and slotted or unslotted frequency, along with uniform distribution in time and frequency domain, is given by:

$$\mathrm{OP} = 1 - e^{-\alpha_t \alpha_f G_{tf}} \tag{3.3}$$

with $G_{tf} = Np_t p_f = \dfrac{N\ \tau\ b}{T_p\ B}$ as the average traffic load during the the considered packet transmission, $\alpha_t = 2$ (resp.1) for time-unslotted (TU) (resp. time-slotted (TS)) case, $\alpha_f = 2$ (resp.1) for frequency-unslotted (FU) (resp. frequency slotted (FS)) case.

Proof. For the slotted frequency selection case, i.e., for $\alpha_f = 1$, Theorem 1 simplifies to 1−eq.(3.2).

The proof now focuses on the unslotted frequency selection $\alpha_f = 2$. In order to derive the expression in this case, we need to consider the pulse shaping filter of UNB signals. The steep filter edges that can be observed in Fig. 3.2, allow us to approximate the transmitted signal spectrum by a rectangular function with bandwidth b centered at the actual carrier frequency. We use this model to derive the theoretical throughput.

Any desired packet will be correctly received if it does not experience collisions. A collision occurs when there is an overlap both in time and frequency domain, between the desired (at the frequency f_0) and an interfering packet (at the frequency f_i). In the frequency domain, this implies that their respective frequencies f_0 and f_i verify: $|f_0 - f_i| \leq b$.

We consider that the transmitting nodes' carrier frequencies are uniformly distributed in the total available bandwidth B. Thus, in the continuous case, spectral collision occurs when at least one undesired user chooses a frequency in the vulnerable band $[f_0 - b, f_0 + b]$. This happens with the probability $2 \cdot b/B$. Thus, the spectral collision probability for a unique potential interferer is $\alpha_f \cdot p_f$ with $\alpha_f = 2$. Therefore, the probability that a packet is successfully received, given k additional simultaneous transmissions, can be expressed as:

$$\mathbb{P}_{s/k} = \left(1 - \alpha_f p_f\right)^k. \tag{3.4}$$

As the total number of packets are generated according to a Poisson point process with rate G_t, the probability to have k users transmitting during (partly or totally) the desired packet's transmission denotes [78]:

$$\mathbb{P}(k) = \frac{(\alpha_t G_t)^k}{k!} \cdot e^{-\alpha_t G_t} \tag{3.5}$$

Therefore, we can have the probability of success for the targeted packet as:

$$\begin{aligned}
\mathbb{P}_s &= \sum_{k=0}^{\infty} \mathbb{P}_{s/k} \cdot \mathbb{P}(k) \\
&= \sum_{k=0}^{\infty} \mathbb{P}_{s/k} \cdot \frac{(\alpha_t\ G_t)^k}{k!} \cdot e^{-\alpha_t G_t} \\
&= e^{-\alpha_t G_t} \cdot \sum_{k=0}^{\infty} \frac{(\alpha_t G_t \cdot \left(1 - \alpha_f p_f\right))^k}{k!} \\
&= e^{-\alpha_t G_t} \cdot e^{(\alpha_t G_t \cdot \left(1 - \alpha_f p_f\right))} \\
&= e^{-\alpha_t \alpha_f G_{tf}}.
\end{aligned} \tag{3.6}$$

Here we complete the proof. □

In practice, the network behaves as if we use the classical ALOHA protocol restricted to the p_f portion of the undesired users. As a consequence, the number of packets created during a time period and in the frequency collision interval is also Poisson distributed, with an average generation rate of potential time-colliding packets $G_{tf} = G_t \cdot p_f$.

Corollary 1. *Time and frequency domain are dual in the ALOHA protocol.*

The relevance of Corollary 1. lies on the fact that the time (α_t and p_t) and frequency (α_f and p_f) parameters can be indifferently interchanged in eq.(3.3). This brings flexibility when designing the network parameters.

3.4 Generalized ALOHA: numerical results

In this section, firstly we validate the analytical expression of the generalized ALOHA expression eq.(3.3). Secondly, we use the expression to derive the network throughput. The we analyze the throughput in all ALOHA cases.

The Monte-Carlo simulations are performed on Matlab, with the same hypothesis of the theories we have derived before. According to different result precisions, the simulations runs vary from 10^3 to 10^6 times. We recall all the hypothesis as the following:

TABLE 3.2: Simulations hypothesis for mono-BS idealized channels

BS number	nodes distribution	desired node	path loss	fading	replicas
1	random	random	no	no	no

3.4.1 Validation

We present simulation results for the frequency-unslotted case ($\alpha_f = 2$) in this section. To be as realistic as possible, we consider typical values used in SigFox's network. Transmissions are performed in the 868 MHz ISM band, and each individual signal occupies a bandwidth $b = 116$ Hz during $\tau = 2$s.

Based on these realistic values, Monte Carlo simulations were conducted for both time-slotted ($\alpha_t = 1$) and unslotted ($\alpha_t = 2$) cases. Besides, we have tested two kinds of signal shape, depending on the considered filter. The first one is the rectangular filter, which corresponds exactly to the case treated in the Theorem 1. of the previous section. The second one is a realistic filter as used in SigFox: a realistic signal spectrum shape obtained by a 1255th order lowpass FIR filter, with a 100 Hz cut-off frequency.

Along with this realistic filter, we can evaluate the accuracy of the rectangular model, as well as the validity of the theorem. These numerical results are compared to the theoretical ones eq.(3.3).

We present on Fig. 3.3-3.5 the comparison of the theoretical and simulation outage probability (OP), as a function of the three unconstrained parameters of the network: total of users $N + 1$, total available bandwidth B, and individual packet period T_p.

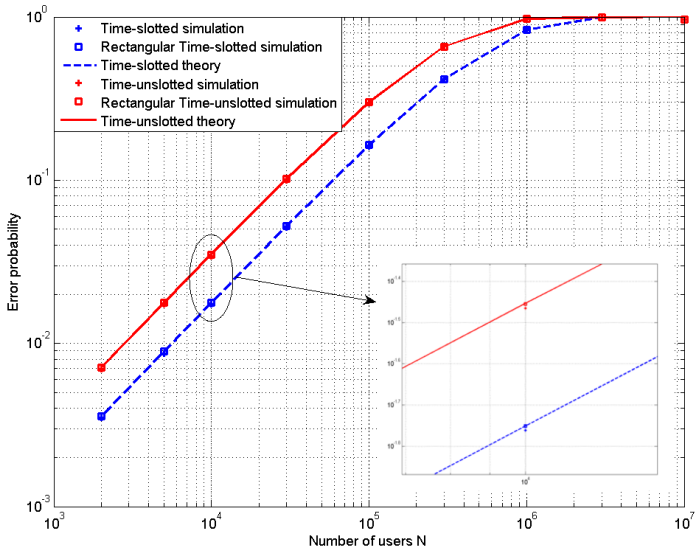

FIGURE 3.3: Simulated and theoretical OP as a function of the number of undesired users N, for the time slotted and unslotted case, for $b = 116$Hz, $B = 12000$Hz, $\tau = 2$s, and $T_p = 12$ hours.

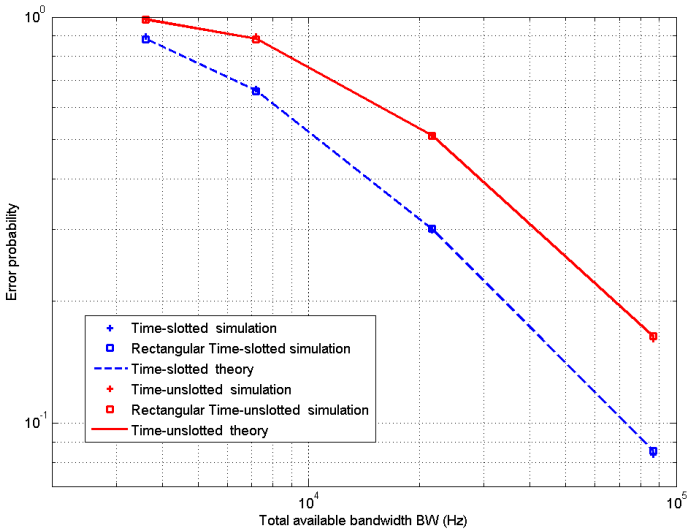

FIGURE 3.4: Simulated and theoretical OP as function of the total available bandwidth B, for the time slotted and unslotted case, for $b = 116$Hz, $N = 1000000$, $\tau = 2$s, and $T_p = 12$ hours.

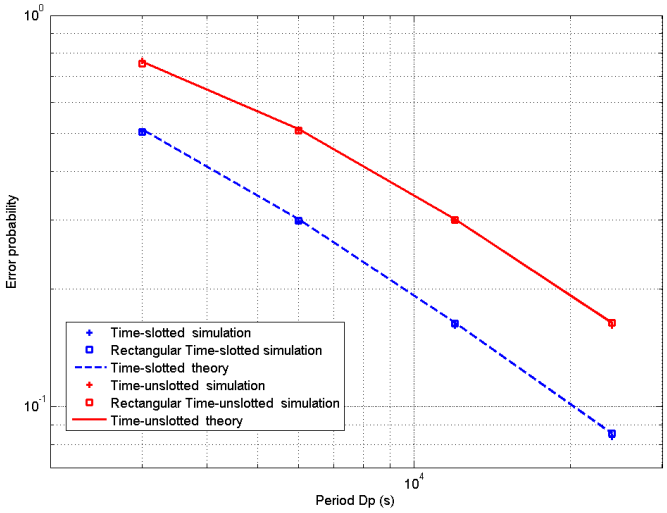

FIGURE 3.5: Simulated and theoretical OP as a function of the temporal generation period T_p, for the time slotted and unslotted case, for $b = 116$Hz, $B = 12000$Hz, $\tau = 2$s, and $N = 100000$.

As expected, we can first note that the error probability increases with the number of users, while it decreases with the available bandwidth and the temporal generation period. More importantly, we verify on all these figures the accuracy of the theoretical analysis. Indeed, both theoretical expression and rectangular model simulation curves coincide, for the time-slotted (in blue) and time-unslotted (in red) cases. Besides, the realistic filter simulation also seems to perfectly coincide. However, if we get more precision (zoom on Fig. 3.3), we can observe that the rectangular model actually overestimates a little the real case. This is due to the fact that the rectangular model slightly overestimates the interference level in the collision band.

To conclude, the proposed theoretical eq.(3.3) provides a tight upper-bound on the realistic frequency-unslotted case.

3.4.2 Throughput derivation and analysis

To further analyze the network behavior, we use eq.(3.3) to deduce the throughput of the network T, as a function of the average total load per time-frequency resource G_{tf}:

$$T = G_{tf} e^{-\alpha_t \alpha_f G_{tf}} = N p_t p_f e^{-N \alpha_t p_t \alpha_f p_f} \tag{3.7}$$

We plot on Fig. 3.6 the throughput as a function of the load G_{tf}. As time and frequency can be independently slotted or unslotted, there are 4 possible scenarios : frequency-slotted (resp. unslotted) time-slotted : FSTS (resp. FUTS), and frequency-slotted (resp. unslotted) time-unslotted : FSTU (resp. FUTU). We can first note that the FSTS case is the best one, as the time-frequency space is divided into orthogonal resources, thus minimizing the probability of collision. On the opposite, FUTU is the worst one as partial overlapping is possible both in time and frequency domain. Finally, FSTU and FUTS coincide due to the time-frequency duality as stated in Corollary (1). Therefore, there are in fact only 3 distinct curves, according to the possible values of the product $\alpha_t \cdot \alpha_f$.

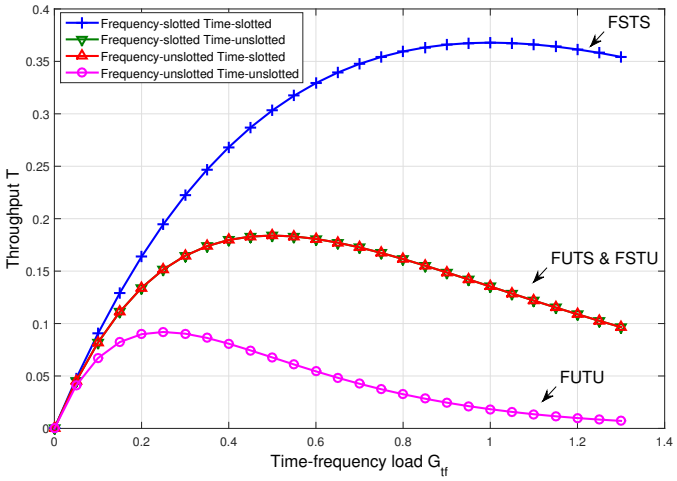

FIGURE 3.6: Network throughput as a function of the load for all $\left(\alpha_t, \alpha_f\right)$.

One may note that the time-frequency duality brings flexibility. Indeed, if the precision of the frequency and of the time are difficult to handle jointly, FSTS can not be achieved. The duality between FSTU and FUTS allows to decide which constraint to relax, independently of the impact on the performances, but based for example, on the network deployment cost.

Furthermore, the best achievable load can be evaluated. We derive eq.(3.7) with respect to G_{tf}. The maximum throughput is obtained when this derivation equals to 0, thus $G_{tf} = Np_tp_f = \frac{1}{\alpha_t\alpha_f}$, and can be expressed as:

$$T = \frac{1}{\alpha_t \cdot \alpha_f} \cdot e^{-1}. \tag{3.8}$$

Besides, we can verify the best achievable load on Fig. 3.6. There are in practice 3 optimum throughputs depending on the values of α_f and α_t: $T = 1/e$ (for FSTS), $1/2e$ (obtained for either FSTU or FUTS), or $1/4e$ (for FUTU).

When we replace p_t and p_f by their original definitions (as shown in Table 3.1), this constraint in eq.(3.8) can also be written as:

$$\frac{N}{B} = \frac{T_p}{\alpha_t \cdot \alpha_f \cdot \tau \cdot b}. \tag{3.9}$$

We can observe that for a given configuration induced by the targeted application and the targeted rate (i.e. τ, T_p and b fixed), and a given configuration for $\alpha_t \cdot \alpha_f$, the ratio N/B is a constant. It is thus straightforward to dimension the network transmission band for a targeted number of users.

In these two sections 3.3-3.4, we have derived and validated the theoretical expression of the outage probability for all the configurations (time slotted or unslotted, and frequency slotted or unslotted). We have exploited the theoretical expression to derive the throughput. This analysis will be exploited and extended in the next two sections.

3.5 Generalized ALOHA with replications: theoretical analysis

In this section, we propose to use the replication mechanism to enhance the networks' reliability. We theoretically extend the outage probability eq.(3.3) of the previous section, to the generalized ALOHA case when considering the number of replications.

3.5.1 Mechanism of replications

To improve the service probability for each transmitting node, we illustrate in Fig. 3.7 the replication mechanism applied to generalized ALOHA systems. We assume that each message (with transmission duration τ) should be transmitted within the message lifetime T_p. The duration of one time-slot is equal to the duration of one transmission τ. For example, in time-slotted case such as Fig. 3.7 (a,c), there are $\frac{T_p}{\tau}$ time-slots available during one message lifetime.

We consider that each message is repeated exactly n_r times during the message lifetime T_p, regardless of the success of previous replications. n_r is thus considered predefined and identical for all nodes.

For slotted (FS or TS) cases, the length of the temporal window allocated for a replication is $\frac{T_p}{n_r \cdot \tau}$, similarly the length of frequency window is $\frac{B}{n_r \cdot b}$. Each node randomly selects a time (or frequency) slot in this window to repeat its message. On the contrary, the emission moment and carrier frequency selection are totally randomly for each replication of each message, in the unslotted (FU or TU) cases.

One message is successfully transmitted when at least 1 of the n_r attempts succeeds. Otherwise, the message is considered lost.

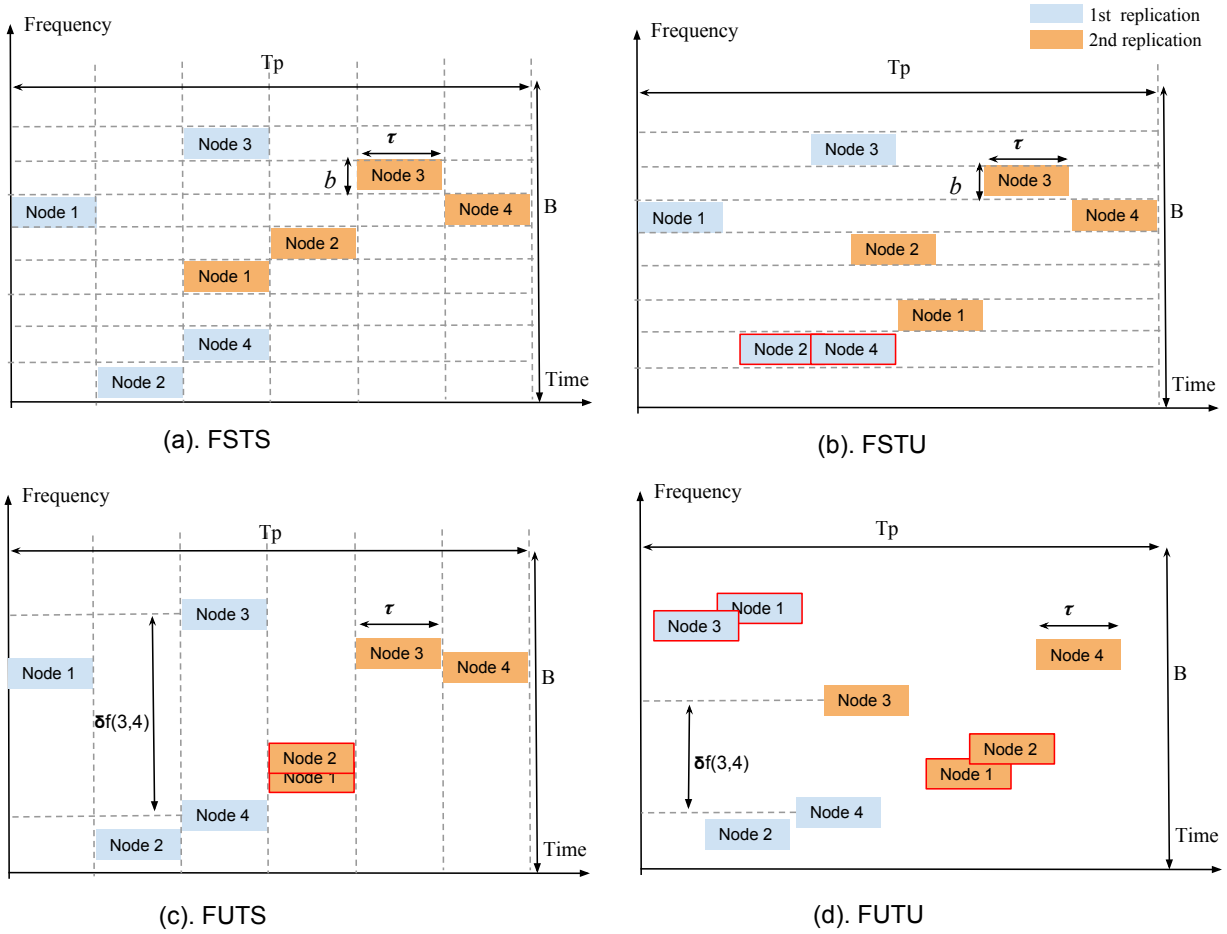

FIGURE 3.7: Illustration of replication $n_r = 2$ for (a). Frequency-Slotted Time-Slotted case; (b). Frequency-Slotted Time-Unslotted case; (c). Frequency-Unslotted Time-Slotted case; (d). Frequency-Unslotted Time-Unslotted case; with duration of message τ, period of message T_p, message frequency occupancy b, and total available band B.

3.5.2 Derivation of generalized ALOHA with replications

The expression eq.(3.3) represents the success probability of one message without replications. With the replication mechanism, the number of packets generated during the observed temporal and spectral interval increases, and the number of potential interfering packet increases.

We assume that the replications of the same message will never be in collision with each other. Therefore, with the presence of N other users' replications, the averaged traffic load becomes $n_r \cdot G_{tf} = \dfrac{n_r\ N\ \tau\ b}{T_p\ B}$.

The number of generated messages follows Poisson distribution, thus the number of all generated replications is Poisson distributed as well [81]. Accordingly, for generalized ALOHA cases, the probability that a given replication is correctly received can be expressed as:

$$\mathbb{P}_s(n_r) = e^{-\alpha_t \alpha_f G_{tf} n_r} \tag{3.10}$$

As replications are identical, one message is successfully received when at least one of its replications is correctly received at the base station. We have made the assumption that the replications experience independent transmission conditions, and that the success probability of any replication is independent of the collision on the previous ones. Accordingly, the outage probability of one useful message is the probability that all of its n_r replications are lost. It can be expressed as:

$$\mathrm{OP}(n_r) = \left(1 - e^{-\alpha_t \alpha_f G_{tf} n_r}\right)^{n_r} \tag{3.11}$$

with $\alpha_t = 1$ for time-slotted case; $\alpha_t = 2$ for time-unslotted case; $\alpha_f = 1$ for frequency-slotted case; $\alpha_f = 2$ for frequency-unslotted case.

3.6 Generalized ALOHA with replications: numerical results

In this section, we compare the numerical results (performed by simulations on Matlab) with the theoretical $\mathrm{OP}(n_r)$ established in eq.(3.11). Then we exploit this expression to estimate the optimum replication number for different parameter designs. At the end, we evaluate the minimum replication number for targeted quality of service, i.e. for a fixed OP.

We recall all the hypothesis (which are identical to the theory ones except the realistic interference model) as the following:

TABLE 3.3: Simulations hypothesis for mono-BS idealized channels with replications

BS number	nodes distribution	desired node	path loss	fading	replicas
1	random	random	no	no	n_r

3.6.1 Validation

As we can see, the expression of $\mathrm{OP}(n_r)$ depends on the following parameters: G_{tf}, α_t, α_f and n_r. We thus consider the impact of 4 parameters: B, T_p, n_r and N, for a given system where α_t and α_f is predefined. We choose the case FUTS to conduct simulations so that we can see the specific spectral collisions of UNB signals (as the phenomenon of temporal randomness is already well-known).

We do not consider b variation, as it is constrained by the transmission technology which typically is 116 Hz. Furthermore, as we verify the time-slotted case, the exact values of τ and T_p are not important, but rather the number of available slots for each message is: $\frac{T_p}{\tau}$. Thus, we fix $\tau = 1$, and only vary T_p.

We have plotted on Fig. 3.8-3.10, the comparison of the theoretical OP with the simulated one, as a function of the replication numbers, when varying N, B, or T_p. We can first observe that the curves do not match perfectly, but theory still provides a good estimation of the observed OP, especially for low n_r. More importantly, the theory correctly describes the evolution of the OP as a function of n_r. The cause of the inaccuracy when n_r is high, comes from the fact that we use

realistic interference model in the simulations. In realistic filter, the interference depends on the frequency spacing between the desired packet and the interfering packet, which is not limited to b. Thus when there are many simultaneous transmissions, the packets having a spacing larger than b can cause the loss of the desired packet (as their contributions can be added together). Whereas in the theory, we have made the assumption that there is no interference if the spacing is larger than b. That's why the numerical OP is higher than the theory.

Besides, we notice that the evolution of OP is convex as the replications n_r increases. For the first part, where OP decreases when n_r rises, We can highlight the fact that the replication mechanism is able to greatly improve the probability of successful transmission of a message. Indeed, for the sake of the n_r's increase, the chance that one message is successfully received rises.

However, for the second part, OP increases when the number of replications n_r goes up. This is because the repetitions multiply the number of packets sent by the nodes within a fixed time interval, and thus increases the channel utilization and the collision probability. Therefore, for a large number of replication n_r, the temporal and frequency resources become overloaded, the increase of collisions thus bypasses the benefit of adding redundancy.

Consequently, there is an optimum number of replications which allows to obtain the highest message throughput (corresponding to the lowest OP), as we can observe on Figure 3.8-3.10.

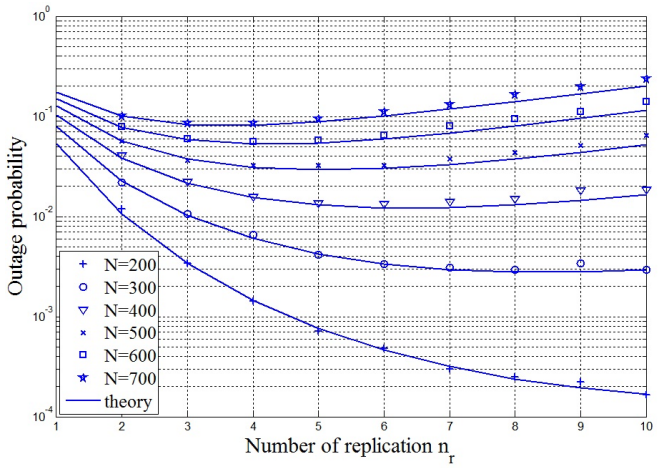

FIGURE 3.8: OP vs number of replications n_r with different number of active users N, for time-slotted frequency-unslotted case, $b =$ 116Hz, $B =$ 12kHz, $\tau =$ 1s, $T_p =$ 75s.

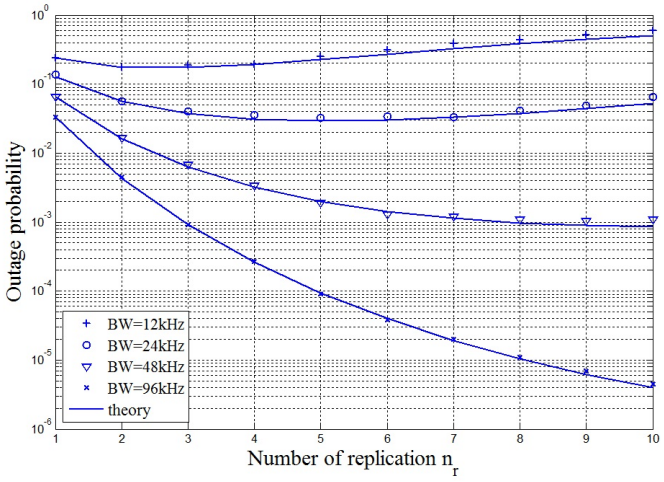

FIGURE 3.9: OP vs number of replications n_r with different bandwidth B, for time-slotted frequency-unslotted case, $N = 1000$, $b = 116$Hz, $\tau = 1$s, $T_p = 75$s.

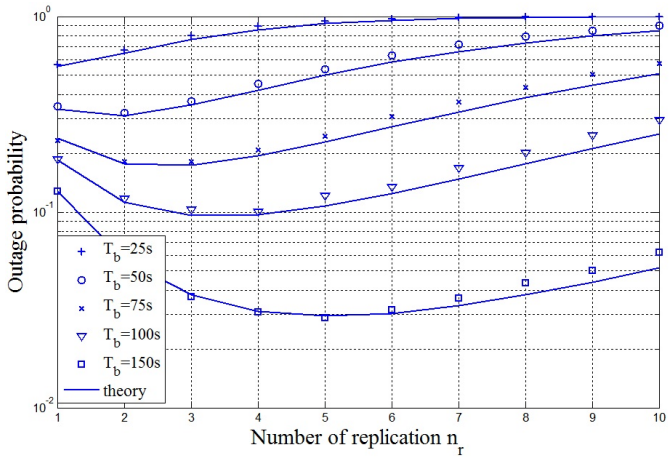

FIGURE 3.10: OP vs number of replications n_r with different message period T_p, for time-slotted frequency-unslotted case, $N = 1000$, $b = 116$Hz, $B = 12$ kHz, $\tau = 1$s.

3.6.2 Replication number optimization

Since the theory evolution is consistent with the simulated one, we use from now on eq.(3.11) to estimate the optimum number of replications which allows to achieve the lowest OP in this part.

As we can see in the figures of the last section, there exists always an optimum number of replications which allows us to achieve the lowest OP. We thus define $n_{r_{opt}}$ as this optimum number.

Therefore, in order to find out the $n_{r_{opt}}$ analytically, we can derive eq.(3.11) with respect to n_r as following:

$$\frac{\mathrm{d}OP}{\mathrm{d}n_r} = \left(1 - e^{-\alpha_t \alpha_f G_{tf} n_r}\right)^{n_r} \cdot \left(\ln\left(1 - e^{-\alpha_t \alpha_f G_{tf} n_r}\right) + \frac{\alpha_t \alpha_f G_{tf} n_r e^{-\alpha_t \alpha_f G_{tf} n_r}}{1 - e^{-\alpha_t \alpha_f G_{tf} n_r}}\right) \quad (3.12)$$

As OP is convex, $n_{r_{opt}}$ can be obtained when $\frac{dOP}{dn_r} = 0$. We do not consider the case where $\left(1 - e^{-\alpha_t \alpha_f G_{tf} n_r}\right)^{n_r} = 0$, as this would lead to a null OP. Thus the expression of $n_{r_{opt}}$ can be deduced from the second term of the multiplication: $\ln\left(1 - e^{-\alpha_t \alpha_f G_{tf} n_r}\right) + \frac{\alpha_t \alpha_f G_{tf} n_r e^{-\alpha_t \alpha_f G_{tf} n_r}}{1 - e^{-\alpha_t \alpha_f G_{tf} n_r}} = 0$.

We note that $n_{r_{opt}}$ can not be solved mathematically by hand. Nonetheless, its value can be numerically evaluated from the eq.(3.12). We have defined the values of G_{tf}, α_t, α_f and a range of n_r on Matlab, according to the expression eq.(3.12), Matlab is able to find the lowest OP. Thus the corresponding replications number is the $n_{r_{opt}}$ that we are look for.

We have plotted on Fig. 3.11 when considering different values of the time-frequency traffic load G_{tf} for all the ALOHA cases.

Globally, we can observe for all the cases that when the traffic load increases, the optimal number of replications $n_{r_{opt}}$ decreases. Indeed, when collision probability is already significant, the replication mechanism makes transmissions even more difficult to succeed. Hence for high traffic load cases, the $n_{r_{opt}} = 1$, which indicates that it is better not to have replications. On the contrary, for low G_{tf}, the replication mechanism allows to take advantage of the under-used resources to improve the transmission reliability.

Thus, from this theoretical analysis, we can confirm that the optimal number of replication decreases when the network is overloaded, which could be caused by: too many active users during the observed time interval; users sending message too often; or limited available frequency resources.

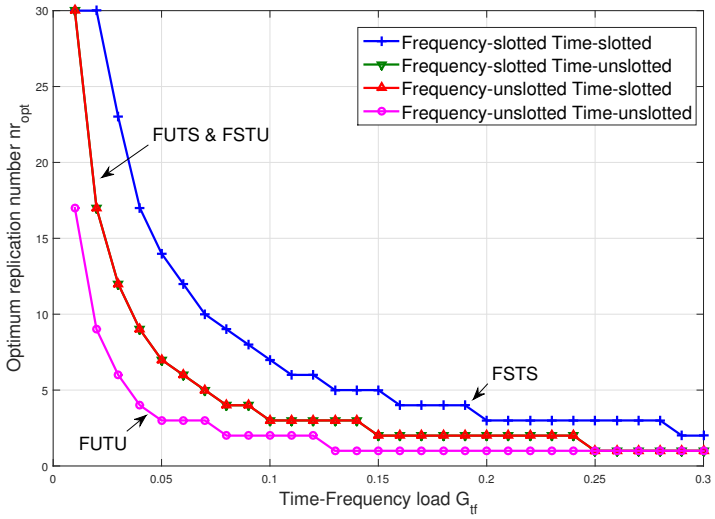

FIGURE 3.11: Optimum replication number $n_{r_{opt}}$ vs time-frequency traffic load G_{tf}, for all ALOHA cases.

However, when we compare the value of $n_{r_{opt}}$ for a given traffic load, in different ALOHA cases, we observe that we need more replications in FSTS case to achieve the best reliability. This is at first glance abnormal, but understandable. To explain this phenomenon, we have plotted in Fig. 3.12 the OP of all ALOHA cases as a function of n_r. In fact, we remark that the lowest OP for each ALOHA scenario is different. The lowest OP of FSTS case (around 10^{-5}) is much lower

than the three other cases (above 10^{-3}), thus FSTS will need more replications to achieve its lowest OP. That's why the $n_{r_{opt}}$ of FSTS is higher than other cases.

The observation gives us another insight to analyze the the impacts of replications, which we present in the next part.

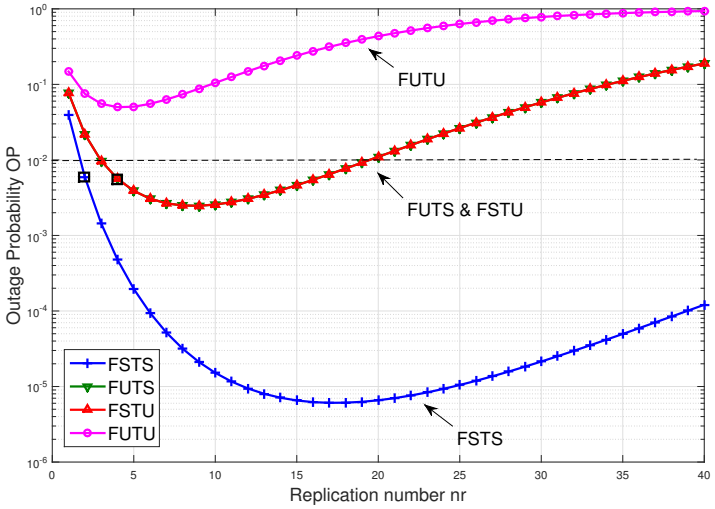

FIGURE 3.12: OP vs replication number n_r, with $G_{tf} = 0.04$, for all ALOHA cases.

3.6.3 Minimum replication number of targeted QoS

In reality, we do not need the reliability to be as low as 10^{-5} (as shown in Fig. 3.12). Reaching the highest achievable reliability is not the purpose for most IoT network users. The objective is usually to maintain a certain predefined quality of service (QoS), such as keeping the error probability below a given threshold (e.x. OP=10^{-2}). To do so, only a minimum replication number is sufficient.

As we can see in Fig. 3.12, if we want to keep OP below 10^{-2}, we only need 2 replications for the FSTS system, meanwhile we need 4 replications for the FSTU/FUTS system. Moreover, the OP of FUTU system is always higher than the targeted 10^{-2} whatever the traffic load is, it can thus never attain the demanded service level.

In this part, we estimate numerically the minimum replication number $n_{r_{min}}$, which is necessary to attain a targeted OP. This minimum number is not only attached to the system design (e.x. slotted or not), but also to the traffic load G_{tf}. Therefore, we have plotted the variation of estimated $n_{r_{min}}$ as a function of traffic load, by keeping the predefined OP=10^{-2} in Fig. 3.13, and OP=10^{-1} in Fig. 3.14.

Firstly, we observe that the value of $n_{r_{min}}$ rises up when G_{tf} increases. Indeed, when the network traffic becomes denser, more replications are needed to achieve the demanded QoS.

Secondly, we remark that for the same traffic load, slotted systems need less replications than unslotted systems when all of them are capable to attain the targeted OP. The exceptions occur when in some cases, the number of replications to achieve the targeted OP does not exist. For example, in Fig. 3.13 where OP= 10^{-2}, the minimum replication number is not found when G_{tf} exceeds certain limits in FUTU and FSTU/FUTS cases.

Thirdly, when we compare this two figures, we can note that the necessary minimum replication number decreases when the targeted OP becomes higher, for the same system. In Fig. 3.14, the $n_{r_{min}}$ of FSTS system is always 1, which indicates that no replications are needed to achieve the demanded QoS.

Finally, we highlight that for FUTU system which corresponds to the realistic Sigfox network, the minimum replications stops mostly at 3. This phenomenon implies that the FUTU system performance is limited when the traffic load is high. But is also confirms the choice of 3 replications [37] in Sigfox system.

However, we note that this analysis represents the worst case. Indeed, the packets are assumed to be received with the same power in this analysis, thus we lose all of them in collisions. But in realistic scenarios, the replications are received with different power levels due to the path losses. This puts an additional degree of freedom in the FUTU system, and we can thus at least decode the strongest one.

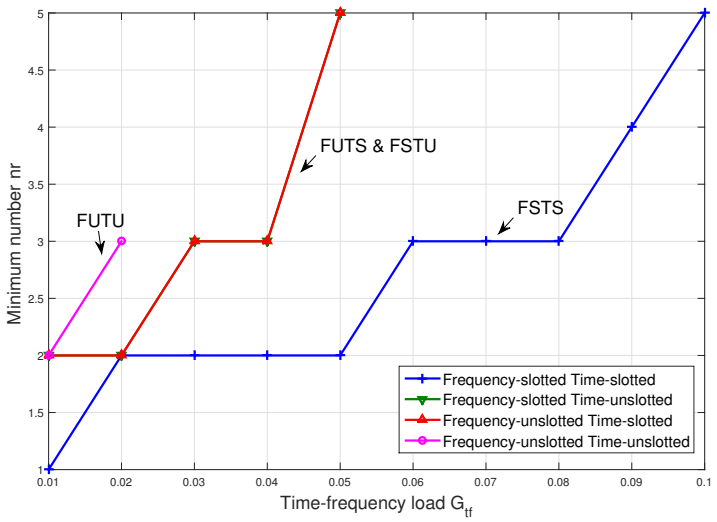

FIGURE 3.13: Minimum replication number $n_{r_{min}}$ vs traffic load G_{tf}, for OP= 0.01, in all ALOHA cases.

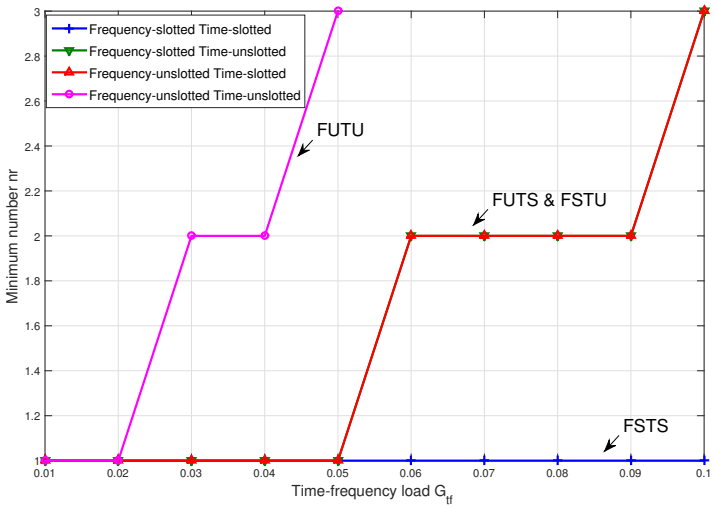

FIGURE 3.14: Minimum replication number $n_{r_{min}}$ vs traffic load G_{tf}, for OP= 0.1, in all ALOHA cases.

3.7 Conclusion

In this chapter, we have firstly evaluated theoretically the extension of the ALOHA scheme to the case of time-frequency random access, as experienced for example the UNB transmissions in IoT networks. Then we have extended the expression of generalized ALOHA with the involvement of replications.

In the first analysis, we have derived and validated the theoretical expression of the outage probability for all the ALOHA configurations (time slotted or unslotted, and frequency slotted or unslotted). We have found out that the OP depends on three parameter: the time-frequency traffic load G_{tf}, the indicator of temporal randomness α_t, and the indicator of spectral randomness α_f. We have exploited the analytical OP to derive the throughput which depends also on the three parameters. We have highlighted that frequency randomness and time randomness identically affect the throughput, and that they can be interchanged without loss of performances. This duality is promising as it opens the field to transposition of all existing results on ALOHA to unslotted-frequency networks. Moreover, we have derived the expression of the highest achievable throughput, as well as the condition to reach it. We have brought to light that the highest throughout is only related to the values of α_t and α_f.

In the second analysis with replications, we have also derived an analytical OP with the number of replications n_r. Similarly to the first analysis, the OP expression is related to the three parameters mentioned above, and we have n_r in addition. Besides, we have highlighted that, for each traffic load density, OP rises up then decreases with the increase of n_r. Thus there exists an optimal number of replications, which allows to achieve the best reliability. At the end, we have evaluated the minimum replication number to achieve targeted quality of service (such as OP=10^{-5}). We have brought to light that this result can be used to design the number of replications in order to adapt to network load, and quality of service demands.

We note that the results of this chapter is constraint by the ideal channel conditions where all messages are received with the same power level. It can thus be followed by further studied with the involvement of signal power attenuation (such as path loss and fading).

Another limitation is the fact that the replication number is predefined (even it corresponds to the realistic case of Sigfox). But it can at least give us an insight about the impact of replication mechanism on UNB systems, and be furthered by self-adapting replication mechanisms.

Chapter 4

Performance of UNB networks with realistic channel

Contents

In this chapter, we quantify the UNB system performance with realistic channel conditions. We derive two theoretical expressions of the outage probability: the first one considers the path-loss due to the propagation, the spectral interference caused by the random radio access of UNB, and the assumption of only one interferer at each collision; the second one includes Rayleigh fading and the aggregated interference (where a failure can come from several collision packets) in addition, always with the path-loss and the spectral interference. We compare the OP in both analysis, in order to evaluate the impact of Rayleigh fading. Then we estimate the maximum number of nodes that the network can support simultaneously by exploiting the two theoretical expressions. We evaluate also the the spectral efficiency of UNB networks without and with guard band. We note that the powerful mathematical tool stochastic geometry is used in the second analysis where fading is involved.

4.1 Introduction

Different from last chapter where we have assumed idealized channel conditions, we consider the power attenuation which is more realistic in this chapter. Particularly, we consider the path-loss and fading as they are representative phenomena in most of the wireless communication scenarios.

4.1.1 Related works of path-loss & fading

In realistic environments, the received signal is attenuated, especially for such long range transmission. According to Shannon [82], the path-loss is the main contributor of the received signal power attenuation, which depends mainly on the distance between the transmitter and the receiver.

Moreover, multiple paths of signals caused by all the obstacles and reflectors in the environment are inevitable. Thus the impact of fading has also to be taken into account when considering realistic channel conditions. There are two types of fading: the slow fading and the fast fading. The dormer refers to the case where the amplitude and phase change imposed by the channel can be considered roughly constant over the period of use, while the latter varies during the period [83]. Studies about the impact of slow fading and fast fading on systems such ALOHA or slotted ALOHA have existed from a long time ago [84, 85]. Nonetheless, to the best of our knowledge, none of the works has considered the interference induced by the spectral randomness of UNB.

We thus consider the impact of path-loss and Rayleigh fading since it is the most applicable one in urban environment. But in this chapter, we only focus on the statistic property of the fading factor, whose impact to the received power is considered constant during the observe temporal interval.

4.1.2 Related works of PPP & Stochastic Geometry

To characterize the performance in large-scale wireless networks, the wireless network node positions are usually modeled by the well-known spatial Poisson point process (PPP) [14]. PPP refers to a type of random mathematical object that consists of points randomly located on a mathematical space. The point process often have convenient mathematical properties, and can be analyzed with the aid of mathematical tools such as stochastic geometry. Other approaches rely on deterministic lattices [86,87] where the geographical area (urban, rural, and downtown) and the population activity are taken into account to approach the real world's non-uniform and irregular traffic distributions.

However, for UNB systems, PPP integrates more efficiently the spatial stochastic nature of the nodes distribution as well as the attenuation laws, compared to deterministic lattices. More importantly, marked PPP [88] provides a means of coping with additional random properties such as shadowing or fading if they are not spatially correlated. A large variety of networks have been studied by the PPP modeling, in particular cellular networks [89], wireless sensor networks [88, 90–93], and cognitive wireless networks [94, 95]. Stochastic geometry is an efficient tool to study the average behavior over many spatial realizations of a network whose nodes are placed according to some probability distribution.

The above mentioned references focus on finding the interference (intra-cell or inter-cell) distribution which can be characterized by its Laplace transform [14],

in large-scale wireless networks. The well-known distributions (such as Gaussian, inverse Gaussian, gamma, and inverse gamma distribution) are often used to characterize the interference's Laplace distribution. The authors in [96] was one of the pioneers to use the Laplace transform method in characterizing the interferences in cellular networks. Besides, there are other different methods which allow to approximate the interference distribution, e.g. with moments matching [97], with the central limit theorem [98–100] or with the cumulants-based method [101]. These approaches mainly allow to obtain the first moments (mean and variance) of the AIP's (Aggregated Interference Power) probability density function (PDF) or the cumulative density function (CDF). Accordingly, closed-form expressions can be derived for both the interference distribution and the signal-to-interference ratio (SIR) which is the main indicator of transmission quality.

However, there does not exist a general closed-form interference Laplace transform which we can apply to any kinds of systems. Several works have been conducted by finding the PDF of interference, in systems where transmissions are performed in adjacent channels (thus barely interfering) [102–107].

4.1.3 Motivation and Contributions of this Chapter

In UNB networks, carrier frequencies are randomly chosen in a continuous interval. This has not been considered in the above-mentioned works, to the best of our knowledge.

A way to introduce this random characteristic in the stochastic geometry model is to consider a marked spatial Poisson Point Process (PPP). In addition to the random parameter (i.e. the nodes' position) included in PPP, the marks can represent other random parameters such as nodes' random emission moments and their randomly chosen carrier frequencies. Thus the marked PPP can model the interference contribution by other simultaneous transmissions (from one given transmission's point of view).

We exploit in this chapter two complementary approaches. Firstly, we derive an analytic expression of a UNB-based system performance, when considering both the path-loss and the specific interference model (which approximates precisely the realistic one) of UNB systems. Secondly, we take into account the Rayleigh fading and use the stochastic geometry to find the distribution of SIR, but with a simplified interference model (because we cannot find tractable expression when considering realistic interference model according to our very first calculations).

One may note that the shadowing which causes the fluctuation of the received signal power (due to obstacles on the propagation path between transmitter and receiver), should also be considered in realistic channels. But It has been shown in [108] that a marked PPP with shadowing is equivalent to a PPP without shadowing by adapting the power strength in the model. It is thus neglected for the sake of simplicity.

The rest of the chapter is constructed as follows: in Section 4.2 we model the network's topology and behavior, and we state all the hypothesis that will be used. In Section 4.3, we derive theoretically the expressions of outage probability in UNB network for two approaches. The first part (Section 4.3.1) considers the impact of path-loss and the Gaussian interference coefficient. And the second part (Section 4.3.2) considers the joint impacts of path-loss, Rayleigh fading and

rectangular interference coefficient. Then, in Section 4.4, we validate the two theoretical analysis by simulations. In Section 4.5, we exploit the theories to estimate the network capacity and the spectral efficiency . Finally, we conclude the chapter in Section 4.6.

4.2 Modeling and assumptions

4.2.1 Network topology

Single base station (BS) is the atomic pattern to analyze the performance of cellular networks. We thus consider in this chapter the uplink of a UNB network, where nodes communicate only with a single BS. The BS covers a finite circular area with a known radius and gathers the information from nodes located inside. Inter-cell interference is therefore not considered for simplicity's sake. Nonetheless, this can be done by modifying the Gaussian additive noise strength distribution as done in [109]. Indeed, the total interference produced by all the nodes beyond a given distance (i.e. the nodes in other cells) tends to become Gaussian additive noise when this distance is large enough [110].

We suppose that nodes are distributed randomly in a disk form area, whose range is $[r_m, r_M]$, as shown in Fig. 4.1. Nodes are positioned inside the cell, except for the inner disk of the radius r_m in the cell. In realistic Sigfox networks, there does not exist the limitation of r_m, but we have made this assumption to ensure the mathematical tractability by avoiding singularity at the base-station location [92]. For example, when the distance r between a node and the BS tends to be 0, the path loss r^{-2} (in free space case) tends to be infinity, which is not convenient to derive closed-form expressions.

The random nodes' positions can be modeled by a spatial homogeneous Poisson point process (HPPP) of density λ_t that lies in the Euclidean plan $\mathbb{R}^2$. In this chapter, we focus on one observed moment. It is like we virtually sample a temporal duration very, and we choose one sampling moment to observe the simultaneous transmissions. Due to the very small duty cycle of the nodes, we prefer to use the *active* nodes density λ (nodes$/m^2$), which is considered stable at the observed moment. One may note that $\lambda << \lambda_t$. The *active* nodes are a subset of the deployed nodes, thus the *active* nodes' positions can also be modeled by a HPPP with density λ. We thus do not consider the temporal interference in this chapter, which helps us to understand how the partial spectral interference impacts solely the network performance .

We assume that all the nodes have the same behaviors: their data packets are transmitted with the same emission power and antenna gain. In realistic networks, the nodes in different categories may have different emission power levels, or they are under fractional power control according to their distance to the BS [111]. But we do not consider this feature in this chapter for the sake of simplicity.

The BS is considered to be always in reception mode, and to scan the whole bandwidth for potential transmissions (as done in SigFox network). For each detected transmission (even simultaneous ones), the BS processes the incoming message(s).

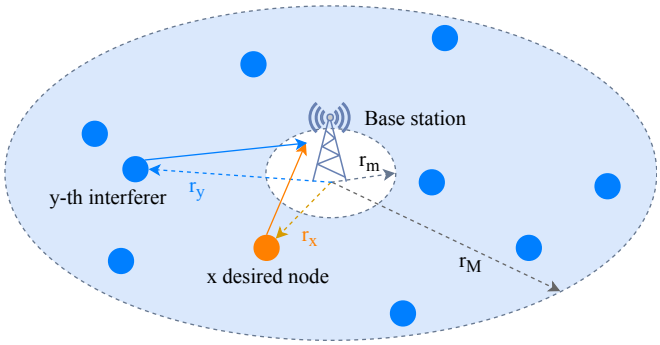

FIGURE 4.1: Illustration of network topology: area range is $[r_m, r_M]$, orange point is the desired node, at a distance of r_x; blue points are interfering nodes, at a distance of r_y

4.2.2 Interference model for a single interferer

We define $\mathcal{A}$ as the set of active nodes at the observed moment. The point process can thus be assimilated as a random sequence, where the set of points $\mathcal{A}$ are successively randomly selected in a space $\mathbb{R}^2$. Without loss of generality, we consider that node x is the *desired node*, while all the others are called *interfering nodes* as they can collide with the desired node. For a given transmission range r, the attenuation of the signal power received at the base-station denotes:

$$h_c(r,t) = g(t) \cdot h_0 \cdot r^{-\alpha},\ r \in [r_m, r_M] \tag{4.1}$$

where $\alpha \geq 2$ is the path loss exponent; g is the Rayleigh channel coefficient, which is a random variable following an exponential distribution of unitary mean $g \sim exp(1)$ considered as constant during the observation instant; and h_0 is the reference channel gain determined at the reference distance $r_0 = 1$ m.

Shadowing is neglected for the sake of simplicity, as stated in Section 4.1.3, but could be introduced with a marked PPP.

At the BS side, the received signal is the sum of active nodes' signals and can be expressed as follows:

$$r(t) = \sqrt{h_c(r_x,t)} * h_e(f_x,t) * s_x(t) + \sum_{y \in \{\mathcal{A}-x\}} \sqrt{h_c(r_y,t)} * h_e(f_y,t) * s_y(t) + w(t) \tag{4.2}$$

where, for any active node $x, y \in \mathcal{A}$, $s(t)$ is the modulated symbol; $h_e(f,t)$ is the transmission FIR filter centered on the randomly chosen carrier frequency f; $*$ denotes the convolution operator; and $w(t)$ is an additive white Gaussian noise with zero mean and variance σ^2.

To recover the desired signal, the sum of the signal received at BS is filtered at the carrier frequency of the desired node f_x, with the matching filter ($h_r(f_x,t) =$

$h_e(f_x, t)$). The filtered desired signal can be thus written as follows:

$$\begin{aligned} r'(f_x,t) &= h_r(f_x,t) * r(t) \\ &= \sqrt{h_c(r_x,t)} \cdot h_e(f_x,t) * h_e(f_x,t) * s_x(t) \\ &+ \sum_{y \in \{\mathcal{A}-x\}} \sqrt{h_c(r_y,t)} \cdot h_e(f_y,t) * h_e(f_x,t) * s_y(t) + h_e(f_x,t) * w(t) \end{aligned} \quad (4.3)$$

where the first term represents the filtered desired signal power; the second term represents the filtered AIP (Aggregated Interference Power); and the third term represents the filtered noise power.

We can extract the received power corresponding to the signal of the desired node x :

$$P_s = h_c(r_x,t) \cdot P_0 = g_x \cdot r_x^{-\alpha} \cdot P_0' \quad (4.4)$$

with $P_0 =< |h_e(f,t) * h_e(f,t) * s(t)|^2 >$ which is identical to all signals, and P_0' stands for $h_0 \cdot P_0$.

Similarly, the interference power I_y caused by a single interferer (at the distance of r_y) on the desired signal denotes:

$$I_y = h_c(r_y,t) \cdot \beta(|f_x - f_y|) \cdot P_0 \quad = g_y \cdot r_y^{-\alpha} \cdot \beta(|f_x - f_y|) \cdot P_0' \quad (4.5)$$

with $\beta(|f_x - f_y|) = \frac{<|h_e(f_y,t) * h_e(f_x,t)|^2>}{<|h_e(f_x,t) * h_e(f_x,t)|^2>}$ the *rejection coefficient*, defined as the reception filter is centered on a different frequency than the transmission filter. The rejection coefficient quantifies the portion of interfering signal which is kept after filtering, it is thus also called *interference coefficient*. It depends on the frequency spacing between the two carrier frequencies $\delta f = |f_x - f_y|$. Since the UNB signals select their carrier frequencies randomly and independently (as stated in Section 2.3.2), this partial overlap between two signals exists. As illustrated in Fig. 4.2, the black curve stands for a realistic interference coefficient in SigFox's network. We can observe that the highest interference level (i.e. $\beta(\delta f) = 1$) is achieved when $\delta f = 0$, while it tends to 0 as the interferer's frequency moves away from the desired node' frequency (i.e. when δf increases).

We can approximate this interference with two models. We can note that the actual interference coefficient can be divided into two main areas. Transition occurs between $200 - 400$Hz, depending on the considered criterion. When δf is small enough, the contribution of a unique interferer can be significant, i.e. until 0 dB when two signals are totally overlapped. Thus a unique interferer in this area has high probability to cause the desired packet's loss. On the contrary, when δf is larger, the interference level becomes much lower, i.e. below -50dB. Hence a unique interferer in this area will have almost no impact on the performance of the desired node. Accordingly, a single interferer's contribution can be approximated by two constants in these two areas, thus by a rectangular function:

$$\beta(\delta f) = \begin{cases} I_{max} & for \quad \delta f \leq \triangle, \\ I_{min} & for \quad \delta f > \triangle. \end{cases} \quad (4.6)$$

where $\triangle$ corresponds to the width of δ_f that creates high interference level.

We can also approximate the interference coefficient by a zero-mean Gaussian function, depending on the frequency difference δf (the pink curve on Fig. 4.2):

$$\beta(\delta f) = \frac{150}{\sigma\sqrt{2\pi}} \exp^{\frac{-\delta f^2}{2\sigma^2}} \tag{4.7}$$

with $\sigma = 60$ for a 100 bit/s transmission [12].

Fig. 4.2 illustrates all the interference models. The black curve represents the realistic UNB interference model, which is traced based on the SigFox network. The pink curve represents the Gaussian function eq.(4.7), which fairly approximates the realistic one, and will be used in section 4.3.1. The rectangles in green, red and blue represent respectively the approximated rectangular model (AR), the upper bound (UB) and the lower bound (LB). They will be used in Section 4.3.2.

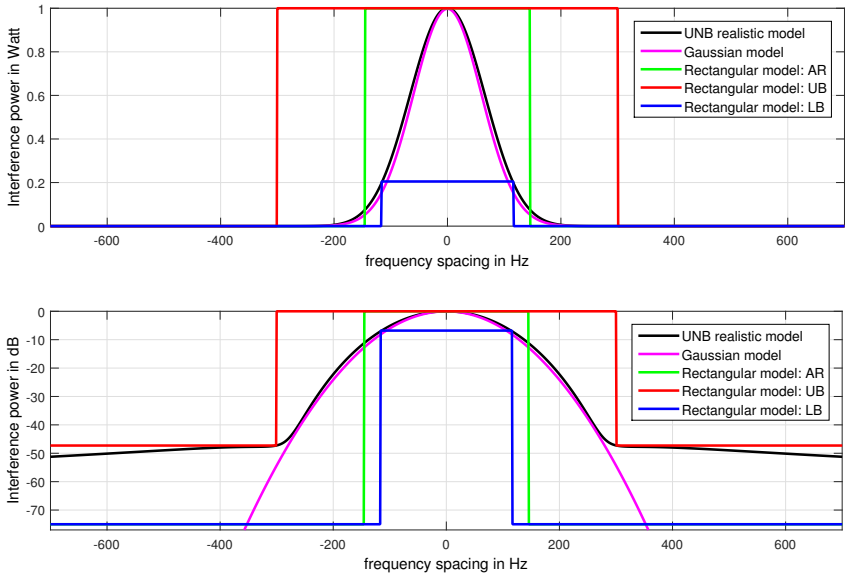

FIGURE 4.2: Behavior of the interference coefficient vs the frequency spacing δf between the desired signal and the interferer

4.3 Theoretical analysis for UNB Networks in Spectral-Spatial Dimensions

In this section, we evaluate the networks performance with regards to the OP (Outage Probability). The OP is defined as the probability that a packet is lost, thus the SINR (Signal to Interference and Noise Ratio) of the desired node is lower than a predefined threshold (we use γ^* to note it). This threshold is normally designed according to the sensibility of the receiver. The OP derivation is thus based on instantaneous SINR, which we assume to be stable at the observed moment. Therefore, the OP of any desired node x located at r_x from the BS denotes:

$$\text{OP} = \mathbb{P}(\text{SINR}_x \leq \gamma^*) = \mathbb{P}\left(\frac{P_s}{P_I + W} \leq \gamma^*\right) \tag{4.8}$$

with $P_s = g_x \cdot r_x^{-\alpha} \cdot P_0'$ the desired node received power as in eq.(4.4), P_I the total interference power, W the noise power and γ^* the predefined SINR threshold. We use $\mathbb{P}$ to represent *probability*, and P to represent *power*.

P_I is obtained by summing the contribution of each interferer, as presented in eq.(4.5):

$$P_I = \sum_{y \in \{\mathcal{A}-x\}} g_y \cdot r_y^{-\alpha} \cdot \beta(\delta f) \cdot P_0' \tag{4.9}$$

In this chapter, the OP will be evaluated in 2 cases. We start with a simple scenario in Section 4.3.1, where we consider a simplified channel gain with only path-loss (no Rayleigh fading and no noise), and the Gaussian interference coefficient is used. We then extend it to a more complete case in Section 4.3.2, where we take into account Rayleigh fading, the noise, and the rectangular interference coefficient.

4.3.1 Impact of path loss and approximated Gaussian model

In order to have a first intuition of the random spectrum access impact on network performance, we first neglect fading and noise, and consider only the free space propagation ($\alpha = 2$) in this section. We derive the OP when considering path-loss and the spectral interference, by evaluating the SIR (Signal to Interference Ratio) as a simplification of the SINR. We use the approximated Gaussian model (pink curve in Fig. 4.2) to measure the interference coefficient. We focus on the spectral interference coming from only one interferer, as this is the most frequent case according to actual SigFox network analysis [12]. A more general case of the aggregation of several interferers will be treated in the next section.

According to the assumptions above, we have OP as:

$$\text{OP} = \mathbb{P}(\text{SIR} \leq \gamma^*) = \mathbb{P}\left(\frac{P_s}{P_I} \leq \gamma^*\right) \tag{4.10}$$

We first consider two active nodes (one desired node x at the distance of r_x, and one interfering node y at the distance of r_y), before generalizing it to N active nodes. From eq.(4.4) and eq.(4.5), the SIR of the desired node can be expressed as:

$$SIR = \frac{P_s}{P_I} = \frac{r_x^{-2} \cdot P_0'}{r_y^{-2} \cdot \beta(\delta f) \cdot P_0'} = \left(\frac{r_y}{r_x}\right)^2 \frac{1}{\beta\,(\delta f)} \tag{4.11}$$

A packet is considered lost if its $SIR \leq \gamma^*$, i.e. when :

$$\text{OP} = \mathbb{P}(r_y \leq r_x \sqrt{\gamma^* \beta\,(\delta f)}) \tag{4.12}$$

this step implies that the outage probability can be transformed into the probability that one interferer y falls into the circular area whose radius is $r_x\sqrt{\gamma^* \beta\,(\delta f)}$. We can call this circular area as *interfering area*.

We decompose eq.(4.12) by using the law of total probability with respect to the conditioning variable δf. Hence, the OP becomes:

$$\begin{aligned} \mathrm{OP} &= \int_0^B \mathbb{P}\left(SIR \leq \gamma^* | \delta f\right) \cdot \mathbb{P}\left(\delta f\right) \, \mathrm{d}\delta f \\ &= \int_0^B \mathbb{P}\left(r_y \leq r_x \sqrt{\gamma^* \beta\left(\delta f\right)} | \delta f\right) \cdot \mathbb{P}\left(\delta f\right) \, \mathrm{d}\delta f \end{aligned} \tag{4.13}$$

with B being the total available frequency resource in Hz, and $\mathbb{P}(\delta f)$ being the probability distribution of δf.

First of all, we express $\mathbb{P}\left(\delta f\right)$. The desired and interfering nodes choose their frequencies f_x and f_y randomly and uniformly within $[0, B]$. Thus, their spectral difference δf has the following probability distribution function:

$$\mathbb{P}\left(\delta f\right) = \begin{cases} \dfrac{2}{B}\left(1 - \dfrac{\delta f}{B}\right) & \text{for } \delta f \in [0, B] \\ 0 & \text{elsewhere} \end{cases} \tag{4.14}$$

Secondly, we calculate $\mathbb{P}\left(r_y \leq r_x \sqrt{\gamma^* \beta\left(\delta f\right)} | \delta f\right)$.

Since the distribution of nodes follows Poisson point process, their respective distance to the BS follows a uniform distribution. $\mathbb{P}\left(r\right)$ represents the probability of being at a random distance (radius r) in a disk form area of $[r_m, r_M]$:

$$\mathbb{P}\left(r\right) = \begin{cases} \dfrac{2r}{r_M^2 - r_m^2} = \dfrac{2r}{k^2} & \text{for } r \in [r_m, r_M] \\ 0 & \text{elsewhere} \end{cases} \tag{4.15}$$

with $k^2 = r_M^2 - r_m^2$.

OP for a given r_x

For any desired node at a given distance r_x, the only random variables in the expression of OP in eq.(4.13) are r_y and δf. We can thus derive the conditional probability with respect to δf, according to the ranges of $r_x \sqrt{\gamma^* \beta\left(\delta f\right)}$:

$$\begin{aligned} &\mathbb{P}\left(r_y \leq r_x \sqrt{\gamma^* \beta\left(\delta f\right)} | \delta f\right) \\ &= \begin{cases} \displaystyle\int_{r_m}^{r_m} \mathbb{P}\left(r_y\right) \, \mathrm{d}r_y & \text{if } r_x \sqrt{\gamma^* \beta\left(\delta f\right)} \leq r_m, \\ \displaystyle\int_{r_m}^{r_x \sqrt{\gamma^* \beta(\delta f)}} \mathbb{P}\left(r_y\right) \, \mathrm{d}r_y & \text{if } r_m \leq r_x \sqrt{\gamma^* \beta\left(\delta f\right)} \leq r_M \\ \displaystyle\int_{r_m}^{r_M} \mathbb{P}\left(r_y\right) \, \mathrm{d}r_y & \text{if } r_x \sqrt{\gamma^* \beta\left(\delta f\right)} \geq r_M \end{cases} \\ &= \begin{cases} 0 & \text{if } r_x \sqrt{\gamma^* \beta\left(\delta f\right)} \leq r_m, \\ \dfrac{{r_x}^2 \gamma^* \beta\left(\delta f\right) - {r_m}^2}{k^2} & \text{if } r_m \leq r_x \sqrt{\gamma^* \beta\left(\delta f\right)} \leq r_M \\ 1 & \text{if } r_x \sqrt{\gamma^* \beta\left(\delta f\right)} \geq r_M \end{cases} \end{aligned} \tag{4.16}$$

The first case in eq.(4.16) (resp. the third case) renders the fact that, the targeted range threshold is so small (resp. so high) that, in the targeted area, no node can be (resp. all the nodes are) closer. The second case is the intermediate case, and its value depends on the desired node location.

We update eq.(4.13) according to eq.(4.16), and replace $\beta(\delta f)$ by the zero-mean Gaussian function as shown in eq.(4.7). After the integration over δf, OP becomes:

$$\begin{aligned}
\mathrm{OP} &= \int_0^B \mathbb{P}\left(r_y \leq r_x\sqrt{\gamma^*\beta(\delta f)}|\delta f\right)\mathbb{P}(\delta f)\ \mathrm{d}\delta f \\
&= 0 + \int_{b_1}^{b_2}\left(\frac{{r_x}^2\gamma^*\beta(\delta f) - {r_m}^2}{k^2}\right)\mathbb{P}(\delta f)\ \mathrm{d}\delta f + \int_{b_0}^{b_1} 1\cdot\mathbb{P}(\delta f)\ \mathrm{d}\delta f \\
&= \left[75a\gamma^*\,\mathrm{erf}\left(\frac{\delta f}{\sqrt{2\sigma^2}}\right) + \frac{150a\gamma^*\sigma}{B\sqrt{2\pi}}\exp\left(\frac{-\delta f^2}{2\sigma^2}\right) + e\frac{\delta f^2}{2} - eB\delta f\right]_{b_1}^{b_2} \\
&\quad + \frac{B}{2}\left[\delta f - \frac{\delta f^2}{2B}\right]_{b_0}^{b_1}
\end{aligned} \tag{4.17}$$

with the following constants:

$$\begin{aligned}
&d = \frac{2{r_x}^2}{Bk^2}, \qquad e = \frac{2{r_m}^2}{B^2k^2}, \qquad b_0 = 0 \\
&b_1 = min\left(\beta^{-1}\left(\left(\frac{r_M}{r_x}\right)^2\frac{1}{\gamma^*}\right), B\right), \qquad b_2 = min\left(\beta^{-1}\left(\left(\frac{r_m}{r_x}\right)^2\frac{1}{\gamma^*}\right), B\right)
\end{aligned}$$

The integral bounds b_0, b_1 and b_2 were obtained as follows. Since $r_m \leq r_x\sqrt{\gamma^*\beta(\delta f)} \leq r_M$ is equivalent to $\frac{r_m}{r_x} \leq \sqrt{\gamma^*\beta(\delta f)} \leq \frac{r_M}{r_x}$, it can be expressed as $\beta^{-1}\left(\left(\frac{r_M}{r_x}\right)^2\frac{1}{\gamma^*}\right) \leq \delta f \leq \beta^{-1}\left(\left(\frac{r_m}{r_x}\right)^2\frac{1}{\gamma^*}\right)$. As the range of δf is $[0, B]$, we have to put a *min* function to constrain these integral bounds in case they exceed B. One may note that $\beta(\delta f) \in [0,1]$ according to its definition. Thus, b_1 exists only if $\left(\frac{r_M}{r_x}\right)^2 \leq \gamma^*$. Otherwise b_1 would be null, and the last term of integral would be null too.

Eq.(4.17) represents the OP when there are 2 active nodes. We now extend it to N active nodes. In this case, any of the $N-1$ nodes (i.e. all nodes except the desired node) can be an interfering node. We recall that we consider only one interferer at each collision, thus no AIP is included. Accordingly, the transmission success means that the desired node is not interrupted by any of $N-1$ nodes. Consequently, the outage probability is given by:

$$\mathrm{OP}_{(N)} = 1 - (1 - \mathrm{OP})^{N-1} \tag{4.18}$$

OP for average r_x

The OP derived in the previous part concerns a given r_x. In practice, the distance of the desired node can vary all over the cell. We show the complementary calculation steps for average r_x in this part.

Different from last part, we now have an additional random variable, i.e. the desired node's distance r_x. We thus complement the steps after the computation of eq. (4.16) which is expressed as the following:

$$\mathbb{P}\left(r_y \leq r_x\sqrt{\gamma^*\beta\left(\delta f\right)}|\delta f \cap r_x\right) \tag{4.19}$$
$$= \begin{cases} 0 & \text{if } r_x\sqrt{\gamma^*\beta\left(\delta f\right)} \leq r_m, \\ \dfrac{{r_x}^2\gamma^*\beta\left(\delta f\right) - {r_m}^2}{k^2} & \text{if } r_m \leq r_x\sqrt{\gamma^*\beta\left(\delta f\right)} \leq r_M \\ 1 & \text{if } r_x\sqrt{\gamma^*\beta\left(\delta f\right)} \geq r_M \end{cases}$$

This probability is conditional on r_x and δf.

We can compute $\mathbb{P}\left(r_y \leq r_x\sqrt{\gamma^*\beta\left(\delta f\right)}|\delta f\right)$ by integrating with respect to r_x from now on. However, as the conditions in eq.(4.19) depends on both r_x and δf, the expression is computed differently depending on the range of δf, which can be very tricky. We have distinguished 4 cases based on the value of $\sqrt{\gamma^*\beta\left(\delta f\right)}$ which characterizes the relative positioning of the desired and interfering node:

- case 1: $\sqrt{\gamma^*\beta\left(\delta f\right)} \leq \frac{r_m}{r_M}$. This case is directly related to the first line in eq.(4.19). Due to inequality transitivity, the $r_x\sqrt{\gamma^*\beta\left(\delta f\right)} \leq r_M\sqrt{\gamma^*\beta\left(\delta f\right)} \leq r_m$ condition and the eq.(4.12) condition imply that $r_2 \leq r_m$. This is not achievable, as there is no nodes distributed inside the exclusion area of radius r_m. Thus, for such δf , it is not possible to find a node close enough to the BS to create sufficient interference. Thus, $\mathbb{P}\left(r_y \leq r_x\sqrt{\gamma^*\beta\left(\delta f\right)}|\delta f\right)$ is null.

- case 2: $\frac{r_m}{r_M} \leq \sqrt{\gamma^*\beta\left(\delta f\right)} \leq 1$. This corresponds to the case where the interfering node must be closer to the receiver than the desired node (but not in the exclusion area). In this case, the left inequality in the second line in eq.(4.19) is verified as $r_m \leq r_x\sqrt{\gamma^*\beta\left(\delta f\right)}$ is equivalent to $\frac{r_m}{r_M} \leq \frac{r_m}{r_x} \leq \sqrt{\gamma^*\beta\left(\delta f\right)} \leq 1$. Hence, all desired nodes satisfying $r_x \in \left[\frac{r_m}{\sqrt{\gamma^*\beta(\delta f)}}, r_M\right]$ contribute to this case.

- case 3: $1 \leq \sqrt{\gamma^*\beta\left(\delta f\right)} \leq \frac{r_M}{r_m}$. Contrarily to the second case, here the interfering node can be further from the receiver than the desired node. In this case, nodes with a distance $r_x \in \left[r_m, \frac{r_M}{\sqrt{\gamma^*\beta(\delta f)}}\right]$ verify the right inequality in the second line of eq.(4.19), while those such that $r_1 \in \left[\frac{r_M}{\sqrt{\gamma^*\beta(\delta f)}}, r_M\right]$ verify the third line.

- case 4: $\sqrt{\gamma^*\beta\left(\delta f\right)} \geq \frac{r_M}{r_m}$. In this last case, even the closest desired user is interfered by any node in the cell. This is directly related to the third line in eq.(4.19), which leads to $\frac{r_y}{r_x} \leq \frac{r_M}{r_m} \leq \sqrt{\gamma^*\beta\left(\delta f\right)}$. So $\mathbb{P}\left(r_y \leq r_x\sqrt{\gamma^*\beta\left(\delta f\right)}|\delta f\right) = 1$.

Accordingly, we can compute the integral with respect to r_x, in the four cases stated above:

$$\mathbb{P}\left(r_y \leq r_x\sqrt{\gamma^*\beta\left(\delta f\right)}|\delta f\right) \tag{4.20}$$

$$= \begin{cases} 0 & \text{if}\sqrt{\gamma^*\beta\left(\delta f\right)} \leq \frac{r_m}{r_M}, \\ \int_{\frac{r_m}{\sqrt{\gamma^*\beta(\delta f)}}}^{r_M} \frac{{r_x}^2\gamma^*\beta\left(\delta f\right) - {r_m}^2}{k^2}\frac{2r_x}{k^2}\,\mathrm{d}r_x & \text{if } \frac{r_m}{r_M} \leq \sqrt{\gamma^*\beta\left(\delta f\right)} \leq 1 \\ \int_{r_m}^{\frac{r_M}{\sqrt{\gamma^*\beta(\delta f)}}} \frac{{r_x}^2\gamma^*\beta\left(\delta f\right) - {r_m}^2}{k^2}\frac{2r_x}{k^2}\,\mathrm{d}r_x & \\ + \int_{\frac{r_M}{\sqrt{\gamma^*\beta(\delta f)}}}^{r_M} 1 * \frac{2r_x}{k^2}\,\mathrm{d}r_x & \text{if } 1 \leq \sqrt{\gamma^*\beta\left(\delta f\right)} \leq \frac{r_M}{r_m} \\ 1 & \text{if}\sqrt{\gamma^*\beta\left(\delta f\right)} \geq \frac{r_M}{r_m} \end{cases}$$

$$= \begin{cases} 0 & \text{if}\sqrt{\gamma^*\beta\left(\delta f\right)} \leq \frac{r_m}{r_M}, \\ \frac{a}{\gamma^*\beta\left(\delta f\right)} + b\gamma^*\beta\left(\delta f\right) + c & \text{if } \frac{r_m}{r_M} \leq \sqrt{\gamma^*\beta\left(\delta f\right)} \leq 1 \\ \frac{d}{\gamma^*\beta\left(\delta f\right)} + e\gamma^*\beta\left(\delta f\right) + f & \text{if } 1 \leq \sqrt{\gamma^*\beta\left(\delta f\right)} \leq \frac{r_M}{r_m} \\ 1 & \text{if}\sqrt{\gamma^*\beta\left(\delta f\right)} \geq \frac{r_M}{r_m} \end{cases}$$

with the following constants :

$$a = \frac{{r_m}^4}{2k^4}, \qquad d = \frac{r_M^4}{2k^4} - \frac{r_m^2 r_M^2}{k^4} - \frac{r_M^2}{k^2}$$

$$b = \frac{{r_M}^4}{2k^4}, \qquad e = -\frac{r_m^4}{2k^4}$$

$$c = -\frac{{r_M}^2{r_m}^2}{k^4}, \qquad f = \frac{r_m^4}{k^4} + \frac{r_M^2}{k^2}$$

This conditional probability segmented in 4 cases is plotted in Fig. 4.3. Each case is plotted with a different color. We can not see the first curve in cyan because it equals to 0 whatever δf is. We can observe that the red line which represents eq.(4.20), is actually composed by different parts of the 4 curves according to the value of δf. the calculation of eq.(4.20) is thus very tricky because of the complex segmentations, as well as all the range bounds and conditions to follow. In order to make sure that we do not make mistakes in the calculations, we have run simulations (the red points) on Matlab. As the red line and red points coincide perfectly, we can prove the accuracy of our theoretical analysis of eq.(4.20).

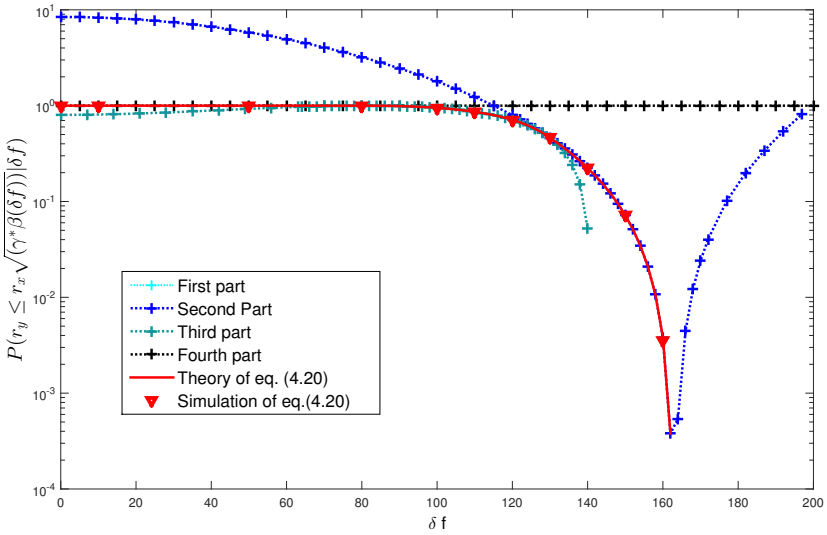

FIGURE 4.3: Validation of eq.(4.20), and its segmentation in the four parts of the conditional probability $\mathbb{P}\left(r_y \leq r_x\sqrt{\gamma^*\beta\left(\delta f\right)}|\delta f\right)$, depending on different values of frequency spacing δf, with $\gamma^* = 10$ dB, $B = 12$ kHz, $r_m = 30$ m, and $r_M = 60$ m.

Similar to the case *OP for a given* r_x, the outage probability is then computed by integrating on δf as following :

$$\begin{aligned}
\mathrm{OP} &= \int_0^B \mathbb{P}\left(r_y \leq r_x\sqrt{\gamma^*\beta\left(\delta f\right)}|\delta f\right)\mathbb{P}\left(\delta f\right)\,\mathrm{d}\delta f \\
&= 0 + \int_{b_2}^{b_1}\left(\frac{a}{\gamma^*\beta\left(\delta f\right)} + b\gamma^*\beta\left(\delta f\right) + c\right)\mathbb{P}\left(\delta f\right)\,\mathrm{d}\delta f \\
&\quad + \int_{b_3}^{b_2}\left(\frac{d}{\gamma^*\beta\left(\delta f\right)} + e\gamma^*\beta\left(\delta f\right) + f\right)\mathbb{P}\left(\delta f\right)\,\mathrm{d}\delta f \\
&\quad + \int_{b_4}^{b_3} 1 * \mathbb{P}\left(\delta f\right)\,\mathrm{d}\delta f
\end{aligned} \tag{4.21}$$

with

$$b_1 = min\left(\beta^{-1}\left(\left(\frac{r_M}{r_m}\right)^2\frac{1}{\gamma^*}\right), B\right) \qquad b_2 = min\left(\beta^{-1}\left(\frac{1}{\gamma^*}\right), B\right)$$

$$b_3 = min\left(\beta^{-1}\left(\left(\frac{r_M}{r_m}\right)^2\frac{1}{\gamma^*}\right), B\right) \qquad b_4 = 0$$

One may note that $\beta\left(\delta f\right) \in [0,1]$. Thus, b_3 exists only if $\left(\frac{r_M}{r_m}\right)^2 \leq \gamma^*$. If not, b_3 would be null, and the last term of integral would be null too.

Similarly, we can extend eq.(4.21) to N users case.

We remark that the expression of OP for both cases are related to: N, B, γ^*. The difference is that *OP for a given* r_x is directly related to the distance of the desired node r_x, where we treat it as a known parameter. Whereas the expression of *OP for average* r_x is related to the range of the cell $[r_m, r_M]$. The first one can

give us the network performance at one specific distance, which can help in positioning some important nodes. The latter provides a global view of performance through the whole cell.

We note that the OP used for the comparison in Sections 4.4-4.5 is the *OP for a given* r_x, in order to keep an homogeneity with Section 4.3.2 (where we can not find tractable expression for average r_x). The numerical validation and exploitation results of *OP for average* r_x (the N users' extension of eq.(4.21)) can be found in Appendix A.

4.3.2 Joint Impact of Path-loss, Rayleigh fading and approximated rectangular model

In this section, we derive the OP for a more complex channel model. In addition to the geometric path-loss, Rayleigh fading and noise are considered. Different from Section 4.3.1 where we consider a unique interferer at each collision, we consider the aggregated interference power (AIP) in this section. However, to obtain tractable expressions, the spectral interference coefficient $\beta(\delta f)$ is now described by the rectangular model (e.g. green, red and blue curves in Fig. 4.2) as presented in eq.(4.6). The expression of $\beta(\delta f)$ becomes less complex when using the rectangular model. The limitation is that, as we can see in Fig. 4.2, the rectangular models can not reflect all the details of the realistic model.

The SINR expression exploited in this section is given by:

$$\text{SINR} = \frac{g_x \cdot r_x^{-\alpha} \cdot P_0'}{P_I + W} \tag{4.22}$$

where W is the filtered additive white Gaussian noise power.

Accordingly, for any node x located at r_x from the BS, OP can be written as:

$$\text{OP} = \mathbb{P}\left(g_x \leq \frac{\gamma^* (W + P_I)}{r_x^{-\alpha} \cdot P_0'}\right) \tag{4.23}$$

Since the AIP (Aggregated Interference Power) P_I is itself a random variable, this probability can be expressed as follows:

$$\text{OP} = \mathbb{E}_{P_I}\left[\mathbb{P}\left(g_x \leq \frac{\gamma^* (W + P_I)}{r_x^{-\alpha} \cdot P_0'} \middle| P_I\right)\right] \tag{4.24}$$

where $\mathbb{E}_{P_I}$ stands for the expected value of the random variable P_I, in probability theory [112].

As g_x represents the coefficient of Rayleigh fading which follows an exponential distribution of unitary mean $g_x \sim exp(1)$, we can use its CDF (Cumulative distribution function), and obtain:

$$\begin{aligned} \text{OP} &= 1 - \mathbb{E}_{P_I}\left[\exp\left(-\frac{\gamma^* (W + P_I)}{r_x^{-\alpha} \cdot P_0'}\right)\right] \\ &= 1 - \exp\left(\frac{-\gamma^* W}{r_x^{-\alpha} \cdot P_0'}\right) \cdot \mathbb{E}_{P_I}\left[\exp\left(-\frac{\gamma^* P_I}{r_x^{-\alpha} \cdot P_0'}\right)\right] \\ &= 1 - \exp\left(-W \cdot s\right) \cdot \mathbb{E}_{P_I}\left[\exp\left(-P_I \cdot s\right)\right] \end{aligned} \tag{4.25}$$

where $s = \frac{\gamma^*}{r_x^{-\alpha} \cdot P_0'}$.

The second term is nothing but the Laplace transform of the AIP's probability density function (PDF) [14]:

$$\mathcal{L}_{P_I}(s) = \mathbb{E}_{P_I}\left[\exp\left(-P_I \cdot s\right)\right]. \tag{4.26}$$

Then, eq.(4.25) can be rewritten as:

$$\mathrm{OP} = 1 - \exp\left(-W \cdot s\right) \cdot \mathcal{L}_{P_I}(s) \tag{4.27}$$

which establishes the relation between OP and the Laplace transform of the AIP's PDF. It is worth noting that this relation holds because the Rayleigh fading has been considered.

Laplace transform of AIP

This section aims at deriving an analytical expression of eq.(4.26), by following the track of existing studies on stochastic geometry for wireless networks. We provide here the steps leading to the final result.

Active nodes are distributed independently and uniformly in a circular area, with a HPPP (Homogeneous Poisson Point Process) of density λ. The Laplace transform derivation first relies on the fact that the AIP P_I is given as a sum, with respect to the active nodes of the HPPP, of a unique function :

$$P_I = \sum_{\Phi} I_y(r_y) \tag{4.28}$$

with:

$$I_y(r_y) = g_y \cdot r_y^{-\alpha} \cdot \beta\left(\delta f\right) \cdot P_0' \tag{4.29}$$

which describes the random interference contribution I_y of a non-desired node eq.(4.9). It depends on the position of the considered node r_y which is the random variable in normal spatial HPPP, and on two additional random variables $\beta\left(\delta f\right)$ and g_y.

In our case, the rejection coefficient $\beta(\delta f)$ along with g_y are not related to the node position, and are generated independently to each other. Thus $M = g_y \cdot \beta(\delta f)$ forms a spatially non correlated and homogeneous random parameter, independently of $r_y^{-\alpha}$, and acts as a mark on the HPPP.

We can now express the Laplace transform of AIP in eq.(4.26) as:

$$\begin{aligned}
\mathcal{L}_{P_I}(s) &= \mathbb{E}_{P_I}\left[\exp\left(-\sum_{y\in\{\mathcal{A}-x\}} I_y(r_y)\cdot s\right)\right] \\
&= \mathbb{E}_{P_I}\left[\prod \exp\left(-I_y(r_y)\cdot s\right)\right] \\
&\overset{(a)}{=} \exp\left(-\int_{\mathbb{R}^2}\left(1-\mathbb{E}_M\left[e^{-I_y(r_y)\cdot s}\right]\right)\lambda dr_y\right)
\end{aligned} \tag{4.30}$$

(a) comes from the PGFL (Probability Generating Functional) of a point process [113], for a function $f(x)$, we can have $\mathbb{E}\left[\prod_{x\in\Phi} f(x)\right] = \exp\left(-\lambda \int_{R^2}\left(1-f(x)\right)dx\right)$; λ is the intensity of the homogeneous point process; $M = g_y \cdot \beta(\delta f)$ represents the

random mark; and $\mathbb{R}^2$ represents the space where we selects randomly our set of active nodes.

In the context of this chapter, the points space $\mathbb{R}^2$ is the single cell bounded by $[r_m, r_M]$. We replace $I_y(r_y)$ by its definition, the Laplace transform of the AIP thus becomes:

$$\mathcal{L}_{P_I}(s) = \exp\left(-\int_0^{2\pi}\int_{r_m}^{r_M}\left(1-\mathbb{E}_{g_y,\beta(\delta f)}\left[e^{-g_y\cdot r_y^{-\alpha}\cdot\beta(\delta f)\cdot P_0'}\cdot s\right]\right)\lambda r_y dr_y d\theta\right) \quad (4.31)$$

with λ is the intensity of HPPP, as well as the node density in nodes/m^2. It is defined as the ratio between the number of simultaneously active nodes N and the surface of the cell where nodes are deployed.

According to probability theory, the moment generating function (MGF) is an alternate way to do mathematical analysis compared to PDF or CDF [114]. For any random variable X, its MGF can be seen as the expectation of the random variable e^{tX}, thus $\mathbb{E}\left[e^{tX}\right]$. The MGF of a random variable following an exponential distribution (with parameter λ), is $\mathbb{E}\left[e^{tX}\right] = \frac{\lambda}{\lambda - t}$ [96]. In our case, the fading factor $g_y \sim exp(1)$ is the exponential random variable with $\lambda = 1$. More importantly, as g_y, $\beta(\delta f)$, and r_y are mutually independent, we can consider $t = -s\cdot\beta(\delta f)\cdot r_y^{-\alpha}\cdot P_0'$. We thus obtain:

$$\mathcal{L}_{P_I}(s) = \exp\left(-2\pi\lambda\int_{r_m}^{r_M}\left(1-\mathbb{E}_{\beta(\delta f)}\left[\frac{1}{1+s\cdot\beta(\delta f)\cdot r_y^{-\alpha}\cdot P_0'}\right]\right)r_y dr_y\right) \quad (4.32)$$

We consider the rectangular model (eq.(4.6)) defined in Section 4.2.2 for $\beta(\delta f)$, the rejection factor follows a Bernoulli distribution with probability $p = \frac{2\triangle}{B}$. Thus, the expectation term in the integral part of eq.(4.32) can be rewritten as:

$$\begin{aligned}
&\mathbb{E}_{\beta(\delta f)}\left[\frac{1}{1+s\cdot\beta(\delta f)\cdot r_y^{-\alpha}\cdot P_0'}\right] \\
&= p\cdot\frac{1}{1+s\cdot I_{max}\cdot r_y^{-\alpha}\cdot P_0'} + (1-p)\cdot\frac{1}{1+s\cdot I_{min}\cdot r_y^{-\alpha}\cdot P_0'} \\
&= p\cdot\frac{1}{1+s\cdot b\cdot r_y^{-\alpha}} + (1-p)\cdot\frac{1}{1+s\cdot c\cdot r_y^{-\alpha}}
\end{aligned} \quad (4.33)$$

where b and c are respectively defined by $b = I_{max}\cdot P_0'$ and $c = I_{min}\cdot P_0'$, and $s = \frac{\gamma^*}{r_x^{-\alpha}\cdot P_0'}$. Combining eq.(4.32) and eq.(4.33), the Laplace distribution of the aggregated interference can be derived as:

$$\begin{aligned}\mathcal{L}_{P_I}(s) &= \exp\left(-2\pi\lambda \int_{r_m}^{r_M} \left(1 - \frac{p}{1+s\cdot b\cdot r_y^{-\alpha}} - \frac{1-p}{1+s\cdot c\cdot r_y^{-\alpha}}\right) r_y dr_y \right) \\ &= \exp\left(-2\pi\lambda \left(\underbrace{\int_{r_m}^{r_M} r_y dr_y}_{A} - \underbrace{\int_{r_m}^{r_M} \frac{p}{1+s\cdot b\cdot r_y^{-\alpha}} r_y dr_y}_{B(s)} \right.\right. \\ &\quad \left.\left. - \underbrace{\int_{r_m}^{r_M} \frac{1-p}{1+s\cdot c\cdot r_y^{-\alpha}} r_y dr_y}_{C(s)} \right) \right) \end{aligned} \tag{4.34}$$

The integral A can be analytically computed and expressed as below:

$$A = \int_{r_m}^{r_M} r_y dr_y = \frac{r_M^2 - r_m^2}{2} \tag{4.35}$$

OP final expression

By using eq.(4.34) and eq.(4.27), we can compute OP, for any desired node x positioned at distance r_x from the base-station, and involving the path-loss and Rayleigh fading effect:

$$\begin{aligned}\text{OP} &= 1 - \exp\left(-W\cdot s\right)\cdot \mathcal{L}_{P_I}\left(s\right) \\ &= 1 - \exp\left(-W\cdot s\right)\cdot \exp\Big(-2\pi\lambda \left(A - B\left(s\right) - C\left(s\right)\right) \Big)\end{aligned} \tag{4.36}$$

with the constants A, $B\left(s\right)$ and $C\left(s\right)$ as shown in eq.(4.34).

One may note that $B\left(s\right)$ and $C\left(s\right)$ can not be analytically expressed for the general case, but are numerically computable. Nonetheless, for specific value of the path-loss exponent α, the theoretical integration is possible. We present in the next part the expressions of OP for two cases of interest: $\alpha = 2$ (free space propagation), and $\alpha = 4$ (relatively lossy environments and for the case of full specular reflection from the earth surface).

OP for free space $\alpha = 2$

When $\alpha = 2$, we can compute $B\left(s\right)$ and $C\left(s\right)$:

$$B\left(s\right) = \int_{r_m}^{r_M} \frac{p}{1+s\cdot b\cdot r_y^{-2}} r_y dr_y = \frac{p}{2}\left(r_M^2 - r_m^2\right) + \frac{p}{2}\cdot s\cdot b\cdot \ln\left(r_M^2 - r_m^2\right) \tag{4.37}$$

$$C\left(s\right) = \int_{r_m}^{r_M} \frac{1-p}{1+s\cdot c\cdot r_y^{-2}} r_y dr_y = \frac{1-p}{2}\left(r_M^2 - r_m^2\right) + \frac{1-p}{2}\cdot s\cdot c\cdot \ln\left(r_M^2 - r_m^2\right) \tag{4.38}$$

Combining with A eq.(4.35), we can have the Laplace function of AIP as:

$$\mathcal{L}_{P_I}(s) = \left(\frac{r_m^2 + sb}{r_M^2 + sb}\right)^{\pi\lambda psb} \cdot \left(\frac{r_m^2 + sc}{r_M^2 + sc}\right)^{\pi\lambda(1-p)sc} \tag{4.39}$$

Then, OP can be obtained as:

$$\begin{aligned} \mathrm{OP} &= 1 - \exp\left(-s \cdot W\right) \cdot \mathcal{L}_{P_I}\left(s\right) \\ &= 1 - \exp\left(-s \cdot W\right) \cdot \left(\frac{r_m^2 + sb}{r_M^2 + sb}\right)^{\pi\lambda psb} \cdot \left(\frac{r_m^2 + sc}{r_M^2 + sc}\right)^{\pi\lambda(1-p)sc} \end{aligned} \tag{4.40}$$

with $s = \dfrac{\gamma^*}{r_x^{-2} \cdot P_0'}$.

OP for flat earth model $\alpha = 4$

Similarly, when $\alpha = 4$, we can compute $B\left(s\right)$ and $C\left(s\right)$ as shown below:

$$\begin{aligned} B\left(s\right) &= \int_{r_m}^{r_M} \frac{p}{1 + s \cdot b \cdot r_y^{-4}} r_y dr_y \\ &= \frac{p}{2}\left(r_M^2 - r_m^2\right) + \frac{p}{2} \cdot \sqrt{sb} \cdot \arctan\left(\frac{r_m^2\sqrt{sb} - r_M^2\sqrt{sb}}{sb + r_M^2 r_m^2}\right) \end{aligned} \tag{4.41}$$

$$\begin{aligned} C\left(s\right) &= \int_{r_m}^{r_M} \frac{1-p}{1 + s \cdot c \cdot r_y^{-4}} r_y dr_y \\ &= \frac{1-p}{2}\left(r_M^2 - r_m^2\right) + \frac{1-p}{2} \cdot \sqrt{sc} \cdot \arctan\left(\frac{r_m^2\sqrt{sc} - r_M^2\sqrt{sc}}{sc + r_M^2 r_m^2}\right) \end{aligned} \tag{4.42}$$

Combining with A eq.(4.35), we can derive the Laplace function of AIP as:

$$\begin{aligned} \mathcal{L}_{P_I}(s) = \exp\Bigg(&\pi\lambda p \cdot \sqrt{sb} \cdot \arctan\left(\frac{r_m^2\sqrt{sb} - r_M^2\sqrt{sb}}{sb + r_M^2 r_m^2}\right) \\ &+ \pi\lambda\left(1-p\right) \cdot \sqrt{sc} \cdot \arctan\left(\frac{r_m^2\sqrt{sc} - r_M^2\sqrt{sc}}{sc + r_M^2 r_m^2}\right)\Bigg) \end{aligned} \tag{4.43}$$

Then, OP can be expressed as:

$$\begin{aligned} \mathrm{OP} = 1 - \exp\left(s \cdot W\right) \cdot \exp\Bigg(&\pi\lambda p \cdot \sqrt{sb} \cdot \arctan\left(\frac{r_m^2\sqrt{sb} - r_M^2\sqrt{sb}}{sb + r_M^2 r_m^2}\right) \\ &+ \pi\lambda\left(1-p\right) \cdot \sqrt{sc} \cdot \arctan\left(\frac{r_m^2\sqrt{sc} - r_M^2\sqrt{sc}}{sc + r_M^2 r_m^2}\right)\Bigg) \end{aligned} \tag{4.44}$$

with $s = \dfrac{\gamma^*}{r_x^{-4} \cdot P_0'}$.

We will use this theoretical expression of OP to evaluate the network capacity in terms of maximum number of simultaneous nodes. Results are shown in the next section.

4.4 Validation

In this section, we compare simulation results of OP for a given distance r_x, to the theoretical ones: eq.(4.18) for the case with path-loss and unique interferer; eq.(4.36) for the case with jointly path-loss, Rayleigh fading and aggregated interference (AIP).

In our simulation framework, transmissions are performed with the UNB modulation technique. Binary data are broadcast with a DBPSK modulation at a very low rate ($R_b = 100$ bps). The transmitted signal thus occupies a very narrow band (i.e. about $b = 100$ Hz). Transmissions are realized at a randomly chosen carrier frequency in a much larger band B. We also target the SINR threshold as $\gamma^* = 6.8$ dB, corresponding to a bit-error-rate of 10^{-3} with a DBPSK modulation. We recall the simulations' hypothesis here:

TABLE 4.1: Simulations hypothesis for mono-BS realistic channels (*notation: wo = without.)

BS number	nodes distribution	desired node	path loss	fading	AIP	replicas
1	random	at given r_x	α	wo/with	wo/with	no

Simulations are performed with different interference rejection coefficients. We consider the real shape of the UNB interference model (black curve on Fig. 4.2), the Gaussian model (pink curve on Fig. 4.2) as well as the rectangular model. For the rectangular model, we consider three set of parameters, which correspond to an approximated rectangular model (AR, green curve on Fig. 4.2), an upper bound (UB, red curve on Fig. 4.2) and a lower bound (LB, blue curve on Fig. 4.2), whose values are:

$$\begin{aligned} AR &: \triangle = 145Hz, \quad I_{max} = 0dB, \quad I_{min} = -75dB \\ UB &: \triangle = 300Hz, \quad I_{max} = 0dB, \quad I_{min} = -47.28dB \\ LB &: \triangle = 116Hz, \quad I_{max} = -6.8dB, \quad I_{min} = -75dB \end{aligned} \tag{4.45}$$

We use the exhaustive research method to determine the AR model parameters. This AR model assures the accuracy for cases where the targeted SINR threshold is 6.8 dB and the desired node at the edge of the cell range. Indeed, we have identified that higher distances lead to a wider rectangle. Thus, $r_x = r_M$ provides the most pessimistic rectangular model over the cell. Since the AR model depends on γ^*, we introduce an UB and a LB of the rectangular model, to estimate the bounds of OP in eq.(4.36).

We present on Fig. 4.4-4.6 the comparison between simulation and theory results. OP is plotted as a function of the desired node's distance r_x, the node density λ, and the frequency resource B respectively. On all these figures, we can observe that for the no-Rayleigh fading case, realistic simulation results match well with

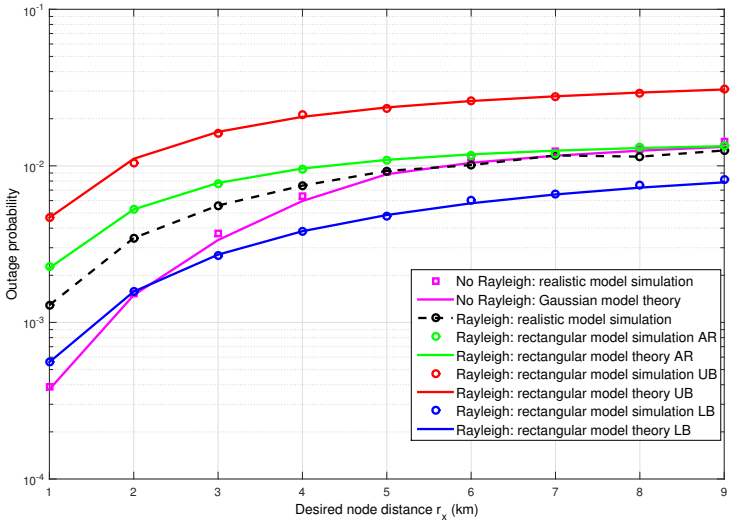

FIGURE 4.4: OP as a function of the desired node's distance r_x, for $B = 96$ kHz, $N = 6$, $r_M = 10$ km, $r_m = 1$ m, $\gamma^* = 6.8$ dB and path loss $\alpha = 2$.

Gaussian theoretical ones eq.(4.18). Besides, for Rayleigh fading case, the OP obtained with the theoretical model eq.(4.36) fits very well with the simulated results obtained with the associated rectangular model. Therefore, we can deduce that the equations eq.(4.18) and eq.(4.36), as well as the accuracy of the approximated Gaussian model, are validated.

In addition, the evolution of OP with realistic UNB filter (black dash curve) lies between the UB (red curves) and LB (blue curves). As regards the AR model (green curves), it slightly overestimates the realistic simulations, which comes from the choice of this model's parameters. Nonetheless, when r_x becomes larger, OP can be more accurately estimated by the AR model. These results all confirm the pertinent choice of the AR model, UB and LB, and the scalability of the rectangular models.

4.5 Numerical results and exploitation

4.5.1 Numerical results analysis

Aside from the validation of theoretical expressions, we can draw further conclusions from Fig. 4.4-4.6. In Fig. 4.4, we can see that OP increases when r_x increases. Indeed, when the desired node x is further from BS, its received power is more attenuated because of the path loss. This makes the desired signal more vulnerable to interferers.

Interestingly, we can observe that OP(no-Rayleigh) is lower than OP(Rayleigh) when r_x is small. But when r_x exceeds a certain distance, these two cases have identical outage probabilities (and close to the real shape simulation results). This phenomenon comes from the impacts of Rayleigh fading.

We have deduced from eq.(4.12) that if one interferer falls into an *interfering area* (whose radius depends on the received power of the desired node x), it will interrupt the desired node.

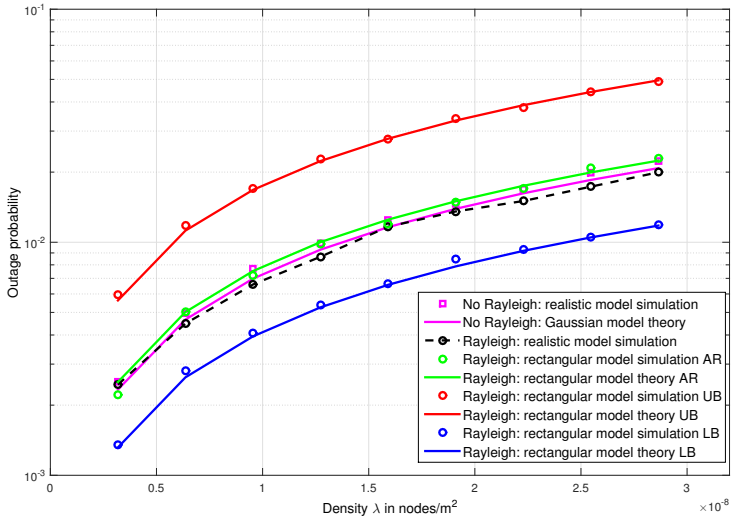

FIGURE 4.5: OP as a function of active nodes density λ, for $B = 96$ kHz, $r_x = 7$ km, $r_M = 10$ km, $r_m = 1$ m, $\gamma^* = 6.8$ dB and path loss $\alpha = 2$.

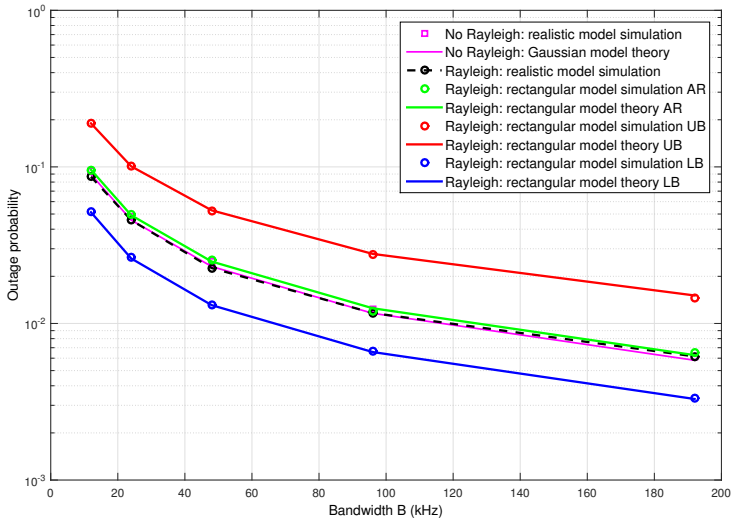

FIGURE 4.6: OP as a function of bandwidth B, for $N = 6$, $r_x = 7$ km, $r_M = 10$ km, $r_m = 1$ m, $\gamma^* = 6.8$ dB and path loss $\alpha = 2$.

Rayleigh fading can amplify or attenuate the received signal power, thus diminish or broaden the *interfering area*. If the received power of the desired node gets attenuated because of the fading, the *interfering area* becomes larger. Because the desired signal becomes vulnerable thus interferers far away from the BS can also interrupt it. Hence we have more potential interfering nodes, thus higher probability to be collided in this case. Meanwhile, if the desired node's received power gets amplified, this *interfering area* becomes smaller. Because the desired signal becomes stronger, thus interferers should be closer to the BS to be able to interrupt it, which leads to less interfering nodes. When r_x is small, the *interfering area*'s increase is much remarkable than its decrease. Thus, such a node (at small

r_x) is sensitive to fading. On the contrary, when r_x is high, the *interfering area*'s increase is bounded by the cell limit r_M, and thus the increase of potential interferers is less significant. Hence, such node (at large r_x) is barely affected by the fading. That's why when the desired node is far from BS, OP(no Rayleigh) is almost at the same level as OP(Rayleigh).

In Fig. 4.5-4.6, we have fixed the desired node's distance so that the same performance is obtained without and with Rayleigh fading. We can see that OP increases when the node density λ increases, or when the bandwidth B decreases. Indeed, as there are more nodes transmitting at the same time, or when the available transmission resource becomes less, the chance that their frequencies fall into the interfering zone gets higher. More interestingly, the gap between OP(no-Rayleigh) and OP(Rayleigh) is not influenced by λ or B. Hence eq.(4.18) can be used for high r_x cases, whereas eq.(4.36) is needed for low r_x ones.

Besides, these results have also confirmed the hypothesis in Section 4.3.1 where we have assumed one unique interferer. Indeed, OP(no Rayleigh) has considered the contribution of a unique interferer, whereas OP(Rayleigh) has considered the aggregated interference (AIP). The fact that these two OPs converge when r_x is high confirms that one interferer has almost the same contribution than AIP.

4.5.2 Estimation of the network capacity

In this section, we exploit the OP theoretical expressions to find out the maximum capacity. This parameter is defined in this study by the maximum number of active nodes N that the network can support simultaneously, while maintaining a given OP constraint. We note that this maximum node number can be obtained because the cell range is bounded. We have reported on Fig. 4.7-4.9 the capacity for a targeted OP$= 10^{-1}$, by considering the no-Rayleigh fading case eq.(4.18); and the Rayleigh fading case eq.(4.36). Capacities estimated by the UB and LB provide us the reliable range of the maximum active nodes, and the AR model provides a good estimation, though not that exact.

In Fig. 4.7, we can observe that the capacity increases almost linearly with the available bandwidth. Indeed, as B increases, we obtain a higher capacity thanks to less interference in the frequency domains. It is thus easy to scale the bandwidth in accordance to the number of nodes to serve, when keeping the same targeted OP.

In Fig. 4.8, we can note that the overall capacity decreases when r_x increases. As the desired node moves progressively away from the BS, its received signal gets strongly attenuated. Hence, in order to successfully detect the desired node, the maximum node number has to be degraded.

Similarly, in Fig. 4.9, we vary the cell radius r_M. As the cell size increases, the overall capacity increases. Indeed, when the cell surface becomes larger, by keeping r_x unchanged, the desired node is perceived closer to BS than other nodes. This makes the desired node's signal more resistant to interference, thus easier to be detected. Therefore, the maximum node number increases for the targeted OP.

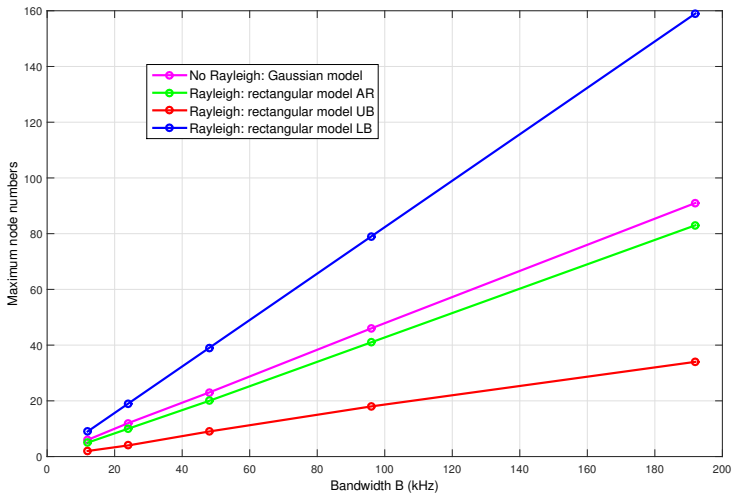

FIGURE 4.7: Maximum node number vs bandwidth B, for targeted $OP = 0.1$, $r_x = 7$ km, $r_M = 10$ km, $r_m = 1$ m, $\gamma^* = 6.8$ dB and path loss $\alpha = 2$.

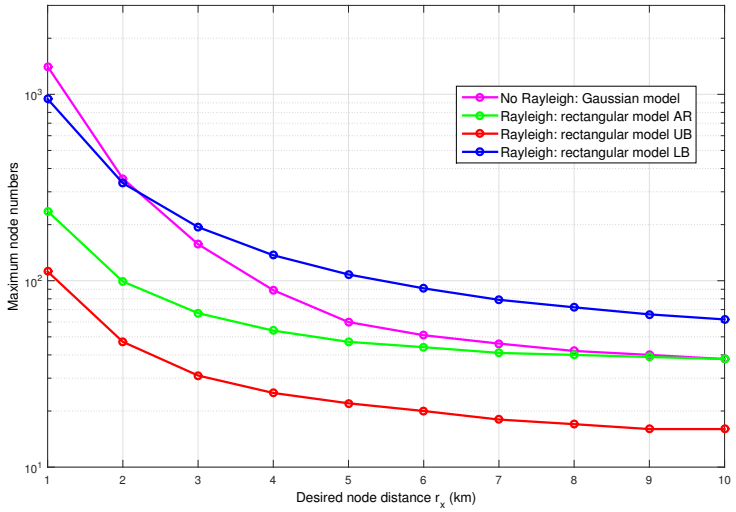

FIGURE 4.8: Maximum node number vs desired node distance r_x, for targeted $OP = 0.1$, $B = 96$ kHz, $r_M = 10$ km, $r_m = 1$ m, $\gamma^* = 6.8$ dB and path loss $\alpha = 2$.

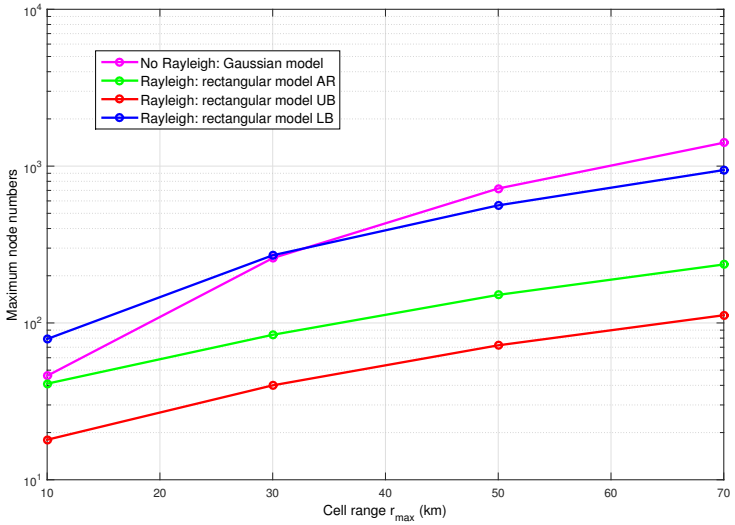

FIGURE 4.9: Maximum node number vs cell range r_M, for targeted $OP = 0.1$, $B = 96$ kHz, $r_x = 7$ km, $r_m = 1$ m, $\gamma^* = 6.8$ dB and path loss $\alpha = 2$.

4.5.3 Evaluation of the Spectral Efficiency

Finally, for a fairer comparison of the effective use of the bandwidth, we consider now the spectral efficiency. This term is determined as the ratio of the maximum node number and the bandwidth $\frac{N_{max}}{B}$.

We compare the spectral efficiency in two cases: without and with a guard band, for different values of α, as shown in Fig. 4.10-4.11. The *without guard band* corresponds to the ideal case, where the nodes' carrier frequencies can be obtained, by random selection on the whole frequency resource B. However, in realistic UNB networks, the oscillator jitter causes imprecise carrier positions, which can cause the carrier frequencies jumping outside of B. Therefore, the frequency resource band B should be separated by a guard interval, which must be taken into account in the spectral efficiency. We consider here a 1736 Hz guard band, which corresponds to the operating frequency transmission 868 MHz and standard deviation of frequency jitter of 2 ppm. This allows to ensure that no actual carrier frequency would fall outside the intended band.

We choose the AR model to study the spectral efficiency, when varying the path loss exponents. By observing Fig. 4.10, we can note that for small bandwidth such as $B = 12$ kHz, the spectral efficiency is highly degraded by the guard band. This is due to the fact that a big portion of the band is wasted for the guard band to counteract the frequency jitter. Meanwhile, the impact of guard band diminishes as B increases. Hence for the large band width, the spectral efficiency seems the same for both cases (e.x. the green ones).

More interestingly, for each B, there exists a highest spectral efficiency obtained with an optimal α. This is because when α increases, the received signal power of both the desired node and interfering nodes diminishes. In the first part of the curves, as the desired node is near to the BS, this decrease of power is more important for interfering nodes which can be anywhere in the cell. Meanwhile,

in the second part, when α exceeds a certain value, the power reduction is so severe that the desired node has no more advantage. Thus N_{max} first increases then decreases.

However, by observing Fig. 4.11, we note that this concave behavior is smoothened when r_x is closer to r_M. Indeed, when the desired node is almost at the edge of the cell, it is disadvantageous compared to all the interfering nodes. Hence the more α grows, the more the spectral efficiency degrades.

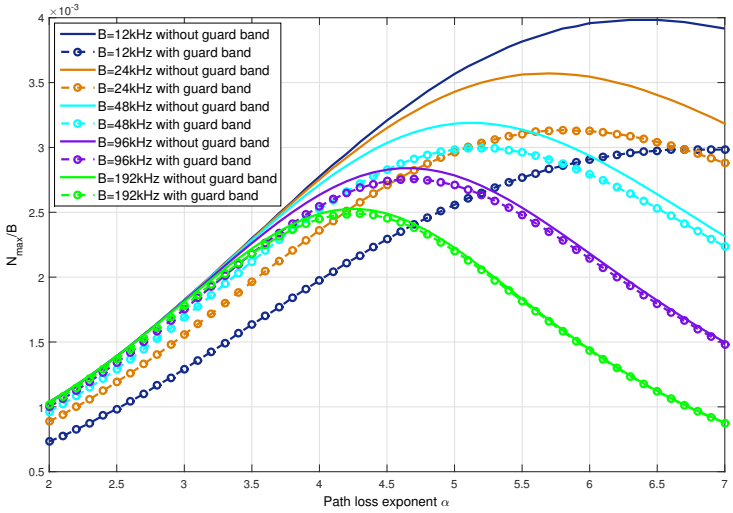

FIGURE 4.10: Maximum node number to bandwidth ratio $\frac{N_{max}}{B}$ (nodes/Hz) vs exponent path-loss α, for $r_M = 10$ km, $r_x = 2$ km, $r_m = 1$ m, $\gamma^* = 6.8$ dB, with and without guard band

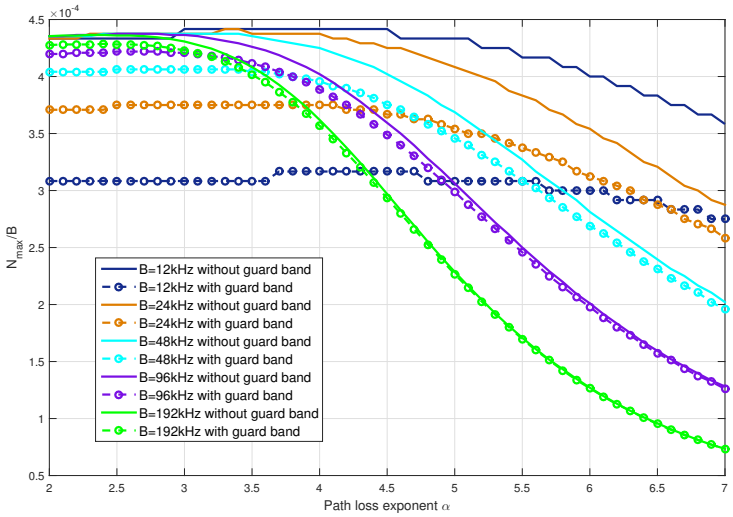

FIGURE 4.11: Maximum node number to bandwidth ratio $\frac{N_{max}}{B}$ (nodes/Hz) vs exponent path-loss α, for $r_M = 10$ km, $r_x = 7$ km, $r_m = 1$ m, $\gamma^* = 6.8$ dB, with and without guard band

Following the previous observation, we have plotted in Fig. 4.12 the optimal

bandwidth B (for the guard band case) to achieve the highest ratio $\frac{N_{max}}{B}$, as a function of the path loss exponent α. This figure provides the optimal choice for B, according to the propagation characteristics. We observe that for urban areas such as $\alpha = 4$, we need a thiner bandwidth than for rural areas to reach the highest spectral efficiency. Hence it also allows us to make effective use of the available bandwidth.

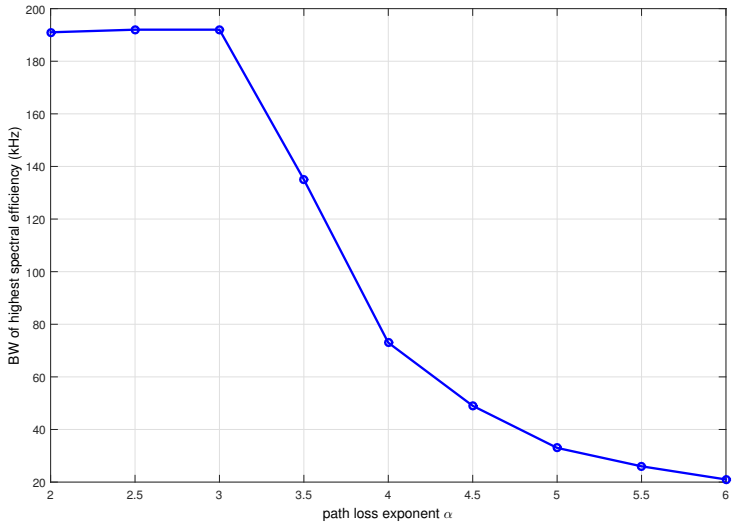

FIGURE 4.12: Bandwidth for highest spectral efficiency ($\frac{N_{max}}{B}$) vs exponent path-loss α, for $r_M = 10$ km, $r_x = 2$ km, $r_m = 1$ m, $\gamma^* = 6.8$ dB, with guard band

4.6 Conclusion

In this chapter, we have studied the UNB network, whose main specificity is the use of Random-FTMA scheme, which leads to a new behavior of the interference. We have considered two models to approximate the interference coefficient: Gaussian model which reflects almost all the details of the realistic one; and rectangular model which facilitates the theoretical analysis. With these two models, we have quantified the performance of the UNB network, in terms of uplink network capacity, when considering realistic channel conditions (path-loss and Rayleigh fading).

In the first case, we have consider only the path-loss in free space propagation (where $\alpha = 2$), and the interference contribution due to a unique interferer. The Gaussian model is used in this case. We have theoretically derived the outage probability (OP) for the case where the desired node situates at a given distance r_x, and then extended it to the case where the desired node can be anywhere in the cell (i.e. at average distance). The former gives us the performance of at one specific distance, which helps in positioning devices having critical demands (e.x. its OP should be under 10^{-6}). The latter gives us a global insight of the whole cell's performance.

In the second case, we have taken into account the Rayleigh fading and the aggregated interference of all the potential interfering node, in addition to the path-loss α which is no more restraint to 2. The rectangular model is used. We

have defined three set of rectangular models in order to have a complete point of view: the approximated one (AR), the upper bound (UB), and the lower bound (LB). The nodes' distribution follows homogeneous PPP, we have thus treated the random variables (i.e. the fading and the frequency spacing) as a mark on the HPPP. We have provided the expression of analytical OP, by deriving the Laplace transform of the aggregated interference in closed form when using the properties of marked HPPP.

We have then compared the two theoretical OP expressions (for given distance of desired node) with the simulations. The results have showed that the theoretical OP obtained by both models conform well to the ones obtained by simulations. We have observed classical network behaviors: the network performance degrades when the traffic is too loaded, or when the frequency resource is too limited, or when the desired node is too far away from the base station. Besides, we have remarked interesting phenomena: the impact of fading diminishes when the desired node moves away from the BSs, and the OP(no-Rayleigh) has identical performance than OP(Rayleigh) when the desired node positions near the cell edge.

Moreover, we have then exploited the analytical expressions to estimate network capacity, with respect to the maximum simultaneous number of nodes that the network can support, for a targeted OP. We have noted that the capacity increases when the cell range increases (while keeping the desired node's position unchanged), or when the desired node moves towards the BS (because it becomes less vulnerable), or when the the frequency resource becomes larger (thus the nodes have less chance to collide).

Finally, we have evaluated the spectral efficiency as a function of the path-loss exponent, for without and with guard bands. We have observed that the guard bands degrades vastly the spectral efficiency when the resource B is limited, and this is improved when the resource becomes larger. We have also remarked that when the desired node is close to the BS, the variation of spectral efficiency is concave as a function of α. And this phenomenon is smoothened when the desired node is further. We have highlighted that the bandwidth which achieves the highest spectral efficiency depends on the propagation condition, which can help us to make efficient use of the available bandwidth.

To conclude, we believe that this theoretical work is very useful for the study of UNB network capacity and its deployment. This study can be furthered by taking into account the temporal activity rate of the nodes. It can also serve as a theoretical basis for further studies such as multiple receivers.

Chapter 5

Mono-BS performance enhancement: SIC

Contents

Now that we have characterized the UNB networks capacity in the two previous chapters, we have clear awareness of what affects the performance: the uncontrolled interference cause by the time-frequency randomness can notably affect the networks' reliability.

In this chapter, we focus on the enhancement of the UNB networks' performance from the single base station's side. We propose to use the well-known SIC (Successive Interference Cancellation) to mitigate the spectral interference of UNB systems in a recursive way. We provide a theoretical analysis of the outage probability, when considering jointly SIC and the specific spectral randomness of UNB. We consider realistic channel conditions with path-loss (without fading), and we exploit the expression of outage probability derived in Section 4.3.1 where we have made the same hypothesis with a simple receiver. Then we numerically compare the performance of SIC for without and with the involvement of Rayleigh fading. We highlight that the fading brings an additional degree of freedom, which improves the performance of SIC.

5.1 Introduction

The dedicated multiple access of UNB is R-FTMA, where the nodes access both the temporal and spectral resources randomly, as presented in Section 2.3.2. The

interference caused by this randomness can significantly affect the networks performance. In Sigfox's networks, in order to keep the advantageous solutions of low-cost and low energy consumption, it is hard to control the interference at the transmitters' (devices) side. We thus focus on the interference mitigation at the BS (Base Station) side in this chapter.

Among the IC (Interference Cancellation) technologies, we can first cite PIC (Parallel Interference Cancellation). PIC processes simultaneously all the users and cancels their interference after they have all been independently decoded. However, PIC is considered unprofitable for massive practical implementations, as it demands precious hardwares [115].

SIC (Successive Interference Cancellation) is another IC technology, which attempts to remove the interference in a recursive way [116, 117], by exploiting the diversity of the received signals strength. Certainly, SIC can only bring benefits if only the signals have different levels of strength, thus not in perfect power control systems.

SIC is expected to be the most efficient IC-based methodology in terms of Bit-Error-Rate performance. Nevertheless, as the accuracy and robustness demand increases, the complexity of iterative detection and decoding process grows too. Hence there is a trade-off between the performance of SIC and its complexity [118]. SIC was proved to be highly beneficial when low-rate codes are used [15]. We thus consider SIC in this chapter.

More recently, the authors in [16] have considered SIC receiver to improve IoT networks performance. A normalized theoretical analysis of the capture probability by considering the MPR (Multiple Packet Reception) and SIC is presented. Different channel models, such as path loss, general fading and shadowing are considered. This study confirms the adequacy of the SIC to IoT. However, the interference model refers only to the aggregated power of interferers' contribution when the same channel is used. In a UNB system, as nodes select their frequency randomly in a continuous space, overlaps of signals can generate interference with an additional degree of freedom. Indeed, in UNB network, the interference also depends on the frequency spacing of potential interferers. For this reason, we cannot directly derive the UNB performances from this generalized analysis.

Therefore, in this chapter, we propose to analyze the SIC benefits in a UNB network. We exploit the results presented in Section 4.3.1, which characterizes analytically the performance of UNB with a simple receiver when considering both the path-loss and the spectrum random access.

The rest of this chapter is organized as follows : Section 5.2 gives the modeling and hypothesis. Section 5.3 provides the theoretical analysis of the performance without and with SIC. The numerical results and the validation of theory are given in Section 5.4, then Section 5.6 concludes.

5.2 Modeling and Assumptions

The network topology and hypothesis are exactly the same as those in Section 4.3.1. We consider a network with a single BS located at the cell center. The BS is supposed to be constantly in reception state. Nodes (devices) are positioned randomly and uniformly in a disk area, defined by the radius $[r_m, r_M]$. r_m corresponds to an exclusion area around the BS where no node is deployed. Thus, free space

propagation model can be used without having the path loss being ∞ when the distance tends to 0.

We suppose that all nodes have the same behavior: the information packets have the same size, are sent with the same emission power and antenna gain, and nodes have the same wake-up duty cycle. The channel condition is realistic where we consider the frees space path-loss (no fading is involved). Since nodes have various positions, their received power at the BS differs because of the path-loss.

We focus on the contribution of a unique interferer as it is the most frequent case [12]. We suppose that the desired node transmits at frequency f_x, and the potential interfering node at frequency f_y. The main parameter is their frequency spacing $\delta f = |f_x - f_y|$, which determines the interference contribution of each interfering node. When two nodes choose their frequency close enough, interference generated would cause packet losses.

We use the Gaussian interference coefficient as presented in Section 4.2.2, which estimates perfectly the interference coefficient compared to the realistic one in Sigfox's network:

$$\beta(\delta f) = \frac{150}{\sigma\sqrt{2\pi}} \exp^{\frac{-\delta f^2}{2\sigma^2}} \tag{5.1}$$

with $\sigma = 60$ for a 100 bit/s transmission.

5.3 Theoretical Analysis

In this section, we derive the outage probability (OP) of UNB systems with SIC receiver. We focus on the $OPforaverage\ r_x$ case where the desired node can be anywhere. Even if this brings more complexity in the computation, it is still more representative for all nodes at different distances in a cell. We firstly recall some principle steps of $OPforaverage\ r_x$ derivation in Section 4.3.1, then we exploit and extend it to the case with SIC receiver. We neglect the noise in this chapter, thus SIR (rather than SINR) is used to decide whether one packet is lost.

5.3.1 Preliminary: OP derivation without SIC

In Section 4.3.1, we have derived the OP for a simple receiver, when considering both the spectral randomness and path-loss. We report here the main derivation steps as a basis for adapting to the SIC case in Section 5.3.2.

We consider the case where there are only two nodes (node x as the desired node and node y as the interfering one) at the observed moment. The OP of the desired node x can be written as:

$$\mathrm{OP} = \mathbb{P}\left(SIR_x \leq \gamma^*\right) \tag{5.2}$$

We suppose that node x (resp. node y) is at a distance of r_x (resp. r_y). P_0 is the signal power at the reference distance r_0. With a free space propagation model (the path-loss coefficient is 2), the SIR of the desired node is:

$$SIR_x = \frac{P_0\left(\frac{r_0}{r_x}\right)^2}{P_0\left(\frac{r_0}{r_y}\right)^2 \beta(\delta f)} = \left(\frac{r_y}{r_x}\right)^2 \frac{1}{\beta(\delta f)} \tag{5.3}$$

Consequently, (5.2) can also be expressed as:

$$\mathrm{OP} = \mathbb{P}\left(r_y \leq r_x\sqrt{\gamma^*\beta\left(\delta f\right)}\right) \tag{5.4}$$

According to the law of total probability, we split eq.(5.4) depending on the value of $\sqrt{\gamma^*\beta\left(\delta f\right)}$, conditionally to δf. We obtain an expression depending on several parameters: the total available bandwidth B, the SIR threshold γ^*, and the range of the area $[r_m, r_M]$:

$$\begin{aligned}
\mathrm{OP} &= \int_0^B \mathbb{P}\left(r_y \leq r_x\sqrt{\gamma^*\beta\left(\delta f\right)}|\delta f\right)\cdot\mathbb{P}\left(\delta f\right)\,\mathrm{d}\delta f \\
&= \int_{b_2}^{b_1}\left(\frac{a}{\gamma^*\beta\left(\delta f\right)} + b\gamma^*\beta\left(\delta f\right) + c\right)\cdot\mathbb{P}\left(\delta f\right)\,\mathrm{d}\delta f \\
&\quad + \int_{b_3}^{b_2}\left(\frac{d}{\gamma^*\beta\left(\delta f\right)} + e\gamma^*\beta\left(\delta f\right) + f\right)\cdot P\left(\delta f\right)\,\mathrm{d}\delta f \\
&\quad + \int_{b_4}^{b_3} 1\cdot\mathbb{P}\left(\delta f\right)\,\mathrm{d}\delta f
\end{aligned} \tag{5.5}$$

with the following constants:

$$\begin{aligned}
a &= \frac{{r_m}^4}{2k^4}, & d &= \frac{r_M^4}{2k^4} - \frac{r_m^2 r_M^2}{k^4} - \frac{r_M^2}{k^2} \\
b &= \frac{{r_M}^4}{2k^4}, & e &= -\frac{r_m^4}{2k^4} \\
c &= -\frac{r_M^2 r_m^2}{k^4}, & f &= \frac{r_m^4}{k^4} + \frac{r_M^2}{k^2}
\end{aligned}$$

where $k^2 = r_M^2 - r_m^2$;

and with the following integral edges: $b_1 = min\left(\beta^{-1}\left(\left(\frac{r_m}{r_M}\right)^2\frac{1}{\gamma^*}\right), B\right)$, $b_2 = min\left(\beta^{-1}\left(\frac{1}{\gamma^*}\right), B\right)$ $b_3 = min\left(\beta^{-1}\left(\left(\frac{r_M}{r_m}\right)^2\frac{1}{\gamma^*}\right), B\right)$, and $b_4 = 0$;

and where $P\left(\delta f\right)$ which represents the probability distribution function of $\delta f = \left|f_x - f_y\right|$. As the carrier frequency of the two nodes are randomly and independently chosen in $[0, B]$, we have:

$$\mathbb{P}\left(\delta f\right) = \begin{cases} \frac{2}{B}\left(1 - \frac{\delta f}{B}\right) & \text{for } \delta f \in [0, B] \\ 0 & \text{elsewhere} \end{cases} \tag{5.6}$$

The final expression of OP without SIC eq.(5.5) will be explored and extended to derive the OP with SIC in the following part.

5.3.2 OP derivation with SIC

In this section, we consider that the BS uses a SIC receiver to extract additional packets. The network behavior and the assumptions remain the same.

The principle of SIC is to successively decode packets contained in the received signal. Its process begins after the simple receiver's process. Suppose that the BS simultaneously receives, for example l packets, which are all in collision. With a simple receiver, only the packet having the highest SIR (or received power, depending on the measure criteria) can be correctly decoded, as long as its SIR is above the required threshold. Meanwhile, with SIC, the knowledge on this packet can be exploited to reconstruct the interfering signal. Then the SIC receiver subtracts the reconstructed signal from the sum of received signals. The SIC receiver performs the decoding on the remaining $l - 1$ packets. The process of reconstruction, retriever and decoding consists one iteration of SIC. The process goes on iteratively until the packet with the highest SIR doesn't fulfill the criteria for successful decoding.

As illustrated in Fig. 5.1, the *iteration 0* represents the simple receiver's process, and the SIC receiver begins from the *iteration 1*. The simple receiver is able to decode singleton signal (i.e. the packets 4, 7 on the scheme), or the strongest signal when in collisions (i.e. the packets 1, 9). Based on the signals decoded by the simple receiver, the SIC receiver reconstruct them and retrieve their contributions, thus now packet 2 and 8 become decodable. SIC process its first iteration, and we can have two more packets (i.e. packet 2 and 8) decoded compared to simple receiver. We can note that the packet 5 and 6 are not decodable by neither the simple receiver nor the SIC receiver. The reason may come from the fact that their received power are already very low, thus their mutual interference renders very low SIR. Since their SIR never surpass the predefined threshold, packet 5 and 6 remain undecodable.

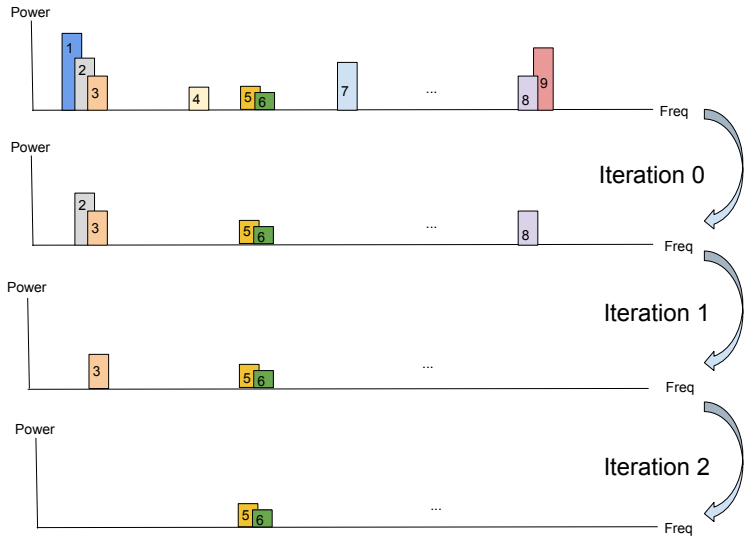

FIGURE 5.1: SIC process scheme. The packets are positioned at different carrier frequencies, and they have different levels of received power. The *iteration 0* represents the simple receiver's process, and the SIC receiver begins from the *iteration 1*.

We evaluate the SIC performance by focusing on the first iteration of SIC (i.e. the *1 iteration*), as we make the assumption that there is only one interferer at each collision. The case where a collision is caused by the aggregation of several interferers is still neglected. Besides, since we neglect the noise, one singleton

packet can always be decoded even its received power is very low (i.e. the packet 4 on the Fig. 5.1), because its SIR tends to be very high when there is no interference. Thus the errors come from the packets that can not be decoded by the simple receiver, such as packets 5 and 6 on Fig. 5.1.

We further suppose that the SIC receiver can perfectly reconstruct decoded signals, and subtract them from the received signals without leaving residues. Hence, when two nodes are interfering each other, once one of them is successfully decoded, the other one will also be decoded thanks to the SIC.

To derive the outage probability, we identify two scenarios where the packet transmitted by the node x can be decoded: (1) when node x is directly decoded by the BS, as its SIR is high enough; (2) when node x is not decoded in the first place, but the interfering node y is: thanks to the SIC receiver, node x can then be decoded. Hence the success probability of the desired node can be expressed as:

$$\mathbb{P}_s = \mathbb{P}\left(SIR_x > \gamma^*\right) + \mathbb{P}\left(SIR_x \leq \gamma^* \cap SIR_y > \gamma^*\right) \tag{5.7}$$

Thus the OP becomes:

$$\begin{aligned} \mathrm{OP}_{SIC} &= 1 - \mathbb{P}_s \\ &= 1 - \left(\mathbb{P}\left(SIR_x > \gamma^*\right) + \mathbb{P}\left(SIR_x \leq \gamma^* \cap SIR_y > \gamma^*\right) \right) \\ &= \mathbb{P}\left(SIR_x \leq \gamma^*\right) - \mathbb{P}\left(SIR_x \leq \gamma^* \cap SIR_y > \gamma^*\right) \end{aligned} \tag{5.8}$$

The first part ($\mathbb{P}\left(SIR_x \leq \gamma^*\right)$) is already available in Section 5.3.1. As the SIR of node x and node y depend on the same frequency difference δf, their related probabilities are correlated. Therefore, we cannot treat the joint probability $\mathbb{P}\left(SIR_x \leq \gamma^* \cap SIR_y > \gamma^*\right)$ by simply multiplying the two issued probabilities.

We derive $\mathbb{P}\left(SIR_x \leq \gamma^* \cap SIR_y > \gamma^*\right)$ in the following part:

$$\begin{aligned} &\mathbb{P}\left(SIR_x \leq \gamma^* \cap SIR_y > \gamma^*\right) \\ &= \int_0^B \mathbb{P}\left(r_y \leq r_x \sqrt{\gamma^* \beta\left(\delta f\right)} \cap r_y < \frac{r_x}{\sqrt{\gamma^* \beta\left(\delta f\right)}} | \delta f \right) \mathbb{P}\left(\delta f\right) \, \mathrm{d}\delta f \end{aligned} \tag{5.9}$$

We use a similar method as in Section 4.3.1 to derive this probability. We compute the inner part of the integral by observing its dependence on the value of $\sqrt{\gamma^* \beta\left(\delta f\right)}$, the intersection of the two inequality constraints can be to 2 cases:

$$\begin{aligned} &\mathbb{P}\left(r_y \leq r_x \sqrt{\gamma^* \beta\left(\delta f\right)} \cap r_y < \frac{r_x}{\sqrt{\gamma^* \beta\left(\delta f\right)}} | \delta f \right) \\ &= \begin{cases} \mathbb{P}\left(r_y \leq r_x \sqrt{\gamma^* \beta\left(\delta f\right)} | \delta f \right) & \text{if} \sqrt{\gamma^* \beta\left(\delta f\right)} \leq 1, \\ \mathbb{P}\left(r_y < \frac{r_x}{\sqrt{\gamma^* \beta\left(\delta f\right)}} | \delta f \right) & \text{if} \sqrt{\gamma^* \beta\left(\delta f\right)} \geq 1 \end{cases} \end{aligned} \tag{5.10}$$

We now evaluate the probabilities eq.(5.10) separately for each case in the following parts.

For the case $\sqrt{\gamma^* \beta (\delta f)} \leq 1$

It is related to the first line in eq.(5.10). In this case, the interfering node is always closer to the receiver than the desired node. This probability is computed by evaluating all cases for r_x:

$$\mathbb{P}\left(r_y \leq r_x \sqrt{\gamma^* \beta (\delta f)} | \delta f\right) \tag{5.11}$$

$$= \begin{cases} 0 & \text{if} \sqrt{\gamma^* \beta (\delta f)} \leq \frac{r_m}{r_M}, \\ \int_{\frac{r_m}{\sqrt{\gamma^* \beta (\delta f)}}}^{r_M} \frac{{r_x}^2 \gamma^* \beta (\delta f) - {r_m}^2}{k^2} \cdot P(r_x)\, \mathrm{d}r_x & \text{if } \frac{r_m}{r_M} \leq \sqrt{\gamma^* \beta (\delta f)} \leq 1 \end{cases}$$

$$= \begin{cases} 0 & \text{if} \sqrt{\gamma^* \beta (\delta f)} \leq \frac{r_m}{r_M}, \\ \frac{a}{\gamma^* \beta (\delta f)} + b \gamma^* \beta (\delta f) + c & \text{if } \frac{r_m}{r_M} \leq \sqrt{\gamma^* \beta (\delta f)} \leq 1 \end{cases} \tag{5.12}$$

with the same constants a, b, c as the no-SIC case eq.(5.5).

$\mathbb{P}(r)$ represents the probability that any node in a disk form area of $[r_m, r_M]$ is located at a distance r from the BS. As nodes positions are distributed uniformly and randomly, we have:

$$\mathbb{P}(r) = \begin{cases} \frac{2r}{r_M^2 - r_m^2} = \frac{2r}{k^2} & \text{for } r \in [r_m, r_M] \\ 0 & \text{elsewhere} \end{cases} \tag{5.13}$$

with $k^2 = r_M^2 - r_m^2$.

For the case $\sqrt{\gamma^* \beta (\delta f)} \geq 1$

This is related to the second case of eq.(5.10). It indicates that the interfering node can be further from the receiver than the desired node. We also decompose it conditionally to r_x as follows:

$$\mathbb{P}\left(r_y < \frac{r_x}{\sqrt{\gamma^* \beta (\delta f)}} | \delta f\right) \tag{5.14}$$

$$= \int_{r_m}^{r_M} \mathbb{P}\left(r_y < \frac{r_x}{\sqrt{\gamma^* \beta (\delta f)}} | \delta f \cap r_x\right) \cdot P(r_x)\, \mathrm{d}r_x$$

The first term inside the integral in the condition of δf and r_x, actually represents the probability that r_y is smaller that a specific value, in the considered range $[r_m, r_M]$:

$$
\begin{aligned}
&\mathbb{P}\left(r_y < \frac{r_x}{\sqrt{\gamma^* \beta\left(\delta f\right)}} | \delta f \cap r_x\right) \\
&= \begin{cases} 0 & \text{if } \frac{r_x}{\sqrt{\gamma^* \beta(\delta f)}} \leq r_m, \\ \int_{r_m}^{\frac{r_x}{\sqrt{\gamma^* \beta(\delta f)}}} P\left(r_y\right) \, \mathrm{d}r_y & \text{if } r_m \leq \frac{r_x}{\sqrt{\gamma^* \beta(\delta f)}} \leq r_M \\ 0 & \text{if } \frac{r_x}{\sqrt{\gamma^* \beta(\delta f)}} \geq r_M \end{cases} \\
&= \begin{cases} 0 & \text{if } \frac{r_x}{\sqrt{\gamma^* \beta(\delta f)}} \leq r_m, \\ \frac{1}{k^2} \frac{{r_x}^2}{\gamma^* \beta\left(\delta f\right)} - \frac{r_m^2}{k^2} & \text{if } r_m \leq \frac{r_x}{\sqrt{\gamma^* \beta(\delta f)}} \leq r_M \\ 0 & \text{if } \frac{r_x}{\sqrt{\gamma^* \beta(\delta f)}} \geq r_M \end{cases}
\end{aligned} \tag{5.15}
$$

The first part is null because the condition implies that node 2 enters the exclusive zone (where the radius is smaller than r_m). As no nodes can be in this zone, the probability is zero. The second part corresponds to the fact that the interfering node is in the area range, but the integral upper limit depends on the location of the desired node. As $\sqrt{\gamma^* \beta\left(\delta f\right)} \geq 1$, the third condition of eq.(5.15) indicates that r_x is larger that r_M. Meanwhile, as r_1 is constrained by $[r_m, r_M]$, thus it leads to a null probability.

The expression of the probability in condition of δf eq.(5.14) can thus be computed by integrating r_x:

$$
\begin{aligned}
&\mathbb{P}\left(r_y < \frac{r_x}{\sqrt{\gamma^* \beta\left(\delta f\right)}} | \delta f\right) \\
&= \begin{cases} \int_{r_m \sqrt{\gamma^* \beta(\delta f)}}^{r_M} \left(\frac{1}{k^2} \frac{{r_x}^2}{\gamma^* \beta\left(\delta f\right)} - \frac{r_m^2}{k^2}\right) \frac{2 r_x}{k^2} \, \mathrm{d}r_x & \text{if } 1 \leq \sqrt{\gamma^* \beta\left(\delta f\right)} \leq \frac{r_M}{r_m} \\ 0 & \text{if} \sqrt{\gamma^* \beta\left(\delta f\right)} \geq \frac{r_M}{r_m} \end{cases} \\
&= \begin{cases} \frac{d_1}{\gamma^* \beta\left(\delta f\right)} + e_1 \gamma^* \beta\left(\delta f\right) + f_1 & \text{if } 1 \leq \sqrt{\gamma^* \beta\left(\delta f\right)} \leq \frac{r_M}{r_m} \\ 0 & \text{if} \sqrt{\gamma^* \beta\left(\delta f\right)} \geq \frac{r_M}{r_m} \end{cases}
\end{aligned} \tag{5.16}
$$

with the following constants:

$$
d_1 = \frac{{r_M}^4}{2k^4}, \quad e_1 = \frac{{r_m}^4}{2k^4}, \quad f_1 = -\frac{{r_M}^2 {r_m}^2}{k^4} \tag{5.17}
$$

Final Expression

Now we have the results of both two cases, eq.(5.12) and eq.(5.16), which are all conditional to δf. We can then derive the joint probability of two correlated events, by integrating on δf:

$$\begin{aligned}
&\mathbb{P}\left(SIR_x \leq \gamma^* \cap SIR_y > \gamma^*\right) \\
&= \int_0^B \mathbb{P}\left(r_y \leq r_x\sqrt{\gamma^*\beta\left(\delta f\right)} \cap r_y < \frac{r_x}{\sqrt{\gamma^*\beta\left(\delta f\right)}} | \delta f\right) \cdot \mathbb{P}\left(\delta f\right) \, \mathrm{d}\delta f \qquad (5.18) \\
&= \int_{b_2}^{b_1} \left(\frac{a}{\gamma^*\beta\left(\delta f\right)} + b\gamma^*\beta\left(\delta f\right) + c\right) \cdot \mathbb{P}\left(\delta f\right) \, \mathrm{d}\delta f \\
&\quad + \int_{b_3}^{b_2} \left(\frac{d_1}{\gamma^*\beta\left(\delta f\right)} + e_1\gamma^*\beta\left(\delta f\right) + f_1\right) \cdot \mathbb{P}\left(\delta f\right) \, \mathrm{d}\delta f
\end{aligned}$$

The integral edges b_1, b_2, b_3 are the same than the OP without SIC in eq.(5.5). Therefore, the OP of the SIC receiver can be written as :

$$\begin{aligned}
\mathrm{OP}_{SIC} &= \mathbb{P}\left(SIR_x \leq \gamma^*\right) - \mathbb{P}\left(SIR_x \leq \gamma^* \cap SIR_y > \gamma^*\right) \\
&= \int_{b_3}^{b_2} \left(\frac{(d-d_1)}{\gamma^*\beta\left(\delta f\right)} + (e-e_1)\gamma^*\beta\left(\delta f\right) + (f-f_1)\right) \cdot \mathbb{P}\left(\delta f\right) \, \mathrm{d}\delta f \\
&\quad + \int_{b_4}^{b_3} 1 \cdot \mathbb{P}\left(\delta f\right) \, \mathrm{d}\delta f \qquad (5.19)
\end{aligned}$$

The result of integral computation is shown as below, the OP with SIC for the 2 users case:

$$\begin{aligned}
\mathrm{OP}_{SIC} =& \frac{2}{B}\left[\frac{(d-d_1)\,\sigma^2\pi}{\gamma^* 150}\,\mathrm{erfi}\left(\frac{\delta f}{\sqrt{2\sigma^2}}\right) + 75(e-e_1)\gamma^*\,\mathrm{erf}\left(\frac{\delta f}{\sqrt{2\sigma^2}}\right)\right]_{b_3}^{b_2} \qquad (5.20) \\
&+ \left[(f-f_1)\,\delta f - \frac{(d-d_1)\,\sigma^3\sqrt{2\pi}}{B\gamma^* 150}\exp^{\frac{\delta f^2}{2\sigma^2}} + \frac{(e-e_1)\,\gamma^* 150\sigma}{B\sqrt{2\pi}\exp^{\frac{\delta f^2}{2\sigma^2}}} - \frac{(f-f_1)\,(\delta f)^2}{2B}\right]_{b_3}^{b_2} \\
&+ \frac{2}{B}\left[\delta f - \frac{\delta f^2}{2B}\right]_{b_4}^{b_3}
\end{aligned}$$

Finally, we can now extend eq.(5.20) to the N users case. We still observe one desired node, while there are $N-1$ potential interfering nodes at the observed moment. As we neglect errors due to aggregated interference, the desired node is successfully decoded when no interfering node succeeds in interrupting the desired node. Therefore the OP with SIC is given by:

$$\mathrm{OP}_{SIC(N)} = 1 - \left(1 - \mathrm{OP}_{SIC}\right)^{N-1} \qquad (5.21)$$

5.4 Validation and Numerical Results

In this section we show the comparison of theoretical and simulation results, in order to validate the analytic expression of OP with SIC, as well as to demonstrate the impacts of SIC.

5.4.1 Validation

In order to validate $OP_{SIC(N)}$ in eq.(5.21), Monte Carlo simulations based on realistic network parameters have been carried out with Matlab. We consider a single BS, with nodes randomly deployed with a spatial Poisson process in the BS coverage. We have considered 4 main network parameters: the number of active nodes N at the considered moment, the total available bandwidth B, the SIR threshold γ^*, and the range of nodes' distribution area $[r_m, r_M]$.

We recall the hypothesis (identical for both the theory and simulations) on Table 5.1, in order to have a more clearer point of view:

TABLE 5.1: Simulations hypothesis for mono-BS SIC with free space

BS number	nodes distribution	desired node	path loss	fading	AIP	replicas
1	random	random	free space	no	no	no

Firstly, we have evaluated the variation in the decoded packet percentages against different SIC iterations, as depicted in Fig. 5.2. The iteration 0 corresponds to the decoding process of a simple receiver. The interference cancellation part of the SIC receiver starts with iteration 1. In this figure, no limitation is imposed on the SIC: decoding is performed until no additional nodes can be decoded. We can notice that when we raise the number of active nodes, the required SIC iterations increase as well. This is due to the fact that the collisions due to several interferers have increased, thus more SIC iterations allow to decode more additional packets.

Nonetheless, the 1st iteration brings the most significant performance improvement in all cases. These results can confirm the hypothesis that only one single interferer is the most frequent case. They can as well confirm that one iteration is accurate to evaluate the SIC performances, as was supposed in Section 5.3.2.

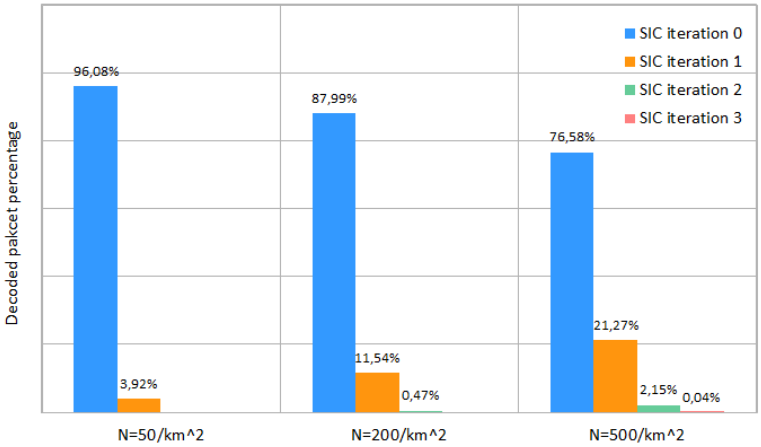

FIGURE 5.2: Decoded packet percentage vs different SIC iterations, for different active node numbers, $B = 96$ kHz, $\gamma^* = 6.8$ dB, $r_m = 30$ m, $r_M = 1000$ m.

Fig. 5.3-5.4 present the performance of the simple receiver and the SIC receiver, when varying the active node number and the SIR threshold, both by simulation and theory. We can observe that simulations (points) coincide perfectly with the theory (lines). Therefore, we can conclude that the theoretical expression eq.(5.21) is validated.

Besides, we verify the classical behavior of the OP when varying the different parameters. Indeed, as the number of active nodes N in a certain bandwidth grows, or as the threshold of SIR γ^* increases, the OP decreases. The choice of γ^* is predefined according to the demanded QoS. These phenomena reveal that when nodes are too dense for the total available bandwidth, or when the condition of success becomes too strict, the network performance degrades.

5.4.2 Analysis of SIC performance

We analyze the impact of SIC in terms of performance improvement in this part. As demonstrated in Fig. 5.3-5.4, the SIC receiver's outage probability is always lower when compared to the simple receiver. This is because the SIC process is based on the signals firstly decoded by the simple receiver, thus SIC allows to decode additional packets. Accordingly, we can conclude that SIC is beneficial in mitigating the interference induced by the random spectrum access of UNB systems.

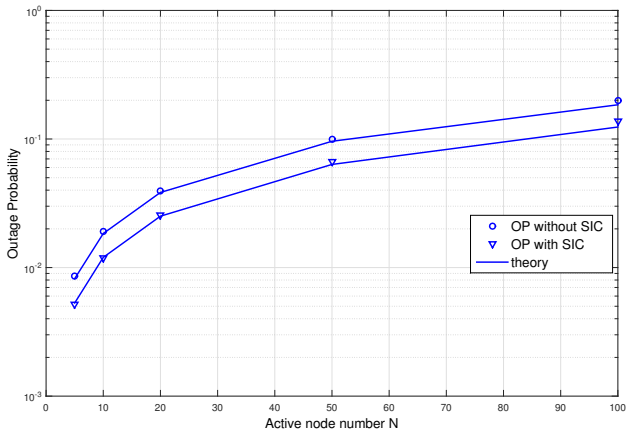

FIGURE 5.3: OP without SIC vs with SIC, for different active node numbers N, $B = 96$ kHz, $r_m = 30$ m, $r_M = 1000$ m, $\gamma^* = 6.8$ dB.

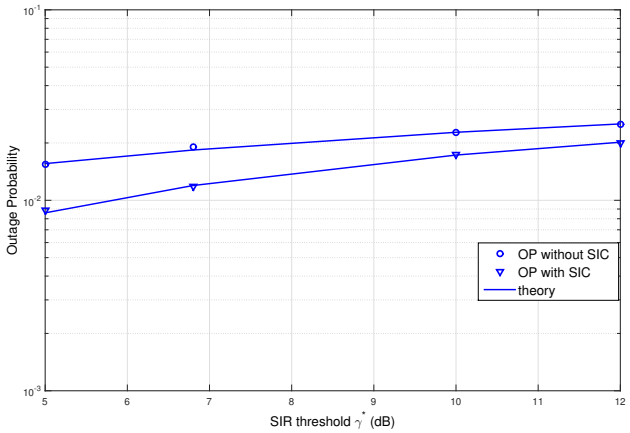

FIGURE 5.4: OP without SIC vs with SIC, for different SIR threshold γ^* (dB), $B = 96$ kHz, $N = 10$, $r_m = 30$ m, $r_M = 1000$ m.

To further evaluate the SIC improvement, we define the *gain of SIC* as $\frac{OP_{noSIC} - OP_{SIC}}{OP_{noSIC}}$, which is the percentage of error reduction thanks to SIC. We use it as an indicator of the SIC efficiency. Besides, for the sake of generality, we characterize the network activity by the normalized spectral use, which is the total active nodes' spectrum occupation over the total bandwidth. Typically one signal occupies 100Hz spectrum in UNB, thus the normalized spectral use is $\frac{100N}{B}$.

We have evaluated the gain of SIC by maintaining the normalized spectral use at a constant level, as demonstrated in Fig. 5.5. The idea is to test whether the SIC gain changes for different scales of node number, while keeping the ratio $\frac{100N}{B}$ fixed. We can observe that no matter how the scale of node number changes, as long as the normalized spectral use is constant, their SIC improvement is identical.

Furthermore, we verify the evolution of SIC gain when the normalized spectral use is not constant. As shown in Fig. 5.6, we can see that the SIC gain degrades as the normalized spectral use increases. And for the same normalized spectral use, when the success decoding criteria becomes more strict (thus γ^* becomes higher), we obtain lower gain of SIC.

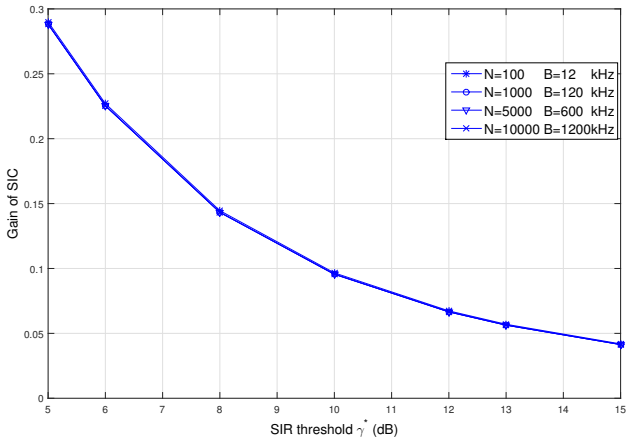

FIGURE 5.5: Gain of SIC, as a function of SIR threshold γ^* (dB), and constant normalized spectral use $\frac{100N}{B}$, $r_m = 30$ m, $r_M = 1000$ m.

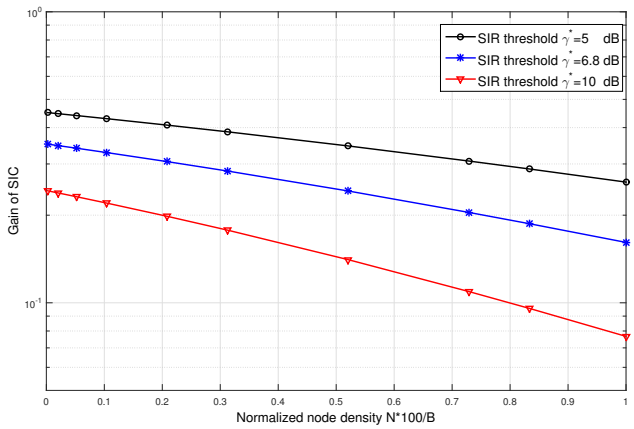

FIGURE 5.6: Gain of SIC, as the function of normalized spectral use $\frac{100N}{B}$, and different SIR thresholds γ^* (dB), $r_m = 30$ m, $r_M = 1000$ m.

Such results can be directly exploited to simply adapt the network parameters to the targeted load. For instance, for a given node number, we can adapt the bandwidth to obtain the expected SIC gain. Furthermore, these results also allow to foresee the SIC performance for different normalized spectral use.

5.5 SIC performance with Rayleigh fading

The performance of SIC that we analyze in the previous sections consider only the free space propagation where the path loss coefficient is $\alpha = 2$, and we have seen that the gain of SIC is somehow limited. In this section, we consider the Rayleigh fading, with the purpose of seeing if the additional degree of freedom will improve the performance of SIC. What's more, we take into account other propagation in addition to verify if the impact of fading is constant for different α. We note that we still focus on the interference due to only one interferer, and thus only one SIC iteration.

5.5.1 Joint impact of free space and Rayleigh fading

Analytical intuition

In the theory, the OP with fading and SIC is the probability that neither the desired node nor the interfering node is decoded by the SIC receiver. It can be expressed as:

$$\begin{aligned} \mathrm{OP}_{SIC} &= \mathbb{P}\left(SIR_x \leq \gamma^* \cap SIR_y \leq \gamma^*\right) \\ &= \mathbb{P}\left(\frac{g_x \frac{r_0^2}{r_x^2}}{g_y \frac{r_0^2}{r_y^2} \beta(\delta f)} \leq \gamma^* \cap \frac{g_y \frac{r_0^2}{r_y^2}}{g_x \frac{r_0^2}{r_x^2} \beta(\delta f)} \leq \gamma^*\right) \\ &= \mathbb{P}\left(\frac{g_x}{g_y} \cdot \frac{{r_y}^2}{{r_x}^2 \beta(\delta f)} \leq \gamma^* \cap \frac{g_y}{g_x} \cdot \frac{{r_x}^2}{{r_y}^2 \beta(\delta f)} \leq \gamma^*\right) \end{aligned} \tag{5.22}$$

with g_x and g_y the Rayleigh fading coefficients, which are independent random parameters following the same exponential distribution, whose mean equals to 1, thus $g \sim exp(1)$.

Compared to OP_{SIC} with only path loss, this above probability has two more random variables, i.e. the fading factors g_x and g_y. Thanks to them, the correlation between the two events diminishes.

We did not compute the OP_{SIC} with fading in eq.(5.22). But we note that it can be derived by considering $\frac{g_x}{g_y}$ and $\frac{g_y}{g_x}$ as Gamma distributed variables. The most important is that this expression gives us an intuition of how the fading coefficient can impact the OP.

Numerical results

We have plotted in Fig. 5.7-5.8 the numerical results of OP without/with SIC, for the cases without/with the influence of fading. The propagation is still free space here. The hypothesis are listed in Table 5.2.

TABLE 5.2: Simulations hypothesis for mono-BS SIC with free space and fading

BS number	nodes distribution	desired node	path loss	fading	AIP	replicas
1	random	random	free space	wo/with	no	no

We can observe that when there is no SIC, the system with or without fading (blue and red lines with triangles) has similar performance. The reason is that the fading factor $g \sim exp(1)$, thus on average it impacts homogeneously the received power of nodes uniformly distributed in the cell. When SIC is not applied in the system, the simple receiver decodes only the strongest signal in collisions. Hence the percentage of decoded signals does not evolve with the presence of fading.

Meanwhile, when there is SIC, the $OP\ with\ fading$ has better performance than $OP\ without\ fading$, as shown the blue and red lines with circles in Fig. 5.7-5.8. Indeed, when we consider only the path loss, the received power level is only related to the distance between nodes and the BS, whose distribution is predictable. However, when we add a random factor, i.e. the fading, the diversity of the received power of each node increases. This diversity helps to release the dependence caused by δf as shown in eq.(5.22), thus helps the SIC receiver in decoding colliding signals.

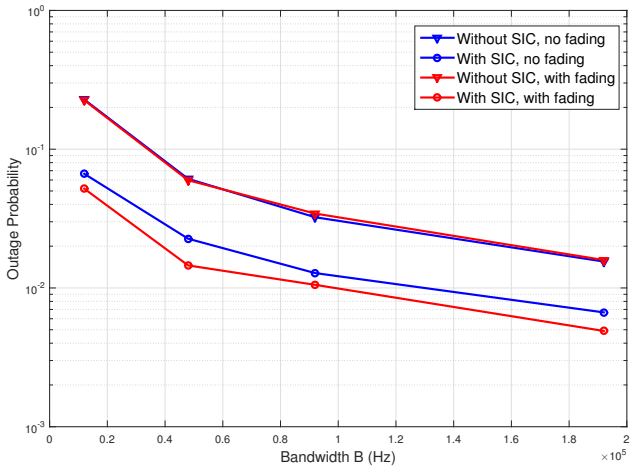

FIGURE 5.7: OP without/with SIC and without/with fading, for different B, $N = 30$, $\gamma^* = 6.8$ dB, $r_m = 30$ m, $r_M = 1000$ m.

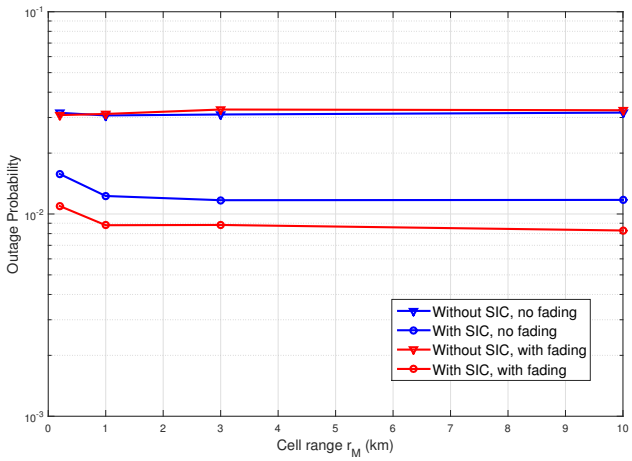

FIGURE 5.8: OP without/with SIC and without/with fading, for different r_M, $N = 30$, $B = 96$ kHz $\gamma^* = 6.8$ dB, $r_m = 30$ m.

5.5.2 Joint impact of various propagation α and Rayleigh fading

We wanted to verify if the fading brings always higher SIC efficiency when the propagation is not free space. The propagation exponent α is normally in the range $\alpha \in [2, 4]$ depending on the environment.

In this condition, the OP_{SIC} becomes:

$$\mathrm{OP}_{SIC} = \mathbb{P}\left(\frac{g_x}{g_y} \cdot \frac{{r_y}^{\alpha}}{{r_x}^{\alpha}\beta\left(\delta f\right)} \leq \gamma^* \cap \frac{g_y}{g_x} \cdot \frac{{r_x}^{\alpha}}{{r_y}^{\alpha}\beta\left(\delta f\right)} \leq \gamma^*\right) \tag{5.23}$$

Through this analytical expression, we can already heave an insight that the higher α is, the faster the received power degrades at a given distance.

We have conducted simulations with the hypothesis listed in Table 5.3:

TABLE 5.3: Simulations hypothesis for mono-BS SIC with α and fading

BS number	nodes distribution	desired node	path loss	fading	AIP	replicas
1	random	random	α	wo/with	no	no

We have thus plotted on Fig. 5.9 the numerical OP without/with SIC for without/with fading, as well as the issued *gain of SIC*, as a function of the propagation exponent α. We can firstly remark that the gain of SIC degrades when α increases. Because the increase of α severely decreases the received power of both the desired node x and the interfering node y. Hence the probability that both SIR_x and SIR_y are below the threshold becomes higher.

Secondly, we note that the $\mathrm{OP}_{(SIC\ with\ fading)}$ tends to converge to $\mathrm{OP}_{(SIC\ without\ fading)}$ when α increases. This is due to the fact that the SIR of all the nodes have degraded (when α increases), which causes less packets being decoded at the simple receiver process. The chance that the signals decoded by the simple receiver are singletons increases, thus the chance that SIC receiver decodes additional packets decreases.

More interestingly, we can observe that in free space propagation (i.e. $\alpha = 2$), the Rayleigh fading brings more gain of SIC. This confirms the phenomena that we have observed in the Section 5.5.1.

Meanwhile, when the environment becomes more lossy and has more specular reflections, (i.e. α tends to 4), the the fading brings slightly worse performance to the SIC receiver. This is not surprising, because the the power of all nodes are already significantly and negatively affected by the increase of α. The randomness brought by the fading has no more benefits in adding the diversity when SIC receiver is decoding. Thus the fading is no more advantageous in improving the SIC performance when the path loss exponent is high.

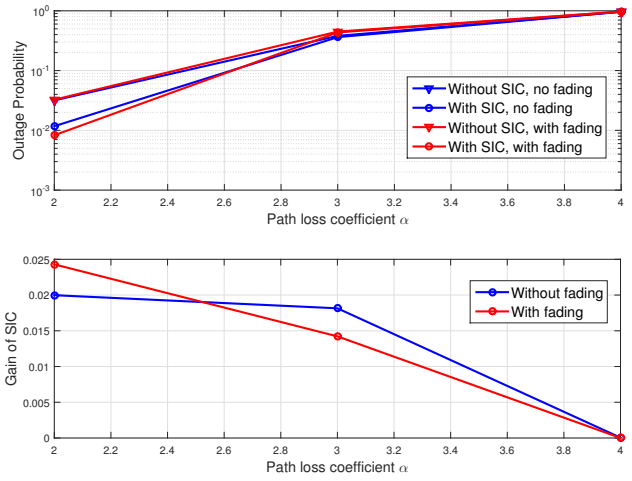

FIGURE 5.9: OP without/with SIC and without/with fading, for different path loss exponent α, $N = 30$, $B = 96$ kHz $\gamma^* = 6.8$ dB, $r_m = 30$ m, $r_M = 10$ km.

5.6 Conclusion

In this chapter, we have considered to enhance the performance of UNB based IoT networks from single base station's side. The specific interference caused by the random radio access is a main limitation of the system. Therefore, we have proposed to apply the Successive Interference Cancellation methodology to the UNB system, in order to mitigate the interference impact.

We have derived the theoretical expression of OP with SIC receiver, by considering the specific random spectrum access of UNB and the free space propagation. We have considered only the contribution of a unique interferer at each collision, and thus only the performance of the one SIC iteration. We have exploited the analytical OP expression in Section 4.3.1 with the same hypothesis, and derived a closed-form expression of $\mathrm{OP}_{(SIC)}$.

Then we have shown numerical results. Primarily, we have conducted the simulations without limiting the SIC iterations. We have found out that it was always the first iteration of SIC that brings the most significant performance improvement. We have thus confirmed the hypothesis of only 1 SIC iteration used in the theoretical analysis. Secondly, we have validated the theoretical $\mathrm{OP}_{(SIC)}$ by comparing it with simulations where we have constrained the SIC iteration to 1. According to the analytic and numerical results, SIC has effectively reduced the probability of errors in UNB system compared to a simple receiver. Besides, we have defined the term normalized spectral use by $\frac{100N}{B}$, and the term SIC gain by the error reduction percentage thanks to SIC. We have used them to evaluate the SIC performance. We have highlighted that the increase of the normalized spectral use would cause the degradation of SIC performance; and that for the same normalized spectral use (no matter what the scale of node number becomes), the SIC efficiency to enhance the network performance maintains constant.

Finally, we have evaluated the SIC performance with the involvement of Rayleigh fading, in different propagation conditions. We have observe that, in free space propagation, the $\mathrm{OP}_{(SIC\ with\ fading)}$ is lower than $\mathrm{OP}_{(SIC\ without\ fading)}$. We have thus deduced that the diversity delivered by the fading is advantageous in enhancing the efficiency of SIC, in free space. But when the propagation exponent increases, the $\mathrm{OP}_{(SIC\ with\ fading)}$ is identical to $\mathrm{OP}_{(SIC\ without\ fading)}$. We have thus brought to light that the fading brings no more benefits in improving the SIC gain when the environment becomes more lossy.

This chapter gives us an insight about how SIC can enhance the performance of UNB networks. Indeed, SIC can be a perfect candidate to mitigate the UNB's partial spectral interference. We note that the high complexity (the many iterations) is still a big constraint to implement it in realistic systems. But one SIC iteration as demonstrated in this chapter is feasible.

One may note that this study can be extended to multiple base stations scenarios, which brings spatial diversity and may increase the SIC efficiency. It can also be furthered when considering the partial temporal interference (as we consider only the spectral interference in this chapter). Moreover, the combination of replications and SIC can be very efficient. Because once one replication (of the same packet) is decoded, it can be reconstructed and retrieve the contribution of its other replications, thus more additional singletons will appear and be decoded.

We have assumed that the SIC receiver can perfectly reconstruct and retrieve

signals without leaving residues, in the analysis in this chapter. But in real implementations, this perfectness is very hard to reach. It demands very high receiver sensibility (to distinguish signals having very similar powers) and high computation resources (to reconstruct the large-scale of signals). Thus imperfect receivers can be considered in future works.

Chapter 6

Multi-BS diversity

Contents

In this chapter, we exploit the spatial diversity of multiple base stations, in the purpose of enhancing the UNB systems performance. We analyze the impact of different combining technologies, which are performed across multiple BSs. Firstly, we analyze theoretically the simplest Selection Combining (SC). In the presence of path-loss and spectral randomness of UNB, we consider the spectral interference viewed by each BS are correlated. Secondly, we continue the analysis of SC, by adding a random factor: the Rayleigh fading. We have derived an expression of outage probability when assuming that the interferences are independent. However, this OP is proved to be not accurate to the simulation results, thus the hypothesis of independence is proved not to be appropriate in UNB systems.

Then we attack more complex ones such as Max Ratio Combining (MRC), Equal Gain Combining (EGC), and even Successive Interference Cancellation (SIC) across cooperated base stations. Finally, we evaluate numerically the multi-BS diversity gain of all the mentioned technologies when compared to single BS.

6.1 Introduction

In most cellular systems, one BS (Base Station) is supposed to serve devices in a specific service area [119]. Nonetheless, when devices send data to their intended BS, they are also captured by adjacent BSs. Thus, a BS actually receives the sum of its useful information, the contribution of devices intended to neighboring BSs, and noise. If the BSs independently decode the signal, the neighbor devices are seen as interferers.

Moreover, in long-distance transmissions, one signal can be perceived by many surrounding or even far-away BSs. Each BS gets a different point of view of the transmitted signals. Indeed, they are not located at the same distance from the transmitting devices, so the transmitted signals experience diverse channel conditions to reach each BS. Similarly, they do not experience the same interference pattern. It is possible that lost packets from a given BS can be properly decoded at another BS. Therefore, taking advantage of the diversity (in time, frequency and space) of multiple BS can be beneficial to improve the system performance.

The earliest works about multiple receivers consider them independent and non-cooperative [120]. As packets experience different channel conditions, when one packet fails to be seized by one BS, it is still possible to be captured by another one. The authors in [121] analyzed a cellular network's performance of non-cooperative receivers, for slotted ALOHA case. A recent theoretical analysis of the throughput for multiple receivers with perfect power control is presented in [122].

Besides, the interaction and cooperation among BSs also came on the scene, by using different combining and interference cancellation technologies. This cooperation is usually operated at the back-haul, where all BSs transmit their perceived signals. This data center collects information from each BS and treats them jointly. This architecture can be referred to Cloud-RAN (radio access network) [123]. This kind of architecture depends on the intelligence of the BSs, and leaves the remote devices simple and light.

Combining technologies, in a general sense, aim at combining the signals each BS receives, even if none of them can decode it. In this case, the desired user's contribution is constructively added, while interference and noise are averaged,

leading to a significant increase in the SINR. Thus, the desired signal is more likely to be decoded. Maximum ratio combining (MRC) and optimum combining are often analyzed for multiple BSs, by using stochastic geometry as tools [124] [125]. The most frequent assumption is that each node is attached to its nearest BS. With the use of Poisson Point Process, the BS is supposed to be within the Veronoi cell of the user [124]. However, this hypothesis is idealized, and does not fit in our network where nodes are not attached to one specific BS.

Selection combining, as one the combining technologies, selects the strongest signal (of the same message) perceived by all the BSs. Once this strongest signal managed to be decoded, the issued message is considered successfully received. The majority of the existing works about selection combining neglect the dependence among the channels, and thus assume that they are independent [126]. Indeed, with the presence of fast fading, this correlation is weakened, but it does not disappear. The assumption of independent channels is only valid for certain node densities as proved by [126] [127]. In this chapter, we consider only the path-loss, which faces directly the dependence among the links between the issued node and each BS.

All the above-mentioned works are based on traditional channel access where there is either no collision (as transmissions are performed on different orthogonal channels), or total overlap in the frequency domain. However, due to the continuous selection of carrier frequency in UNB networks, partial frequency overlapping has to be considered. To the best of our knowledge, no such analytical studies of multiple BSs for R-FTMA (the specific radio access of UNB, can be refereed to Section 2.3.2) has been conducted.

Therefore, the novelty of this chapter is to:

1. analyze the spatial diversity (namely SC, selection combining) of multiple BSs for a UNB system, by taking into account the spatial correlation between the received signals. The main contribution is to provide a closed-form theoretical expression of the performance for 2 BSs case with selection combining, as well as to promote this methodology to general K BSs.

2. verify that the hypothesis in most literature that the interference viewed by each BS is independent, is not valid in UNB systems. This confirms the uniqueness of UNB systems (especially its random frequency access), and the necessity to analyze the performance when considering the correlation (i.e. the last contribution).

3. implement MRC/EGC and SIC across distributed multi-BS systems where the radio access is not controlled. The contribution is the performance enhancement evaluation and comparison of these techniques, and an overview of their implementation complexity.

The rest of this chapter is organized as follows: we give the network topology and hypothesis Section 6.2. We analyze theoretically the selection combining when considering that the interference is correlated in Section 6.3. Then we continue the SC analysis but when considering that the interferences are independent in Section 6.4. Afterwards, we introduce the principle and algorithms of MRC and EGC in Section 6.5, and multi-BS by applying SIC in Section 6.6. We give the performance evaluation of all the proposed technologies in Section 6.7. Finally, we conclude the chapter in Section 6.8.

6.2 Modeling and Hypothesis

6.2.1 Multi-BS topology

Different from the previous chapters, the topology has changed from mono BS to multiple BSs. As illustrated in Fig. 6.1, the distribution of nodes (blue points) follows a HPPP (Homogeneous Poisson Point Process). For the BSs, there are globally two distributions. The traditional one (Fig. 6.1(a)) where the locations of BSs form square lattice, and the distance between each BS is constant and predefined. The other one is shown in Fig. 6.1(b), where the BSs distribution also follows a HPPP. The latter is often used in the literary [124,128] to model the positions of multiple receivers, for the reason that it can reflects the actual BSs' global deployment (from urban to rural areas). Also because the HPPP of base stations is independent from the one of nodes, these two point process can help facilitating theoretical analysis.

We don't impose a cell range for BSs, since the range is defined automatically by the distance limit where the SIR of nodes is below a predefined threshold. Therefore, if one singleton transmission is not interfered, it can be literally decoded by BSs very far away. We note that the traditional BS distribution as shown in Fig. 6.1(a) is used in Section 6.3, whereas the HPPP BS distribution as shown in Fig. 6.1(b) is used in Sections 6.4-6.7.

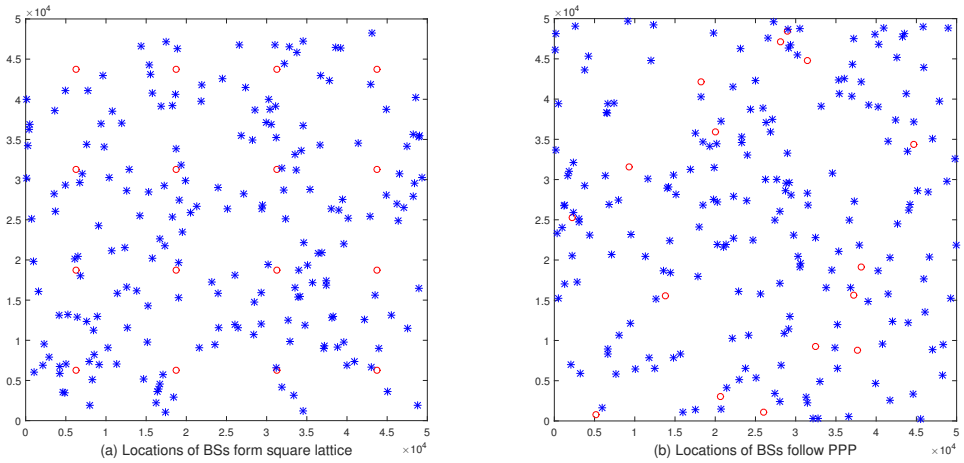

FIGURE 6.1: Topology of multiple BSs. The blue points are distributed nodes, the red points are BSs. (a) the locations of BSs form square lattice, where the distance between each BS is the same; (b) the locations of BSs follow Poisson point process.

6.2.2 Nodes and BSs behaviors assumptions

We consider the uplink case, where nodes transmit data to BSs by using the UNB technology. The emission of data is not continuous in time. Nodes are distributed randomly and uniformly in a wide area with a node density λ_t. Due to the very small duty cycle of the considered nodes, we prefer to use the *active* nodes density λ (nodes/m^2), which is considered stable at the observed moment. One may note that $\lambda << \lambda_t$. We focus on λ in this chapter. All transmissions are performed with the same emission power and antenna gain. BSs are assumed to be powered

all the time. Each BS transmits its received messages to the back-haul via wired networks, where the process of signal combining happens.

Nodes broadcast their small data packets to potential multiple BSs with UNB technology. Since nodes select their carrier frequency randomly and independently, a packet may be lost at one BS due to collisions when simultaneous transmissions happen. In this chapter, from one BS's point of view:

1. We firstly consider in Section 6.3 the collisions due to a unique interfering node at the observed moment, where we consider only the free space path loss. Indeed, a unique interferer is the most frequent case due to the very limited signal bandwidth of UNB [12], and this can facilitate the correlated interference calculation.

2. Then we consider the AIP (aggregated interference power) in the rest of the chapter, where we consider fading in addition to the path loss. As stated in Section 4.3.2, the AIP aggregates the interference contribution of all the active nodes (except the observed node itself). It reflects exactly what happen during realistic transmissions. Moreover, the outage probability can be calculated by the Laplace transform of AIP, as used in Section 4.3.2 and will be recalculated differently in Section 6.4.

Besides, we neglect the noise power as it is much lower compared to the interference power level. More importantly, the white noise's power is related to the individual signal bandwidth, thus identical to all the UNB transmissions. Therefore, the noise power impacts the SINR homogeneously to all the transmissions. As a consequence, its ignorance does not change the network's behavior.

One may note that the interference level depends not only on the interferer's received power at the BS, but also on δf the frequency spacing between the desired node and the interfering node. We use the Gaussian interference coefficient which estimates perfectly the realistic filters used in SigFox's network, as presented in Section 4.2.2. We recall this spectral interference function here, for its use in the next sections:

$$\beta(\delta f) = \frac{150}{\sigma\sqrt{2\pi}} \exp^{\frac{-\delta f^2}{2\sigma^2}} \tag{6.1}$$

with $\sigma = 60$ for a 100 bit/s transmission.

6.3 SC: Correlated interference, impact of path loss and multi-BS

In this section, we consider the impact of path loss (of free space) and selection combing (SC) among multiple BSs. The received power of each node viewed by each BS is only related to its respective distance to each BS. Hence we considered that, for one given packet, its spectral interference viewed by each BS is correlated.

We derive a closed-form OP (outage probability) expression for 2 base stations: BS_1 and BS_2, with selection combining and the spectral randomness of UNB. Indeed, two BSs is the atomic pattern for any multiple BSs case, which can give us an intuition of their behaviors. Then we extend the methodology to K BSs in the next section.

6.3.1 Theoretical analysis

Without loss of generality, we consider the topology of the BSs form square lattice in this section, as shown in Fig. 6.1(a). We consider that the 2 BSs are vertically centered while their horizontal position depends on the relative distance d between each other, as shown on Fig. 6.2.

We focus on the performance of one targeted desired node, which is at a known position. The desired node is not necessarily aligned with the 2 BSs. All other nodes are potential interfering nodes (i.e. the blue points), and their positions are random. We define r_{xi} (resp. r_{yi}) (for $i \in \{1,2\}$) as the distance between the desired node x (resp. the interfering node y) and BS_i.

Due to different interference contributions, BS_1 and BS_2 perceive the desired user's signal with different SIR. Taking example of BS_1, the SIR_1 can be expressed as:

$$SIR_1 = \frac{P_0 \left(\frac{r_0}{r_{x1}}\right)^2}{P_0 \left(\frac{r_0}{r_{y1}}\right)^2 \beta(\delta f)} = \left(\frac{r_{y1}}{r_{x1}}\right)^2 \frac{1}{\beta(\delta f)} \tag{6.2}$$

with P_0 the power at the reference distance r_0.

In the single BS case, OP represents the probability that the SIR (Signal to Interference Ratio) of the desired node is lower than a predefined threshold γ^*. As a consequence, and as shown in Section 4.3.1, for the single BS case, a failure is observed when an interferer, whose carrier frequency differs from the desired user of δf, falls within a circle of radius $r_{x1}\sqrt{\gamma^* \beta(\delta f)}$.

Similarly, in the 2 BSs case, the transmitted data is lost when the SIRs perceived by both BSs are lower than γ^*. Thus OP becomes:

$$\begin{aligned} \mathrm{OP} &= \mathbb{P}(SIR_1 < \gamma^* \cap SIR_2 < \gamma^*) \\ &= \mathbb{P}(r_{y_1 1} < r_{x1}\sqrt{\gamma^* \beta(\delta f)} \cap r_{y_2 2} < r_{x2}\sqrt{\gamma^* \beta(\delta f)}) \\ &= \mathbb{P}(r_{y_1 1} < R_{x1}(\delta f) \cap r_{y_2 2} < R_{x2}(\delta f)) \end{aligned} \tag{6.3}$$

with $R_{x1}(\delta f) = r_{x1}\sqrt{\gamma^* \beta(\delta f)}$ and $R_{x2}(\delta f) = r_{x2}\sqrt{\gamma^* \beta(\delta f)}$. One may note that $R_{x1}(\delta f)$ and $R_{x2}(\delta f)$ will be written as R_{x1} and R_{x2} in the rest of the chapter.

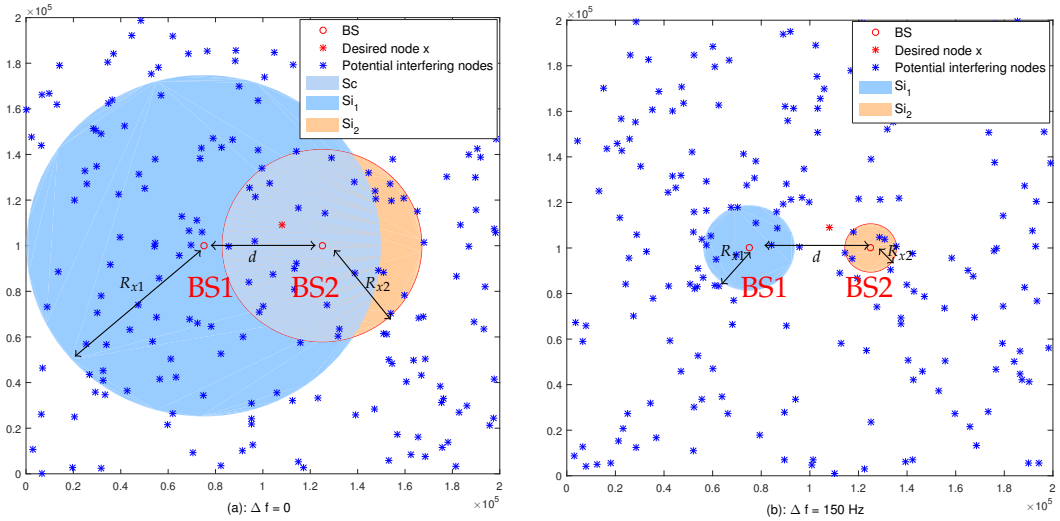

FIGURE 6.2: Topology of the network of (a) $\delta f = 0$ and (b) $\delta f = 150$ Hz. S_c is the common interfering area, Si_1 is the interfering circle of BS_1, and Si_2 is the interfering circle of BS_2

We can see that R_{x1} and R_{x2} may depend on the same δf, thus these two events are correlated. We cannot thus express them independently as the product of two probabilities (i.e. $OP = OP_1 \cdot OP_2$). This also confirms our hypothesis of correlated interference in Section 6.1. This correlation comes from the fact that there might be one common interferer for both BSs. Thus according to the interferer's location, OP in eq.(6.3) can be divided into two cases:

Common interferer: The same interferer $y = y_1 = y_2$ leads to error in both BSs. In this case, OP is obtained by computing the probability that y falls into the intersection of two circles. The first circle is centered on BS_1, with a R_{x1} radius (in blue on Fig. 6.2), while the second circle is centered on BS_2 with a R_{x2} radius (in orange). We call this intersection area Sc as the *common interfering area*, whose surface is s_c. One may note that this area depends on the radius of two circles, thus the value of δf (γ^* is predefined). For example, the light blue area on Fig. 6.2(a) is the non-null intersection Sc when $\delta f = 0$, while this area is empty on Fig. 6.2(b) when $\delta f = 150$Hz.

Distinct interferers: The interferers are different for the 2 BSs, which means that there is one specific interferer for each BS. In this case, OP is the probability that the interferer y_1 falls into the interfering area of BS1 but not inside the *common interfering area* (i.e. y_1 is in the blue area Si_1 in Fig. 6.2(a) which interferes inside BS_1), while at the same time, another interferer y_2 falls into Si_2 (i.e. the orange area).

Therefore, by combining these two disjoint cases, OP becomes:

$$\mathrm{OP} = \mathbb{P}(node\ y \in Sc) + \mathbb{P}(node\ y_1 \in Si_1) \cdot \mathbb{P}(node\ y_2 \in Si_2) \tag{6.4}$$

Common Interferer Calculation

Firstly, we focus on the case *Common interferer*. This is the probability that one node in the the considered area falls into the common interfering area Sc. For the 2 users case:

$$\mathbb{P}(node\ y \in Sc) = s_c \cdot \lambda = \lambda \cdot \int_0^B s_c\left(\delta f\right) \cdot \mathbb{P}\left(\delta f\right)\ \mathrm{d}\delta f \tag{6.5}$$

with λ the node density in nodes/m^2, and $\mathbb{P}\left(\delta f\right) = \frac{2}{B}\left(1 - \frac{\delta f}{B}\right)$ as nodes select their carrier frequency randomly within BW.

We then compute the common interfering area's surface s_c. We define d as the distance between two BSs, and use it as an indicator to determine if there is an overlap between the two circles [129]:

$$s_c\left(\delta f\right) = \begin{cases} R_{x1}^2 \arccos\left(\frac{R_{x1}^2 - R_{x2}^2 + d^2}{2dR_{x1}}\right) + R_{x2}^2 \arccos\left(\frac{R_{x2}^2 - R_{x2}^2 + d^2}{2dR_{x2}}\right) \\ \quad -\frac{\sqrt{((R_{x1}+R_{x2})^2 - d^2)\cdot(d^2 - (R_{x1}-R_{x2})^2)}}{2} & \text{if } \mid R_{x1} - R_{x2} \mid < d < R_{x1} + R_{x2} \\ 0 & \text{if } d \geq R_{x1} + R_{x2} \\ \pi \min\left(R_{x1}, R_{x2}\right)^2 & \text{elsewhere} \end{cases} \tag{6.6}$$

There are 3 cases for the intersection of two circles, depending on d and both radius R_{x_1}, R_{x_2}, as reported in eq.(6.6). For the first case, there is a partial overlap between the two circles; for the second case, the two circles are disjoint or too far away, thus no overlap; for the third case, one circle is contained entirely within the other.

Thus the expression of eq.(6.5) for 2 users in the 2 BS case, can be further written as:

$$\begin{aligned} \mathbb{P}(node\ y \in Sc) = &\int_0^{b_1} \left(\pi \min\left(R_{x1}, R_{x2}\right)^2 \cdot \lambda|\delta f\right) \cdot \mathbb{P}\left(\delta f\right)\ \mathrm{d}\delta f \\ &+ \int_{b_1}^{b_2} \left(R_{x1}^2 \arccos\left(\frac{R_{x1}^2 - R_{x2}^2 + d^2}{2dR_{x1}}\right) \cdot \lambda|\delta f\right) \cdot \mathbb{P}\left(\delta f\right)\ \mathrm{d}\delta f \\ &+ \int_{b_1}^{b_2} \left(\left(R_{x2}^2 \arccos\left(\frac{R_{x2}^2 - R_{x1}^2 + d^2}{2dR_{x2}}\right) - \frac{\sqrt{t}}{2}\right) \cdot \lambda|\delta f\right) \cdot \mathbb{P}\left(\delta f\right)\ \mathrm{d}\delta f \end{aligned} \tag{6.7}$$

with the integral edges defined as following:

$$\begin{aligned} b_1 &= min\left(\beta^{-1}\left(\frac{d^2}{(r_{x1} - r_{x2})^2 \gamma^*}\right), B\right) \\ b_2 &= min\left(\beta^{-1}\left(\frac{d^2}{(r_{x1} + r_{x2})^2 \gamma^*}\right), B\right) \end{aligned} \tag{6.8}$$

We note that b_1 and b_2 only exist when both $\frac{d^2}{(r_{x1}-r_{x2})^2\gamma^*}$ and $\frac{d^2}{(r_{x1}+r_{x2})^2\gamma^*}$ are in the range of $[0, 1]$, otherwise the intersection Sc is empty, e.g. the case in Fig. 6.2(b).

Distinct Interferers Calculation

Secondly, we compute the case *distinct interferers*. In this case, BS_1 cannot decode the desired packet because an interferer y_1 enters its interfering circle, but not in the common area:

$$\begin{aligned}&\mathbb{P}(node\ y_1 \in Si_1) \\ &= s_{i_1} \cdot \lambda = (\pi {R_{x1}}^2 - s_c) \cdot \lambda \\ &= \int_0^B (\pi {R_{x1}}^2 \lambda | \delta f) \cdot \mathbb{P}(\delta f)\ \mathrm{d}\delta f - \int_0^B (s_c \cdot \lambda | \delta f) \cdot \mathbb{P}(\delta f)\ \mathrm{d}\delta f\end{aligned} \tag{6.9}$$

where the second term is already computed in eq.(6.7). The first term represents in fact the OP when there is only one BS, whose calculation steps are demonstrated in Section 4.3.1, and is given by:

$$\begin{aligned}&\int_0^B (\pi {R_{x1}}^2 \lambda | \delta f) \cdot \mathbb{P}(\delta f)\ \mathrm{d}\delta f \\ &= \frac{300\pi {r_{x1}}^2 \gamma^* \lambda}{\sigma\sqrt{2\pi}B} \cdot \left(\frac{\sqrt{\sigma^2 \pi}}{\sqrt{2}} \operatorname{erf}(\frac{B}{\sqrt{2\sigma^2}}) + \frac{\sigma^2}{B} \left(\exp(\frac{-B^2}{2\sigma^2}) - 1 \right) \right)\end{aligned} \tag{6.10}$$

Similarly, we can have the expression of $\mathbb{P}(node\ y_2 \in Si_2)$ by using the same method:

$$\begin{aligned}&\mathbb{P}(node\ y_2 \in Si_2) \\ &= \int_0^B (\pi {R_{x2}}^2 \lambda | \delta f) \cdot \mathbb{P}(\delta f)\ \mathrm{d}\delta f - \int_0^B (s_c \cdot \lambda | \delta f) \cdot \mathbb{P}(\delta f)\ \mathrm{d}\delta f\end{aligned} \tag{6.11}$$

with the first term similar to eq.(6.10) where we only have to change r_{x1} to r_{x2}, and the second term computed in eq.(6.7).

Final Expression

We now extend the OP to more users' case. The number of active nodes N depends on the node density λ and the considered surface, and it is assumed stable at the observed moment. We have thus N nodes (including the desired node) transmitting simultaneously. With the hypothesis of only one interferer, OP becomes the probability that one out of the $N-1$ nodes enters the common interfering area s_c, in addition to the probability that two out of $N-1$ nodes enter separately into S_{i_1} and S_{i_2}.

Therefore, the final expression of OP for 2 BSs, and N users is:

$$\begin{aligned}\mathrm{OP} = &\mathbb{P}(node\ y \in Sc) \binom{N-1}{1} \\ &+ \mathbb{P}(node\ y_1 \in Si_1) \cdot \mathbb{P}(node\ y_2 \in Si_2) \binom{N-1}{2}\end{aligned} \tag{6.12}$$

with the three issued probabilities presented in eq.(6.7), eq.(6.9) and eq.(6.11).

This derivation of OP gives an intuition for K ($K > 2$) BSs, where we transform OP into the probability that one or several nodes fall into certain areas. And the surface of these areas changes depending on the frequency spacing. The complete derivation for K BSs with correlated interferences has not been carried out because of its complexity, but should be deduced by using the same methodology shown above.

6.3.2 Validation of OP expression for 2 BSs

In this section, we present the simulation results comparing with the theoretical ones of eq.(6.12) for 2 BSs in order to validate the previous analysis.

In the expression of OP eq.(6.12), the considered parameters are: the relative distance between the desired node and each BS r_{x1} and r_{x2}, the distance between two BSs d, the node density λ, the total bandwidth B, the number of active nodes N and the SIR threshold γ^*. We note that the Monte-Carlo simulations are performed with Matlab, by varying these parameters. We recall the hypothesis of the simulations in Table 6.1 below:

TABLE 6.1: Simulations hypothesis for multi-BS SC (*notation: db= distribution)

BS number	BS db	nodes db	desired node	path loss	fading	AIP
2; K	square lattice	random	at given position	free space	no	no

As illustrated in Fig. 6.3-6.4, we have the outage probability as a function of the node density λ and the total bandwidth B. We compare the OP obtained from eq.(6.12) and the one from simulations.

We can note that the theory (in solid lines) coincide well with the the simulations results (in points). The theoretical OP in eq.(6.12) is hence validated.

At the same time, we can observe on Fig. 6.3-6.4 the same variation of outage probability than the case of one BS in previous chapters. When the node density λ rises, the number of interferers increases accordingly, the OP thus rises up. However, OP declines when the total bandwidth B increases. This is because when the frequency resource becomes larger, the chance that the desired signal gets interfered becomes lower.

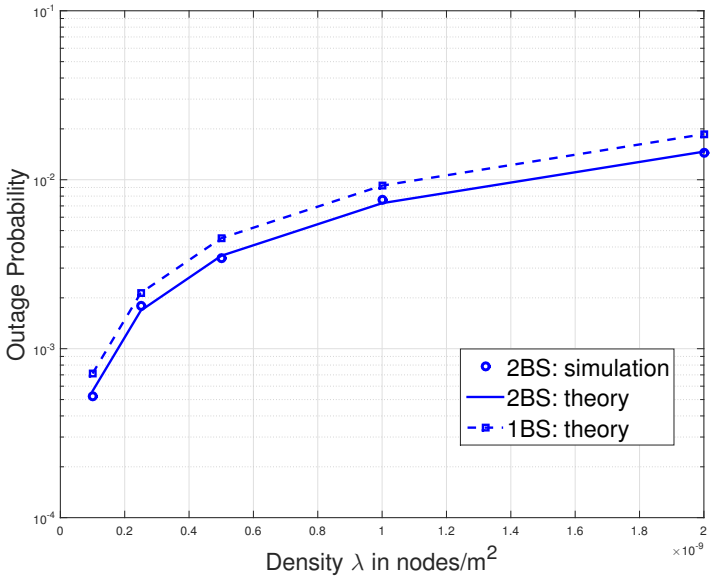

FIGURE 6.3: OP vs λ, distance between 2 BS $d = 5$ km, distance between desired node and both BSs $(r_{x_1}, r_{x_2}) = (18, 22)$ km, $B = 96$ kHz, $\gamma^* = 6.8$ dB.

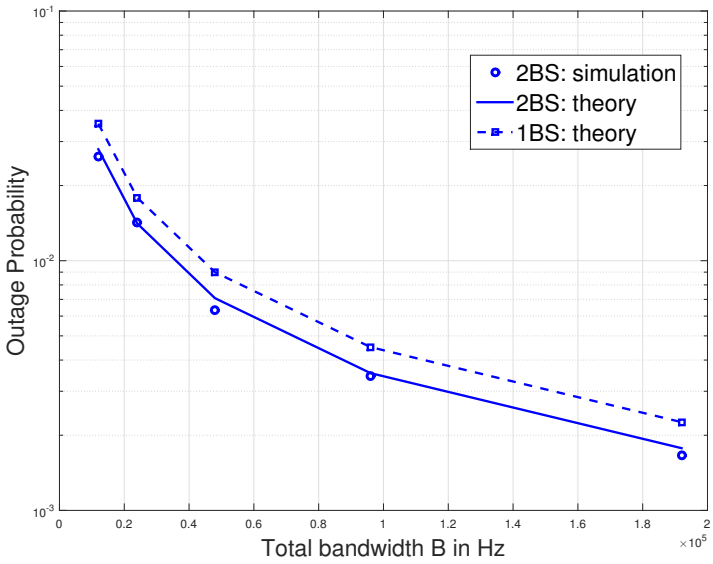

FIGURE 6.4: OP vs B, the active node number $N = 20$, distance between two BS $d = 5$ km, distance between desired node and both BSs $(r_{x_1}, r_{x_2}) = (18, 22)$ km, $\lambda = 5 \times 10^{-10}$ nodes$/m^2$, $\gamma^* = 6.8$ dB.

6.3.3 Exploitation of the OP expression for 2 BSs

We now exploit the theoretical OP expression in eq.(6.12) to observe how specific parameters of the 2 BSs case impact it, and the benefits of two BSs compared to the single BS case.

We have firstly varied the distance between two BSs d, by maintaining the position of the desired node fixed, as shown in Fig. 6.5. Consequently, the distances

between the desired node and both BSs are varying. We observe that when the two BSs drift apart, OP first drops off and then rises. This is due to the fact that the intersection's surface changes, as illustrated on Fig. 6.6 which shows the variation of Sc as d increases. Accordingly, the number of interferers included in the interfering area differs, which makes the OP vary. When d is small the desired node is close to the BSs. Thus R_{x1} and R_{x2} are small but the circles are almost perfectly overlapping. Thus, any node interferes at BS_1 is also interfering at BS_2. When d increases, the circles are parted, so the overlap diminishes and Sc decreases. However, when d exceeds a certain value, the increase of d leads to the growth of circle radius much sharper than the overlapping reduction. Thus Sc increases. Therefore, we can identify the optimal point, such that for a fixed desired node, there exists a distance d which delivers a lowest OP.

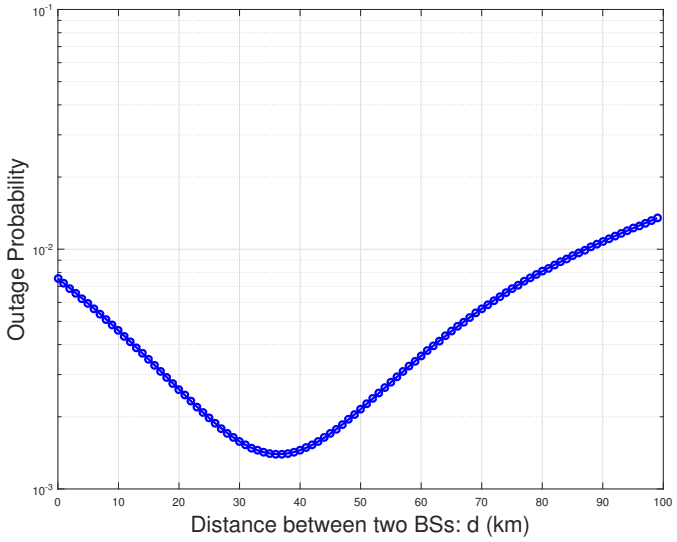

FIGURE 6.5: OP vs the distance between two BSs d, the active node number $N = 200$, the desired node is fixed, $\lambda = 8 \times 10^{-10}$ nodes$/m^2$, $B = 96$ kHz, $\gamma^* = 6.8$ dB.

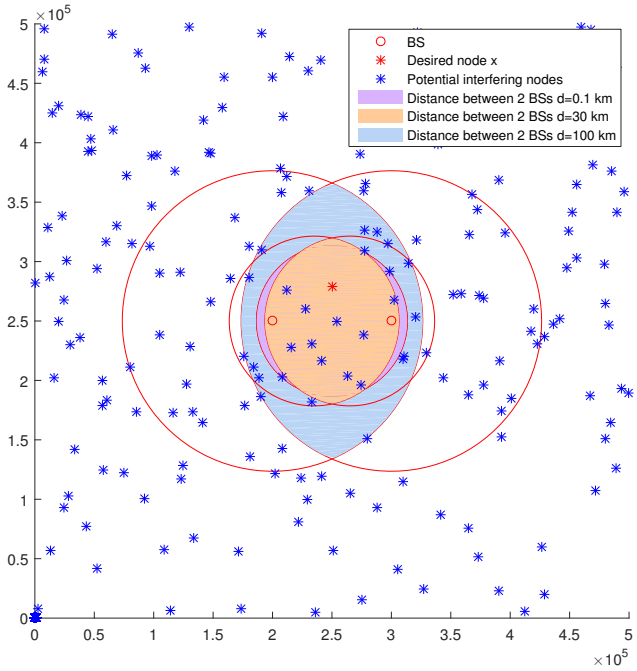

FIGURE 6.6: The intersection Sc vs different distance between two BSs d (km)

In a second step, we focus on the improvement brought by the use of a second BS. To quantify such improvement, we define $\frac{OP_{1BS}}{OP_{2BS}}$ as the *gain* of two BSs. The higher is the gain, the better is the improvement. One may note that we consider in this chapter only nodes that are in the reception capabilities of the 2 BSs, as the others will not benefit from the second BS. To evaluate this gain, we have plotted OP of a single BS (6.10) on Fig. 6.3-6.4, in dotted lines. We can verify that taking advantage of 2 BSs can improve the network performance, compared to only one BS's case. Indeed, as there is no cell planning among the BSs, and as the nodes broadcast their messages, they can be received by any BS at reach. Thus, the second BS does not affect the performance of the first BS, while bringing an additional chance to receive the packet.

In Fig. 6.7, we have plotted the variation of the gain as a function of the desired node's position, which is defined by the distance between the desired node and both BSs: r_{x1} and r_{x2}. We can observe that the gain is always higher when $r_{x1} = r_{x2}$, compared to other cases. And we note that the highest gain can be achieved when the desired node is located in between the two BSs, where its distance to both BSs is equal to $\frac{d}{2}$.

These results can give us an insight about the best gain we can achieve with an additional BS.

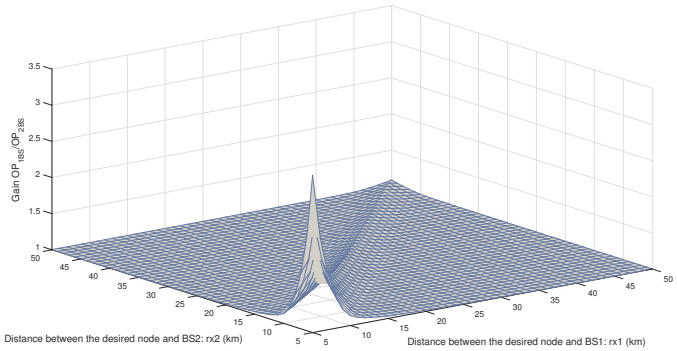

FIGURE 6.7: Gain of two BSs vs the position of desired node presented by r_{x1} and r_{x2}, the active node number $N = 200$, distance between 2 BSs $d = 10$ km, $\lambda = 8 \times 10^{-10}$ nodes$/m^2$, $B = 96$ kHz, $\gamma^* = 6.8$ dB.

6.3.4 Gain of K BSs

Last but not least, we present in Fig. 6.8 the numerical results for K BSs (where K is not limited to 2). The locations of BSs form a square lattice, with equal distance d between adjacent BSs. Similarly, we define the gain of K BSs as $\frac{OP_{1BS}}{OP_{KBS}}$. We observe that when the number of BSs increases, the gain enhances. Indeed, when the BSs becomes denser, their spatial diversity becomes more advantageous. This can also help in the BS deployment and densification.

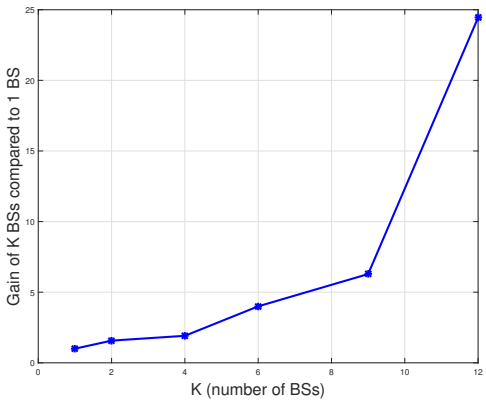

FIGURE 6.8: Gain of multiple BSs vs K the number of BSs, the active node number $N = 200$, distance between each BS $d = 10$ km, $\lambda = 8 \times 10^{-10}$ nodes$/m^2$, $BW = 96$ kHz, $\gamma^* = 6.8$ dB.

6.4 SC: independent interference, joint impact of path loss, fading, and multi-BS

In most of the literature, the case of *common interferer* is rarely seen. Because the interference viewed by each BS is mostly assumed to be independent with the presence of fading [14, 124, 126]. The independence facilitates significantly the

calculation. Meanwhile, in UNB systems, we are not sure if adding one more random coefficient (i.e. the fading) can cancel the correlation of the specific spectral interference.

Therefore, we analyze the selection combining with K BS in this section, with the assumption that the spectral interferences viewed by each BS is independent. We will verify this analysis with simulation results, in order to figure out if the independence assumption holds in UNB networks.

6.4.1 Assumptions different from last section

We take into account the Rayleigh fading which allows the independence of interferences to be possible. The Rayleigh fading follows exponential distribution $g \sim exp(1)$. Indeed, the fading coefficient affects independently the received power of each packet (including the desired node and all interfering nodes). This reduces the probability of having one *common interferer* as demonstrated in the previous section, thus the correlation is reduced.

Additionally, we consider the propagation for all cases (thus the path-loss coefficient $\alpha \in [2, 4]$). And we include the aggregated interference in this section. One may note that these assumptions are identical to those in the Section 4.3.2 for mono-BS case.

The distribution of both nodes and base stations follow independent homogeneous PPP (Poisson Point Process), with the density as λ_n for active nodes, and λ_b for BSs. One can refer this topology to Fig. 6.1(b). Different from last section, we do not predefine the location of the desired node in this section. Therefore, the desired node x is randomly chosen, and can be anywhere in the considered area.

6.4.2 Theoretical analysis

The SIR of the desired node perceived by the ith base station can be expressed as:

$$SIR_{xi} = \frac{g_{xi} \cdot r_{xi}^{-\alpha} \cdot P'_0}{P_{Ii}} \tag{6.13}$$

with the aggregated interference as $P_{Ii} = \sum_{y_i \in \{\mathcal{A}-x\}} g_{yi} \cdot r_{yi}^{-\alpha} \cdot \beta(\delta f_i) \cdot P'_0$.

In the case of selection combining, we have the OP for K BSs as the probability that the SIR received by all the BSs are lower than the predefined value γ^*:

$$\text{OP} = \mathbb{P}(SIR_{x1} < \gamma^* \cap SIR_{x2} < \gamma^* \cap \cdots SIR_{xK} < \gamma^*) \tag{6.14}$$

With the presence of fading, we suppose that the interferences P_{Ii} for each BS is mutually independent. Thus all the SIR_{xi} are independent variables, and their issued events can be treated independently as well. We can thus have eq.(6.14)

rewritten as:

$$\begin{aligned} \mathrm{OP} &= \prod_i \mathbb{P}(SIR_{xi} < \gamma^*) && (6.15) \\ &= \mathbb{E}_{r_{xi}} \left[\prod_i \mathrm{OP}_i(r_{xi}) \right] \\ &\overset{(a)}{=} \exp\left(-2\pi\lambda_b \int_0^\infty (1 - \mathrm{OP}_i(r_{xi})) \cdot r_{xi} dr_{xi} \right) && (6.16) \end{aligned}$$

with λ_b the density of base stations whose distribution follows PPP; (a) comes from the PGFL of PPP [113], for a function $f(x)$, we can have $\mathbb{E}\left[\prod_{x\in\Phi} f(x)\right] = \exp\left(-\lambda \int_{R^2} 1 - f(x)dx\right)$.

We note that $OP_i(r_{xi})$ here is the probability derived in Section 4.3.2. We recall its expression as follows:

$$\mathrm{OP}_i(r_{xi}) = 1 - \mathcal{L}_{P_I}(s) \tag{6.17}$$

with $s = \dfrac{\gamma^*}{r_{xi}^{-\alpha} \cdot P_0'}$.

We can express thus OP of selection combining depending on the Laplace transform of the interference $\mathcal{L}_{P_I}(s)$:

$$\mathrm{OP} = \exp\left(-2\pi\lambda_b \int_0^\infty \mathcal{L}_{P_I}(s) \cdot r_{xi} \cdot \mathrm{d}r_{xi} \right) \tag{6.18}$$

The difference between the $OP_i(r_{xi})$ of mono-BS and the one here, is that the distance between nodes and BSs are no more restraint into the base stations' range, but to $[0, \infty]$. Indeed, as nodes are distributed randomly in the whole considered area, the packets that are not interfered can be perceived by very far away BSs. This range of $[0, \infty]$ has been considered in many studies [108, 126, 130], which has a lot facilitated their analysis.

Laplace transform of $\mathcal{L}_{P_I}$

Therefore, we have to recalculate the expression of $\mathcal{L}_{P_I}(s)$ as follows:

$$\mathcal{L}_{P_I}(s) = \mathbb{E}_{P_I}\left[\exp\left(-P_I \cdot s\right)\right] \tag{6.19}$$
$$= \mathbb{E}_{g_y, r_y, \delta f}\left[\exp\left(-\sum_{y\in\{\mathcal{A}-x\}} g_y r_y^{-\alpha}\beta(\delta f)P_0' \cdot s\right)\right]$$
$$= \mathbb{E}_{g_y, r_y, \delta f}\left[\prod \exp\left(-g_y r_y^{-\alpha}\beta(\delta f)P_0' \cdot s\right)\right]$$
$$\overset{(a)}{=} \exp\left(-\lambda_n \int_{R^2}\left(1 - \mathbb{E}_{g_y,\delta f}\left[\exp\left(-g_y r_y^{-\alpha}\beta(\delta f)P_0' \cdot s\right)\right] \cdot r_y\right) dr_y\right)$$
$$= \exp\left(-2\pi\lambda_n \int_0^\infty r_y dr_y\right) \cdot \exp\left(2\pi\lambda_n \mathbb{E}_{g_y,\delta f}\left[\int_0^\infty \exp\left(-g_y r_y^{-\alpha}\beta(\delta f)P_0' \cdot s\right) \cdot r_y dr_y\right]\right)$$
$$\overset{(b)}{=} 1 \cdot \exp\left(2\pi\lambda_n \mathbb{E}_A\left[\int_0^\infty \exp\left(-r_y^{-\alpha}A\right) \cdot r_y dr_y\right]\right)$$
$$\overset{(c)}{=} \exp\left(2\pi\lambda_n \frac{1}{\alpha} \cdot \mathbb{E}_A\left[\int_0^\infty \exp\left(-tA\right) \cdot t^{-\frac{2}{\alpha}-1} \cdot dt\right]\right)$$
$$\overset{(d)}{=} \exp\left(2\pi\lambda_n \frac{1}{\alpha} \cdot \mathbb{E}_A\left[\frac{\Gamma(-\frac{2}{\alpha})}{A^{-\frac{2}{\alpha}}}\right]\right)$$
$$\overset{(e)}{=} \exp\left(-\pi\lambda_n \cdot \Gamma(1-\frac{2}{\alpha}) \cdot \mathbb{E}_A\left[A^{\frac{2}{\alpha}}\right]\right)$$

(a) comes from the PGFL of PPP [113]. In (b), we replace with $A = g_y\beta(\delta f)P_0's$. In (c), we do a simple variable change where $t = r_y^{-\alpha}$. (d) comes from the definition of Gamma function [131] where we can have: $\int_0^\infty \exp\left(-tA\right) \cdot t^n \cdot dt = \frac{\Gamma(n+1)}{A^{n+1}}$. (e) comes from the property of Gamma function [131], when $n \leq 0$: $\Gamma(n) = \frac{1}{n}\Gamma(n+1)$.

Then we express eq.(6.19) by giving back $A = g_y\beta(\delta f)P_0's$, with the knowledge that $g_y \sim \exp(1)$:

$$\mathcal{L}_{P_I}(s) = \exp\left(-\pi\lambda_n\Gamma(1-\frac{2}{\alpha})\mathbb{E}_{g_y,\delta f}\left[\left(g_y\beta(\delta f)P_0's\right)^{\frac{2}{\alpha}}\right]\right) \tag{6.20}$$
$$\overset{(a)}{=} \exp\left(-\pi\lambda_n\Gamma(1-\frac{2}{\alpha})P_0'^{\frac{2}{\alpha}}s^{\frac{2}{\alpha}} \cdot \int_0^\infty g_y{}^{\frac{2}{\alpha}}e^{-g_y}\mathrm{d}g_y \cdot \mathbb{E}_{\delta f}\left[\beta(\delta f)^{\frac{2}{\alpha}}\right]\right)$$
$$\overset{(b)}{=} \exp\left(-\pi\lambda_n\Gamma(1-\frac{2}{\alpha})\Gamma(1+\frac{2}{\alpha})P_0'^{\frac{2}{\alpha}}s^{\frac{2}{\alpha}} \cdot \mathbb{E}_{\delta f}\left[\beta(\delta f)^{\frac{2}{\alpha}}\right]\right)$$

(a) calculates the expectation by using the PDF of $x \sim \exp(1)$: $f(x) = e^{-x}dx$ for $x \geq 0$; (b) comes from the definition of Gamma function $\Gamma(a) = \int_0^\infty t^{a-1}e^{-t}dt$ for $Re(a) > 0$.

We note that the form of eq.(6.20) confirms well with the expression in [126], where the $\mathcal{L}_{P_I}(s)$ is calculated for ALOHA and slotted-ALOHA case. But in our case, we have the term containing the frequency interference in addition, i.e. $\mathbb{E}_{\delta f}\left[\beta(\delta f)^{\frac{2}{\alpha}}\right]$.

Then we can derive the expression of $\mathbb{E}_{\delta f}\left[\beta(\delta f)^{\frac{2}{\alpha}}\right]$ in the following steps:

$$\mathbb{E}_{\delta f}\left[\beta(\delta f)^{\frac{2}{\alpha}}\right] = \int_{-\infty}^{\infty} \beta(\delta f)^{\frac{2}{\alpha}} \cdot \mathbb{P}(\delta f) d\delta f \tag{6.21}$$
$$= \left(\frac{150}{\sigma\sqrt{2\pi}}\right)^{\frac{2}{\alpha}} \cdot \frac{1}{B}\left(\sqrt{\sigma^2\alpha\pi}\text{erf}\left(\frac{B}{\sqrt{\sigma^2\alpha}}\right) + \frac{\sigma^2\alpha}{B}\left(e^{-\frac{B^2}{\sigma^2\alpha}} - 1\right)\right)$$

with $\beta(\delta f) = \frac{150}{\sigma\sqrt{2\pi}} \exp^{\frac{-\delta f^2}{2\sigma^2}}$, and $P(\delta f) = \frac{2}{B}\left(1 - \frac{\delta f}{B}\right)$, for $\delta f \in [0, B]$.

Final expression

Now we combine the expression of $\mathcal{L}_{P_I}(s)$ with eq.(6.18), and we have the expression of OP with selection combining as:

$$\text{OP} = \exp\left(-2\pi\lambda_b \int_0^{\infty} \mathcal{L}_{P_I}(s) \cdot r_{xi} \cdot \text{d}r_{xi}\right) \tag{6.22}$$
$$= \exp\left(-2\pi\lambda_b \int_0^{\infty} \exp\left(-\pi\lambda_n \Gamma(1 - \frac{2}{\alpha})\Gamma(1 + \frac{2}{\alpha})\gamma^{*\frac{2}{\alpha}} \mathbb{E}_{\delta f}\left[\beta(\delta f)^{\frac{2}{\alpha}}\right] \cdot r_{xi}^2\right) \cdot r_{xi} \cdot \text{d}r_{xi}\right)$$
$$= \exp\left(-\frac{\lambda_b}{\lambda_n \Gamma(1 - \frac{2}{\alpha})\Gamma(1 + \frac{2}{\alpha})\gamma^{*\frac{2}{\alpha}} \mathbb{E}_{\delta f}\left[\beta(\delta f)^{\frac{2}{\alpha}}\right]}\right)$$

with λ_n being the density of nodes, λ_b being the density of base stations, α being the path loss exponent, γ^* being the threshold of SIR.

We can see that this OP expression, with the assumption that the interferences viewed by each BS are independent, is directly related to the ratio between the BSs' density and the active nodes' density $\frac{\lambda_b}{\lambda_n}$. Since we have two Gamma functions containing α, the OP is easily impacted by the path loss exponent.

6.4.3 Validation

We compare the numerical results with the theoretical OP expression eq. (6.22) in this part. The simulations are conducted with the same assumptions than in th theory. The only difference is that, in the theoretical analysis, we have assumed that the distance between each node and each BS is among $[0, \infty]$. But the in simulations, we have to define an area with bounds. We have thus defined the considered area as a square of $200km \times 200km$. We recall the basis hypothesis in the following table:

TABLE 6.2: Simulations hypothesis for multi-BS SC with fading (*notation: db= distribution)

BS number	BS db	nodes db	desired node	path loss	fading	AIP
$\lambda_b \times$ area surface	random	random	random	α	yes	yes

As plotted in Fig. 6.9, we have illustrated the variation of OP as a function of fours parameters: the node density λ_n, the BS density λ_b, the total available

frequency resource B and the predefined SIR threshold γ^*. Unfortunately, the numerical results do not always coincide with the theoretical ones.

The main reasons causing the inaccuracy can be the following:

- the independent hypothesis does not hold in the UNB systems. Even though the fading adds a new degree of freedom in the received power, the case that one common interferer is perceived by multiple BSs still exists. Thus the correlation of UNB interference cannot be totally canceled by the fading.
- we have assumed that the nodes (and BSs) distributed area can by extended to infinity, thus the OP expression depends strongly on the path loss exponent α. But in the simulations this area is bounded. As shown in Fig. 6.10, the theoretical OP degrades very fast with the increase of α, meanwhile the numerical one tends to be more smooth. This difference can cause the gap between theoretical and numerical results.

However, we can still remark something useful, such as in Fig. 6.9(A), when the node density is high enough, the simulations somehow coincide with the theory. Similarly, in Fig. 6.9(B)-(C) the two curves cross at certain points. This observation confirms with the paper [126], where the authors have concluded that the independence assumption only holds for certain traffic loads.

In the expression of eq.(6.22), the OP depends directly on the ratio $\frac{\lambda_b}{\lambda_n}$. We have thus defined the normalized load as $\frac{\lambda_n}{\lambda_b}$, which is the reciprocal of the ratio. We have plotted the OP in Fig. 6.11 when maintaining the load constant, for different scales of λ_n. We can observe that the numerical OP remains constant (whatever the scale of node density is), as predicted by the theory.

Therefore, the theory when considering independent interferers can give us an insight of the variation of the OP, as well as the essential influencing parameter (i.e. the ratio of nodes and BSs density $\frac{\lambda_b}{\lambda_n}$), whereas it is not accurate enough.

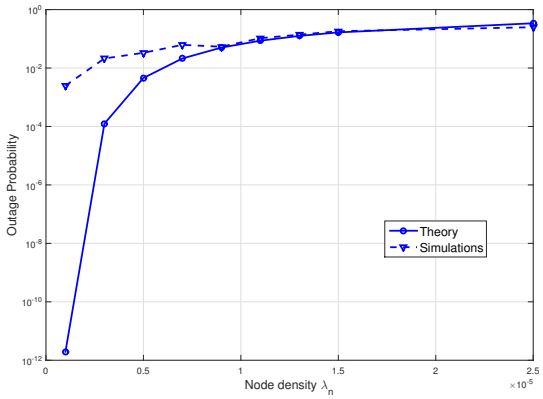

(A) OP vs λ_n, for $\lambda_b = 2 \times 10^{-6}$, $B = 12$ kHz, $\gamma^* = 6.8$ dB, $\alpha = 3.5$

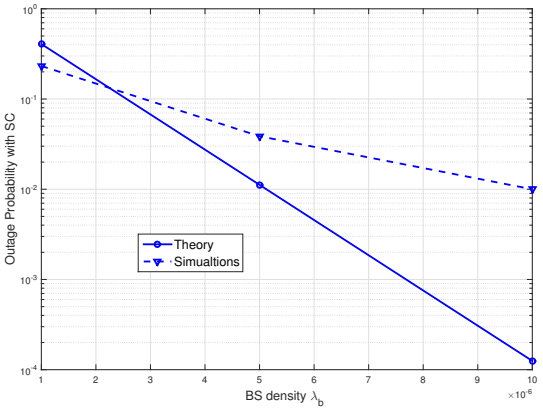

(B) OP vs λ_b, for $\lambda_n = 15 \times 10^{-6}/km^2$, $B = 12$ kHz, $\gamma^* = 6.8$ dB, $\alpha = 3.5$

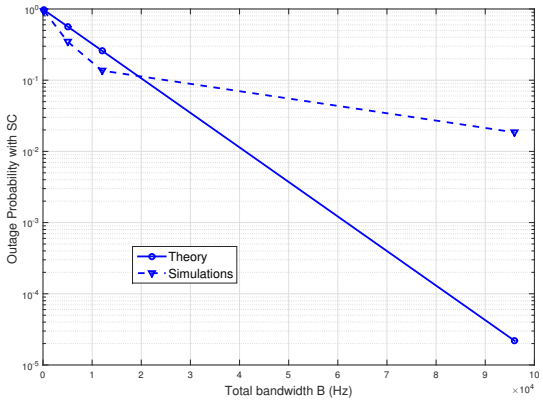

(C) OP vs B, for $\lambda_n = 15 \times 10^{-6}/km^2$, $\lambda_b = 1 \times 10^{-6}/km^2$, $\gamma^* = 6.8$ dB, $\alpha = 3.5$

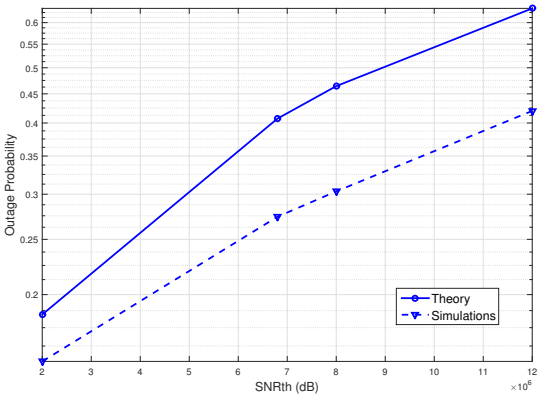

(D) OP vs γ^*, for $\lambda_n = 15 \times 10^{-6}/km^2$, $\lambda_b = 1 \times 10^{-6}/km^2$, $B = 12$ kHz, $\alpha = 3.5$

FIGURE 6.9: Comparison of OP in simulations and theory. (A) the normalized load $\frac{\lambda_n}{\lambda_b}$ =[0.5, 1.5, 2.5, 3.5, 4.5, 5.5, 6.5, 7.5, 12.5]; (B) the load $\frac{\lambda_n}{\lambda_b}$ =[15, 3, 1.5]; (C) the load $\frac{\lambda_n}{\lambda_b} = 15$; (D) the load $\frac{\lambda_n}{\lambda_b}$ =15.

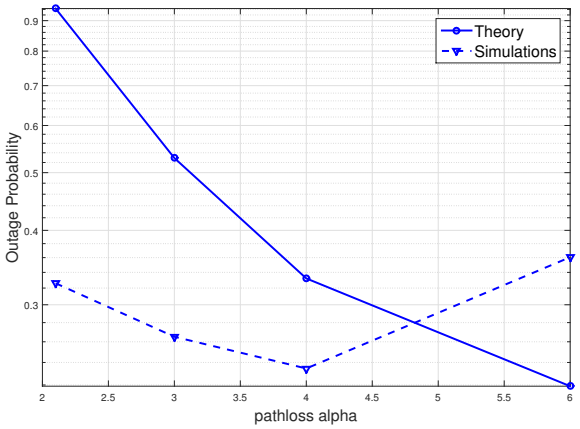

FIGURE 6.10: OP vs path loss exponent α, with $\frac{\lambda_n}{\lambda_b} = 15$, for $B = 12$ kHz, $\gamma^* = 6.8$

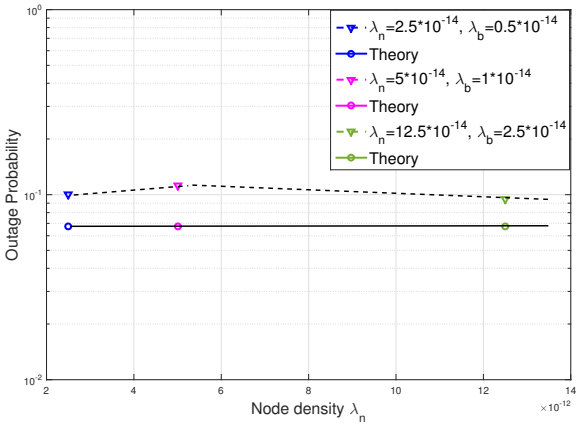

FIGURE 6.11: OP vs constant $\frac{\lambda_n}{\lambda_b}$ =5, for $B = 12$ kHz, $\gamma^* = 6.8$, $\alpha = 3.5$

To conclude, we have added Rayleigh fading in the selection combining of multiple BSs. We have assumed that the correlated interference (presented in the last section) disappears with the presence of fading. We have thus treated the OP as a joint probability eq.(6.14) composed by independent events, and we have a beautiful OP expression. However, this analytical OP does not provide enough accuracy to predict the network performance. We conclude that the assumption of independent interference does not hold in UNB systems.

6.5 MRC and EGC

In this section, we consider two other common signal combining technologies: Max ratio combining (MRC) and Equal gain combining (EGC). They are more complex than the simple selection combining, but can help us to take better advantage of the spatial diversity in UNB systems.

6.5.1 Existing studies

Combining technologies such as MRC and EGC are originally used in multiple-antennas system [132]. One BS combines the signals from all of its antennas (or branches) to obtain an output signal. These signals experience the same propagation path loss, but independent fading paths. The combining is mostly carried out after the detection of signals, then the output will pass through a standard demodulator.

However, the receiver complexity of MRC and EGC is directly proportional to the number of branches, which makes them rarely used in real systems. The suboptimal is SC, which is simple to implement but cannot take the maximum advantages of the diversity. The authors in [133] have proposed to combine SC and MRC together, where they select only the three branches with the highest SINR and then combine them with MRC techniques, in Rayleigh fading channels. This makes a compromise between the complexity and the performance.

More recently, these combing techniques are compared and hybrid for more complicated channels, such as a highly faded two-wave with diffuse power environment in [134].

Different from traditional multi-antennas systems, the BSs that we consider in this thesis have only one antenna each. Since we want to combine the signals (of the same packet) received by each BS, our system can be seen as distanced multi-antennas, thus distributed SIMO (single input multiple output) system. The only random parameter is the fading in traditional SIMO systems, whereas the distributed ones have one more random parameter: the distance between one given packet and each BS.

To the best of our knowledge, there exist rarely works about applying MRC or EGC in distributed SIMO systems. What's more, the specific UNB spectral interference has never been considered in this kind of signal combining receivers. Our contribution is thus to measure the efficiency of such combining technologies in distributed SIMO systems where the nodes' carrier frequencies are random (in time also, but we don't consider it in this section).

6.5.2 Principle of MRC/EGC

In both combining technologies, the combiner output is envelop of the weighted sum of all branches' signal amplitude. The purpose of MRC is maximize the output signal's SINR by choosing the weights. The intuition is that the branches having good channel conditions should be weighted more than branches with bad conditions. However, in EGC the weights for each branch are identical.

Normally, the linear combing requires co-phasing, which can be achieved by an phase removal operation [135]. Without co-phasing, the branch signals would not add up coherently in the combiner, so the resulting output could still exhibit significant fading due to constructive and destructive addition of the signals in all the branches. Therefore, we consider that all the signals are co-phasing in this section.

We have illustrated the algorithm of MRC and EGC in Fig. 6.12. One symbol x (whose amplitude can be ± 1) is transmitted, and perceived by all the BSs (i.e. the branches). At the ith branch, its amplitude is affected by h_i which represents the channel condition (thus the channel gain) of BS_i. During the transmission, the noise and interference are added, which also change the symbol's amplitude.

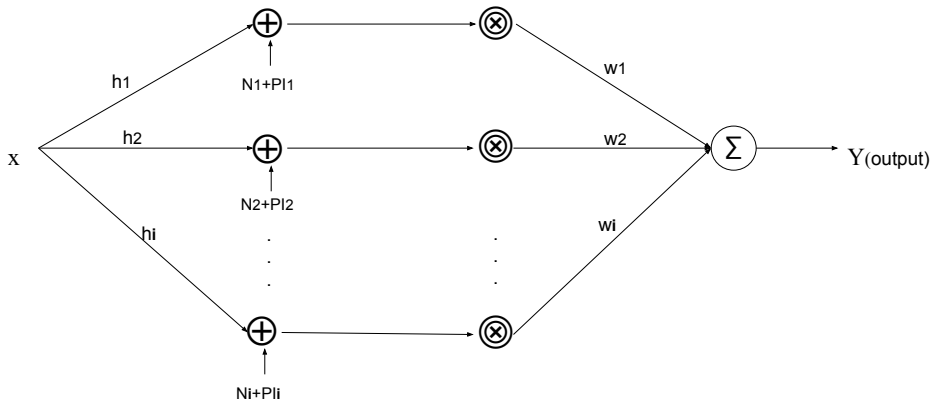

FIGURE 6.12: Algorithm of MRC/EGC. x represents the transmitted symbol, h_i is the channel gain of BS_i, N_i and PI_i are the AWGN noise and the interference experienced by the expected signal in the branch BS_i, w_i is the weight at the ith branch.

In most of the literature , the interference is not considered [132]. The noise is AWGN noise whose amplitude follows zero-mean normal distribution $\sqrt{N_i} \sim \mathbb{N}(0, \sigma_0^2)$. Under these conditions, we can express the transmitted symbol's amplitude at each branch:

$$x_i = x \cdot h_i + \sqrt{N_i} \tag{6.23}$$

Accordingly, after the process of MRC/EGC, the output signal's amplitude denotes:

$$\begin{aligned} y &= \sum_{i=1}^{K} x_i \cdot w_i \\ &= \sum_{i=1}^{K} x \cdot h_i \cdot w_i + \sum_{i=1}^{K} \sqrt{N_i} \cdot w_i \end{aligned} \tag{6.24}$$

with K the number of the branches.

As the purpose of combining is to maximize the SNR (when the interference is not considered) of the output y, the signal power P_s and the noise power P_N denote respectively:

$$P_s = \frac{1}{2} |x \cdot \sum_{i=1}^{K} h_i \cdot w_i|^2; \qquad P_N = |\sum_{i=1}^{K} \sqrt{N_i} \cdot w_i|^2 = \sigma_0^2 \cdot |\sum_{i=1}^{K} \cdot w_i|^2 \tag{6.25}$$

We can thus express the SNR of the output signal y as the following:

$$\begin{aligned} SNR_y &= \frac{P_s}{P_N} \\ &= \frac{|x|^2}{2} \cdot \frac{|\sum_{i=1}^{K} h_i \cdot w_i|^2}{\sigma_0^2 \cdot |\sum_{i=1}^{K} w_i|^2} \\ &\overset{(a)}{\leq} \frac{|x|^2}{2} \cdot \frac{|\sum_{i=1}^{K} h_i|^2 \cdot |\sum_{i=1}^{K} w_i|^2}{\sigma_0^2 \cdot |\sum_{i=1}^{K} \cdot w_i|^2} \\ &= \frac{|x|^2}{2} \cdot \frac{|\sum_{i=1}^{K} h_i|^2}{\sigma_0^2} \\ &= \sum_{i=1}^{K} SNR_i \end{aligned} \tag{6.26}$$

(a) comes from the Swartz inequality [136] where the equality can be achieved when $w_i = c \cdot h_i$, with c being a constant.

We can see that the combiner output's maximum SNR becomes the sum of the SNR in each branch. And the best weight which maximizes the SINR of the output signal is linearly proportional to the channel gain h_i. This confirms our intuition about MRC at the very beginning of this subsection.

6.5.3 MRC/EGC in UNB multiple BSs

However, in our systems where the medium access is random, the interference cannot be ignored. Accordingly, when including the interference, the envelop of the combiner output becomes:

$$y = \sum_{i=1}^{K} x \cdot h_i \cdot w_i + \sum_{i=1}^{K} \sqrt{N_i} \cdot w_i + \sum_{i=1}^{K} \sqrt{PI_i} \cdot w_i \tag{6.27}$$

We can express the SINR of the MRC combiner output as the following:

$$SINR_y = \sum_{i=1}^{K} w_i \cdot SINR_i \tag{6.28}$$

For EGC combiner, the weight is identical for each branch, and it denotes:

$$w_i(EGC) = 1 \tag{6.29}$$

For MRC combiner, the question comes: is the weight $w_i(MRC)$ to maximize $SINR_y$ still proportional to the channel gain h_i? Indeed, the channel gain h_i reflects the quality of the channel conditions, but it cannot give us any information about the level of the interference PI_i. On the contrary, the signal to interference and noise ratio $SINR_i$ can give us all the information. We thus propose to two ways to compute the w_i: the first one is proportional to h_i, and the second one is proportional to $SINR_i$.

When w_i is proportional to channel gain h_i

If we consider that the best-fitting branch weight w_i is proportional to h_i, for K inputs at the MRC combiner, the best weight denotes:

$$w_i(MRC) = \frac{h_i}{\sum_{i=1}^{K} h_i} \cdot K \tag{6.30}$$

with $h_i = \frac{g_i}{\sqrt{d_i^{\alpha}}}$ composed by the Rayleigh fading variable g_i, the distance between the given node and each BS d_i, and the path loss exponent α.

When w_i is proportional to the $SINR_i$

If we consider that the best-fitting branch weight w_i is proportional to the $SINR_i$ of each branch, for K inputs at the MRC combiner, this weight denotes:

$$w_i(MRC) = \frac{SINR_i}{\sum_{i=1}^{K} SINR_i} \cdot K \tag{6.31}$$

Evaluation of two w_i propositions for MRC

Now we evaluate these two propositions of best-fitting weight for MRC combiner. We have a representative example of one packet (whose original amplitude $x = \pm 1$) perceived by 3 BSs in Table 6.3.

We have neglected noise here to make it simpler. We have assumed the threshold of SIR to $\gamma^* = 15$ (which is a linear value, but not in dB). We can thus see that the SIR_i of all the 3 BSs are below this threshold, hence this packet cannot be decoded by any of these three base stations alone. We apply MRC to maximize the output's SIR, thus we consider these BSs as 3 branches. Each branch has its own channel gain h_i, interference level PI_i, and the according SIR_i.

If we compute w_i given by the channel gain h_i, as illustrated in eq.(6.30), we have the fifth column. And if we compute it proportionally to the SIR_i as illustrated in eq.(6.31), we have the sixth column.

We can observe the MRC output's SIR_y at the last line, which indicates that the $w_i(MRC)$ given by SIR_i gives better output. Indeed, BS_1 has the best channel gain, but the signal envelop is strongly affected by the interference, which causes a very low SIR_1. If we insist in computing the weight according to h_i, this branch would have the highest weight regardless its low SIR_1. However, if it is computed proportionally to the SIR_i, we can see that it is the second branch which weights the most, and that it delivers a higher output SIR_y.

What's more, the tricky part in the first method is to estimate the channel gain h_i, as it depends not only on the respective distance (which we can obtain by the localization of devices), but also the Rayleigh fading (which is not realistic to predict). Thus the first method is very complex to be implemented in realistic systems.

In conclusion, we opt the second method, which is proportional to the SIR_i of each branch as shown in eq.(6.31), to calculate the best-fitting MRC weight. One may say that this example can be just a particular case, but we note that the case, where both the channel gain and the interference are high (i.e. the first line in Table 6.3), happens frequently in the UNB systems. Since h_i and PI_i are independently

random variables, they are nor correlated, so the chance that PI_i is higher than h_i is identical to the inverse case. Therefore, the example in Table 6.3 is representative.

	h_i	PI_i	$SIR_i = \frac{0.5(x \cdot h_i)^2}{PI_i}$	$w_i(MRC)$ given by h_i	$w_i(MRC)$ given by SIR_i
BS_1	5	6	2.1	$\frac{5}{8} \times 3$	$\frac{2.1}{16.6} \times 3$
BS_2	1	0.2	12.5	$\frac{1}{8} \times 3$	$\frac{12.5}{16.6} \times 3$
BS_3	2	1	2	$\frac{2}{8} \times 3$	$\frac{2}{16.6} \times 3$
SIR_y				10.13	29.76

TABLE 6.3: Example of 3 inputs of MRC combiner, with h_i as the channel gain of each branch, PI_i as the interference level of each branch, x as the amplitude of the transmitted symbol which equals to ± 1, SIR_i the ratio of each branch and SIR_y the ratio of the MRC combiner output.

6.5.4 Process of MRC/EGC combiner

The process steps of a MRC/EGC combiner are the following:

1. Firstly, we start with the process of selection combing. For each packet, we compare the $SINR_i$ of each base station to the predefined threshold γ^*:
   - If any of these $SINR_i > \gamma^*$, we consider this packet successfully decoded. No MRC or EGC is needed.
   - On the contrary, if none of these $SINR_i$ is above the threshold, we process MRC or EGC. We consider all the BSs as the input branches of the combiner.
2. The combiner applies the weight w_i to each branch. The best-fitting weights for MRC are determined by eq.(6.31), and EGC by eq.(6.29).
3. Now we have the combiner output's $SINR_y$, which is computed by eq.(6.28). Then we check if $SINR_y$ has surpassed the threshold γ^*. If yes, we consider that the packet is successfully decoded, otherwise we consider it lost.

Intuitively, MRC is the ideal candidate as it takes into account the channel quality and interference, and adapts them to the weights. A EGC combiner needs not to estimate the $SINR$, which makes it easier to implement. But the equal weight in EGC equalizes the signals (in good quality and bad quality) in each branch, which does not maximize the output's SINR.

We will demonstrate the performance of MRC and EGC in Section 6.7.

6.6 SIC for multiple BSs

We have analyzed the performance of SIC (Successive Interference Cancellation) in single BS case in chapter 5, where the gain of SIC turns to be very limited. In

this section, we propose to apply SIC in multiple BSs case, in order to mitigate the interference by exploiting the spatial diversity.

6.6.1 Existing studies

As presented in chapter 5, the technology SIC is mostly used to mitigated interference due to random access systems, in single base station case. The very first works, which proposed to do interference cancellation across multiple receivers, are in the context of TDMA (time division multiple access) [137] or CDMA (code divisionn multiple access) [138].

Then multi-BS systems applying SIC are mostly focused in the slotted ALOHA scheme. The authors in [139] brought up in 2015 to apply the usage of SIC in multiple BSs case, in the slotted ALOHA (plus the replications) framework. They have considered several cooperation modes among the BSs: non-cooperated (the same as selection combining), temporal (BSs process SIC locally), spatial (SIC across cooperated BSs) and spatio-temporal (where spatial and temporal cooperation are alternated over several decoding iterations). They have shown fundamental results for all the modes of cooperation. Similarly, the authors in [122] have provided numerical results of SIC across multiple in slotted ALOHA scheme, where they have found out that non co-located receivers provide higher gain in SIC. The authors in [140] provided experimental results.

Multiple BSs combined with SIC in the context of M2M is evaluated in [141], still in slotted Aloha scheme. Interestingly, they have considered the devices using directional antennas where an additional degree of freedom, i.e. the randomly chosen beam, has been added in the analysis.

Among the existing studies, none of them has considered a totally random radio access scheme where the partial interference exists. Our contribution of this section is to apply SIC across multiple BSs, when taking into account the specific partial interference of UNB systems.

6.6.2 Advantages of SIC + multi-BS

The combination of SIC and multi-BS allows us to take advantage of the received power diversity and the spatial diversity jointly. As the distance between one node and each BS is random, thus not only its received power, but also the interference power perceived by each BS vary. In single BS case, sometimes none of the iterations of SIC is possible, because the desired node's signal is strongly influenced by the interference.

However in multiple BS systems, the undesired phenomenon (where SIC is stopped by strong interference) can be largely reduced. A packet is considered successfully received if it is decoded at any BSs. We kindly remind that the criteria that one packet can be decoded is that its SINR should be above a predefined threshold: $SINR > \gamma^*$. The decoded packet's contribution can thus subtracted from collisions at all the BSs (where it is found in collision with other packets). Consequently, new singletons would be generated and be decoded by iterative procedures at other BSs. We assume that all the BSs can reconstruct and subtract the signals perfectly, without leaving residues.

There are two ways to perform SIC across multi-BS: a local way and a global way, which will be introduced in the following parts.

6.6.3 Local SIC

In the local SIC across multi-BS, the base stations do not communicate directly with each other. They proceed SIC locally until the last iteration, then they all send their decoded packets to the back-haul, as illustrated in Fig. 6.13. With the presence of spatial diversity, the packets decoded in one BS may be undecodable in another BS. But since the back-haul collects the decoded packets from all the existing BSs, naturally the performance is better than only one BS. This procedure can be seen as a combination of selection combing across multi-BS which perform SIC locally. We note that the iteration number is normally predefined to avoid spending too many calculation resources.

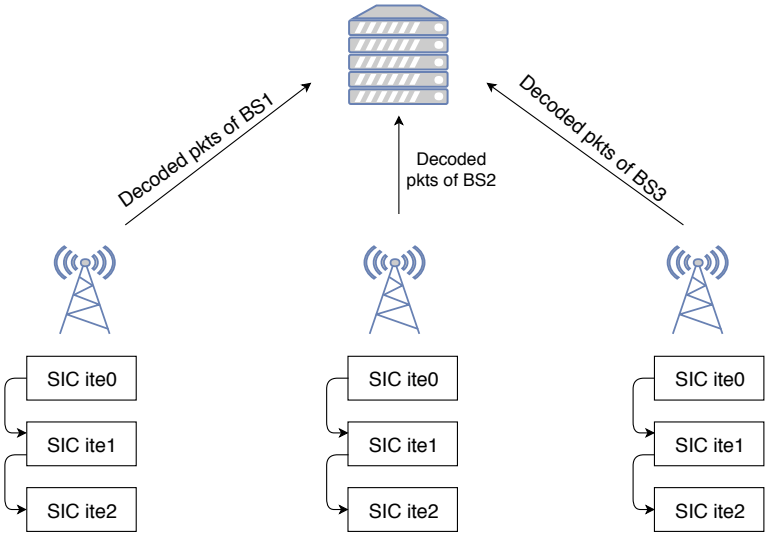

FIGURE 6.13: Algorithm of local SIC across multiple BSs. The BSs perform SIC locally, then forward their decoded packets to the back-haul. *Ite*0 represents the procedure of a simple receiver; the maximum SIC iteration is defined to 2.

6.6.4 Global SIC

In the global case, the base stations cooperate to carry out SIC. All the BS, after each SIC iteration, will send their decoded packets to all the neighboring BSs directly via dedicated links. These links are assumed to be in-expensive and provides low-latency, high data rate communication. As demonstrated in Fig. 6.14, the term $\mathbb{D}(i,j)$ contains the packets decoded by BS_i, after the jth SIC iteration. We assume that $\mathbb{D}(i,j)$ contains all the signal details which allow other BSs to reconstruct them.

After each SIC iteration, $\mathbb{D}(i,j)$ will be broadcast to all the neighboring BSs. We assumed that the base stations have the propriety to relay packets for those which are physically far away, i.e. the decoded packets' exchange between BS_1 and BS_3 can be carried out by BS_2 in Fig. 6.14. Afterward, the BSs can exploit $\mathbb{D}(i,j)$ coming from other BSs, to reconstruct the packets they need and eliminate the issued packets' contributions. As a result, the strongly interfered packets become decodable in some BSs thanks to $\mathbb{D}(i,j)$. This procedure is performed by all the BSs, after each iteration.

At the end of the last SIC iteration, all the BSs group their decoded packets through all the iterations sum($\mathbb{D}(i,j)$), then forward them to the back-haul.

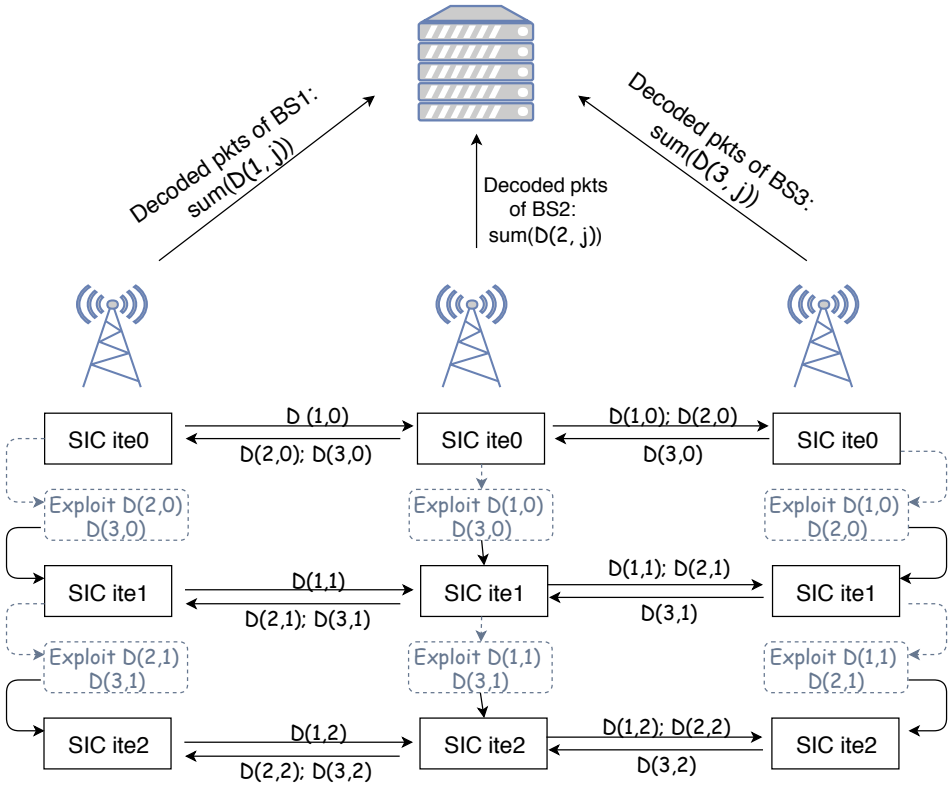

FIGURE 6.14: Algorithm of global SIC across multiple BSs. $\mathbb{D}(i,j)$ contains the packets decoded by the ith BS, after the jth SIC iteration. Firstly, each BS performs 0th iteration locally, then they exchange their own decoded packets $\mathbb{D}(i,0)$ with other BSs. Then each BS exploits (reconstruct and subtract) the decoded packets they receive, and carried out a new iteration of SIC. The procedure stops at the end of the 2nd iteration, and each BS forwards the sum of their decoded packets from all the iterations sum($\mathbb{D}(i,j)$) to the back-haul.

6.7 Performance evaluation

In this section, we demonstrate the performance evaluation of all the technologies mentioned in the chapter: SC (selection combining), MRC (max ratio combining), EGC (equal gain combining), local SIC of multi-BS and global SIC across multi-BS. In order to perceived the gain of multiple BSs compared to single BS, we have also shown the performance of single BS. Additionally, we have added the performance of the nearest BS.

6.7.1 OP measurement

The term to measure the performance is still OP (outage probability). One packet is considered decoded if its SIR turns out above the predefined threshold γ^*. However, according to different technologies, the approach to calculate OP can vary:

- **For single BS**: OP is simply the probability that one packet can't be decoded by this only BS: OP $= \mathbb{P}(SINR < \gamma^*)$.
- **For the nearest BS**: for each transmission, we focus on the performance of the nearest (with respect to the physical distance) BS. Thus for one packet, OP is the probability not to be decoded by its nearest BS:
  OP $= \mathbb{P}(SINR_{(nearestBS)} < \gamma^*)$.
- **For SC**: for one packet perceived by all the base stations (the ith BS perceives the packet with $SINR_i$), if any of the $SINR_i$ is higher than the threshold, we consider that the given packet is successfully decoded. Hence OP is the probability that one packet is decoded by none of the BSs:
  OP $= \mathbb{P}\left(max(SINR_i) < \gamma^*\right)$.
- **For MRC**: one packet is perceived with $SINR_i$ by the ith BS, we combine all the adequate SINR with a best fitting weight w_i. Supposing that there are K adequate branches (if the SINR of the branch is above the threshold), the MRC combiner output will be a weighted sum of these K branches. Therefore, OP is the probability that the combiner output's SINR turns out lower that the threshold: OP $= \mathbb{P}\left(\sum_{i=1}^{K} w_i(MRC) \cdot SINR_i < \gamma^*\right)$
- **For EGC**: similar to the MRC case. The difference is that the EGC combiner output applies equal weight for each qualified branch:
  OP $= \mathbb{P}\left(\sum_{i=1}^{K} w_i(EGC) \cdot SINR_i < \gamma^*\right)$
- **For local SIC + multi-BS**: each BS carries out SIC locally, then forwards their decoded packets to the back-haul. One packet is thus considered lost if it is not decoded by any of the base stations, at the end of all the SIC iterations:
  OP $= \mathbb{P}\left(max(SINR_{(local\ SIC)i}) < \gamma^*\right)$.
- **For global SIC + multi-BS**: all the BSs cooperates to perform SIC, they exchange with each other their decoded packets after each iteration. Then the all the decoded packets can be reconstructed and subtracted at each BS, which helps to perform the next SIC. One packet is thus considered lost if it is still not decoded after the global SIC procedure across all the BS:
  OP $= \mathbb{P}\left(max(SINR_{(global\ SIC)i}) < \gamma^*\right)$.

6.7.2 Simulation hypothesis

We have carried out Monte-Carlo simulations based on Matlab. The distribution of the nodes follows homogeneous Poisson point process (HPPP) with density λ_n, whereas the locations of BSs follows a HPPP (independent from the nodes' HPPP) with density λ_b. This topology can be refereed to Fig. 6.1(b) at the beginning of this chapter.

We consider the path loss exponent α whose value is normally between $[2, 4]$. The free space propagation corresponds to $\alpha = 2$. We take into account the Rayleigh fading, which follows an exponential distribution of the mean equaling to 1. The fading adds a novel degree of freedom in the signal power diversity, which aids the techniques of multi-BS. We assume that the spectral interference is the aggregated interference power (AIP) caused by all the active nodes (except

the randomly chosen observed node itself). One can refer to Section 4.3.1 where the term AIP is characterized.

We assume that the links between each BS and the back-haul provide low-latency and high data rate communication. We also suppose that all the SIC processors are able to reconstruct and subtract signals perfectly. We note that the SIC iteration starts with the 0th iteration which is the process of a simple receiver. The maximum iteration number is predefined to avoid spending too many calculation resources.

We list the basis hypothesis in the Table 6.4 for a clearer view:

TABLE 6.4: Simulations hypothesis for all multi-BS technologies (*notation: db= distribution)

BS number	BS db	nodes db	desired node	path loss	fading	AIP
$\lambda_b \times$ area surface	random	random	random	α	yes	yes

6.7.3 Comparison of all technologies

We have carried out Monte-Carlo simulations based on matlab, with the following parameters: the nodes and BSs are distributed in a $200km \times 200km$ square area; the Rayleigh fading which follows an exponential distribution with the mean equals to 1.

We have plotted in Fig. 6.15 the OP with respect to the normalized load $\frac{\lambda_n}{\lambda_b}$, in Fig. 6.16 the OP with regards to the SIR threshold γ^*, for both 1 and 2 maximum SIC iterations, and for all the technologies.

Firstly, we can observe that the technologies taking advantage of multi-BS have always better performance than single BS. Then we remark that $OP_{(nearest\ BS)}$ has worse performance than SC. This is because there are random factors such as fading, and the UNB spectral interference. Thus the shortest distance (i.e. nearest BS) delivers worse performance than the highest SIR (i.e. selection combining).

Secondly, we notice that MRC/EGC are always better performing than SC. This is due to the fact that the process of MRC and EGC are based on the results of selection combining. If one packet can be decoded by any one of the BSs, there is no need to send it into the MRC/EGC combiner. We only combine the packets whose SIR_i is in poor quality in all branches. Therefore, it is relevant that MRC and EGC outperform SC.

Furthermore, we remark that MRC outperforms EGC. Indeed, the weights of MRC take into account the channel gain and interference, i.e. they are proportional to the SIR of each branch. Hence the MRC weights are be able to maximize the MRC combiner output's SIR. However, the EGC weights are identical in all the branches, which equalize the signals both in good and bad quality. In a consequence, even though EGC is easier to implement, its performance still falls behind MRC.

Thirdly, we can note that the global SIC across multi-BS has better performance than local SIC at each BS. This is not surprising since the global SIC allows all the BSs to share information with each other, and thus to reconstruct and subtract the packets decoded by other BS. This results in decoding more packets than the SIC

performed locally at each BS. It is also the reason why global SIC outperforms MRC, as MRC adds up both the signals and the interferences, while global SIC can retrieve interferences.

Fourthly, when we compare Fig. 6.15(A, B) or Fig. 6.16(A, B), we remark that local and global SIC only have slight performance enhancement when the maximum iteration number increases. Moreover, the higher the SIC iteration becomes, the higher the system complexity becomes, and the more computation resource we need. Thus through this result, we know that we can gain almost the same with 1 SIC iterations, without spending more computation resource to increase it to 2.

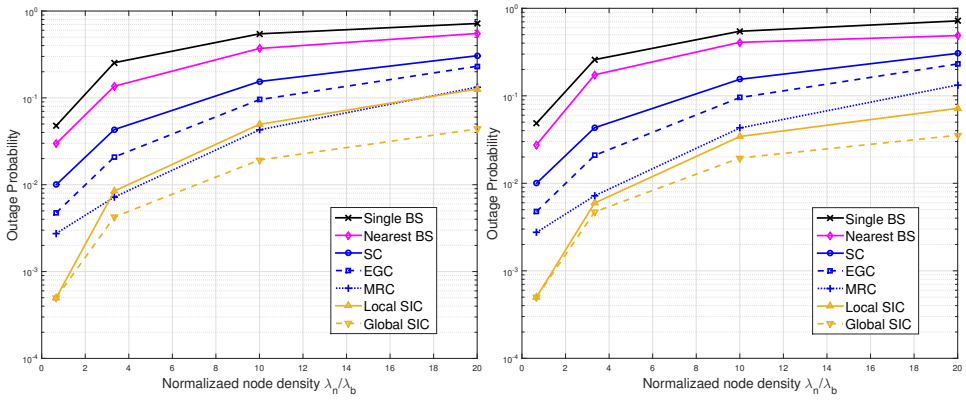

(A) Maximum 1 SIC iteration

(B) Maximum 2 SIC iteration

FIGURE 6.15: OP vs normalized load $\frac{\lambda_n}{\lambda_b}$, with $B = 12$kHz, $\gamma^* = 6.8$dB, and $\alpha = 2$.

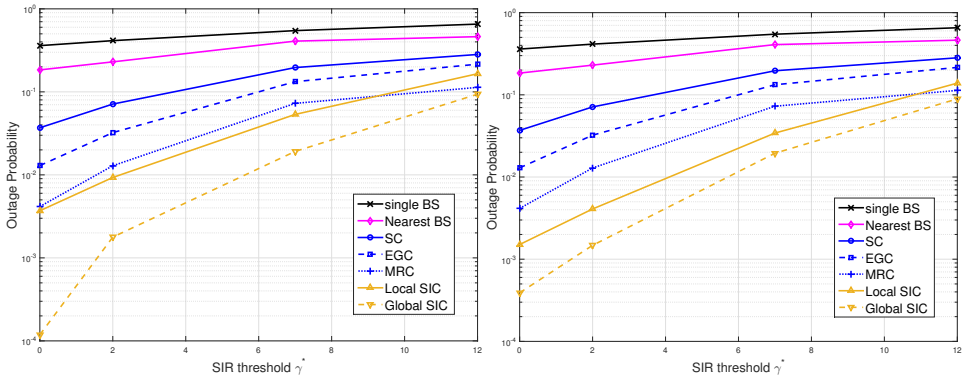

(A) Maximum 1 SIC iteration

(B) Maximum 2 SIC iteration

FIGURE 6.16: OP vs SIR threshold γ^*, with $\frac{\lambda_n}{\lambda_b} = 10$, $B = 12$kHz, and $\alpha = 2$.

Interestingly, when we observe Fig. 6.15-6.17, the performance of different technologies have the same tendency, i.e. the classical behaviors: when the traffic load are denser, or when the frequency resource becomes more limited, or when

the threshold to successfully decode a packet becomes more strict, the OP increases. Meanwhile, when we observe Fig. 6.18 where we vary the path loss exponent α, the variation of OP is not identical to all the technologies. The OP increases slightly for single BS, which is not surprising as the increase of α makes the packets become vulnerable to interference.

The OP fluctuates when α increases for most technologies, while it decreases gradually in both local and global SIC cases. We can deduce that SC/MRC/EGC are not sensible to the increase of α, which gives similar performance when α is higher than free space. Meanwhile, the increase of α has positive impacts on the performance of SIC across multi-BS. This is probably due to the fact the desired node's power is significantly reduced because of the increase of α, thus the circular zone where potential interferers can fall into is narrowed down. Consequently, the number of interferers which are common for all the BSs become very low. Therefore, one decoded packet can help the maximum packets to be relieved from its interference. So when we collect all the packets decoded from all the BSs, the number of decoded packets increases, which results in less OP in the case of SIC across multi-BS.

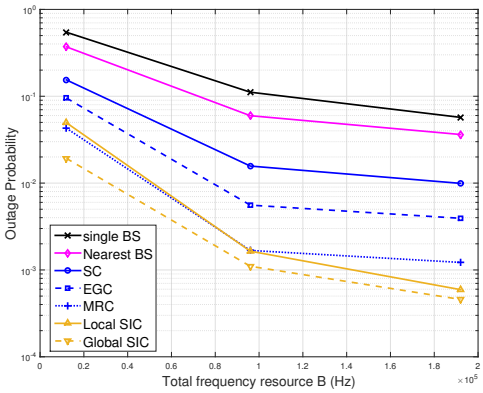

FIGURE 6.17: OP vs B, with $\frac{\lambda_n}{\lambda_b} = 10$, $\gamma^* = 7$dB, and $\alpha = 2$, maximum 1 SIC iteration.

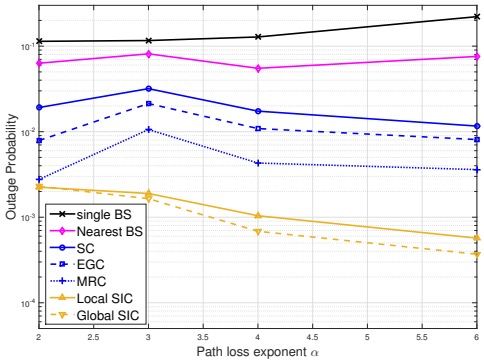

FIGURE 6.18: OP vs α, with $\frac{\lambda_n}{\lambda_b} = 10$, $\gamma^* = 7$dB, and $B = 96$kHz, maximum 1 SIC iteration.

Finally, we report the multi-BS diversity gain when compared to single BS case: $\frac{OP_{(singleBS)}}{OP_{(multiBS)}}$, as well as the implementation complexity of each technology in Table 6.5. We can observe that when the normalized traffic load becomes denser, the multi-BS gain of all the technologies degrades. Meanwhile, when the frequency resources become larger, the gain rises up. Global SIC always brings the highest benefits. Contrary to the cases where local SIC brings similar gain than MRC, we can observe that when $B = 192$kHz or when the BSs are denser than nodes (i.e. $\frac{\lambda_n}{\lambda_b} = 0.7$), local SIC brings much more gain than MRC. This is due to the fact that we limit the maximum SIC iteration to 1, so the case where aggregated interference causes the packet loss is more rare when B is large or when the load is sparse. Thus 1 iteration is sufficient for local SIC to decode most of the collided packets. We can deduce that local SIC can be more advantageous than MRC when the base stations are denser or when the frequency resources are larger.

As regards the implementation, we consider that interference cancellation is in general more complex than signal combining. Because the former demands all

the details of all the signals (in the purpose of reconstructing them), high resolution of receivers (in order to distinguish signals having similar SINR), and high computation resources (to proceed iteratively); whereas the latter only needs the SINR estimation of each branch.

We note that these results give us a choice among these technologies, depending on the performance improvement we need, the budgets we have, and the infrastructure complexity we expect. For example, if we intended to implement local SIC at each BS with no more than 1 iteration (maybe due to the computation limitations), now we know that MRC can also meet our needs as they deliver similar performance (when the active nodes are denser than BSs). We can thus choose MRC rather than local SIC, which is less complex to implement without loss of performance.

TABLE 6.5: Multi-BS diversity gain compared to single BS (with $\gamma^* = 7$dB, $\alpha = 2$, maximum 1 SIC iterations), and implementation complexity.

	Nearest BS	SC	EGC	MRC	local SIC	global SIC
Multi-BS gain $\frac{\lambda_n}{\lambda_b} = 0.7$, B=12kHz	1.7	8	19	65	97	97
Multi-BS gain $\frac{\lambda_n}{\lambda_b} = 10$, B=12kHz	1.5	4	6	12	11	28
Multi-BS gain $\frac{\lambda_n}{\lambda_b} = 20$, B=12kHz	1.4	3	4	8	6	16
Multi-BS gain $\frac{\lambda_n}{\lambda_b} = 10$, B=96kHz	1.9	7	20	67	68	101
Multi-BS gain $\frac{\lambda_n}{\lambda_b} = 10$, B=192kHz	1.6	6	15	47	96	125
Complexity	*	*	**	***	****	*****

6.8 Conclusion

In this chapter, we have exploited the spatial diversity of multiple bases stations in the purpose of enhancing UNB systems' performance. We have firstly analyzed the simplest selection combining (SC) with 2 BSs case, when considering the specific spectral interference of UNB and only path loss. Thus the interferences are considered correlated among BSs. The positions of BSs are assumed to be predefined. We have transformed the OP calculation into the probability that one node falls into certain areas. The theoretical OP is validated, but its derivation is very complex to be extended to more than 2 BSs case. We highlight that SC is beneficial to enhance the UNB systems performance, and that its gain is related to the distance between each of the BSs.

Secondly, we stayed in SC, but we have considered Rayleigh fading in addition where we have assumed that the interferences perceived by the BSs are independent. We have assumed that the positions of BSs are random. We have derived the OP with the density of BSs (thus the number of BSs can be more than 2) when

modeling the the probability as marked PPP with the aid of stochastic geometry as. However, this analytical OP is validated only for certain node/BS densities. Therefore, we have deduced that the interference independence does not always hold in UNB systems, which is contradictory to traditional systems.

Then we have proposed to apply more complex signal combining technologies such as MRC and EGC, and even local/global interference cancellation across multi-BS. We have evaluated and the performance of all the proposed technologies, and compared them with single BS case. These technologies exploiting multi-BS diversity are proved to be significantly beneficial in improving UNB networks' scalability. We have shown that the global SIC has the best performance (we can gain until 125 times better performance with 1 SIC iteration for high traffic load), whereas it has also the highest complexity to implement. The suboptimal ones are MRC and local SIC which deliver similar enhancement, but MRC is less complex to local SIC. We have highlighted that the results provide a global view of the mentioned technologies' diversity gain and implementation complexity.

Chapter 7

Experiments

Contents

All the previous chapters give fundamental limits of UNB network's capacity, they are all proved by Monte-Carlo simulations. But sometimes the simulations can not reflect all the details of what's going on in realistic environment. Therefore, we have initiated experiments where we emulate UNB signals by USRP transceivers (Universal Software Radio Peripheral), and the signal receptions are done by a real Sigfox base station. We will verify the interference coefficient and the OP under idealized conditions with the experimental results, in this chapter.

7.1 Presentation of tools

7.1.1 FIT/Cortexlab

In the experiments, we use the radio platform FIT/Cortexlab (future internet of things cognitive radio testbed) which allows us to evaluate different aspects of cognitive radio in realistic scenarios [17]. CorteXlab uses the network architecture developed in IoT-lab and integrates SDR (software defined radio) nodes to offer a remotely accessible development platform for distributed Cognitive Radio (CR).

The testbed is installed in a shielded room (isolated from any external interference) and also partly covered with electromagnetic absorbing material. Thus

the radio channel characteristics (path-loss, fading, shadowing, or paths etc.) can totally be controlled by the users. More importantly, the experiments can be repeated many times as all are isolated from the outside-world and controllable.

The nodes are able to accept implementations from the PHY (physical) layer on both hardware, i.e. Field Programmable Gate Array (FPGA), and software on general purpose CPUs. The nodes that we use in the experiments are SDR nodes which consist of 22 USRP (Universal Software Radio Peripheral) transceivers, whose frequency can be set from 400 MHz to 4.4 GHz for both emission and reception. These USRPs allow to achieve very precise carrier frequencies, which guarantees a precision of up to 0,01 ppb (part per billion). Thus for a targeted frequency at 868 MHz, the precision can be until 0.00868 Hz. Meanwhile, they are also very expensive such as several thousand of dollars per equipment. We recall that a regular low-cost (several dollars) oscillators can only have a precision about 0.25 ppm (part per million). Therefore, the signals will be at the carrier frequencies where we have indicated, thus there will not be frequency drift phenomenon with these USRPs.

7.1.2 GNU Radio

The USRP transceivers are only programmable with GNU Radio for the moment. GNU Radio is a free and open-source software development toolkit that provides signal processing blocks to implement software radios [18]. A software radio is a radio system which performs the required signal processing in software instead of using dedicated integrated circuits in hardware [142].

GNU Radio perform signal processing thanks to its various blocks, such as filters, channel codes, equalizers, modulators and demodulators, etc. One can write his/her own blocks in programing languages such as C++ and Python.

We use GRC (GNU Radio companion), the graphical tool of GNU Radio to create different chains of communications. We have to choose or create the blocks which correspond to our expectational use, then change the necessary properties, and then connect these blocks together to generate a flow-graph. As illustrated in Fig. 7.1, we have a flow-graph which consists of a cosine signal source block, a throttle block which prevents GRC to consume 100% of the CPU cycles, and a time sink block which allows to observe the signal in real time.

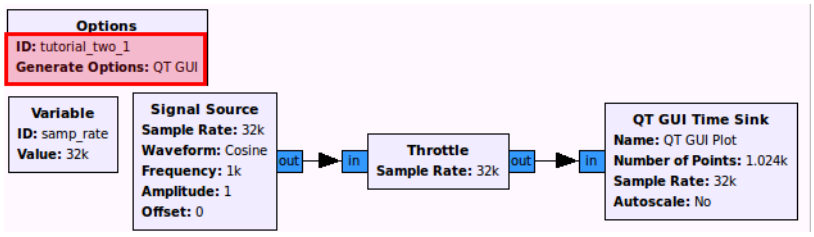

FIGURE 7.1: An example of a flow-graph in GNU Radio companion.

Once the flow-graphs is executed, GRC will generate automatically the corresponding python files. And we can use the python files to submit tasks on the USRP transceivers via the CorteXlab platform.

7.2 Experiments planning

7.2.1 Placements

As shown in Fig. 7.2, in our experiments, we use the USRP equipments (the green and blue points) to transmit and emulate the ultra-narrow-band signals. The reception is performed by a Sigfox base station installed at the corner. As the room is covered with electromagnetic absorbing material, the walls and the floors don not induce undesirable reflection. But the power attenuation of the paths from USRPs to the Sigfox BS can be different because of the obstacles.

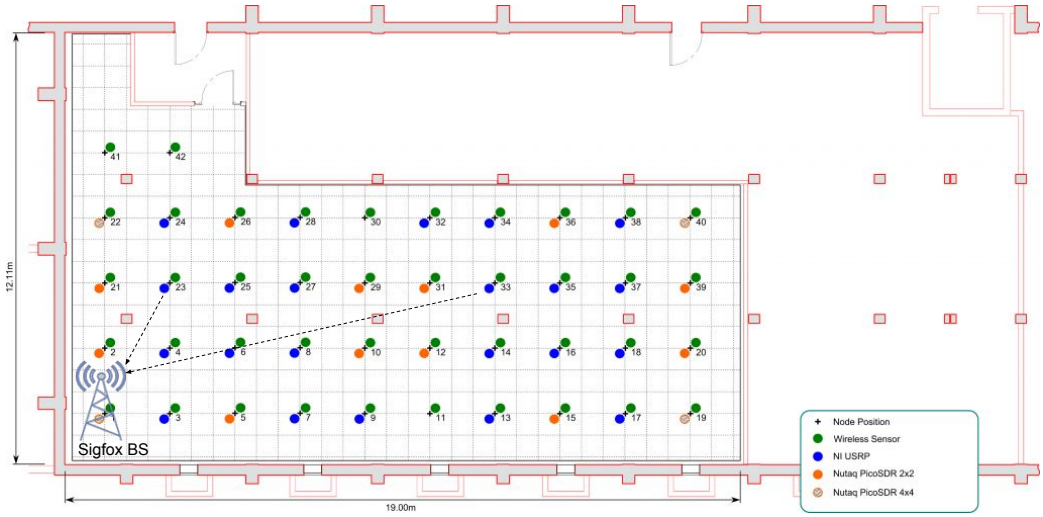

FIGURE 7.2: The placement of USRP nodes and Sigfox BS in the isolated CorteXlab room.

7.2.2 UNB signal emulation

The UNB signals are first simulated on GRC, and then submit to USRPs to transmit. We present in Fig.7.3 the main blocks that we use to generate UNB signals.

The *vector source* block contains Sigfox specific identifier code and the information to transmit. These information sequences that we use in the experiments are generated by Sigfox in order to make them decodable for the Sigfox BS. Unfortunately, we can not show the original values in this block because of the confidential issue. But we note that the vectors in this block are in decimal format.

The modulation is performed by a simple and efficient DBPSK modulator where one bit represents one symbol. We recall that the UNB signals in Sigfox networks have 100 bps (bit per second) as symbol rate. This value is unachievable by the USRPs, because they has a minimum sampling clock which induces a minimum sample rate at 200k bps. In order to reach this minimum sample rate, we have to do the interpolation. This is conducted by the block *Interpolating FIR filter* which integrates automatically a finite impulse response filter, in the purpose of eliminating the undesirable side lobs during the interpolation. Then we put a gain where the signal amplitudes are multiplied by a constant value. The purpose is to reduce the signal power to a normal level, otherwise they would be too strong to saturate all the band and affect the decoding. At the end, the modulated signals

are sent to the *USRP sink* block. Once we submit this flow-graph to a chosen USRP which is inside CorteXlab room, the issued USRP will transmit the signal.

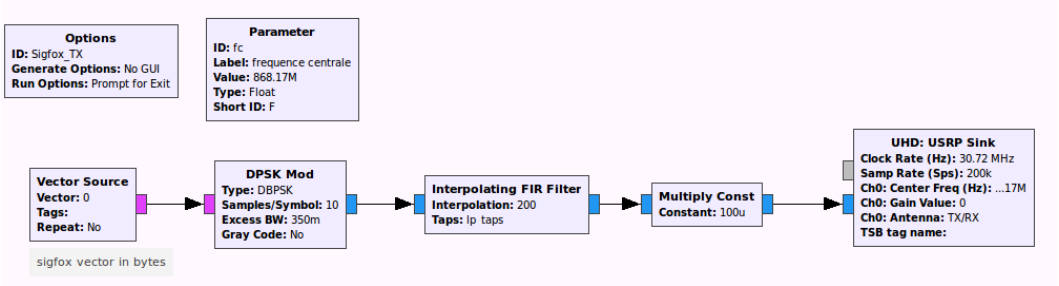

FIGURE 7.3: The flow-graph of the UNB Sigfox signals transmission chain on GNU Radio companion.

7.2.3 Reception

The BS of Sigfox does its normal work: it scans the dedicated band whose bandwidth is 192 kHz and centered at 868 MHz. As the experimental room is isolated from out-side world, it can only receive the signals transmit in the room. Thus the signals are free of unexpected external interferences in the band such as LoRa signals. The BS can identify Sigfox UNB signals by the specific signature (a sequence predefined by Sigfox company). Once the BS finds Sigfox signals, it will decode the whole sequence through the DBPSK demodulation only if the estimated SINR (or SIR) of the signal surpasses 7 dB. Then it performs the cyclic redundancy check (CRC). One packet is decoded if its CRC is OK. The information of decoded packets will be recorded by the Sigfox back-end.

We use an API (Application programming interface) of the Sigfox back-end to access the informations (including the time stamp, the frequency, the estimated RSSI and SNR, etc) of all the packets decoded by the BS in the shielded room.

7.3 Interference coefficient validation

We verify first of all the interference coefficient, as it is the basis of all the theoretical analysis in this thesis.

7.3.1 Hypothesis and experimental process

We set one signal as the desired signal x whose carrier frequency f_x is fixed. And the other signal is defined as the interfering signal y, whose carrier frequency f_y is firstly at the same position as f_x, then shifted manually away from the desired one's. This shift creates the frequency spacing $\delta f = |f_x - f_y|$ we have mentioned in all the previous chapters. These two signals are set to be at the same power level so that we can focus only on the impact of frequency shift.

In order to make the experiment as accurate as possible, we have chosen to transmit these two signals on the same USRP. Since each USRP could have different gains due to their electronic component properties and due to the path-loss, which can cause an unexpected power difference between two signals (if they were sent by two USRPs). Besides, the USRPs are not totally synchronized in time

(there can be 2 seconds of difference). More importantly, the USRPs have different frequency drifts as the oscillators of each USRP is not exactly the same (still due to the electronic components). In this experiment, the accuracy of frequency is very essential. Therefore, we choose to transmit them on the same USRP so that the frequency drift for both f_x and f_y are the same, and we can obtain the exact value of the frequency spacing δf.

As we have mentioned before, from the Sigfox back-end, we can only have the information of whether a signal is successfully received or not. Thus we do not have the estimated SINR of non-decoded signals. This is a bit problematic, since we can not measure the interference coefficient directly. Indeed, if we send two signals of the same power and try to make them collide, we lose both of them without knowing which one is interfered to which level. The interference coefficient represents the contribution of the interfering signal on the desired signal. At one moment, it can be so high that we lose the desired node. We have thus found a way to conduct the experiments, stated as the following:

1. Firstly we set the $\delta f = 0$, then we increase gradually the power of one the signal (for example the desired signal x), until the moment we can perceive that x is successfully received. Because if we don't create a power difference, we can never receive any signals when they are totally collided. The increase of power δ_{P_0} to reach this moment can reflect interference coefficient when $\delta f = 0$. As δ_{P_0} indicates the amount of the power that x needs to overcome the interference contribution of y when they are totally overlapped.

2. Secondly, we shift the frequency spacing to for example $\delta f = 5$ Hz, and we decrease gradually the δ_{P_0} of x until the moment we lose x. Because if we keep δ_{P_0} unchanged, the desired message x will always be received. Thus when we relax the δf, the interference normally decreases, consequently the x does not need such higher δ_{P_0} to survive the interference of y. Therefore, we decrease manually δ_{P_0} in order to find the limit.

3. Then we repeat the step 2, until the δf is large enough or when the interference coefficient tends to be stable.

7.3.2 Experimental results

As illustrated in Fig. 7.4, we have plotted the experimental interference coefficient (black line), when comparing it with the Gaussian model (blue line) and the AR (approximated rectangular) model (red line) that we use in all the previous theoretical analysis. The values of the AR model is the same as used in Section 4.4, we recall it here:

$$\triangle = 145Hz, \quad I_{max} = 0dB, \qquad I_{min} = -75dB$$

We can firstly observe that the experimental coefficient is globally lower than the Gaussian and AR models, except for the two high peaks around ± 50 Hz. When f_x and f_y are totally covered (i.e. when $\delta f = 0$), the Gaussian and AR models has $\beta(\delta f) = 0$ dB, while the experimental one has less. This means that when $\delta f = 0$, the desired signal x needs 7 dB (i.e. the threshold predefined by the Sigfox BS) more power to survive in Gaussian and AR coefficients, whereas

it only needs 2.3 dB more in the realistic case (i.e. in experimental interference coefficient).

Besides, if we check with more precision, we can note that the experimental coefficient remains constant inside $[-47, 47]$ Hz, which resembles actually a rectangular model; it has two high peaks inside $[-51, 48]\&[48, 51]$ Hz, which may be due to the DBPSK modulation at 100 bps; then it degrades gradually inside $[-63, -52]\&[52, 63]$ Hz; and it drops dramatically inside $[-116, -64]\&[64, 116]$ Hz; finally it tends to be very low and stable.

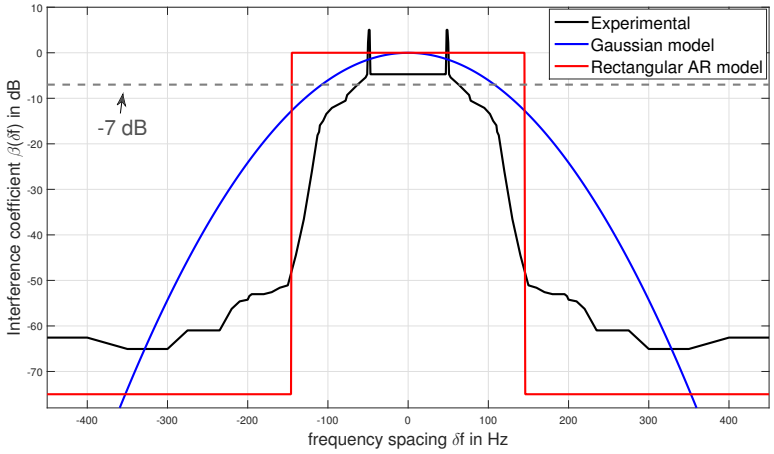

FIGURE 7.4: The experimental Sigfox interference coefficient as a function of the frequency spacing between two signals δf.

In our experiments, all the packets have the same received power. And if one packet's SIR is lower than the predefined threshold $\gamma^* = 7$ dB, the BS will not decode it. When we consider only one interferer at each collision, we can express the OP as:

$$\begin{aligned} \text{OP} &= \mathbb{P}\left(\frac{P_r}{P_r \cdot \beta(\delta f)} < \gamma^*\right) \\ &= \mathbb{P}\left(P_r - P_r - \beta(\delta f) < \gamma^*\right) \ in\ dB \\ &= \mathbb{P}\left(\beta(\delta f) > -\gamma^*\right) \ in\ dB \end{aligned} \tag{7.1}$$

with P_r the identical received power of all the signals, and γ^* the predefined threshold. It turns the OP into the probability that the interference coefficient is higher than -7 dB.

We have thus plotted the line (gray dashed line in Fig. 7.4) when the interference coefficient equals to -7 dB. We can have the value of δf when $\beta(\delta f)$ reaches -7dB, as the following:

$$Experimental : \delta f \in [-63, 63];\ \Delta = 63Hz \tag{7.2}$$

$$Gaussian : \delta f \in [-110, 110];\ \Delta = 110Hz \tag{7.3}$$

$$RectangularAR : \delta f \in [-145, 145];\ \Delta = 145Hz \tag{7.4}$$

These values indicate that if one interferer falls into these frequency zone away from the desired signal, it will cause the desired signal's loss, under the assumption that a unique interferer is sufficient to induce packet loss. We can see that

the experimental one have a narrow zone (i.e. $\Delta = 63$ Hz) where the $\beta(\delta f)$ surpasses -7 dB, thus there is a low probability that the frequency spacing falls into this zone. Whereas the Gaussian and rectangular model have larger interfering frequency zone (i.e. $\Delta = 110$ or 145 Hz), thus there is a higher probability that δf falls into these zones.

In order to ensure that the experimental results are not the particular cases, we have conducted the experiments at different carrier frequencies, by using different USRP equipments, and by changing the message contents. The experimental coefficient shape remains the same (i.e. the two peaks are still high, and the Δ is still narrower then Gaussian or AR) in all the cases. This gap between the experimental coefficient and the Gaussian (or rectangular) one will induce a difference between the experimental OP and the theoretical ones.

To conclude, the Gaussian and the AR rectangular models that we used have both over-estimated the experimental interference coefficient. However, we note that the experimental coefficient can be appropriately approximated by a narrower rectangular model, since its level remains constant inside $\delta f \in [-47, 47]$ Hz.

7.4 Capacity validation in idealized channels

After checking the interference coefficient, we verify by the experiments the theoretical capacity derived with the Gaussian and rectangular interference coefficients, under idealized channel conditions. Thus the received power of each signal is assumed (and set in experiments) to be at the same level. We only focus on the spectral interference, thus the signals are assumed to be transmitted at the same moment. The noise is neglected in the theoretical analysis.

7.4.1 Theoretical OP

We still use the OP as the criteria to represent capacity. The OP with the above hypothesis resembles the OP under idealized channels in chapter 3. The difference is that we do not consider the temporal impact in this chapter.

In the experiments, we do not have enough information to verify whether the packet loss is due to a unique interferer or the aggregated contribution of several interferers (AIP). But we know at least that the more loaded the networks become (more nodes or less frequency resources), the higher chance we have AIP.

If we consider that there are only two signals(i.e. a unique interferer and the desired signal), the probability that this interferer can induce the desired packet loss is expressed in eq.(7.1). This probability is transformed into the probability the δf falls into the frequency zones (i.e. the Δ) expressed in eq.(7.2)-(7.4). With the presence of N simultaneous transmissions, the OP is the probability that at least one of the $N-1$ potential interfering signal chooses its carrier frequency inside the indicated zones (i.e. the Δ). We can thus express theoretically the OP for each

model:

$$Experimental : \mathrm{OP}_{th} = 1 - \left(1 - \frac{2 \cdot \Delta_{experimental}}{B}\right)^{(N-1)} \tag{7.5}$$

$$Gaussian : \mathrm{OP}_{th} = 1 - \left(1 - \frac{2 \cdot \Delta_{Gaussian}}{B}\right)^{(N-1)} \tag{7.6}$$

$$RectangularAR : \mathrm{OP}_{th} = 1 - \left(1 - \frac{2 \cdot \Delta_{AR}}{B}\right)^{(N-1)} \tag{7.7}$$

with $\Delta_{experimental} = 63$ Hz, $\Delta_{Gaussian} = 116$ Hz, and $\Delta_{AR} = 145$ Hz.

7.4.2 Experimental OP and comparison

A big limitation of the available USRPs in the Cortexlab room, is that they are not synchronized in time, and that they don't have the same frequency drift. Thus we have to transmit all the signals from the same USRP, in order to have the same characteristics (such as the frequency drift, the emission moment and the equipment gain) and ensure the idealized channel condition set. In the experiments, we have thus fixed the signal number at $N = 10$. Each of them selects their carrier frequencies randomly and independently. This is realized by modifying the python file generated by the GRC flow-graph.

We present in Fig. 7.5 the experimental OP (black dashed line) by comparing it with the theoretical OP_{th} deduced with the experimental, Gaussian and the rectangular interference coefficients. We can observe that the OP obtained by experiments and the OP_{th} obtained by experimental coefficient are close to each other. The OP achieved by experiments is slightly higher than its theory. This is due to the unique interferer assumption in the OP_{th}, meanwhile in the realistic experiments the aggregated interference's case could happen. Another reason may be the fact that we have neglected the noise in the OP_{th}. However, in the realistic experiments, the noise exists. Therefore, we have the experimental OP close to its theory, but slightly higher. This result can validate the experimental interference coefficient's obtained in Section 7.3.2 in a global point of view.

Moreover, we can observe that OP obtained by experiments and the OP_{th} obtained by experimental coefficient (black solid and dash lines in Fig. 7.5) are both lower than the OP_{th} achieved by the Gaussian coefficient (blue lines), meanwhile the AR model (red lines) brings the worst performance (i.e. the highest OP). This is not surprising since the interfering frequency zone of the rectangular model Δ_{AR} is the largest. Thus it induces the highest chance to collide. The $\Delta_{Gaussian}$ is a bit narrower, thus less probability to be in collision. Then the experiment interference frequency zone $\Delta_{experimental}$ is the narrowest, thus the least chance to be collided.

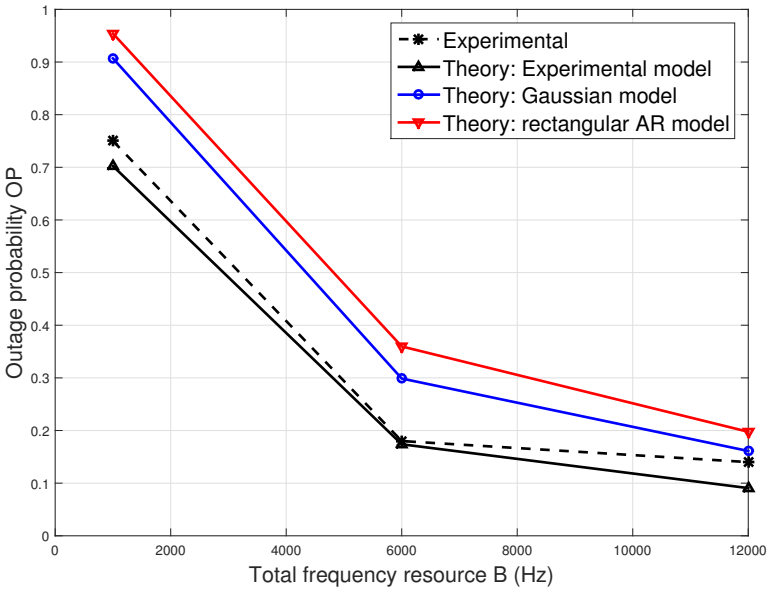

FIGURE 7.5: OP vs total frequency resource B in Hz. The number of simultaneous transmissions is $N = 10$, the Sigfox bast station's received sensibility is $\gamma^* = 7$ dB.

We note that these experimental results have not been verified by the signals transmitted by realistic Sigfox devices. Thus the shape of the interference coefficient and the gaps of OP we observe may come from the signal emulation blocks (e.x. the filter that we use to after the interpolation), or from the implementation on the USRP equipments which cause unexpected and undetected phenomena. The experiments by using real Sigfox devices is feasible but can be very tricky, because we need to put many devices in the shielded room, and make them transmit at the same moment (this means all the devices need to be synchronized in the milliseconds). What's more, all the manipulations have to be done at distance because physical presence of human can destroy the ideal channel conditions in the testbed room.

7.5 Conclusion

In this chapter, we have conducted experiments on the radio testbed FIT/Cortexlab. We have presented the planning of the experiments as well as the flow-graph and its issued blocks from which we have emulated the UNB signals on GNU Radio.

We have firstly verified the interference coefficient that we have used in all the theoretical analyses in the previous chapters. We have drawn the experimental interference coefficient by comparing it with the Gaussian and the rectangular AR models. We have observed that the Gaussian and AR models have both overs-estimated the experimental coefficient. In the experimental coefficient, the frequency zone that will generate packet loss (i.e. when the interference level surpasses -7 dB) is only at $\Delta = 63$ Hz, whereas this zone in Gaussian and AR models are much larger. Moreover, we have found out that the interference coefficient remains constant when the frequency spacing δf is inside $[-47, 47]$ Hz, it can thus be approximated by a more adapted rectangular model.

We have then verified the outage probability (OP) when maintaining the simultaneous transmission number constant and varying the total frequency resource B, under ideal channel conditions. We have derived 3 theoretical expressions of OP_{th} by using respectively the experimental, the Gaussian and the AR interference coefficients, under the assumption that there is only one interferer at each collision and the negligence of noise. Then we have compared them with the OP obtained by the experiments. We have observed that the OP obtained by experiments is very close to the OP_{th} obtained by the experimental interference coefficient. The former is slightly higher than the latter, which may be due to the possible aggregated interference (which is not considered in the OP_{th}) in the experiments, or due to the existence of noise in the equipments and the environments (which is neglected the in OP_{th}). But globally, the OP_{th} obtained by the experimental coefficient can describe well the variation of the realistic OP, though there is a slight lack of precision. This result can validate the general shape and accuracy of the experimental interference coefficient.

Moreover, we have observed that both the experimental OP and its OP_{th} are lower than the OP_{th} obtained by the Gaussian and AR models. This is not surprising since the Gaussian and AR models have over-estimated the interference level.

The limitation of these experimental results are the fact that the UNB signals are emulated by USRP equipments and not verified by real Sigfox devices. There may be a lack of precision on the shape of the experimental interference coefficient, especially the two peaks around $\delta f = \pm 50$ Hz.

Despite the possibly inconsistency brought by the implementation on the USRPs, these experiments have provided us a global view of the gaps between our theoretical analysis and what happens in the realistic environments, and how to reduce these gaps (by using a more adapted interference coefficient). We note that these experiments can be furthered by varying other parameters such as the number of simultaneous transmission, or by including the temporal impact.

Chapter 8

Conclusion and Perspectives

Contents

8.1 Conclusion

In the thesis, we have introduced the promising candidate: ultra narrow band (UNB), out of other LPWAN technologies which are dedicated to long-distance and low-power communications. In the presence of carrier frequency imprecision (which is larger than UNB individual signal bandwidth) caused by oscillators, it is not realistic to obtain orthogonal channels in UNB system. Thus the multiple access dedicated to UNB is random in time and in frequency. The radio access of UNB, which is uncontrolled, can cause specific partial interference when simultaneous transmissions happen. In the literature, the approach like UNB has never been studied, and its network capacity remains unknown.

The objective of this thesis was to provide a scientific vision to the first technology commercially initiated for IoT purpose (i.e. ultra-narrow-band) about its scalability and the possibilities to improve it, focusing on the uplink. My contributions thus consist of evaluating UNB network capacity, and further proposing solutions to enhance the system performance.

We have started the thesis by characterizing the outage probability which indicates the network capacity, in single BS case, under idealistic channel conditions. We have evaluated the extension of the ALOHA scheme to the case of time-frequency random access, as experienced the UNB transmissions. We have derived and validated the theoretical expression of the outage probability for all the configurations (time slotted or unslotted, and frequency slotted or unslotted). We have brought to light that frequency randomness and time randomness identically affect the throughput, and that they can be interchanged without loss of performances. Then we have extended the expression of generalized ALOHA with the involvement of replications. Besides, we have highlighted that, for each traffic load density, there is an optimal number of replications, which allows to achieve the best reliability.

Then we continue the scalability evaluation for single BS case, but under realistic channel conditions this time. We have derived theoretically two outage

probabilities: the first one has considered the frees space path-loss and the interference induced by a unique interferer; and the second one has taken into account the Rayleigh fading, the path-loss for all propagations, and the aggregated interference (AIP). The specific UNB spectral interference coefficient has been approximated by a Gaussian model and by a rectangular model. In the second analysis, we have used stochastic geometry as a tool since the objects are distributed randomly in one cell. Both the specific UNB interference coefficient and the fading factor have been used as marks in a homogeneous Poisson point process, which helps in deriving the closed-form Laplace transform of the AIP. We have compared the OP obtained by both analysis, and we have observed the impact of fading (which is only sensible for nodes close to the BS) and the impact of AIP (which has almost the same performance of the contribution of a unique interferer). Besides, we have evaluated the spectral efficiency as a function of the path-loss exponent, for without and with guard bands. And we have highlighted that the bandwidth which achieves the highest spectral efficiency depends on the propagation condition.

From the two previous performance evaluation, we have realized that the specific interference caused by the random radio access is a severe limitation of the system. We have thus considered to optimize the performance by applying the SIC (successive interference cancellation) methodology, in order to mitigate the interference impact, from single base station's side. We have derived the theoretical OP expression, by considering the SIC receiver and the specific random spectrum access of UNB. SIC is proved to be beneficial to improve the system performance. We have brought to light that in the free space propagation, the diversity delivered by the fading is advantageous in enhancing the efficiency of SIC. But when the environment becomes lossier, the fading brings no more benefits in improving the SIC receiver's performance.

After the studies in the case of mono-BS, we have started to exploit the spatial diversity of multi-BS which may balance the spectral interference. Since the nodes in UNB systems are not attached to one specific cell, one message can be perceived by many surrounding BSs. We have thus applied signal combining and interference cancellation technologies across multi-BS, in the purpose of improving the UNB networks performance. We have conducted theoretical OP analysis for the simplest selection combining (SC), when considering path-loss and the correlation (comes from the fact the interference may lean on the same frequency spacing) between the interference perceived by each BS. Nonetheless, the correlation renders the analysis very complex when the number of BS increases. Thus we have added Rayleigh fading, and we have assumed that the novel degree of freedom brought by the fading can totally canceled the correlation. We have derived an OP when considering the independent interference, and compared it with the simulations. Meanwhile, this independence is proved to be not valid in UNB systems. Therefore, we have concluded that the interference viewed by each BS is correlated even with the presence of fading.

Afterwards, we have applied more complicated signal combining technologies such as EGC (equal gain combining) and MRC (max ratio combining). Different from most of the literature, we have defined the weight of MRC to be proportional to the SINR of each branch. Then we have identified two methods to apply SIC: a local way where SIC is performed at each BS, then the decoded packets of all the BSs are grouped together; and a global way where the SIC is performed globally

across the cooperated BS which exchange their decoded packets' information with each other to decode more additional packets. We have presented and compared the numerical results of all the technologies, as well as their implementation complexity. All the technologies which have taken advantage of multi-BS diversity are proved to be better performing than mono-BS. We have observed that the the global SIC offers the best performance, but it has also the highest complexity. The suboptimal is the local SIC and MRC, both of which deliver similar performances while MRC is less complicated to implement. We have highlighted that these results can provide us the choice among all the multi-BS technologies, according to the performance enhancement needs, the available computation resources and the acceptable implementation complexity.

Finally, we have conducted the experiments on the radio testbed FIT/Cortexlab, in the purpose of verifying the interference coefficient that we have used in all the theoretical analysis and the networks capacity. The testbed is installed in a totally shelded and isolated room which provides an idealized channel condition. We have used the programmable USRP equipments to emulate the UNB signals and to transmit them, and a Sigfox base station to receive and decode the signals. We have drawn the experimental interference coefficient when comparing it with the Gaussian and the approximated rectangular (AR) models. We have observed that the Gaussian and AR models have both over-estimated the experimental coefficient. Thus the realistic interference coefficient can in fact be approximated by a more adapted rectangular model. We have then verified the network capacity (represented by OP) under idealized conditions. The OP obtained by the experiments is compared with the theoretical OP_{th} obtained by the experimental, the Gaussian and the AR interference coefficients. We have observed that the OP_{th} obtained by the experimental coefficient can describe the variation of OP obtained by the experiments, despite a slight lack of precision. We have emphasized the pertinence of the experiments, which not only give us an insight about the network's behavior in realistic environments, but also provide an intuition to adjust our theoretical models (such as using a more adapted rectangular interference coefficient).

8.2 Perspectives and future works

The future works related to each contribution is already stated in the conclusion of each chapter. In this part, we will talk about perspectives in a more global way.

First of all, we can include the temporal impact into the capacity characterization under realistic channel conditions. Indeed, in all the analysis with power attenuation (path-loss or fading), we have focused on the specific spectral interference of UNB. We have considered only simultaneous transmissions. Nonetheless, the diversity in the time domain can also bring a degree of freedom which can help, for example, to improve the SIC performance.

Then we can consider to combine the methods to improve the network capacity together. For example, we can use the technology SIC when involving the replication mechanism in mono-BS or multi-BS scenarios. The replications of the same packet are collided with other packets. When one of the replication is successfully decoded, we can reconstruct it and retrieve the contribution of all the other replications. This results in decoding more additional packets. And in multi-BS scenario, this process is even more efficient, because the BSs exchange

the decoded replication's information. Therefore, one replication decoded, the packets collided with the replications of the same packet can be freed of their interference contribution in all the BSs. We can certainly combine other technologies such as the global SIC and MRC. This combination can be very powerful, but also very expensive.

Besides, we should include studies about mobile devices. The scenarios that we have considered have all assumed the stable channel conditions during the observed interval. However, in the realistic scenarios, the nodes can be moving at the speed of cars or even flights. In this cases, the channel can also be varying during the transmission. Thus it is very important to measure the channel characteristics when the objects are moving, by taking into account the Doppler shifts, or the empirical fading factor, etc.

We can also further the studies by considering the downlink of the systems. Indeed, we have only considered the uplink in this thesis because of its random and unpredictable properties. But the downlink is normally scheduled. We can thus work on the strategy of the downlink such as how to respond to the requirements of nodes more efficiently in terms of energy efficiency and resource (frequency and time) reuse efficiency.

Furthermore, we can change the uncontrolled radio access of UNB. Such as adding channel coding schemes, or change it to a more scheduled access like slotted-ALOHA. But it will be very important to evaluate whether the additional cost brought by the new access can be compensated by it enhancement in the capacity. One last bold idea is to predict the channel conditions by machine learning, so that the random radio access can be totally prevented from the collisions.

Appendix A

Validation and Numerical results of *OP for average rx* eq.(4.21)

In this appendix, we present the validation and numerical results of the $OP\ for\ average\ r_x$ in Section 4.3.1, i.e. the N users' extension of eq.(4.21).

A.1 Validation

The N users' extension of eq.(4.21), when condiering only one interferer at each collision, denotes:

$$OP_{(N)} = 1 - (1 - OP)^{N-1} \tag{A.1}$$

with OP the expression in eq.(4.21) which represents the outage probability when there are only two nodes.

We present simulation results (obtained on Matlab) based on realistic network configurations (based on SigFox one). We compare them to our theoretical values, to validate the expression of $OP_{(N)}$ eq.(A.1), and thus validate indirectly eq.(4.21). We consider the following key parameters: number of active nodes N, bandwidth B, range of transmission area $[r_m, r_M]$, and the threshold of signal-interference-ratio γ^*. For a better understanding, we provide here the unit of γ^* in dB. But in the theoretical expression, the linear value of γ^* must be used ($10^{\frac{\gamma^*}{10}}$).

We recall the simulation hypothesis here:

TABLE A.1: Simulations hypothesis

BS number	nodes distribution	desired node	path loss	fading	AIP	replicas
1	random	random	$\alpha = 2$	no	no	no

We present on Fig. A.1-A.3, the evolution of $OP_{(N)}$ by varying B, and along with another different parameter for each figure. From a global point of view, we can observe that the simulation results match well with theoretical ones. Therefore, we can deduce that the formula eq.(A.1) and eq.(4.21) are validated.

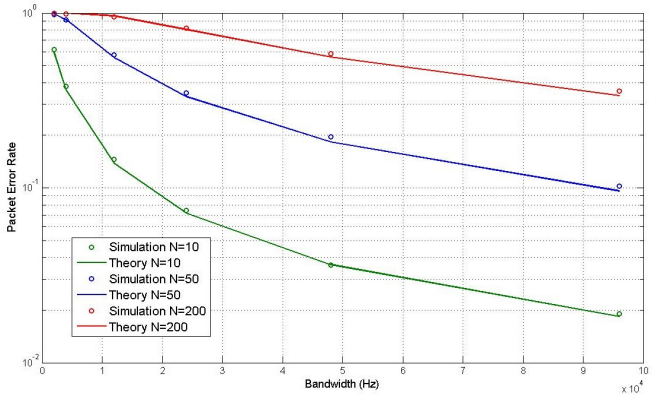

FIGURE A.1: OP vs bandwidth B, with different number of active nodes N, $r_M = 1000$ m, $r_m = 30$ m, $\gamma^* = 6.8$ dB.

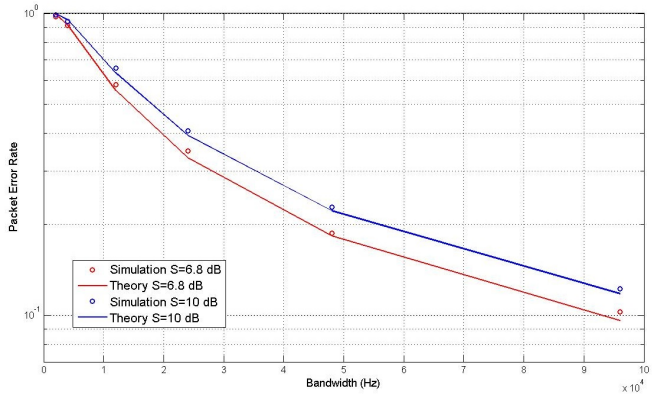

FIGURE A.2: OP vs bandwidth B, with different signal-interference-ratio threshold γ^* dB, $N = 50$, $r_M = 1000$ m, $r_m = 30$ m.

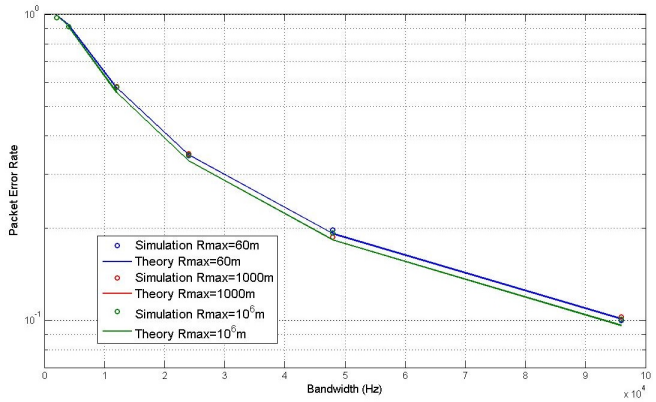

FIGURE A.3: OP vs bandwidth B, with different maximum range of area r_M, $N = 50$, $r_m = 30$ m, $\gamma^* = 6.8$ dB.

A.2 Performances analysis

We now analyze these figures more precisely. In Fig. A.1, the area ranges are set to $[30, 1000]$. We can see that OP decreases when B increases. Indeed, as there are more available transmission resources, there are less risks that nodes would collide. In addition, OP increases with N. When numerous active nodes transmit at the same time, the chance that their frequencies fall into the interfering zone gets higher.

Furthermore, we verify that OP increases when the threshold γ^* becomes higher, as shown in Fig. A.2. When the success criteria becomes stricter, nodes have less chances to attain γ^*, so the network performance becomes worse. Fig. A.3 shows that when the maximum range r_M changes from 60 to 1000, we have a little bit more errors. Meanwhile, when r_M changes from 1000 to 10^6, their OP evolution totally overlap. It indicates that, when the area is already large, the cell range has no more impact on network performance.

To sum up, the usual performance statements are verified: more network load induces more errors, such as small bandwidth and too many nodes; a more strict SIR threshold leads to a higher OP; while the influence of area range to network performance depends on the scale.

A.3 Results Exploitation

In this section, we exploit the theoretical expression of OP to find out the maximum capacity. This parameter is defined by the maximum number of active nodes N that the network can support simultaneously, while maintaining a targeted OP. We have reported on Fig. A.4, the capacity when the OP is targeted to be lower than 0.1. We can observe that with a larger bandwidth, the system can contain more nodes. Nevertheless, with a stricter signal interference ratio threshold, less active nodes can be served. More importantly, we can observe that the capacity increases linearly with the available bandwidth. It is thus easy to scale the bandwidth in accordance to the number of nodes to serve, when keeping the same targeted SIR.

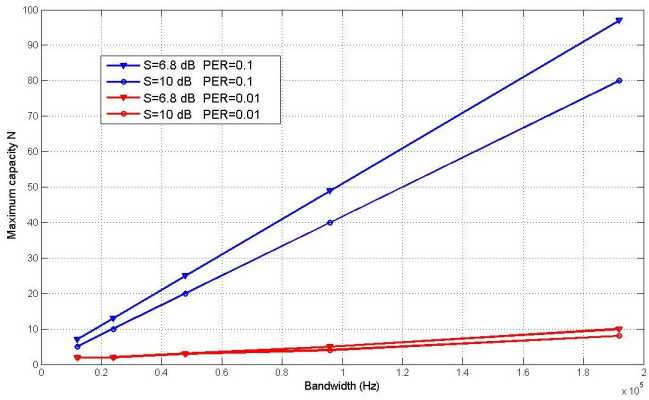

FIGURE A.4: Maximum capacity N vs bandwidth B, with different signal-interference-ratio threshold γ^* dB, and OP, $r_m = 30$ m, $r_M = 60$ m.

Lists of publications

Journal

[4] Y. Mo, M. T. Do, C. Goursaud, and J.-M. Gorce: **"Up-Link Capacity Derivation for Ultra-Narrow-Band IoT Wireless Networks"**. in *International Journal of Wireless Information Networks Springer*, Jun. 2017.

International conferences

[7] Y. Mo, C. Goursaud, and J.-M. Gorce: **"Uplink Multiple Base Stations Diversity for UNB based IoT networks" (invited paper)**. in *2018 IEEE International Conference on Antenna Measurement and Applications (CAMA)*, Sep. 2018, Västerås, Sweden.

[6] Y. Mo, C. Goursaud, and J.-M. Gorce: **"Multiple Base Stations Diversity for UNB Systems: Theoretical Analysis and Performances"**. in *2018 International Symposium on Networks, Computers and Communications (ISNCC)*, Jun. 2018, Rome, Italy, pp. 1–6.

[5] Y. Mo, C. Goursaud, and J.-M. Gorce: **"On the benefits of successive interference cancellation for ultra narrow band networks : Theory and application to IoT"**. in *2017 IEEE International Conference on Communications (ICC)*, May. 2017, Paris, France, pp. 1–6.

[3]Y. Mo, C. Goursaud, and J.-M. Gorce: **"Theoretical analysis of UNB-based IoT networks with path loss and random spectrum access"**. in *2016 IEEE 27th Annual International Symposium on Personal, Indoor, and Mobile Radio Communications (PIMRC)*, Sep. 2016, Valencia, Spain, pp. 1–6.

[1] C. Goursaud and Y. Mo: **"Random unslotted time-frequency ALOHA: Theory and application to IoT UNB networks"**. in *2016 23rd International Conference on Telecommunications (ICT)*, May. 2016, Thessaloníki, Greece, pp. 1–5.

[2] Y. Mo, M. T. Do, C. Goursaud, and J.-M. Gorce: **"Optimization of the predefined number of replications in a Ultra Narrow Band based IoT network"**. in *2016 Wireless Days (WD)*, March. 2016, Toulouse, France, pp. 1–6.

National conferences

[143] Y. Mo, C. Goursaud, and J.-M. Gorce: **"Bénéfice de l'Annulation Successive d'Interférence pour des Réseaux Ultra Narrow Band : Théorie et Application à l'IoT"**. in *ALGOTEL 2018 - 20èmes Rencontres Francophones sur les Aspects Algorithmiques des Télécommunications*, May. 2018, Roscoff, France, pp. 1–4.

[144] Y. Mo, C. Goursaud, and J.-M. Gorce: **"Performance théorique de réseaux IoT basés sur UNB avec Path Loss"**. in *GRETSI 2017*, Sep. 2017, Juan-les-Pins, France.

[145] Y. Mo, M. T. Do, C. Goursaud, and J.-M. Gorce: **"Impact du nombre de répliques sur les performances d'un réseau IoT basé sur des transmissions Ultra Narrow Band"**. in *ALGOTEL 2016 - 18èmes Rencontres Francophones sur les Aspects Algorithmiques des Télécommunications*, May. 2016, Bayonne, France.

Bibliography

[1] C. Goursaud and Y. Mo, "Random unslotted time-frequency aloha: Theory and application to iot unb networks," in *2016 23rd International Conference on Telecommunications (ICT)*, May 2016, pp. 1–5.

[2] Y. Mo, M. T. Do, C. Goursaud, and J. M. Gorce, "Optimization of the predefined number of replications in a ultra narrow band based iot network," in *2016 Wireless Days (WD)*, March 2016, pp. 1–6.

[3] Y. Mo, C. Goursaud, and J. M. Gorce, "Theoretical analysis of unb-based iot networks with path loss and random spectrum access," in *2016 IEEE 27th Annual International Symposium on Personal, Indoor, and Mobile Radio Communications (PIMRC)*, Sep. 2016, pp. 1–6.

[4] Y. Mo, M. T. Do, C. Goursaud, and J.-M. Gorce, "Up-link capacity derivation for ultra-narrow-band iot wireless networks," *International Journal of Wireless Information Networks*, Jun 2017. [Online]. Available: http://dx.doi.org/10.1007/s10776-017-0361-4

[5] Y. Mo, C. Goursaud, and J. M. Gorce, "On the benefits of successive interference cancellation for ultra narrow band networks : Theory and application to iot," in *2017 IEEE International Conference on Communications (ICC)*, May 2017, pp. 1–6.

[6] ——, "Multiple base stations diversity for unb systems: Theoretical analysis and performances," in *2018 International Symposium on Networks, Computers and Communications (ISNCC)*, Rome, Italy, 2018, pp. 1–6.

[7] ——, "Uplink multiple base stations diversity for unb based iot networks (invited paper)," in *2018 IEEE International Conference on Antenna Measurement and Applications (CAMA)*, Västerås, Sweden, September 2018.

[8] C. Goursaud and J.-M. Gorce, "Dedicated networks for iot: Phy/mac state of the art and challenges," *EAI endorsed transactions on Internet of Things*, 2015.

[9] M. T. Do, C. Goursaud, and J. M. Gorce, "On the benefits of random FDMA schemes in ultra narrow band networks," in *2014 12th International Symposium on Modeling and Optimization in Mobile, Ad Hoc, and Wireless Networks (WiOpt)*, May 2014, pp. 672–677.

[10] N. M. Abramson, "The aloha system: another alternative for computer communications," in *AFIPS Fall Joint Computing Conference*, 1970.

[11] G. Choudhury and S. Rappaport, "Diversity aloha–a random access scheme for satellite communications," *IEEE Transactions on Communications*, vol. 31, no. 3, pp. 450–457, 1983.

[12] M.-T. Do, C. Goursaud, and J.-M. Gorce, "Interference modelling and analysis of random fdma scheme in ultra narrowband networks," in *AICT 2014*, 2014.

[13] K. A. Hamdi, "Packet-error probability analysis for fh-cdma unslotted packet networks," *IEEE Transactions on Communications*, vol. 51, no. 2, pp. 151–154, Feb 2003.

[14] M. Haenggi and R. K. Ganti, *Interference in large wireless networks*. Now Publishers Inc, 2009.

[15] X. Zhang and M. Haenggi, "The performance of successive interference cancellation in random wireless networks," *IEEE Transactions on Information Theory*, vol. 60, no. 10, pp. 6368–6388, Oct. 2014.

[16] A. Zanella and M. Zorzi, "Theoretical analysis of the capture probability in wireless systems with multiple packet reception capabilities," *IEEE Transactions on Communications*, vol. 60, no. 4, pp. 1058–1071, Apr. 2012.

[17] L. S. Cardoso, G. Villemaud, T. Risset, and J.-M. Gorce, "Cortexlab: A large scale testbed for physical layer in cognitive radio networks," in *EUROPEAN COOPERATION IN THE FIELD OF SCIENTIFIC AND TECHNICAL RESEARCH*, may 2012.

[18] E. Blossom, "Gnu radio: tools for exploring the radio frequency spectrum," *Linux journal*, vol. 2004, no. 122, p. 4, 2004.

[19] J. Gubbi, R. Buyya, S. Marusic, and M. Palaniswami, "Internet of things (iot): A vision, architectural elements, and future directions," *Future Generation Computer Systems*, vol. 29, no. 7, pp. 1645–1660, 2013.

[20] L. D. Xu, W. He, and S. Li, "Internet of things in industries: A survey," *IEEE Transactions on Industrial Informatics*, vol. 10, no. 4, pp. 2233–2243, Nov. 2014.

[21] A. Al-Fuqaha, M. Guizani, M. Mohammadi, M. Aledhari, and M. Ayyash, "Internet of things: A survey on enabling technologies, protocols, and applications," *IEEE Communications Surveys Tutorials*, vol. 17, no. 4, pp. 2347–2376, Fourthquarter 2015.

[22] R. Khan, S. U. Khan, R. Zaheer, and S. Khan, "Future internet: The internet of things architecture, possible applications and key challenges," in *2012 10th International Conference on Frontiers of Information Technology*, Dec 2012, pp. 257–260.

[23] D. Miorandi, S. Sicari, F. D. Pellegrini, and I. Chlamtac, "Internet of things: Vision, applications and research challenges," *Ad Hoc Networks*, vol. 10, no. 7, pp. 1497 – 1516, 2012.

[24] S. Andreev, O. Galinina, A. Pyattaev, M. Gerasimenko, T. Tirronen, J. Torsner, J. Sachs, M. Dohler, and Y. Koucheryavy, "Understanding the iot connectivity landscape: a contemporary m2m radio technology roadmap," *IEEE Communications Magazine*, vol. 53, no. 9, pp. 32–40, September 2015.

[25] K. Zheng, S. Ou, J. Alonso-Zarate, M. Dohler, F. Liu, and H. Zhu, "Challenges of massive access in highly dense lte-advanced networks with machine-to-machine communications," *IEEE Wireless Communications*, vol. 21, no. 3, pp. 12–18, June 2014.

[26] E. Morin, M. Maman, R. Guizzetti, and A. Duda, "Comparison of the device lifetime in wireless networks for the internet of things," *IEEE Access*, vol. 5, pp. 7097 – 7114, 2017.

[27] "Ieee standard for local and metropolitan area networks–part 15.4: Low-rate wireless personal area networks (lr-wpans) amendment 1: Mac sublayer," *IEEE Std 802.15.4e-2012 (Amendment to IEEE Std 802.15.4-2011)*, pp. 1–225, April 2012.

[28] C. Gomez, J. Oller, and J. Paradells, "Overview and evaluation of bluetooth low energy: An emerging low-power wireless technology," *Sensors*, vol. 12, no. 9, pp. 11 734–11 753, 2012.

[29] Y.-C. Tseng, C.-S. Hsu, and T.-Y. Hsieh, "Power-saving protocols for ieee 802.11-based multi-hop ad hoc networks," *Computer Networks*, vol. 43, no. 3, pp. 317 – 337, 2003.

[30] R. Want, "Near field communication," *IEEE Pervasive Computing*, vol. 10, no. 3, pp. 4–7, July 2011.

[31] R. J. M. Cramer, R. A. Scholtz, and M. Z. Win, "Evaluation of an ultra-wide-band propagation channel," *IEEE Transactions on Antennas and Propagation*, vol. 50, no. 5, pp. 561–570, May 2002.

[32] U. Raza, P. Kulkarni, and M. Sooriyabandara, "Low power wide area networks: An overview," *IEEE Communications Surveys Tutorials*, vol. 19, no. 2, pp. 855–873, Secondquarter 2017.

[33] "Lora," http://lora-alliance.org/What-Is-LoRa/Technology, accessed: 2018-04-09.

[34] C. Goursaud and J.-M. Gorce, "Dedicated networks for iot: Phy/mac state of the art and challenges," *EAI endorsed transactions on Internet of Things*, 2015.

[35] "Ingenu," http://www.ingenu.com/, accessed: 2018-04-09.

[36] Y. P. E. Wang, X. Lin, A. Adhikary, A. Grovlen, Y. Sui, Y. Blankenship, J. Bergman, and H. S. Razaghi, "A primer on 3gpp narrowband internet of things," *IEEE Communications Magazine*, vol. 55, no. 3, pp. 117–123, March 2017.

[37] "Sigfox," http://www.sigfox.com/en/#!/technology, accessed: 2018-04-09.

[38] K. Mekki, E. Bajic, F. Chaxel, and F. Meyer, "A comparative study of lpwan technologies for large-scale iot deployment," *ICT Express*, 2018.

[39] K. Mikhaylov, . J. Petaejaejaervi, and T. Haenninen, "Analysis of capacity and scalability of the lora low power wide area network technology," in *European Wireless 2016; 22th European Wireless Conference*, May 2016, pp. 1–6.

[40] M. C. Bor, U. Roedig, T. Voigt, and J. M. Alonso, "Do lora low-power wide-area networks scale?" in *Proceedings of the 19th ACM International Conference on Modeling, Analysis and Simulation of Wireless and Mobile Systems*, ser. MSWiM '16. New York, NY, USA: ACM, 2016, pp. 59–67.

[41] J. Petajajarvi, K. Mikhaylov, A. Roivainen, T. Hanninen, and M. Pettissalo, "On the coverage of lpwans: range evaluation and channel attenuation model for lora technology," in *2015 14th International Conference on ITS Telecommunications (ITST)*, Dec 2015, pp. 55–59.

[42] B. Reynders, W. Meert, and S. Pollin, "Power and spreading factor control in low power wide area networks," in *2017 IEEE International Conference on Communications (ICC)*, May 2017, pp. 1–6.

[43] M. Lauridsen, I. Z. Kovacs, P. Mogensen, M. Sorensen, and S. Holst, "Coverage and capacity analysis of lte-m and nb-iot in a rural area," in *2016 IEEE 84th Vehicular Technology Conference (VTC-Fall)*, Sept 2016, pp. 1–5.

[44] N. Mangalvedhe, R. Ratasuk, and A. Ghosh, "Nb-iot deployment study for low power wide area cellular iot," in *2016 IEEE 27th Annual International Symposium on Personal, Indoor, and Mobile Radio Communications (PIMRC)*, Sept 2016, pp. 1–6.

[45] M. Centenaro, L. Vangelista, A. Zanella, and M. Zorzi, "Long-range communications in unlicensed bands: The rising stars in the iot and smart city scenarios," *IEEE Wireless Communications*, vol. 23, no. 5, pp. 60–67, 2016.

[46] A.-A. A. Bouleogeorgos, P. D. Diamantoulakis, and G. K. Karagiannidis, "Low power wide area networks (lpwans) for internet of things (iot) applications: Research challenges and future trends," *arXiv preprint arXiv:1611.07449*, 2016.

[47] X. Xiong, K. Zheng, R. Xu, W. Xiang, and P. Chatzimisios, "Low power wide area machine-to-machine networks: key techniques and prototype," *IEEE Communications Magazine*, vol. 53, no. 9, pp. 64–71, September 2015.

[48] K. E. Nolan, W. Guibene, and M. Y. Kelly, "An evaluation of low power wide area network technologies for the internet of things," in *2016 International Wireless Communications and Mobile Computing Conference (IWCMC)*, Sept 2016, pp. 439–444.

[49] L. Krupka, L. Vojtech, and M. Neruda, "The issue of lpwan technology coexistence in iot environment," in *2016 17th International Conference on Mechatronics - Mechatronika (ME)*, Dec 2016, pp. 1–8.

[50] B. Reynders, W. Meert, and S. Pollin, "Range and coexistence analysis of long range unlicensed communication," in *2016 23rd International Conference on Telecommunications (ICT)*, May 2016, pp. 1–6.

[51] H. Walker, "Ultra narrow band modulation," pp. 19–22, Apr 2004.

[52] S. Zhang, "Spectrum aanlyses of unb modulation formats," in *Consumer Electronics, Communications and Networks (CECNet), 2013 3rd International Conference on*. IEEE, 2013, pp. 594–597.

[53] P. Karn, "The vmsk delusion," http://www.ka9q.net/vmsk/, accessed: 2018-04-09.

[54] F. Xiong, F. Xiong, and F. Xiong, *Digital modulation techniques*. Artech House Boston, 2000, vol. 1886.

[55] M. Perrott, J. Salvia, F. Lee, A. Partridge, S. Mukherjee, C. Arft, J. Kim, N. Arumugam, P. Gupta, S. Tabatabaei, S. Pamarti, H. Lee, and F. Assaderaghi, "A temperature-to-digital converter for a mems-based programmable oscillator with $< \pm 0.5 - ppm$ frequency stability and $< 1 - ps$ integrated jitter," *Solid-State Circuits, IEEE Journal of*, vol. 48, no. 1, pp. 276–291, 01 2013.

[56] A. Laya, C. Kalalas, F. Vazquez-Gallego, L. Alonso, and J. Alonso-Zarate, "Goodbye, aloha!" *IEEE Access*, vol. 4, pp. 2029–2044, 2016.

[57] S. Kumar, V. S. Raghavan, and J. Deng, "Medium access control protocols for ad hoc wireless networks: A survey," *Ad Hoc Networks*, vol. 4, no. 3, pp. 326 – 358, 2006. [Online]. Available: http://www.sciencedirect.com/science/article/pii/S1570870504000873

[58] A. C. V. Gummalla and J. O. Limb, "Wireless medium access control protocols," *IEEE Communications Surveys Tutorials*, vol. 3, no. 2, pp. 2–15, Second 2000.

[59] M. Anteur, V. Deslandes, N. Thomas, and A. L. Beylot, "Ultra narrow band technique for low power wide area communications," in *2015 IEEE Global Communications Conference (GLOBECOM)*, Dec 2015, pp. 1–6.

[60] ——, "Modeling and performance analysis of ultra narrow band system for m2m," in *2016 8th Advanced Satellite Multimedia Systems Conference and the 14th Signal Processing for Space Communications Workshop (ASMS/SPSC)*, Sept 2016, pp. 1–6.

[61] H. Sallouha, A. Chiumento, and S. Pollin, "Localization in long-range ultra narrow band iot networks using rssi," in *2017 IEEE International Conference on Communications (ICC)*, May 2017, pp. 1–6.

[62] Y. Cao, M. Jia, J. Ma, and M. J. Abdoli, "Adjustable ultra narrow-band pulse for asynchronous 5g m2m communications," in *2015 IEEE 26th Annual International Symposium on Personal, Indoor, and Mobile Radio Communications (PIMRC)*, Aug 2015, pp. 883–888.

[63] T. Šolc, T. Gale, and C. Fortuna, "Optimization of ultra-narrowband wireless communication: An experimental case study," in *2017 IEEE Conference on Computer Communications Workshops (INFOCOM WKSHPS)*, May 2017, pp. 523–528.

[64] G. Zheng, I. Krikidis, C. Masouros, S. Timotheou, D. A. Toumpakaris, and Z. Ding, "Rethinking the role of interference in wireless networks," *IEEE Communications Magazine*, vol. 52, no. 11, pp. 152–158, Nov 2014.

[65] O. del Rio Herrero and R. De Gaudenzi, "Generalized analytical framework for the performance assessment of slotted random access protocols," *IEEE Transactions on Wireless Communications*, vol. 13, no. 2, pp. 809–821, 2014.

[66] S. Crozier and P. Webster, "Performance of 2-dimensional sloppy-slotted aloha random access signaling," in *Wireless Communications, 1992. Conference Proceedings., 1992 IEEE International Conference on Selected Topics in*. IEEE, 1992, pp. 383–386.

[67] K. N. Modi, S. Ponnaluri, S. G. Wilson, and M. Brandt-Pearce, "Aloha for wireless sensor networks with random frequency offsets," in *Information Sciences and Systems, 2007. CISS'07. 41st Annual Conference on*. IEEE, 2007, pp. 782–782.

[68] M. A. Mahmood, W. K. Seah, and I. Welch, "Reliability in wireless sensor networks: A survey and challenges ahead," *Computer Networks*, vol. 79, pp. 166–187, 2015.

[69] W. Riihinen and S. Johansson, "Link layer acknowledgement and retransmission for cellular telecommunications," Feb. 24 2004, uS Patent 6,697,331.

[70] H. Weatherspoon and J. D. Kubiatowicz, "Erasure coding vs. replication: A quantitative comparison," in *International Workshop on Peer-to-Peer Systems*. Springer, 2002, pp. 328–337.

[71] S. B. Wicker and V. K. Bhargava, *Reed-Solomon codes and their applications*. John Wiley & Sons, 1999.

[72] S.-Y. Chung, G. D. Forney, T. J. Richardson, and R. Urbanke, "On the design of low-density parity-check codes within 0.0045 db of the shannon limit," *IEEE Communications letters*, vol. 5, no. 2, pp. 58–60, 2001.

[73] D. J. MacKay, "Fountain codes," *IEE Proceedings-Communications*, vol. 152, no. 6, pp. 1062–1068, 2005.

[74] H. Wen, C. Lin, F. Ren, Y. Yue, and X. Huang, "Retransmission or redundancy: Transmission reliability in wireless sensor networks," in *Mobile Adhoc and Sensor Systems, 2007. MASS 2007. IEEE International Conference on*. IEEE, 2007, pp. 1–7.

[75] L. Tong, Q. Zhao, and G. Mergen, "Multipacket reception in random access wireless networks: From signal processing to optimal medium access control," *IEEE Communications Magazine*, vol. 39, no. 11, pp. 108–112, 2001.

[76] R. S. Sudhaakar, S. Yoon, J. Zhao, and C. Qiao, "A novel qos-aware mac scheme using optimal retransmission for wireless networks," *IEEE Transactions on Wireless Communications*, vol. 8, no. 5, 2009.

[77] X. Liu and H. Zhu, "Novel packet retransmission in ofdma systems using frequency diversity," in *Vehicular Technology Conference (VTC Spring), 2011 IEEE 73rd*. IEEE, 2011, pp. 1–5.

[78] J. F. C. Kingman, *Poisson processes*. Wiley Online Library, 1993.

[79] L. G. Roberts, "Aloha packet system with and without slots and capture," *ACM SIGCOMM Computer Communication Review*, vol. 5, no. 2, pp. 28–42, 1975.

[80] C. Artigue, "Method for searching for a useful signal in a multiplexing band," Sep. 19 2017, uS Patent 9,768,897.

[81] Y. Chen, "Introduction to probability theory," *Lecture Notes on Information Theory, Duisburg-Essen Univ., Duisburg, Germany*, 2010.

[82] C. E. Shannon, "A mathematical theory of communication," *The Bell System Technical Journal*, vol. 27, no. 3, pp. 379–423, Jul. 1948.

[83] M. K. Simon and M.-S. Alouini, *Digital communication over fading channels*. John Wiley & Sons, 2005, vol. 95.

[84] I. M. Habbab, M. Kavehrad, and C.-E. Sundberg, "Aloha with capture over slow and fast fading radio channels with coding and diversity," *IEEE Journal on selected areas in communications*, vol. 7, no. 1, pp. 79–88, 1989.

[85] J. Arnbak and W. Van Blitterswijk, "Capacity of slotted aloha in rayleigh-fading channels," *IEEE Journal on Selected Areas in Communications*, vol. 5, no. 2, pp. 261–269, 1987.

[86] J. Goseling, M. Gastpar, and J. H. Weber, "Line and lattice networks under deterministic interference models," *Information Theory, IEEE Transactions on*, vol. 57, no. 5, pp. 3080–3099, 2011.

[87] Z. Bharucha and H. Haas, "The distribution of path losses for uniformly distributed nodes in a circle," *Research Letters in Communications*, vol. 2008, p. 4, 2008.

[88] B. François and B. Bartłomiej, "Stochastic geometry and wireless networks: Volume i theory," 2009.

[89] H. ElSawy, E. Hossain, and M. Haenggi, "Stochastic geometry for modeling, analysis, and design of multi-tier and cognitive cellular wireless networks: A survey," *IEEE Communications Surveys Tutorials*, vol. 15, no. 3, pp. 996–1019, 2013.

[90] J. Lee and C. Tepedelenlioglu, "Stochastic ordering of interference in large-scale wireless networks," *Signal Processing, IEEE Transactions on*, vol. 62, no. 3, pp. 729–740, 2014.

[91] M. Haenggi, J. G. Andrews, F. Baccelli, O. Dousse, and M. Franceschetti, "Stochastic geometry and random graphs for the analysis and design of wireless networks," *IEEE Journal on Selected Areas in Communications*, vol. 27, no. 7, pp. 1029–1046, Sep. 2009.

[92] F. Baccelli, B. Błaszczyszyn, and P. Mühlethaler, "Stochastic analysis of spatial and opportunistic aloha," *Selected Areas in Communications, IEEE Journal on*, vol. 27, no. 7, pp. 1105–1119, 2009.

[93] M. Haenggi, "On distances in uniformly random networks," *IEEE Transactions on Information Theory*, vol. 51, no. 10, pp. 3584–3586, 2005.

[94] C. h. Lee and M. Haenggi, "Interference and outage in poisson cognitive networks," *IEEE Transactions on Wireless Communications*, vol. 11, no. 4, pp. 1392–1401, Apr. 2012.

[95] A. H. Sakr and E. Hossain, "Cognitive and energy harvesting-based d2d communication in cellular networks: Stochastic geometry modeling and analysis," *IEEE Transactions on Communications*, vol. 63, no. 5, pp. 1867–1880, May 2015.

[96] J. G. Andrews, F. Baccelli, and R. K. Ganti, "A tractable approach to coverage and rate in cellular networks," *Communications, IEEE Transactions on*, vol. 59, no. 11, pp. 3122–3134, 2011.

[97] M. Kountouris and N. Pappas, "Approximating the interference distribution in large wireless networks," in *Wireless Communications Systems (ISWCS), 2014 11th International Symposium on*. IEEE, 2014, pp. 80–84.

[98] M. Aljuaid and H. Yanikomeroglu, "Investigating the gaussian convergence of the distribution of the aggregate interference power in large wireless networks," *Vehicular Technology, IEEE Transactions on*, vol. 59, no. 9, pp. 4418–4424, 2010.

[99] H. Inaltekin and S. V. Hanly, "On the rates of convergence of the wireless multi-access interference distribution to the normal distribution," in *Modeling and Optimization in Mobile, Ad Hoc and Wireless Networks (WiOpt), 2010 Proceedings of the 8th International Symposium on*. IEEE, 2010, pp. 453–458.

[100] H. Inaltekin, "Gaussian approximation for the wireless multi-access interference distribution," *Signal Processing, IEEE Transactions on*, vol. 60, no. 11, pp. 6114–6120, 2012.

[101] M. Aljuaid and H. Yanikomeroglu, "A cumulant-based characterization of the aggregate interference power in wireless networks," in *Vehicular Technology Conference (VTC 2010-Spring), 2010 IEEE 71st*. IEEE, 2010, pp. 1–5.

[102] P. Huang, L. Xiao, S. Soltani, M. W. Mutka, and N. Xi, "The evolution of mac protocols in wireless sensor networks: A survey," *Communications Surveys & Tutorials, IEEE*, vol. 15, no. 1, pp. 101–120, 2013.

[103] A. Bachir, M. Dohler, T. Watteyne, and K. K. Leung, "Mac essentials for wireless sensor networks," *Communications Surveys & Tutorials, IEEE*, vol. 12, no. 2, pp. 222–248, 2010.

[104] H. K. Le, D. Henriksson, and T. Abdelzaher, "A practical multi-channel media access control protocol for wireless sensor networks," in *Proceedings of the 7th international conference on Information processing in sensor networks*. IEEE Computer Society, 2008, pp. 70–81.

[105] Y. Wu, J. A. Stankovic, T. He, and S. Lin, "Realistic and efficient multi-channel communications in wireless sensor networks," in *INFOCOM 2008. The 27th Conference on Computer Communications. IEEE*. IEEE, 2008.

[106] Q. Yu, J. Chen, Y. Fan, X. S. Shen, and Y. Sun, "Multi-channel assignment in wireless sensor networks: A game theoretic approach," in *INFOCOM, 2010 Proceedings IEEE*. IEEE, 2010, pp. 1–9.

[107] N. Abramson, "Multiple access in wireless digital networks," *Proceedings of the IEEE*, vol. 82, no. 9, pp. 1360–1370, 1994.

[108] B. Błaszczyszyn, M. K. Karray, and H. P. Keeler, "Using poisson processes to model lattice cellular networks," in *INFOCOM, 2013 Proceedings IEEE*, April 2013, pp. 773–781.

[109] J.-M. Gorce, D. Tsilimantos, P. Ferrand, and H. V. Poor, "Energy-capacity trade-off bounds in a downlink typical cell," in *Proc. IEEE 25th International Symposium on Personal, Indoor and Mobile Radio Communications (PIMRC)*, 2014.

[110] E. B. Hamida, G. Chelius, and J.-M. Gorce, "Scalable versus accurate physical layer modeling in wireless network simulations," in *Proceedings of the 22nd Workshop on Principles of Advanced and Distributed Simulation*. IEEE Computer Society, 2008, pp. 127–134.

[111] T. D. Novlan, H. S. Dhillon, and J. G. Andrews, "Analytical modeling of uplink cellular networks," *IEEE Transactions on Wireless Communications*, vol. 12, no. 6, pp. 2669–2679, Jun. 2013.

[112] R. Durrett, *Probability: theory and examples*. Cambridge university press, 2010.

[113] D. J. Daley and D. Vere-Jones, *An introduction to the theory of point processes: volume II: general theory and structure*. Springer Science & Business Media, 2007.

[114] R. V. Hogg and E. A. Tanis, *Probability and statistical inference*. Pearson Educational International, 2009.

[115] J. G. Andrews, "Interference cancellation for cellular systems: a contemporary overview," *IEEE Wireless Communications*, vol. 12, no. 2, pp. 19–29, Apr. 2005.

[116] R. Liu, Y. Shi, K. S. Lui, M. Sheng, Y. Wang, and Y. Li, "Bandwidth-aware high-throughput routing with successive interference cancelation in multi-hop wireless networks," *IEEE Transactions on Vehicular Technology*, vol. 64, no. 12, pp. 5866–5877, Dec. 2015.

[117] S. Sen, N. Santhapuri, R. R. Choudhury, and S. Nelakuditi, "Successive interference cancellation: A back-of-the-envelope perspective," in *Proceedings of the 9th ACM SIGCOMM Workshop on Hot Topics in Networks*, ser. Hotnets-IX. New York, NY, USA: ACM, 2010, pp. 17:1–17:6.

[118] N. I. Miridakis and D. D. Vergados, "A survey on the successive interference cancellation performance for single-antenna and multiple-antenna OFDM systems," *IEEE Communications Surveys Tutorials*, vol. 15, no. 1, pp. 312–335, 2013.

[119] J. Laiho, A. Wacker, and T. Novosad, *Radio network planning and optimisation for UMTS*. John Wiley & Sons, 2006.

[120] T. L. Marzetta, "Noncooperative cellular wireless with unlimited numbers of base station antennas," *IEEE Transactions on Wireless Communications*, vol. 9, no. 11, pp. 3590–3600, 2010.

[121] M. Corson and A. Ephremides, "An analysis of multi-receiver, non-adaptive, slotted aloha with capture for wireless communications in factories," in *IEEE INFOCOM 1993 The Conference on Computer Communications, Proceedings*. IEEE Comnput. Soc. Press.

[122] A. Munari, F. Clazzer, and G. Liva, "Multi-receiver aloha systems - a survey and new results," in *2015 IEEE International Conference on Communication Workshop (ICCW)*, Jun. 2015, pp. 2108–2114.

[123] A. Checko, H. L. Christiansen, Y. Yan, L. Scolari, G. Kardaras, M. S. Berger, and L. Dittmann, "Cloud ran for mobile networks: A technology overview," *IEEE Communications Surveys Tutorials*, vol. 17, no. 1, pp. 405–426, Firstquarter 2015.

[124] M. D. Renzo and P. Guan, "Stochastic geometry modeling and system-level analysis of uplink heterogeneous cellular networks with multi-antenna base stations," *IEEE Transactions on Communications*, vol. 64, no. 6, pp. 2453–2476, Jun. 2016.

[125] T. Bai and R. W. Heath, "Analyzing uplink sinr and rate in massive mimo systems using stochastic geometry," *IEEE Transactions on Communications*, vol. 64, no. 11, pp. 4592–4606, Nov 2016.

[126] Q. Song, X. Lagrange, and L. Nuaymi, "Evaluation of macro diversity gain in long range aloha networks," *IEEE Communications Letters*, vol. 21, no. 11, pp. 2472–2475, Nov 2017.

[127] M. Haenggi and R. K. Ganti, "Interference in large wireless networks," *Found. Trends Netw.*, vol. 3, no. 2, pp. 127–248, Feb. 2009. [Online]. Available: http://dx.doi.org/10.1561/1300000015

[128] J. G. Andrews, F. Baccelli, and R. K. Ganti, "A tractable approach to coverage and rate in cellular networks," *IEEE Transactions on Communications*, vol. 59, no. 11, pp. 3122–3134, Nov. 2011.

[129] A. M. J. E. Handricks, *The analyst. a journal of pure and applied mathematics*, 1876.

[130] B. Blaszczyszyn and P. Mühlethaler, "Interference and SINR coverage in spatial non-slotted aloha networks," *CoRR*, vol. abs/1411.3130, 2014.

[131] E. Artin, *The gamma function*. Courier Dover Publications, 2015.

[132] A. Goldsmith, *Wireless communications*. Cambridge university press, 2005.

[133] T. Eng, N. Kong, and L. B. Milstein, "Comparison of diversity combining techniques for rayleigh-fading channels," *IEEE Transactions on communications*, vol. 44, no. 9, pp. 1117–1129, 1996.

[134] R. Sodhi and R. Khanna, "Analysis of hybrid diversity combining technique over twdp fading channel," *Indian Journal of Science and Technology*, vol. 9, no. 47, 2016.

[135] D. Brennan, "Linear diversity combining techniques," *Proceedings of the IEEE*, vol. 91, no. 2, pp. 331–356, 2003.

[136] R. V. Kadison, "A generalized schwarz inequality and algebraic invariants for operator algebras," *Annals of Mathematics*, pp. 494–503, 1952.

[137] E. Aktas, J. Evans, and S. Hanly, "Distributed decoding in a cellular multiple-access channel," in *International Symposium onInformation Theory, 2004. ISIT 2004. Proceedings.*, June 2004, pp. 484–.

[138] D. Gesbert, S. Hanly, H. Huang, S. S. Shitz, O. Simeone, and W. Yu, "Multi-cell mimo cooperative networks: A new look at interference," *IEEE Journal on Selected Areas in Communications*, vol. 28, no. 9, pp. 1380–1408, December 2010.

[139] D. JakovetiÄ‡, D. BajoviÄ‡, D. VukobratoviÄ‡, and V. CrnojeviÄ‡, "Cooperative slotted aloha for multi-base station systems," *IEEE Transactions on Communications*, vol. 63, no. 4, pp. 1443–1456, Apr. 2015.

[140] M. A. Weitnauer, Q. Lin, H. Zhang, H. Tian, S. Nowlan, G. Nyengele, S. M. Chakkedath, and J. Slratigos, "Reliability and longer range for low power transmitters with on demand network mimo," in *2016 IEEE International Conference on RFID (RFID)*, May 2016, pp. 1–10.

[141] A. Mastilovic, D. Vukobratovic, D. Jakovetic, and D. Bajovic, "Cooperative slotted ALOHA for massive M2M random access using directional antennas," *CoRR*, vol. abs/1706.09817, 2017.

[142] M. Dillinger, K. Madani, and N. Alonistioti, *Software defined radio: Architectures, systems and functions*. John Wiley & Sons, 2005.

[143] Y. MO, C. Goursaud, and J.-M. Gorce, "Bénéfice de l'annulation successive d'interférence pour des réseaux ultra narrow band : Théorie et application à l'iot," in *ALGOTEL 2018 - 20èmes Rencontres Francophones sur les Aspects Algorithmiques des Télécommunications*, Roscoff, France, May 2018, pp. 1–4.

[144] Y. Mo, C. Goursaud, and J.-M. Gorce, "Performance théorique de réseaux iot basés sur unb avec path loss," in *GRETSI 2017*, ser. XXVIe Colloque GRETSI, Juan-les-Pins, France, 2017.

[145] Y. Mo, M.-T. Do, C. Goursaud, and J.-M. Gorce, "Impact du nombre de répliques sur les performances d'un réseau iot basé sur des transmissions ultra narrow band," in *ALGOTEL 2016 - 18èmes Rencontres Francophones sur les Aspects Algorithmiques des Télécommunications*, ser. ALGOTEL 2016 - 18èmes Rencontres Francophones sur les Aspects Algorithmiques des Télécommunications, Bayonne, France, May 2016.

FOLIO ADMINISTRATIF

THESE DE L'UNIVERSITE DE LYON OPEREE AU SEIN DE L'INSA LYON

NOM : MO
(avec précision du nom de jeune fille, le cas échéant)

DATE de SOUTENANCE : 26/09/2018

Prénoms : Yuqi

TITRE : Ultra Narrow Band based IoT networks

NATURE : Doctorat

Numéro d'ordre : 2018LYSEI069

Ecole doctorale : Electronique, Electrotechnique, Automatique

Spécialité : Traitement du Signal et de l'Image

RESUME :

La compagnie Sigfox est reconnue comme un acteur prometteur pour des transmissions de longue-distance et faible consommation, dans le contexte de l'IoT. La modulation à bande ultra étroite (Ultra Narrow Band (UNB)), la technologie de communication choisie par Sigfox, permet de transmettre des informations dans des bandes de signal très étroites (typiquement 100 Hz). A cause de l'imprécision fréquentielle causée par les oscillateurs générateurs de fréquence, il n'est pas réaliste de transmettre des signaux UNB dans des canaux parfaitement orthogonaux. L'accès naturel au canal radio pour le système de UNB est de type ALOHA, avec un aspect aléatoire à la fois en en temps et en fréquence. Cet accès aléatoire peut introduire des collisions qui dégradent la performance du réseau.

Le but de cette thèse est de caractériser la capacité des réseaux basés sur UNB, ainsi que d'améliorer la performance en considérant l'aspect aléatoire en temps et en fréquence.

La première contribution de cette thèse, est une évaluation de la capacité en théorie et en simulation pour une seule station de base (BS), sous des conditions de canal idéaliste ou réaliste. En conditions idéalistes, nous avons exprimé la capacité pour le cas de l'ALOHA généralisé, et l'avons étendu aux cas de réplications. Pour les conditions réalistes, nous avons pris en compte l'interférence spectrale d'UNB et le path loss (sans et avec Rayleigh fading) afin de caractériser la performance des réseaux UNB, avec l'outil géométrie stochastique.

La deuxième contribution est d'appliquer l'annulation successive d'interférence (SIC), qui nous permet d'atténuer les interférences, dans des réseaux de UNB. Nous avons fourni une analyse théorique de la performance des réseaux en considérant le SIC et l'interférence spectrale de UNB, pour le cas de mono-BS. Nous avons démontré que le SIC permet d'améliorer efficacement les performances des systèmes UNB.

La troisième contribution est l'amélioration de la performance des réseaux UNB, en exploitant la diversité de multi-BS. Nous avons fait une analyse théorique de performance en considérant multi-BS et selection combining (SC). En particulier, nous avons considéré que l'interférence vue par chaque BS est corrélée. Nous avons ainsi démontré mathématiquement que cette corrélation ne peut pas être supprimée dans des systèmes UNB. Ensuite, nous avons appliqué les technologies de la combinaison des signaux plus complexes comme MRC (max ratio combining) et EGC (equal gain combining), ainsi que le SIC à travers multi-BS. Nous avons évalué l'amélioration de performance que chaque technologie apporte, et les avons comparées. Nous avons souligné l'efficacité de ces technologies qui nous permettent d'obtenir des gains importants comparés au cas mono-BS (e.x. 125 fois plus de réduction d'erreur avec SIC globale).

La dernière contribution est une validation expérimentale du modèle d'interférence spectrale de UNB, ainsi que la capacité des réseaux UNB, sur un testbed de radio FIT/Cortexlab.

MOTS-CLÉS : IoT, LPWAN, Sigfox, UNB, interférence spectrale, évaluation de performance, mult-BS

Laboratoire (s) de recherche : CITI

Directeur de thèse: Jean-Marie GORCE

Président de jury : Maryline HELARD

Composition du jury :

ANTON-HARO Carles	Directeur de recherche	Centre technology de Télécommunications de Catalunya, Catalunya	Rapporteur
DI RENZO Marco	HDR	Université Paris-Saclay, France	Rapporteur
HELARD Maryline	Professeur	INSA-Rennes, France	Examinatrice
VERDONE Roberto	Professeur	University of Bologna, Italie	Examinateur
GORCE Jean-Marie	Professeur	INSA-Lyon, France	Directeur de thèse
GOURSAUD Claire	HDR	INSA-Lyon, France	Co-directrice de thèse
PONSARD Benoît	Ingénieur	Sigfox, France	Invité